Magnetic field sensor based on micro-structured magnetoelastic surface acoustic waves devices

Harshad Mishra

To cite this version:

Harshad Mishra. Magnetic field sensor based on micro-structured magnetoelastic surface acoustic waves devices. Physics [physics]. Université de Lorraine, 2019. English. NNT : 2019LORR0147 . tel-03137749

HAL Id: tel-03137749

https://hal.univ-lorraine.fr/tel-03137749

Submitted on 10 Feb 2021

THÈSE

Pour l’obtention du titre de :

Docteur de l’université de Lorraine

Doctorale Spécialité : *Physique*

Scientific area : Département Sciences pour l’ingénieur

Présentée par :

Harshad Mishra

Magnetic field sensor based on micro-structured magnetoelastic surface acoustic waves devices

---

Thèse soutenue publiquement 18 Novembre 2019 à Nancy devant jury composé de :

Mme. Pallavi Dhagat	Professeur, Oregon State University	Rapporteur
M. Keekeun Lee	Professeur, Ajou University	Rapporteur
M. Michel Hehn	Professeur, Université de Lorraine,	Examinateur
M. Sergei Zhgoon	Professeur, Moscow Power Engineering Institute	Examinateur
M. Sami Hage-Ali	Maitre de Conférence, Université de Lorraine	Co-Directeur de thèse
M. Omar Elmazria	Professeur, Université de Lorraine	Directeur de thèse

Institut Jean Lamour – UMR 7198 – Département N2EV – Equipe 405
Campus Artem – 2 allée André Guinier – 54011 Nancy Cedex
Université de Lorraine

I was born not knowing and have had only a little time to change that here and there.

- Richard Feynman

Acknowledgement

Earning this PhD would not have been possible alone. And hence I take this opportunity to convey my heartfelt gratitude to all those who help, motivated and guided me all along this challenging three year journey.

First, I would like to extend a sincere thanks to the members of the thesis review committee, Pallavi Dhagat and Keekeun Lee for their time and interest in reviewing my thesis. I am grateful for the insightful comments they have made on the thesis thereby improving the quality of my work. I would also like to thank Sergei Zhgoon for his time and patience with my thesis and improving it through his insightful questions and comments.

My sincere thanks goes to Michel Hehn for all his help and guidance in these three years. His demand for a thorough scientific knowledge during my PhD has driven me to seek explanations for every single aspect of research. He has been an inspiration for me and I shall always carry his advice and guidance for the long journey of my career that lies ahead. I have been very fortunate to have him as one of my principal collaborators during this PhD.

I would also like to extend my thanks to my PhD advisors Omar Elmazria and Sami Hage-Ali for their insightful advice and guidance during this PhD. Their constructive reviews of my work has helped me a lot. The memories and experiences I had while in their team, will remain with me always.

I would also like to thank my collaborators, Nicolas Tiercelin, Abdelkrim Talbi, Olivier BouMatar, Yannick Dusch and Aurelien from IEMN, Lille for their help and guidance during this PhD. I also thank Nicolas for the multi-layered samples that virtually laid the foundation of my work. I also thank collaborators from the Nanomagnetism and Spintonics team at IJL especially Daniel Lacour, Karine Dumesnil and Sebastien Petit-Watelot for their helpful discussions, motivation and many more. I also thank Sebastien for his allowing me to use his experimental setup for the measurements of the magneto-acoustic responses.

I wish also to thank all my colleagues in the team 405 who have extended their help and support in many different forms. I also thank the interns in the lab for their assistance whenever needed especially Louis and Clement. I convey my thanks to Prince Warel for his assistance is running the simulations and also growing a nice friendship ! Talking of friendship, I also especially thank Vincent Polewczyk and Jeremy Streque who have not only been helpful colleagues but also grown to be very good friends over time.

I also extend my sincere thanks to the members of the MINALOR nanofabrication centre, especially Laurent Badie, Gwladys Lengaigne and Carlos Rojas Sanchez for their unending support during the many hours I have spent in the clean room. Their guidance and support in my training with the different equipments and also subsequent help whenever I requested for it has brought me a long way. Of course with Laurent, I will miss also our culinary exchanges...

I would also like to thank Thomas Hauet, Stephane Suire, Crossby Chang and Tom Fert for their help and training with the CC Magnetism equipments.

I also extend my thanks to all my friends here in Nancy and at IJL. I am not taking any of their names here for fear of missing out anyone from the large list. The memories made shall last a lifetime and so will the friendships.

In the end, I thank my family, especially my parents Sandhyarani Palo and Nihar Ranjan Mishra and my wife Annya for their unending support and patience with me throughout this challenging journey. Without them, this journey would not have been possible. I also thank my family-in-law of Soubhagyalaxmi Acharya and Prashanta Kar for their belief in me and their love and support.

Abstract

The last few decades has seen tremendous growth in the area of sensor technologies. The field has grown from simple micro-machined silicon based devices to more complex integrated microsystems combining high performance transducers as well as wireless interfaces. Primarily, these devices are based on measurement of associated parameters which may be physical, chemical, electrical or magnetic in nature. Thus, acoustic waves come into prominence by virtue of their simultaneous sensing as well as actuation ability. Not only do they reduce the complexity but also impart a multifunctionality to the device. Magnetic sensors available today in the market may be classified as high field, medium field or low field devices depending on the range of field in which they measure. However, almost all of these devices operate with a complex mechanism while simultaneously being externally powered as well as expensive. Thus there arises a deep need to develop a magnetic sensor that overcomes the challenges. This research work focused on the development of surface acoustic wave (SAW) sensors for the detection of magnetic field.

Owing to the possibility of wireless interrogation, SAW devices of the resonator configuration have been considered in this study. In the magnetic surface acoustic wave (MSAW) devices, it is known that the resonance frequency is sensitive to external magnetic field, primarily through both static effects related to the field-induced magnetization changes, and the magnetoelastic dynamic effects related to the acoustic wave. In our work, we have attempted to study and relate the magneto-acoustic responses of the MSAW devices to its magnetic anisotropy. On a more generalized perspective, we have investigated the possibility to engineer the magneto-acoustic response, and thereby the sensitivity of the device, by optimizing the magnetic properties as well as thermal effects on the elastic and magnetic properties, to suit specific requirements.

The first part of our work aims to address the physics and interaction between the acoustic waves and magnetostrictive layers when subjected to a magnetic field. We investigated SAW devices of the resonator geometry using LiNbO3 as the substrate and multi-layered [$TbCo_2$/FeCo] as the electrode and sensitive material. We showed the role of the shape effect in magnetism arising

from the electrode geometry. In our work, we have taken the opportunity to show that depending on factors such as the crystalline orientation of the substrate, the relative magnetization direction, the effective magnetic anisotropy as well as the nature of the acoustic wave, it is possible to design the sensor to be effective in a concerned magnetic field region with a specific sensitivity. A model experimental set-up is developed with one of the device to demonstrate an application of the fabricated devices as a sensor for detection of current along a cable. However, this specific work brought to light the need for a sensor that is able to provide a stable measurement even under unstable thermal environments. Thus in the next part of our work, we developed a device that is self-compensated, for the drift of the resonance frequency with an increase of the temperature. The multi-layered sensor was based on ST-cut Quartz as the substrate whose positive temperature coefficient of frequency (TCF) was compensated for by the negative TCF of ZnO and CoFeB. The CoFeB layer provided the requisite effect for sensing the external magnetic field. A Love wave based structure was chosen for this study to provide a sensitivity higher than conventional Rayleigh wave based devices. Experimental results show that a high sensitivity MSAW sensor with almost zero TCF was achieved.

Subsequently, we address another important aspect due to temperature, the change of the magnetic anisotropy. A rising temperature causes an increase of the energy of the system and thus leads to the effective anisotropy of the sensitive magnetic layer to decrease, thereby causing changes to the MSAW response as well. Therefore, in this section, we combine our understandings of the shape effects of magnetism with the temperature compensated multi-layered structure. The developed sensor is therefore immune to the effects of temperature on the resonance frequency as well as on the magnetic anisotropy. The first owing to its multi-layered structure and the later due to CoFeB layer that is microstructured as stripes, instead of a full film. In addition, this structure also presents the possibility of a proof-of-concept multi-sensory device, because in addition to the temperature compensated resonance peak, there exist other resonances which are highly sensitive to any change in the temperature while at the same time immune to magnetic field.

Sommaire en Français

Au cours des dernières décennies, on a assisté à une croissance considérable dans le domaine des technologies de capteurs. Le domaine est passé de simples dispositifs micro-usinés à base de silicium à des microsystèmes intégrés plus complexes combinant des transducteurs de haute performance ainsi que des interfaces sans fil. Ces appareils sont principalement basés sur la mesure de paramètres associés qui peuvent être de nature physique, chimique, électrique ou magnétique. Ainsi, les ondes acoustiques prennent de l'importance en raison de leur capacité de détection simultanée ainsi que de leur capacité d'activation. Non seulement ils réduisent la complexité, mais ils confèrent également une multifonctionnalité à l'appareil. Les capteurs magnétiques disponibles aujourd'hui sur le marché peuvent être classés en appareils à champ élevé, moyen ou faible, selon la plage de champ dans laquelle ils mesurent. Cependant, presque tous ces appareils fonctionnent avec un mécanisme complexe tout en étant alimentés simultanément de l'extérieur et coûteux. Il y a donc un besoin profond de développer un capteur magnétique qui surmonte les défis. Ces travaux de recherche ont porté sur le développement de capteurs à ondes acoustiques de surface (SAW) pour la détection des champs magnétiques.

Les dispositifs SAW sont le résultat de décennies de recherche et de développement dans le domaine des dispositifs micro-électromécaniques et des technologies de fabrication à l'échelle micro/nano. Ils sont utilisés dans un large éventail de domaines d'application, des télécommunications à l'automobile, en passant par l'aéronautique et même dans l'industrie biomédicale. Les dispositifs SAW sont des composants clés des systèmes de communication et sont largement utilisés comme filtres, lignes de retard ou résonateurs. Parce qu'ils sont très sensibles aux paramètres physiques externes et à toute perturbation pouvant affecter la vitesse, la distance parcourue ou même le mode de propagation des ondes, les dispositifs SAW offrent également des solutions prometteuses dans un large éventail d'applications, notamment les capteurs physiques et chimiques.

Les appareils SAW représentent donc un marché considérable, notamment dans le domaine des télécommunications en raison de leurs performances. Par conséquent, ce domaine des appareils SAW est aujourd'hui une technologie industrielle très mature grâce à son faible coût de fabrication, sa petite taille, sa robustesse et les possibilités d'applications innovantes en tant que capteurs. De plus, ces appareils ont l'avantage d'être sans batterie (passive), sans fil et sans emballage dans des configurations spécifiques. L'utilisation de dispositifs SAW en tant que capteurs passifs (sans batterie ni électronique intégrée) et sans fil leur permet de fonctionner dans des pièces rotatives et/ou dans des conditions extrêmes telles que des niveaux élevés de rayonnement, des températures élevées ou des interférences électromagnétiques, dans lesquelles aucun autre capteur sans fil ne peut fonctionner. Ceci est évidemment conditionné par le fait que les matériaux constituant l'appareil peuvent résister à ces conditions difficiles. Associés à des substrats souples, les capteurs SAW trouveront des applications dans le domaine biomédical et du bien-être pour une surveillance continue des paramètres du corps humain.

Qu'il s'agisse de capteurs physiques tels que la température, la pression, la contrainte, l'accélération et la détection magnétique, chimique ou gazeuse ou même biologique, les dispositifs SAW ont marqué leur excellence dans de nombreux domaines. La technologie de détection du champ magnétique a également évolué depuis ses débuts en tant qu'outil de navigation à travers les océans non marqués jusqu'à l'époque actuelle où l'on utilise des réseaux de capteurs magnétiques pour détecter la présence, la force et la direction d'un champ magnétique, non seulement de la terre elle-même mais aussi d'autres sources.

En raison de la possibilité d'interrogation sans fil, les dispositifs SAW de la configuration du résonateur ont été considérés dans cette étude. Dans les dispositifs à ondes acoustiques de surface magnétiques (MSAW), on sait que la fréquence de résonance est sensible au champ magnétique externe, principalement en raison des effets statiques liés aux changements de magnétisation induits par le champ et des effets magnéto-élastiques dynamiques liés à l'onde acoustique.

Dans notre travail, nous avons tenté d'étudier et de relier les réponses magnéto-acoustiques des dispositifs MSAW à leur anisotropie magnétique. D'un point de vue plus général, nous avons étudié la possibilité de concevoir la réponse magnéto-acoustique, et donc la sensibilité du dispositif, en optimisant les propriétés magnétiques ainsi que les effets thermiques sur les propriétés élastiques et magnétiques, en fonction des besoins spécifiques.

La première partie de notre travail vise à étudier la physique et l'interaction entre les ondes acoustiques et les couches magnétostrictives lorsqu'elles sont soumises à un champ magnétique. Nous avons étudié les dispositifs SAW de la géométrie du résonateur en utilisant LiNbO3 comme substrat et multicouches[$TbCo_2$/FeCo] comme électrode et matériau sensible. Nous avons montré le rôle de l'effet de forme dans le magnétisme résultant de la géométrie de l'électrode. Dans notre travail, nous avons profité de l'occasion pour montrer qu'en fonction de facteurs tels que l'orientation cristalline du substrat, la direction de magnétisation relative, l'anisotropie magnétique effective ainsi que la nature de l'onde acoustique, il est possible de concevoir le capteur pour être efficace dans une région concernée du champ magnétique avec une sensibilité spécifique. Un montage expérimental modèle est développé avec l'un des dispositifs pour démontrer une application des dispositifs fabriqués en tant que capteur pour la détection du courant le long d'un câble. Cependant, ce travail spécifique a mis en évidence le besoin d'un capteur capable de fournir une mesure stable même dans des environnements thermiques instables. C'est ainsi que dans la suite de notre travail, nous avons développé un dispositif d'auto-compensation de la dérive de la fréquence de résonance en fonction de l'augmentation de la température. Le capteur multicouche était basé sur le quartz découpé ST comme substrat dont le coefficient de température positif (TCF) était compensé par le TCF négatif du ZnO et du CoFeB. La couche CoFeB a fourni l'effet nécessaire pour détecter le champ magnétique externe. Une structure basée sur l'onde de Love a été choisie pour cette étude afin de fournir une sensibilité supérieure à celle des dispositifs conventionnels à ondes de Rayleigh. Les résultats expérimentaux montrent qu'un capteur MSAW à haute sensibilité avec un TCF presque nul a été obtenu.

Ensuite, nous abordons un autre aspect important dû à la température, le changement de l'anisotropie magnétique. Une augmentation de la température entraîne une augmentation de l'énergie du système et donc une diminution de l'anisotropie effective de la couche magnétique sensible, ce qui entraîne également des modifications de la réponse MSAW. Par conséquent, dans cette section, nous combinons notre compréhension des effets de forme du magnétisme avec la structure multicouche à compensation thermique. Le capteur développé est donc immunisé contre les effets de la température sur la fréquence de résonance ainsi que sur l'anisotropie magnétique. Le premier en raison de sa structure multicouche et le second en raison de la couche de CoFeB qui est microstructurée en bandes, au lieu d'un film complet. De plus, cette structure présente également la possibilité d'un dispositif multisensoriel de preuve de concept, car en plus du pic de résonance compensé en température, il existe d'autres résonances qui sont très sensibles à tout changement de température tout en étant immunes au champ magnétique.

Comparés aux mesures électriques conventionnelles, ces systèmes micro-électromécaniques (MEMS) offrent un système de mesure rapide et sans contact avec la possibilité d'une meilleure résolution. De plus, contrairement aux systèmes à base de SQUID, ces dispositifs ont le potentiel de fonctionner sans aucun système de refroidissement ou de blindage à grande échelle et sont donc beaucoup plus rentables. Ces dispositifs sont également de nature non invasive et non destructive. Ce travail de recherche vise donc à répondre aux besoins fondamentaux d'un capteur adapté à des applications industrielles telles que la stabilité thermique, une conception simple mais fiable, facilement reproductible et à faible coût de fabrication.

Les applications ciblées des capteurs développés dans cette étude concernent des applications industrielles telles que la détection de proximité, la détection et le positionnement de déplacement, la détection de rotation, la détection de courant et la détection de mouvement de corps ferreux (par ex. voitures). En tant que capteurs de proximité, ils utilisent les champs magnétiques DC, tandis que les applications liées à la détection de déplacement et de position se concentrent davantage sur l'utilisation du profil de champ parasite de l'objet contrôlé. Ainsi, les appareils peuvent également agir comme une version sans contact d'un interrupteur. De plus, en tant que capteurs de courant, les appareils sont capables d'effectuer des mesures sans contact et électriquement découplées dans le courant continu à quelques centaines de MHz et peuvent également fonctionner comme gradimètres. Les corps ferreux déforment les lignes de champ magnétique, ce qui constitue la base de leur détection par les capteurs. Une surveillance synchrone de la carrosserie à l'aide de deux réseaux perpendiculaires de capteurs peut fournir des informations sur sa présence, sa direction et sa vitesse, tandis qu'un positionnement sur trois axes permet également une classification du véhicule. Les principaux avantages de ces appareils dans tous ces domaines d'application possibles sont leur taille, leur poids et leur consommation électrique.

Ne se limitant pas aux applications industrielles comme mentionné ci-dessus, la polyvalence de ces dispositifs peut être facilement étendue pour les études biomédicales en les combinant avec des techniques électroniques et de réduction du bruit appropriées ainsi que des algorithmes de traitement de données spécialisés. Ainsi, la réalisation de capteurs de champ magnétique à base de SAW nous permet de bénéficier des avantages classiques de la technologie SAW tels que le faible coût, l'ouverture minimale, la robustesse et la fiabilité tout en nous permettant d'explorer des configurations de dispositifs passifs (sans batterie) et interrogeables à distance (sans fil), ouvrant ainsi la voie à de nouvelles applications sans précédent.

Organisation de la thèse : La thèse est organisée en cinq chapitres, chacun abordant et décrivant en détail des aspects spécifiques du travail de recherche allant de la conception du dispositif et de sa fabrication à sa caractérisation.

Le premier chapitre est consacré à l'introduction du sujet et est divisé en trois sous-sections. Dans la première sous-section, nous traitons des dispositifs SAW, de la physique derrière leur fonctionnement et de leurs applications générales. Dans la deuxième sous-section, nous présentons et discutons les technologies de capteurs magnétiques actuellement disponibles et leurs principes de fonctionnement. Enfin, dans la troisième sous-section, nous nous concentrons sur les capteurs magnétiques SAW et discutons de leur physique et de leurs domaines d'application possibles.

Dans le deuxième chapitre, nous étudions, au moyen de simulations, l'effet du changement des divers paramètres géométriques du dispositif SAW sur sa réponse magnéto-acoustique. L'étude considère un comportement de magnétisation idéal basé sur le modèle Stoner-Wohlfarth comme un standard pour tous les appareils. Ce chapitre constitue donc une base pour notre compréhension du dispositif et nous permet de développer les stratégies expérimentales nécessaires pour la prochaine partie de l'étude.

Le troisième chapitre présente les dispositifs fabriqués en utilisant une couche multicouche[$TbCo_2$/FeCo] comme couche magnétostrictive sensible à partir de laquelle les électrodes sont fabriquées. L'objectif de ce chapitre est d'étudier les effets de l'anisotropie de forme dans l'appareil et d'approfondir notre compréhension de sa réponse magnéto-acoustique. Il ouvre également la voie à la conception de l'appareil pour qu'il soit sensible dans une gamme spécifique de champ magnétique. Le chapitre détaille les différentes étapes de fabrication, suivies des caractérisations expérimentales effectuées et de leurs résultats. Afin de démontrer l'aspect pratique de notre appareil, un prototype de structure est conçu et mis en œuvre pour l'utiliser comme capteur pour surveiller le courant dans un câble. Les défis liés à la température associés au prototype sont également abordés, ce qui mène aux travaux de recherche subséquents présentés dans les chapitres suivants.

Le quatrième chapitre présente un résonateur SAW amélioré basé sur une structure de dispositif multicouche dans le but d'atténuer les effets de la température. La structure est basée sur un effet d'annulation obtenu en optimisant les épaisseurs des couches de ZnO et de CoFeB sur un substrat de quartz découpé ST. Les effets de la température sur la fréquence de résonance sont d'abord présentés, suivis d'une description du procédé de fabrication. Les caractérisations et les résultats obtenus sont ensuite présentés et discutés.

Au-delà de l'effet bien connu de la température sur la fréquence de résonance du dispositif SAW, le cinquième chapitre porte sur un autre effet important associé à une température instable. L'effet de la température sur l'anisotropie magnétique est d'abord décrit et les effets de forme en magnétisation qui ont été étudiés précédemment, sont utilisés pour proposer une solution. Les différentes étapes du processus de fabrication sont ensuite détaillées, suivies des caractérisations magnétiques et acoustiques. Les résultats obtenus sont enfin présentés et discutés. Un comportement magnétique presque sans hystérésis est obtenu dans les couches magnétostrictives. Une possibilité unique de dispositif multifonctionnel est également proposée dans le chapitre où le dispositif concerné montre une sensibilité à la fois à la température et au champ magnétique, tout en étant indépendant les uns des autres.

Enfin, un résumé des travaux de recherche entrepris dans le cadre de cette thèse est présenté ainsi qu'une perspective des diverses possibilités futures dans les conclusions générales.

Contents

Chapter 1: Surface Acoustic Wave Devices for Magnetic Field Detection

Chapter 2: Optimization of the SAW structure

Chapter 3: Studies on magnetic SAW sensors based on [$TbCo_2$/FeCo] multi-layered electrodes

Chapter 4: Temperature compensated magnetic field sensor

Chapter 5: Multi-sensory SAW device

General Introduction

Surface Acoustic Wave (*SAW*) devices are the result of decades of research and development in the field of micro-electro-mechanical devices and micro/nano-scale fabrication technologies. They are used in a wide range of application fields, from telecommunications to automotive, aeronautics and even in the biomedical industry. SAW devices, are key components in communication systems and are widely used as filters, delay lines or resonators. Because SAW devices are highly sensitive to external physical parameters and to any disturbance that may affect the velocity, distance travelled or even the mode of wave propagation, they also offer promising solutions in a wide range of applications including physical and chemical sensors.

SAW devices thus present a considerable market especially in the field of telecommunications owing to their performance. Therefore, this field of SAW devices is now a very mature industrial technology thanks to its low manufacturing cost, small size, robustness and the possibilities for innovative applications as sensors. Moreover, these devices have the advantage of being batteryless (passive), wireless and packageless in specific configurations. The use of SAW devices as passive (no battery or embedded electronics) and wireless sensors allows them to operate in rotating parts and/or in extreme conditions such as those with high levels of radiation, high temperatures, or electromagnetic interference, in which no other wireless sensor can operate. This is obviously conditioned by the fact that the materials constituting the device can withstand these harsh conditions. When combined with flexible substrates, SAW sensors will find applications in the biomedical and welfare for a continuous monitoring of the human body's parameters.

Be it physical sensing such as temperature, pressure, stress, acceleration and magnetic or chemical or gas sensing or even biological sensing SAW devices have marked their excellence in many fields. Magnetic field sensing technology has also evolved from its earliest days as a tool for navigation across the unmarked oceans to the present era of using arrays of magnetic sensors detecting the presence, strength and direction of a magnetic field, not only from the earth itself but also from other sources.

The primary research objective of the thesis is on developing SAW devices for magnetic field sensing, a novel area of research in the *Micro & Nano Systems Research Group* at the *Institut Jean Lamour* under the guidance of *Prof. Omar Elmazria and Dr. Sami Hage-Ali*.

Compared to conventional electrical measurements, these micro-electro-mechanical systems (*MEMS*) based devices provide a fast and contactless measurement system with the possibility for a better resolution. Further, unlike SQUID based systems, these devices have the potential to operate without any cooling systems or large scale shielding setups and are thus much more cost effective. These devices are also non-invasive and non-destructive in nature. This research work therefore aims to address the core necessities of a sensor fit for industrial applications such as thermal stability, simple yet reliable design, easily reproducible and with cheap manufacturing cost.

The targeted applications of the sensors developed in this study pertain to industrial applications such as proximity sensing, displacement sensing and positioning, rotational sensing, current sensing and ferrous body (e.g. cars) movement detection. As proximity sensors they make use of DC magnetic fields, while applications related to displacement and position sensing are more focused on using the stray field profile of the monitored object. Thus, the devices also potentially act as a contactless version of a switch. Additionally, as current sensors, the devices are capable of contactless and electrically decoupled measurements in the DC to a few hundred MHz and can also function as gradiometers. Ferrous bodies distort magnetic field lines, and this fact forms the basis for their detection by the sensors. A synchronous monitoring of the body using two perpendicular arrays of sensors can provide information on its presence, direction and speed while a three-axis placement will also allow a classification of the vehicle. The major advantage of these devices in all these possible application areas are their size, weight and power consumption.

Not limiting to industrial applications as mentioned above, the versatility of these devices can be readily extended for biomedical studies by combining it with suitable electronics and noise reduction techniques as well as specialized data processing algorithms. Thus the realization of SAW based magnetic field sensors allows us to benefit from the classic advantages of SAW technology such as low cost, minimal aperture, robustness and reliability while at the same time qualifies us to explore passive (battery-less) and remotely interrogable (wireless) device configurations as well, thereby paving the way for unprecedented new applications.

The work presented here is focused on an experimental study of surface acoustic wave devices of the resonator configuration for the detection of magnetic fields. The primary aim of the work has been to understand the physics that governs and controls the operation of the sensor, to better optimize the magnetic properties of the magnetostrictive layer in the device and also to engineer the device itself to address the concerns arising from the effects of temperature. The thesis is organized into five chapters, each addressing and describing in detail specific aspects of the research work ranging from the design of the device and fabrication to their characterisation.

The first chapter is devoted to an introduction of the subject matter and is divided into three sub-sections. In the first sub-section, we discuss SAW devices, the physics behind their operation and their general applications. In the second sub-section, we introduce and discuss the currently available magnetic sensor technologies and their principles of operations. Finally, in the third sub-section we focus on magnetic SAW sensors and discuss their physics and the possible areas of applications.

In the second chapter we investigate, through simulations, the effect of change in the various geometric parameters of the SAW device on its magneto-acoustic response. The study considers an ideal magnetisation behaviour based on the *Stoner-Wohlfarth* model as a standard for all the devices. This chapter thus forms a basis for our understanding of the device and allows us to develop the necessary experimental strategies for the next part of the study.

The third chapter presents devices fabricated using multi-layered [$TbCo_2$/FeCo] as the sensitive magnetostrictive layer from which the electrodes are fabricated. The objective of this chapter is to study the effects of shape anisotropy in the device and can deepen our understanding of its magneto-acoustic response. It also paves the way for engineering the device to be sensitive in a specific range of magnetic field. The chapter details the various fabrication steps involved, followed by the experimental characterizations done and their outcomes. In order to demonstrate the practicality of our device, a prototype structure is designed and implemented to use it as a sensor to monitor the current in a cable. The temperature dependent challenges associated with the prototype are also discussed, leading to the subsequent research work presented in the next chapters.

The fourth chapter presents an improved SAW resonator based on a multi-layered device structure with an aim to mitigate the effects of temperature. The structure is based on a cancellation effect achieved by optimizing the thicknesses of the ZnO and CoFeB layers on ST-cut Quartz substrate. The effects of the temperature on the resonance frequency is first introduced followed by a description of the fabrication process. The characterizations and the achieved results are then presented and discussed.

Beyond the well-known effect of temperature on the resonance frequency of the SAW device, the fifth chapter is focused on addressing another important effect associated with an unstable temperature. The effect of the temperature on magnetic anisotropy is first described and the shape effects in magnetisation that were investigated previously, are used to propose a solution to it. The various stages of the fabrication process are then detailed followed by the magnetic and acoustic characterisations. The results obtained are finally presented and discussed. A near-hysteresis free magnetic behaviour is obtained in the magnetostrictive layers. A unique possibility of a multi-functional device is also proposed in the chapter wherein the concerned device shows a sensitivity to both temperature as well as magnetic field, while simultaneously being independent of each other.

Finally, a summary of the research work undertaken in this thesis is presented along with a perspective of the various future possibilities in the general conclusions.

Chapter 1

Surface Acoustic Wave sensors for magnetic field detection

Introduction:

Surface acoustic wave devices or SAW sensors as they are better known are a results of years of evolution and innovation in many related fields such as RF technology, acoustic wave propagation in solids, thin film technology, micro or nano fabrication technologies etc. They have found applications in virtually every field of technology, from telecommunication, aeronautics and even the medical field, for both wired as well as wireless communication. Compared to the other different types of sensors available in the market today, SAW sensors present the additional advantage of being passive, i.e. requiring no external power source, as well as a wirelessly interrogable system which may also be imperceptibly small. When fabricated in bulk, they are also cheap. Added to all of these, SAW sensors are perfectly suited as multifunctional sensors in a single device which is extremely difficult using conventional sensors. All of these abilities enable the SAW devices to be useful especially in harsh environments. They have thus found use not only in conventional areas as RF filters but also in novel areas related to microfluidics *[Ngu'02, Las'04]*, lab-on-a-chip *[Mar'10, Gop'14, Dit'06]*, gyroscopes *[Bhu'17]*, ID tags *[Rei'93]*, structural health monitoring *[Nic'19, Wil'09]* and many more. Our work aims to contribute in this field by focusing on the development of wireless SAW sensors for magnetic field detection through engineering based on a deep understanding of the physics.

This first chapter is aimed at defining and providing a background to magnetic SAW sensors. In the first segment of this chapter, we give a general idea on magnetic sensors currently in use. Following this, we briefly present the basics of SAW devices and then amalgamate the two sections to form a third section describing the use of SAW sensors for magnetic field detection.

Part 1: Magnetic Sensors

1.1.1 Introduction:

Of late, there has been a tremendous rise in the interest to develop sensors for the detection of magnetic fields. They have found use in many different applications. Almost all of these sensors can be primarily classified into three basic categories based on their limit of detection.

1. **High field application:** Sensors are categorized into this range when they are able to measure magnetic fields of 1 mT and above. i.e. when the measured field is stronger than the geomagnetic field. Applications for these sensors include magnetic switches, measurement of current flowing through wires as well as magnetic memory read-outs and rotational sensors for automobile applications.

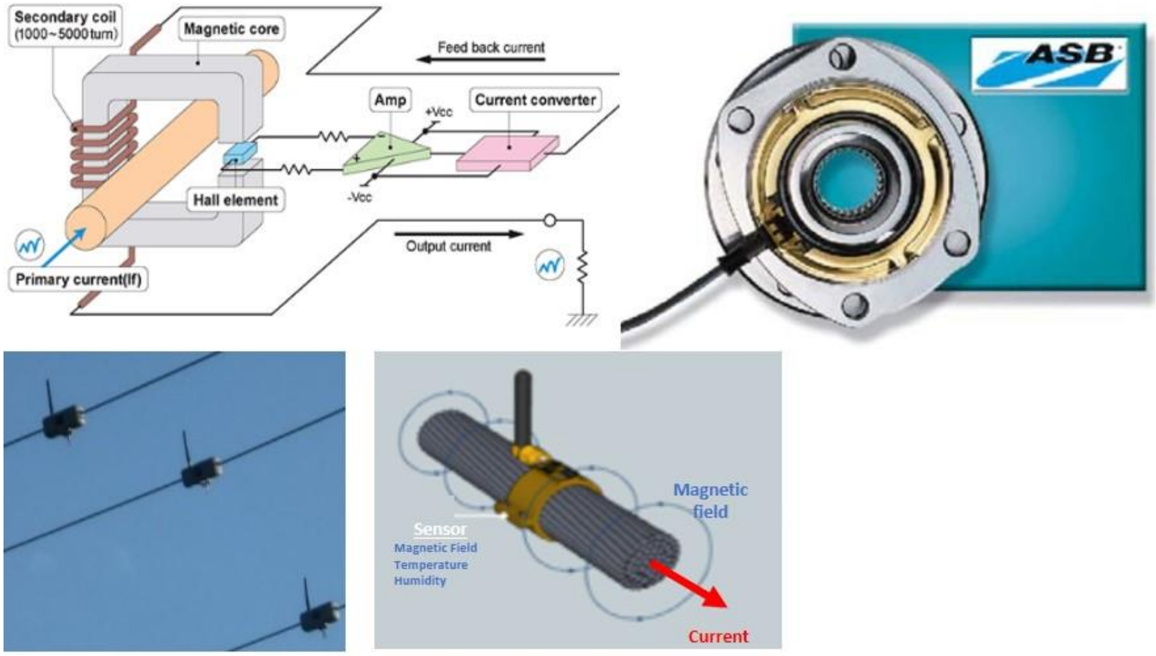

Figure 1.1: Schematic and example of a magnetic flux closed loop current sensor developed by Tamura SS co [www.tamura-ss.co.jp/electronics/en/currentsensors/circuit_system_description] and a rotational sensor developed by our collaborators at the university [Press Release, SNR ROULEMENTS - 23/10/2007].

2. **Medium field application:** The magnetic field that is measured by sensors in this range is based on any measurable change to the magnitude or direction of Earth's magnetic field. The Earth's magnetic field ranges around 50 µT and so the limit of these sensors is usually between 0.1 to 10 µT. They have often been used for such applications as proximity sensors and ammunition fuses.

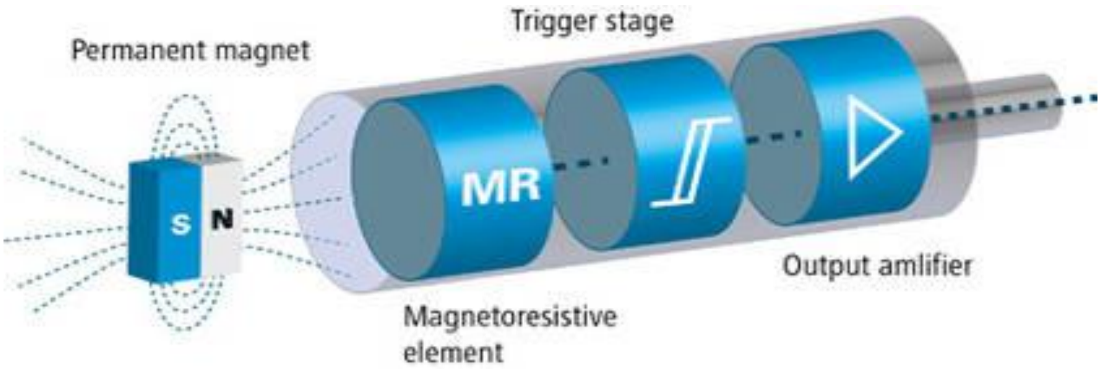

Figure 1.2: Schematic of a proximity switch.
[http://www.baumer.com/ch-en/products/presence-detection/magnetic-sensors/magnetic-proximity-switches/]

3. **Low field application:** These sensors are the most sensitive of all magnetic sensors. They are able to measure magnetic field gradients that are induced (in the presence of Earth's magnetic field) or even permanent dipole moments (in the absence of Earth's magnetic

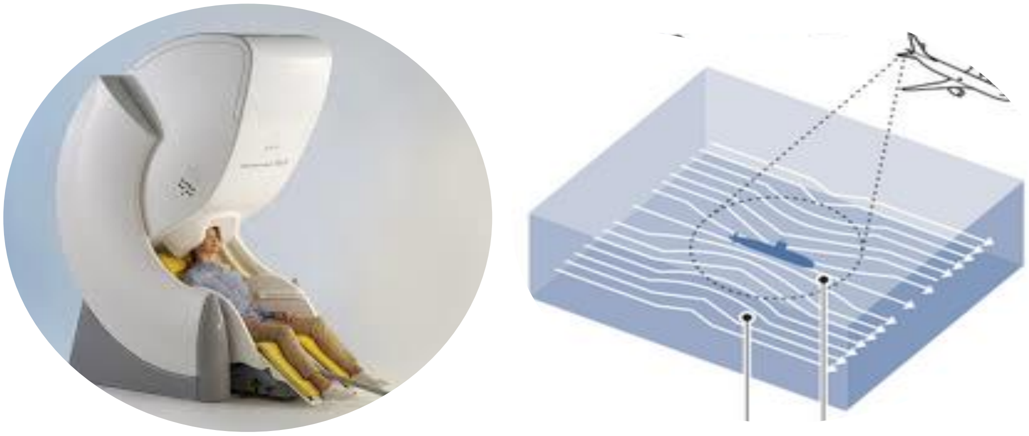

Brain mapping by MEG **Magnetic anomaly detection**

Figure 1.3: Examples of commercially available brain mapping system [https://www.elekta.com/diagnostic-solutions/elekta-neuromag-triux/] and magnetic anomaly detection system developed by Boeing Corp. [Boeing Northrop Grumman Corporation, Barra Sonobuoy Design].

field). The field measured by these sensors is in the limit of 1 nT and below. Hence they find an enormous applications area in the biomedical field such as magnetoencephalography (neural mapping in brains), magnetic resonance imaging. Also a growing area of application is in the field of magnetic anomaly detection.

1.1.2 Types of magnetic sensors:

a) ***Search coil magnetic sensors:*** These vector magnetometric sensors use Faraday's law of induction to measure any change of the magnetic flux density surrounding them. The change of the magnetic flux leads to a proportional voltage and thus allows us to measure any difference *[Coi'09]*. Mostly, a ferromagnetic core is also placed in the centre of the coil to enhance the magnetic flux. These types of sensors are limited by the inductance and resistance of the coil. The sensitivity of such sensors however is very high and they can detect magnetic fields as weak as 20×10^{-12} T in the frequency range of 1 Hz to 1 MHz with state-of-the-art electronics. They find the best use as proximity sensors and can also be used in harsh environments. However, the large size of these sensors (typically between 50mm to 100cm) limits their use in micro systems. Considering the micro-scale dimensions of MEMS devices, one major concern for their use in such structures would be the complex fabrication procedure associated with making helical micro-coils of an appropriate aspect ratio, even apart from the consideration that such a system would be extremely fragile.

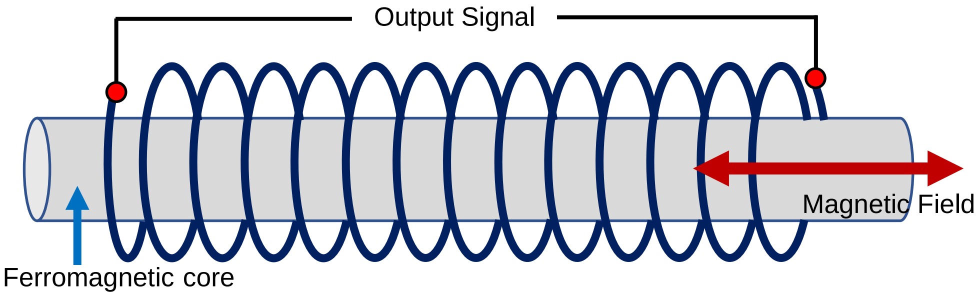

Figure 1.4: Schematic of a search-coil magnetometer.

b) ***Hall Effect sensor:*** When a thin plate of gold or semiconductor is exposed to a strong out-of-plane magnetic field and an electric current is passed through the length of the plate, it is observed that a voltage difference is created across the thin plate of gold or semiconductor. The electrons moving through the magnetic field experience what is called the Lorentz force (acting perpendicular to both the direction of field and the motion of the electron), thus creating a *Hall voltage*. This physical principle is used to create the Hall sensor *[HonR]*. They are very cheap to fabricate and quite robust in design. These sensors can detect a magnetic field in the range of 10^{-3} to 10^{-1}T. They are normally used to measure static fields but can also be used to measure varying fields (maximum 1 MHz).

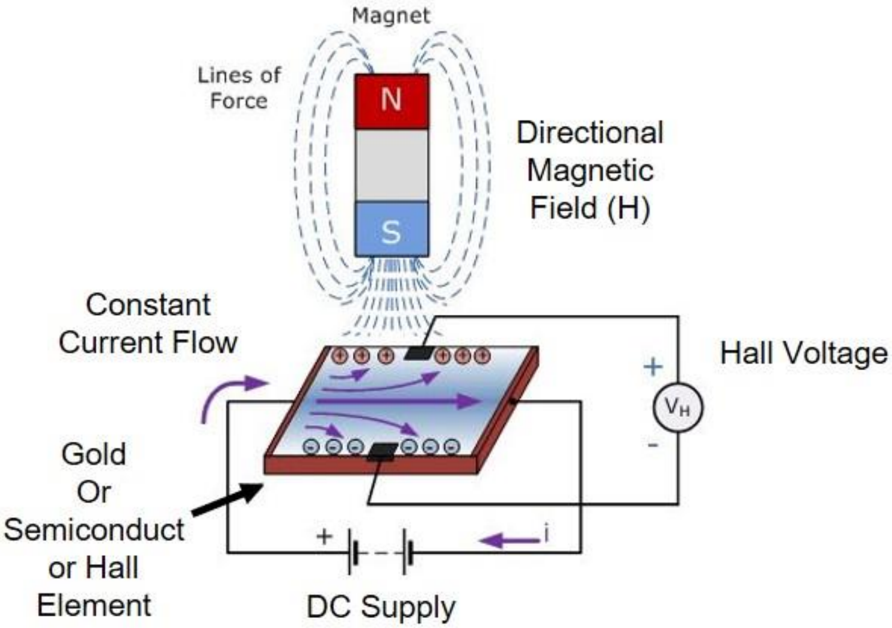

Figure 1.5: Schematic of the working principle of a Hall effect sensor.

c) ***Anisotropic magnetoresistance (AMR) sensors:*** The principle of anisotropic magnetoresistance refers to the dependence of the resistance in certain materials to the relative direction of magnetisation. When exposed to a magnetic field, the magnetisation in the AMR sensors re-orients, so the angle by which it rotates (determined by the strength of the field) gives us a measure of the field *[MurR, Jog'15]*. Owing to its large magnetoresistance property, permalloy (an alloy of Ni and Fe) has been found as the most suitable material for this type of sensors. AMR sensors are sensitive to magnetic fields in the range from 10^{-6} T to 5×10^{-3} T. Although the measured field needs to be relatively high in strength, one interesting aspect of these sensors is their ability to measure fields from DC to 1 GHz frequency. These light weight sensors can also operate in temperatures from -55°C up to 200°C.

d) ***Giant magnetoresistance (GMR) sensors:*** Simply put, GMR sensors are a type of AMR sensors but with much larger magnetoresistance effect, achieved through engineering of the structural layers. The simplest GMR sensors consist of four layers: two ferromagnetic layers separated by a conductor layer and a fourth anti-ferromagnetic pinning layer. A spin valve structure is thus created leading to better control of the flow of electrons. In certain cases, the above described layered structure may also be repeated leading to a multi-layered geometry with higher resistance *[Nob'07]*. This type of structure also ensures a better control of the change in resistance. Further, in another configuration of the layered structure, the antiferromagnetic pinning layer is also eliminated by optimizing the thickness of the conductor layer to provide the same pinning effect. The layers that constitute the structure of the GMR sensors have an optimal thickness of about 1nm, thus ensuring that these type of sensors are extremely thin and light weight. GMR sensors can detect a very wide range of magnetic fields from 10^{-9} T to about 10^{-1} T at a frequency of 1 Hz.

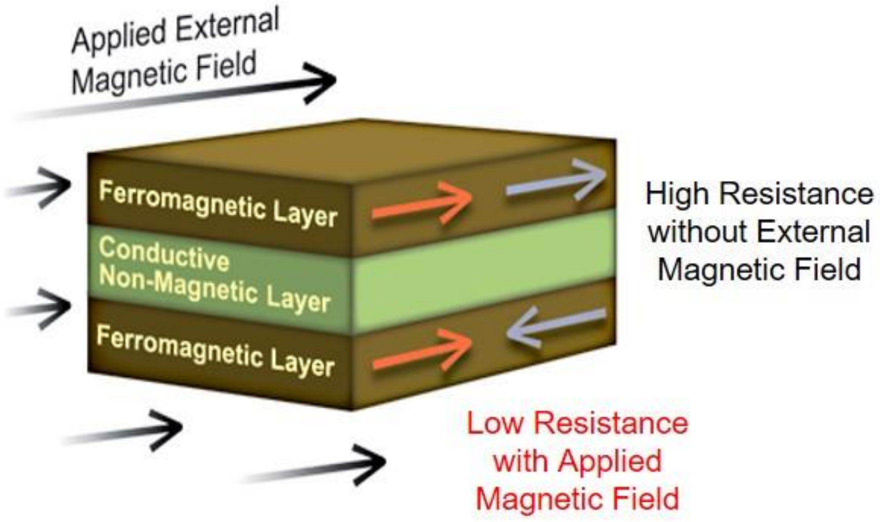

Figure 1.6: Schematic of the working principle of a GMR based sensor.

e) ***SQUID sensors:*** When certain materials are cooled below their superconducting transition temperatures, they exhibit an extraordinary level of interaction between the electric current flowing through them and the magnetic field they are exposed to. The flow of current experiences an almost zero resistance. Thus, in the absence of any intrusion, the current flowing through the coils is a direct measure of the external magnetic field *[Mar'12]*. Superconducting quantum interference device (SQUID) magnetometers consist of two such superconductors connected by thin insulation layers (forming two parallel Josephson junctions). The primary principle behind the operation of these sensors is based on the discovery made by Josephson that the magnetic flux is quantized. Thus while maintaining a constant bias current in the SQUID, the changing magnetic flux leads to a oscillating voltage due to a change in the phase at the junctions. The number of oscillations thus allows for measurement of the changing flux. Thus, as expected, SQUID magnetometers are extremely sensitive. Indeed, with a measurement scale of 10^{-14} T, they do offer the very best in magnetic field sensing. The control of the bias field in the device allows it to measure extremely small changes to the ambient field. However, the cryogenic operating

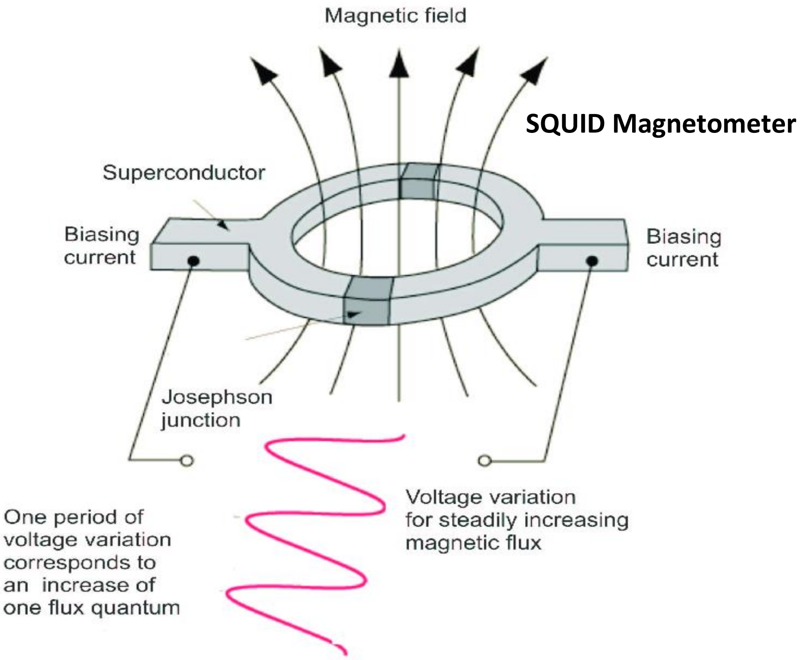

Figure 1.7: Schematic of the working principle of a SQUID based magnetometer.

temperature leads to a quite bulky size of the machine and thus severely limits its use for very specialized applications. The high cost of operation further limits their use.

f) ***Other types of magnetic field sensors:*** As described in the previous sections, the magnetic field sensors not only differ in the range of field they measure but also significantly differ in their sensitivity, limit of detection as well as dynamicity. Further, the sensors described above are vector magnetometers; meaning, their sensitivity depends on the direction of the magnetic field they are measuring. There are other types of magnetic field sensors which can be classified as total field sensors. They are insensitive to the direction of the magnetic field and make use of the principle of splitting between nuclear spin energy levels that is proportionate to the magnitude of the magnetic field. The limitation however is that the sensitivities of these sensors decreases rapidly for magnetic fields with a frequency of 10Hz and above. Proton precession magnetometers *[WikA]*, Overhauser effect magnetometers *[GemR]* and Caesium/Potassium vapour magnetometers *[SciR]* are some very specific types of scalar or total field magnetometers. Scalar magnetometers however find limited and very specific use in the detection of minerals on the Earth's crust.

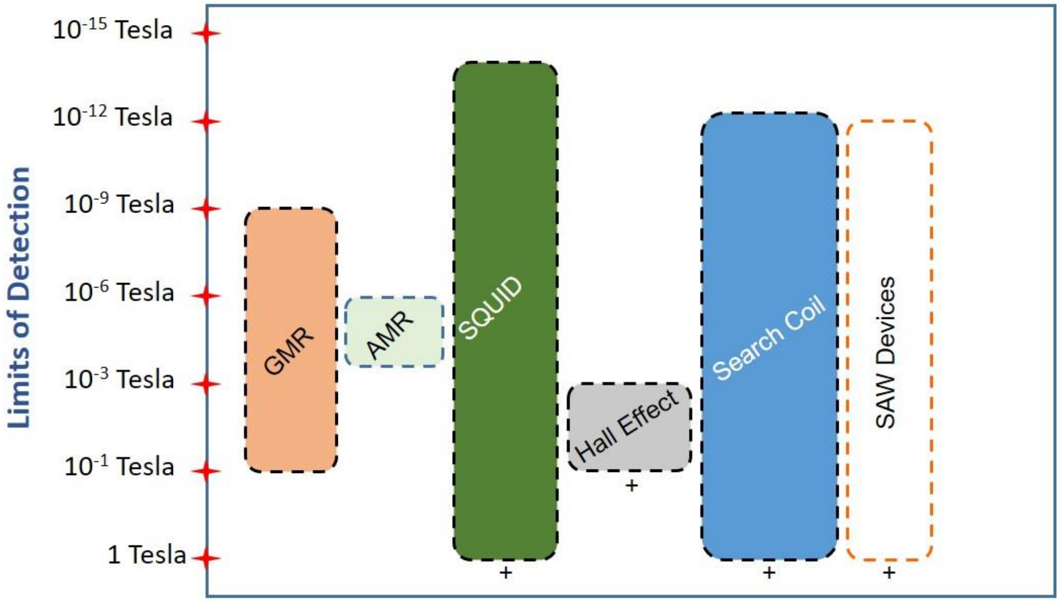

Figure 1.8: An approximate depiction of the limits of detection of some of the various magnetic sensors available in comparison to SAW devices (with required electronics that minimize noise).

Part 2: SAW devices: State-of-the-Art

1.2.1 SAW Devices:

The origin: The invention of radar technology in 1922 led to some serious developments related to communication devices based on the principle of reflected power. Harry Stockman first suggested the idea of radio frequency based identification in 1948 thus laying the foundation of RFID sensors with the first patent coming up in 1973 by Charles Walton. The working principle of SAW devices is based on the natural phenomenon of piezoelectricity dating back to 1880 and 1881 and credited to the Curie brothers (direct effect) and Lippmann (inverse effect). The first patent for SAW devices date back to 1963, while the first interdigital transducers (IDTs) were reported in 1965. The modern day sees these RFID sensors being developed on SAW devices that find use in our everyday life. Further, the state-of-the-art usage includes an extensive use of SAW based filters in various industries, especially those related to the telecom. SAW devices have found use not only as ID-tags and sensors but also as a combination of both.

1.2.2 Principle of operation of SAW sensors:

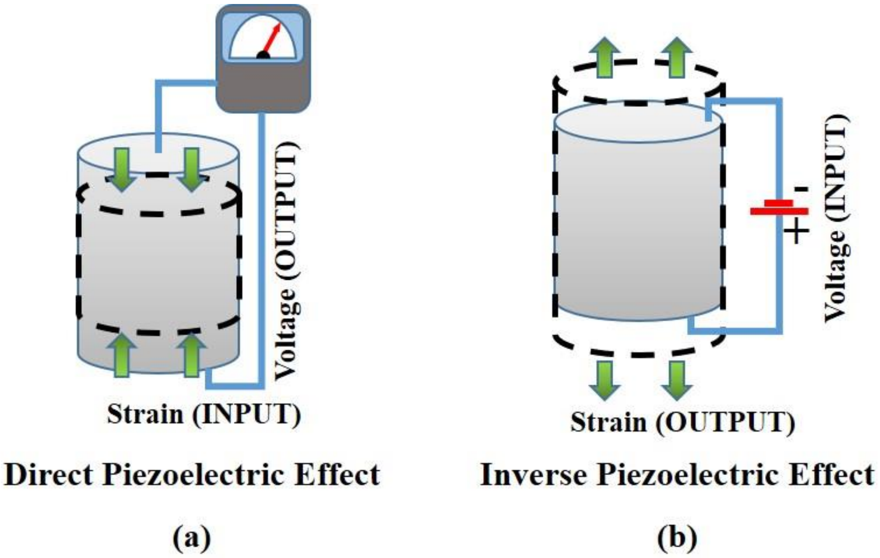

Figure 1.9: Schematic of the piezoelectric effect; (a) the direct piezoelectric effect and (b) the inverse piezoelectric effect.

The Piezoelectric effect: Piezoelectricity is the phenomenon exhibited by certain materials allowing them to transduce between their electric and mechanical energies. As shown in *Figure 1.9 (b)*, when a voltage is applied across it, the inverse piezoelectric effect causes the material to exhibit a mechanical strain along with an electric polarization. Conversely, a mechanical stress causes the material to exhibit the direct piezoelectric effect (*Figure 1.9 (a)*), leading to the generation of an electric voltage across the ends, along with a mechanical strain. This transduction effect is generally a linear interaction, in materials that do not have inverse symmetry. In crystalline materials, the external stress (and thus strain) causes a relative displacement of electric charges in the ions, thus leading to a rise of polarization in the material. Without the external stress, the charges nullify each other and hence no polarization is observed. Piezoelectricity may be exhibited by crystals, ceramics, polymers and composites. Single and polycrystalline piezoelectric materials may be produced through sintering. Their dielectric, mechanical and piezoelectric properties are often controlled and optimized as per requirement. Piezoelectric polymers have found numerous applications in the electronic industry owing to their flexibility, lightweight nature as well as their ability to exhibit large strains without damage. Piezo-composites had been developed to overcome problems inherent to ceramics (such as fragility and stiffness). They allow great freedom to have better properties, including electromechanical coupling factor and suitable acoustic impedance. In this study, we shall consider piezoelectric crystals such as lithium niobate or quartz that enable very low propagation losses.

Tensor notation: The piezoelectric constitutive equations define the behaviour of the piezoelectric materials. For a linear piezoelectric material these equations are represented as below:

$$\varepsilon_i = S_{ij}^{E}\sigma_j + d_{mi}^{T}E_m \text{ ------------- (Eq. 1.1)}$$

$$D_m = d_{mi}\sigma_i + \xi_{ik}^{\sigma}E_k \text{ ------------- (Eq. 1.2)}$$

where,

σ is the stress vector (N/m^2)

ε is the strain vector

E is the applied electric field vector (V/m)

ξ is the permittivity (F/m)

d is the electromechanical coupling matrix (m/V)

S is the compliance matrix (m^2/N)

D is the electric displacement vector (m^2/C)

Elastic Waves: Whenever the particles in a medium undergo a displacement that causes a deformation (in the medium) in the form of an alternative expansion and contraction, a mechanical wave is generated in it. Primarily they are classified as either volume waves or as surface waves.

a) **Volume Waves**: These are characterized by waves that are transmitted inside the material and hence appropriately called volume waves / bulk waves *[Bri'07]*. They are again of two main types: compressional waves also called longitudinal bulk waves (refer Fig. 1.10(a)) and transverse shear waves (refer Fig. 1.10(b)). The longitudinal waves are polarized along their propagation direction with the particles vibrating back and forth along the same direction. Thus from the perspective of a minuscule portion of the material these waves cause it to expand and contract alternately thus propagating the wave forward. The propagation velocity of these waves are known to be the highest.

b) **Surface Waves**: These waves are characterized by traveling displacements that have a higher amplitude but with lower velocities *[Lov'67, Dob'51, Vic'81, Ray'85]*. Primary among these surface waves are the ones with longitudinal and transverse displacements known as *Rayleigh waves* (named so after the British scientist Lord Rayleigh) (refer Fig. 1.10(c)), the *Shear Horizontal* waves with lateral shear displacements and a category of shear waves (also with lateral shear displacements) in layered structures, known as the *Love waves* (named so after another British mathematician Augustus Edward Hough Love) (refer Fig. 1.10 (d)). These waves propagate along the surface of the material or as is mostly the case the strongest displacements caused by them are along the surface of the substrate. Their displacements may be observed as vibration along one direction and propagation perpendicular to that direction.

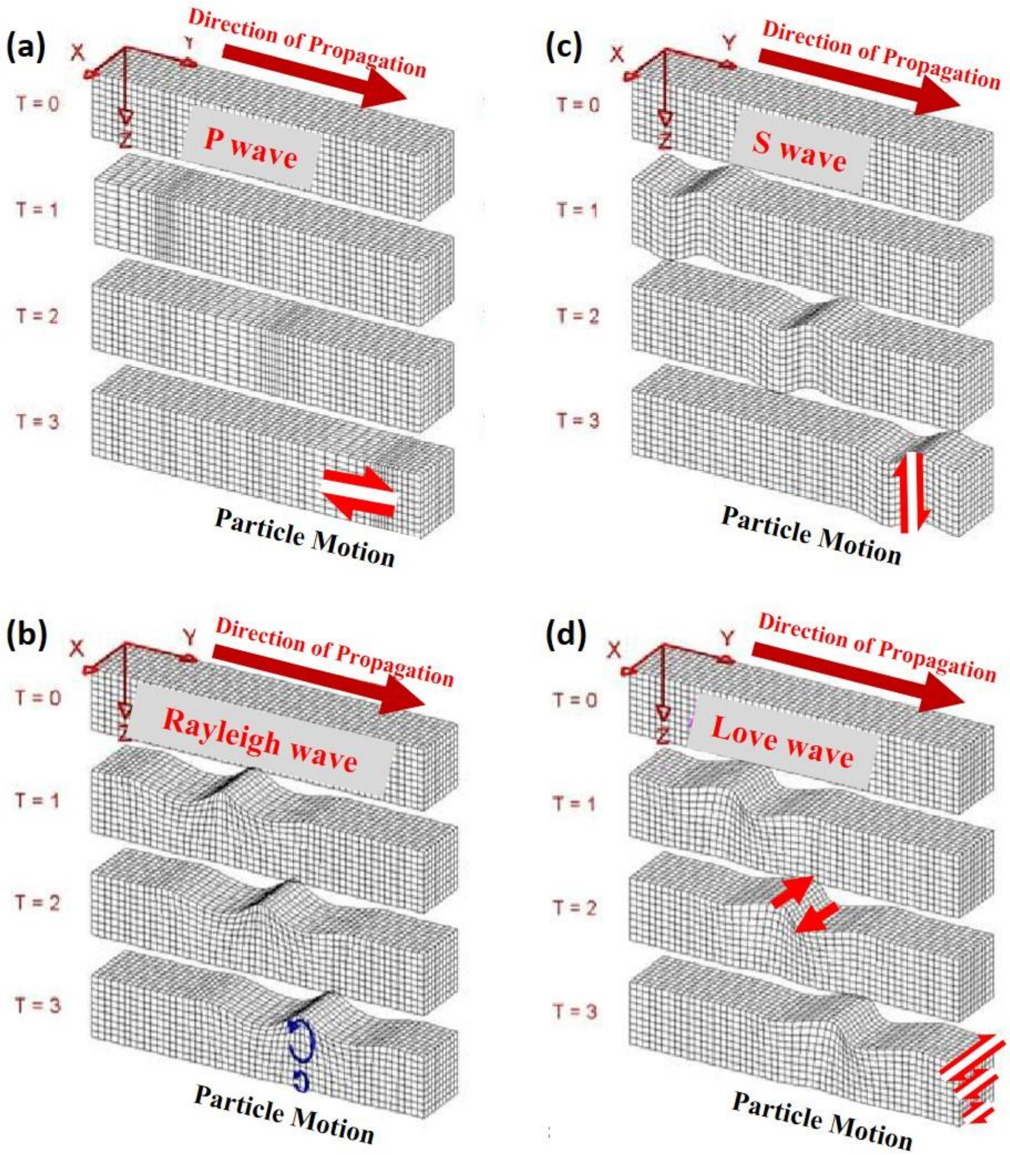

Figure 1.10: A schematic of the different types of elastic waves propagating in a solid medium. (a) Longitudinal volume waves; (b) Transverse shear waves (also called *Shear-Vertical* waves); (c) Rayleigh waves & (d) Shear horizontal waves (and also Love waves) *[Bra'00]*.

The Surface Acoustic Wave (SAW) sensors**:** SAW devices work on the principles of elastic wave propagation in piezoelectric substrates. Inter-digited transducers (IDTs) are used to apply an electric potential or voltage across sections of the substrate, thus creating an electric field in those areas. With the application of a sinusoidal pulse, the fields can be applied in alternating polarities. This leads to the generation of elastic waves that propagate. The sensing aspect of these devices take place during this stage. When these waves encounter the IDTs again (either after passing through a sensing region as in delay lines and RFIDs, or after reflection as in resonators) they initiate the direct piezoelectric effect and thus recreate a voltage across the IDTs. The change in the output signal with respect to the input signal is a direct measure of the sensed parameter. SAW sensors have established their mark as passive sensors suitable for continuous monitoring. In certain configurations, they are also readily interrogated wirelessly, thereby increasing their versatility. As mentioned just before, SAW sensors primarily come in three different geometries:

a) **Delay line geometry:** In SAW sensors of the delay line type the acoustic waves are generated by the input IDTs. They are propagate through the empty area where the actual sensing of the parameter takes place and finally are detected at the other end by the output IDTs. These types of SAW devices are however best suited for only wired applications.

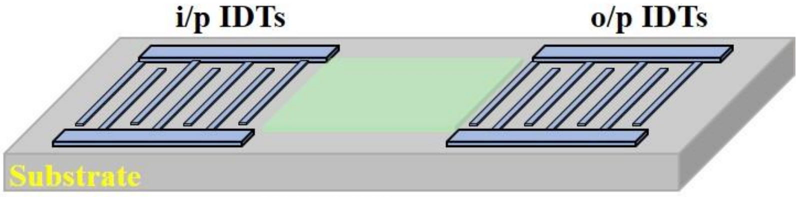

Delay-line

b) **Resonator geometry:** In the resonator geometry, SAW devices are more compact compared to delay lines. In these structures, the waves are generated by the centrally located IDTs and propagate to both sides in-plane. They are then reflected by the reflector gratings on both sides and are re-sensed by the IDTs. In such a geometry therefore, the input IDTs themselves act as the output IDTs and hence this type of geometry is the most suitable for wireless sensing applications. Indeed, when the IDTs are connected to a suitable antenna, the RF signals couple be applied and retrieved from the device wirelessly.

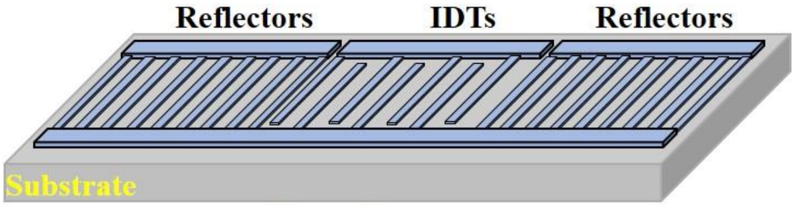

Resonator

c) **ID-Tags:** Better known as (radio frequency identification tags) RFID tags, these devices have a combination of both the above geometries. In these structures the acoustic waves that are generated at one end travel through the device to the other end, from where they are reflected back to the same IDTs where they were generated. The positon and configuration of the reflector gratings in the device act as a bar-code marking for identification of the device. These sensors are also very well suited for wireless applications.

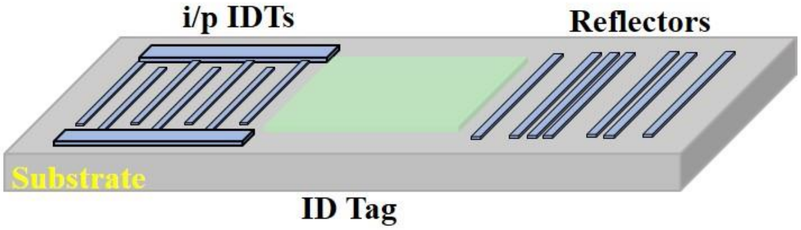

<u>Principle of wireless interrogation of SAW resonators</u>: The setup for wireless interrogation of SAW resonators, as shown in Figure 1.11, is composed of three essential steps. In the first step, a burst of RF signal around the same frequency as the SAW device is sent by the interrogating unit. The antenna of the device captures this signal and causes the device to self-resonate at its operating frequency. The frequency of the back-scattered signal is then transmitted by the device antenna and received by the interrogating unit to be analysed.

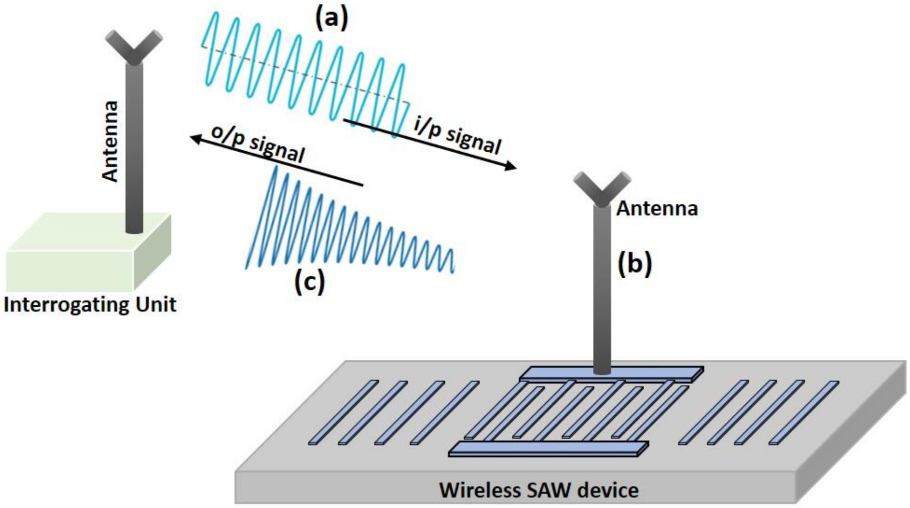

Figure 1.11: General setup of a single-port wireless SAW resonator.

1.2.3 Applications of SAW sensors:

In the previous section we have seen that the inherent design and structure of SAW sensors allows them to be very sensitive to disturbances in its surrounding environment. Additionally, SAW sensors have the advantage of being interrogated wirelessly. This increase in the versatility of these sensors, has opened the avenues of sensing in hostile environments *[Aub'10, Aub'13]*. Indeed, there is growing need of wireless sensors in high temperature environments and highly radioactive and corrosive environments where no other sensors could survive.

SAW sensors are not only sensitive, reliable and versatile, but are also quite capable of monitoring changes in mass (density), elastic modulus, viscosity etc. in real-time and more importantly wirelessly. Thus there has been a sharp rise in the use of SAW based sensors for sensing temperature *[Aub'10, Aub'13]*, pressure *[Rod'13, Nic'08, Hou'17]*, humidity *[Guo'14, Xua'14]*, strain *[Eun'16]*, force, acceleration, electric field, magnetic field, pH levels, radiation fields, explosives *[Afz'13]* as well as biochemical pathogens and biomarkers *[Gra'18, Gro'07, Bro'16, Lan'08]*. The fundamental principle underlying the sensing capability of SAW sensors lies in the change of the acoustic wave velocity. We know that this change in the velocity can be attributed to either intrinsic factors such as density, elasticity, viscosity, conductivity etc. or to extrinsic factors such as temperature, deformation, mass loading, pressure, humidity etc. The acoustic phase velocity (v), under isothermal and adiabatic conditions, is related to the resonant frequency as $f_r = v/\lambda$, where λ is the wavelength of the device. Thus the rate of change of frequency is directly proportional to the rate of change of the velocity and can be expressed as:

$$\frac{\Delta f}{f_0} = \frac{\Delta v}{v} \text{ ------------- (Eq. 1.3)}$$

Further, if we consider the different contributing sources of any change to the velocity *[Fu]*:

$$\frac{\Delta f}{f_0} = \frac{1}{v} \times \left(\frac{\partial v}{\partial m}\Delta m + \frac{\partial v}{\partial \sigma}\Delta\sigma + \frac{\partial v}{\partial c}\Delta c + \frac{\partial v}{\partial \varepsilon}\Delta\varepsilon + \frac{\partial v}{\partial T}\Delta T + \frac{\partial v}{\partial P}\Delta P + \frac{\partial v}{\partial \eta}\Delta\eta + \frac{\partial v}{\partial \rho}\Delta\rho \ldots \right) \text{ --------(Eq. 1.4)}$$

where, Δm is the change in mass load, $\Delta\sigma$ the change in conductivity, Δc the change in elastic constants, $\Delta\varepsilon$ the change in dielectric constant, ΔT the change in temperature etc. Thus any change in any of these parameters (considering the effect of all other parameters is zero) causes a shift of the resonance frequency of the device. There also lies the additional principle of sensing induced by a change in the device geometry caused by deformation or strain induced externally.

Part 3: Magnetic SAW sensors

1.3.1 Introduction:

Over the last few decades, the field of SAW sensors has seen a massive boom. Historically they have found applications related to sensing of various stimuli such as temperature, pressure, strains etc, as we saw in the previous section. But of late, numerous other areas of application of SAW sensors are also coming up. These include magnetic field sensing *[Kad'11, Han'87, Yam'80, Gan'76]*, chemical sensing, gas sensing *[Liu'14, Jak'11]* as well as biomarker sensing *[Gro'07, Lan'08]*. Thus out of this ever expanding application area of SAW devices, our work intends to contribute to the niche area of magnetic field sensing. SAW sensors are highly sensitive, small in size, passive devices which are quite easily fabricated. Added to that, these sensors can very easily be coupled to simple antennas and hence be operated wirelessly. This allows the integration of SAW sensors in not only microsystems and lab-on-chip devices but also extends its operations to remote inaccessible and hostile environments.

1.3.2 Magnetic sensors based on SAW devices and their applications:

Magnetic SAW sensors are designed either in the delay line configuration with a full film of magnetostrictive layer as the sensitive part *[Yam'80, Gan'76, Elh'16]* or in the resonator configuration with the IDTs made from the magnetostrictive material *[Kad'11]*. As discussed previously, one of the primary attractions for using SAW sensors pertains to the ease of wireless functioning while at the same time offering a passive and batteryless operation. This attraction is fulfilled by the resonator geometry, which is the most suitable for wireless interrogation. Several advancements have been made in the field of magnetic SAW sensors starting from as early as 1975 when Ganguly *et.al. [Gan'76]* proposed a magnetically tuned SAW phase shifter. Over the years several pioneering research has been made to understand, describe as well as optimize magnetic SAW sensors. Yamaguchi *et.al. [Yam'80]* designed a SAW delay line based on $TbFe_2$ and studied the variation of the SAW velocity with applied magnetic field. Kadota *et.al. [Kad'11]* pioneered to develop and study in detail SAW sensors with magnetostrictive IDTs (Ni electrodes). Recent developments in the area of 5G technology has rendered SAW devices a huge technological momentum and is thereby promoting more research into sensors based on SAW technology. Thus exploration of SAW devices for magnetic field detection has again taken a leap and is now at the forefront.

Applications of a magnetic SAW sensor:

The previous sections have enumerated the different types of magnetic sensors available in the market today. Thus it becomes imperative that the applications of such a varied number of devices are also numerous. In the current section we aim to enlist the applications of magnetic SAW (MSAW) sensors. Owing to their wireless and battery-less configuration, SAW sensors find tremendous applications, especially in areas of hostile conditions and thus their magnetic counterparts are no exception. SAW based magnetic sensors are primarily of two types: (i) Magnetostrictive SAW sensors *[Gan'76, Yam'80, Kad'11]*; (ii) Giant magneto-impedance (GMI) – SAW sensors *[Hau'00, Hau'06, Ste'00, Kon'18]*.

From magnetic switches for implantable biomedical devices to current, torque or rpm sensors in the automobile industry the applications of SAW sensors are indeed varied. Of late, a new use of these sensors for detection of vehicular traffic along marked tracks has also developed. Not only does this kind of sensing allow the monitoring of the number of vehicles but also its speed. With giant leaps in the field of electric vehicles, it is not long before magnetic SAW sensors find use in the segment either as current, temperature or speed sensors etc. Long term monitoring of structural health using the localised perturbation of the magnetic field in ferromagnetic pipes for example, is another important avenue for these sensors and thus provides enormous potential to find possible uses in the construction as well as pipeline industries.

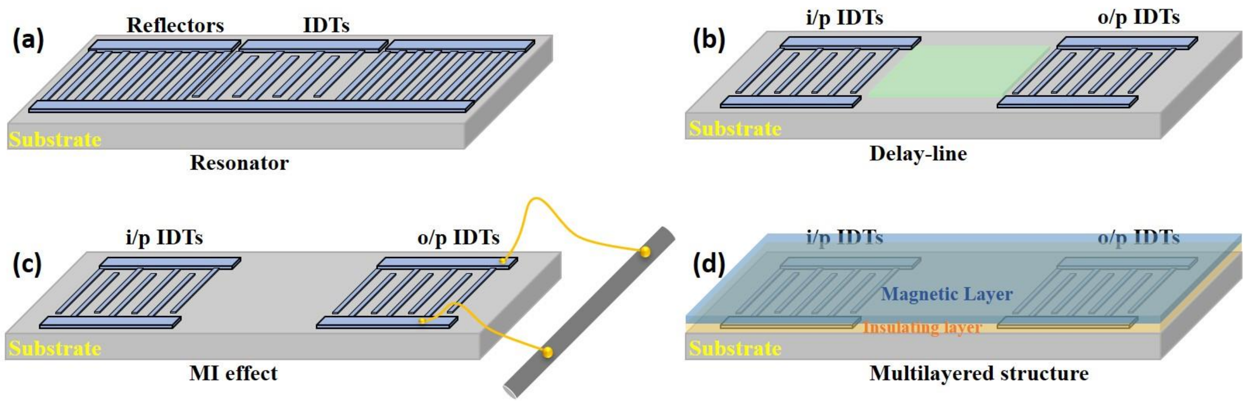

Figure 1.12: A schematic representation of the different possible SAW device configurations for magnetic field sensing. (a) Resonator configuration, (b) Delay line configuration, (c) SAW-GMI based sensor and (d) Multi-layered delay line device structure.

A schematic of the four different configurations of SAW devices used for sensing of magnetic field are presented in Figure 1.12. In the resonator configuration, the IDTs are fabricated from the magnetostrictive sensitive material and provide a sensitivity to the magnetic field by the change of resonance frequency *[Kad'11, Pol'17]*. The delay line geometry includes a magneto-sensitive layer between the input and output electrodes and provides a measure of the magnetic field by the shift of its phase *[Zho'14]*. The magneto-impedance based sensor is based on the Giant-Magneto-Impedance effect and provides sensitivity by a change in attenuation and shifting of the phase *[Hau'00, Kon'18]* while the multi-layered delay line structure measures in the same way as a delay line SAW device and provides an output based on a shift of its phase.

1.3.3 Physics behind the working of a magnetic SAW sensor:

The dynamics of the surface acoustic wave devices used for magnetic field sensing is governed by complex quantum mechanical phenomena. These phenomena are based on interactions between magnons and phonons that exist in the constituent layers. Over the years several studies have been made to try and explain the particular behaviour of magnetic SAW devices. However, an exact

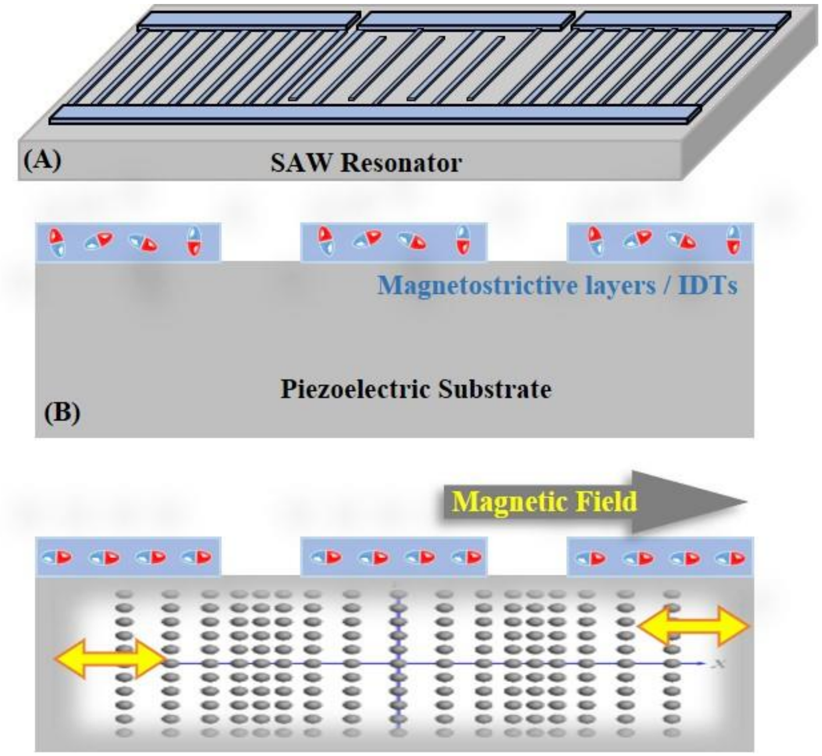

Figure 1.13: Schematic of a SAW resonator with magnetostrictive IDTs.

description is still missing. Not only will a detailed understanding lead to precisely engineered devices but also throw a lot of insight into the magnetism in microscale geometries. In this section we attempt to understand and describe the *Magnetic SAW* (MSAW) or magneto-acoustic response.

Consider a SAW resonator as shown in Figure 1.13. It consists of two parts (refer Figure 1.13 (A)): the piezoelectric substrate in which the acoustic waves generate and propagate and the magnetostrictive IDTs which are sensitive to a magnetic field. Thus while functioning, the SAW resonator is affected by both. Unlike in SAW delay lines where the wave generation itself is not affected by the magnetic field, in the resonator configuration the generation of the acoustic wave itself may be affected due to the magnetostrictive nature of the IDTs. On a larger perspective the behaviour of the MSAW response has been reported to be governed by the ΔE effect and the dynamic magneto-elastic coupling *[Yam'80, Kad'11, Smo'03]*. The final effect that is observable however, is the change or shift of the resonance frequency.

The velocity of longitudinal wave in a medium may be given by the equation *[Yam'80]*:

$$V = \left\{\frac{E.(1-K_{33}^{2})}{\rho}\right\}^{\frac{1}{2}} \text{------------- (Eq. 1.5)}$$

where, E is the Young's modulus, ρ is the density and K_{33} is the magneto-elastic coupling coefficient of the material.

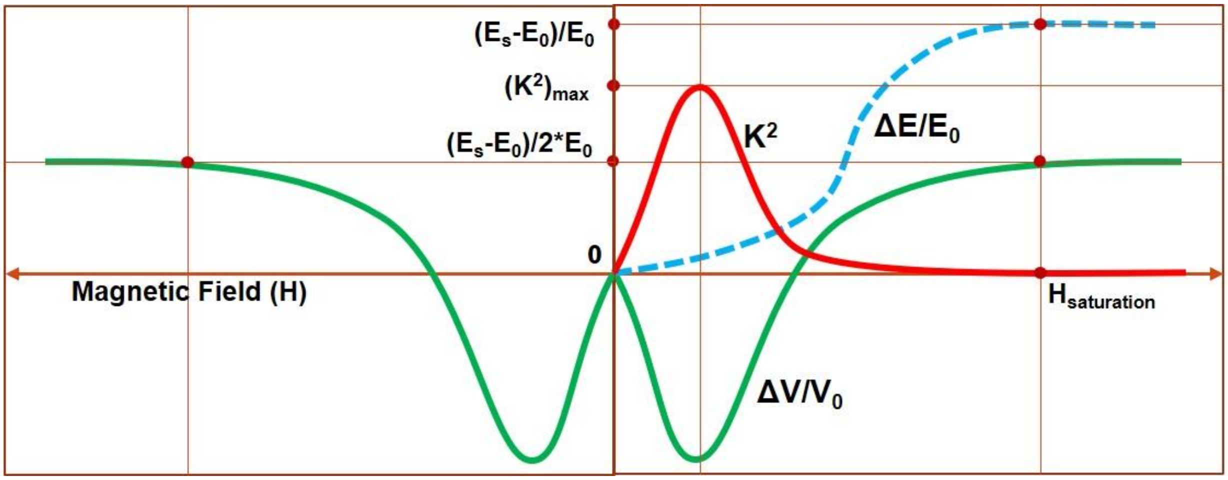

Figure 1.14: Representative curves showing the variation of the magnetoelastic coupling (K^2); ΔE effect and the change of velocity.

On simplification of Eq. 1.5 using Binomial Theorem and neglecting higher powers in the equations we obtain:

$$\frac{\Delta v}{v_l} = \frac{1}{2} \times \left(\frac{\Delta E}{E_H} - K_{33}^2\right) \text{------------- (Eq. 1.6)}$$

As can be observed from Eq. 1.6 as well as from the representative Figure 1.14, the change of the wave velocity (and thus the shift of the resonance frequency) is influenced by the ΔE effect and the magneto-elastic coupling factor (K^2), both properties exclusive of the magnetostrictive layer. The K^2 inversely affects the acoustic response and any increase in the K^2 leads to a decrease of the ΔV/V, wherein the minima of the ΔV/V-curve occurs at the maxima of the K^2 curve. The magneto-elastic coupling is an effect governed by the rotation of the magnetic moments. The ($K_{33}^2 = K^2$) on the other hand, has a maximum value when the angle between the magnetic moment and the applied magnetic field is at 45°.

Unlike a simple longitudinal wave where the displacements of the particles are in one direction only (Figure 1.15 (a)), a SAW wave generally comprises of a combined effect of displacements in all the three directions. Thus an understanding based solely on the previously explained longitudinal wave effect is not sufficient to exactly describe the MSAW response. However, a Rayleigh wave (Figure 1.15 (b)), which has a longitudinal component along with a vertical component, may be explained based on the above postulations. Our understanding of this points to the fact that in the case of a Rayleigh wave, if we consider an infinitely spread thin film over the substrate then for a longitudinal width less than the wavelength of the acoustic wave, it would undergo a case of plain strain, akin to the deformations on it in case of the longitudinal wave. Examining the magneto-acoustic response for a Rayleigh wave (refer Figure 1.16), when a magnetic field is applied perpendicular to the magnetic anisotropy direction of the SAW device (hard axis direction), the magnetic moments rotate and try to realign along the magnetic field. Thus the behaviour is heavily influenced by the dynamic magneto-elastic coupling. This is in combination with the ΔE effect causing a variation of the stiffness of the magnetic layer. However, beyond the saturation magnetic field and at the coercive field, there is no rotation of the moments and thus there is no response from the device. Therefore, we obtain the characteristic W-shaped MSAW response (Figure 1.16 (a)). On the other hand, when the magnetic field is applied parallel to the anisotropy (easy axis direction) the magnetic moments have only an instantaneous switch with a change in the direction of the magnetic field while the ΔE effect is directly proportional to the strength of the applied field (until saturation kicks in). Thus the magneto-mechanical effects that governs the MSAW response are smaller than before (hard axis case) and this results in the characteristic V-shaped MSAW response (Figure 1.16 (b)). Our analysis of the curved region in the response seen in the figure indicate towards the role of a precession of the magnetic moment before the actual switching takes place.

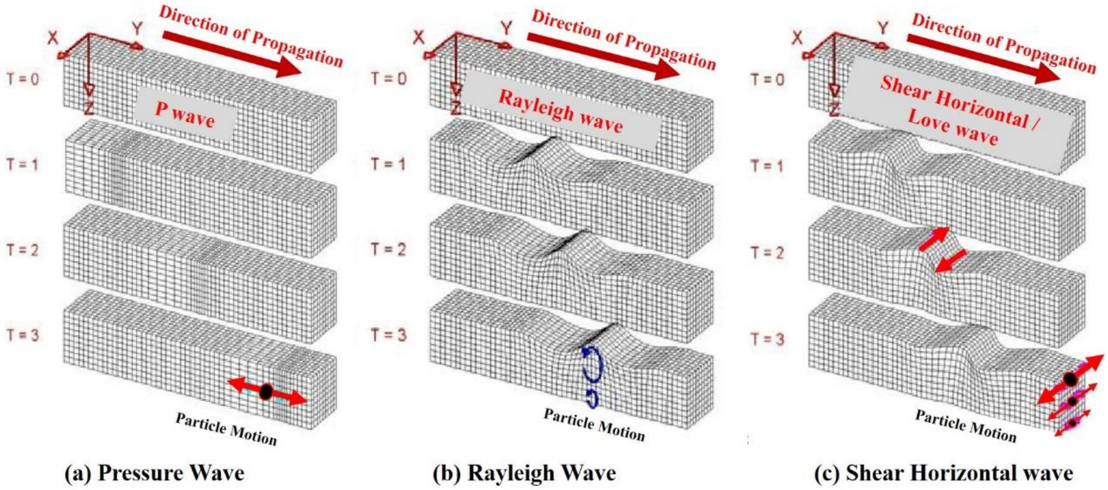

Figure 1.15: Schematic of displacements observed in (a) Pressure / Longitudinal wave; (b) Rayleigh wave and (c) Shear Horizontal wave.

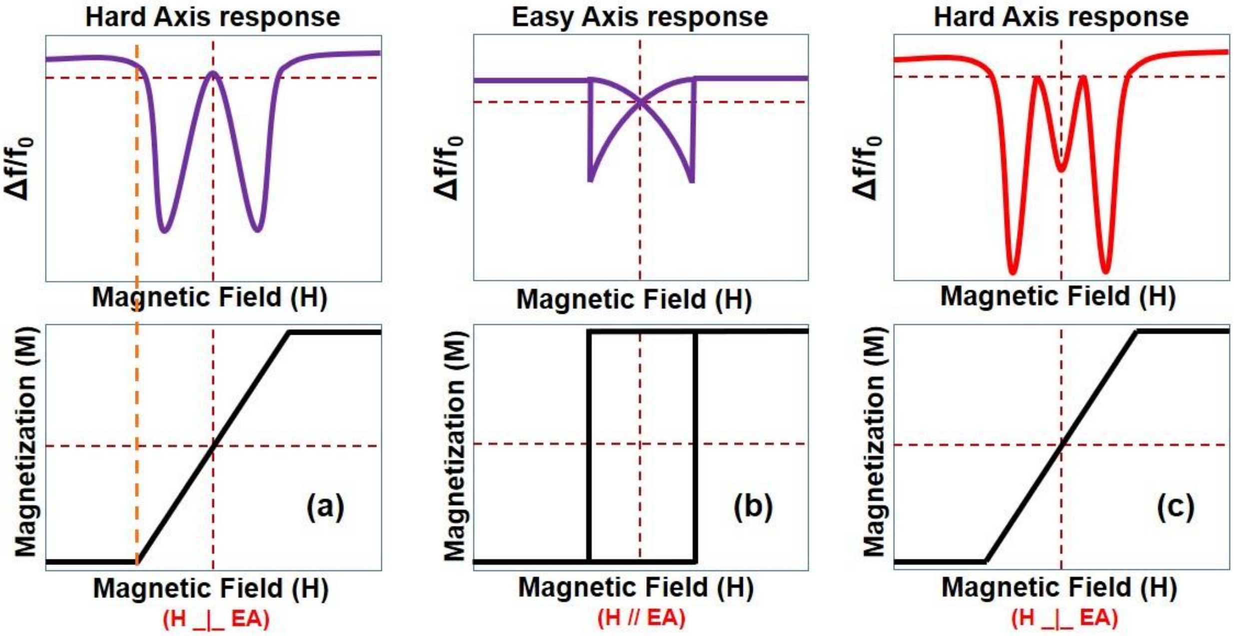

Figure 1.16: Expected theoretical magneto-acoustic behaviour along (a) hard axis; (b) easy axis of the Rayleigh wave; and (c) hard axis of the Shear Horizontal wave.

For a shear horizontal wave, as can be seen from the Figure 1.15 (c), the deformations are much more complex, thereby complicating the interplay between acoustic and magnetic energies. It may be noted here that in the case of shear horizontal waves, if the magnetic anisotropy is also along the same plane as the acoustic wave (or deformation), then a stronger interaction between the two takes place leading to a higher magneto-acoustic response of the device (compared to a Rayleigh wave in the same device) (Figure 1.16 (c)). However, relating the magneto-acoustic response of the shear-horizontal wave to the magnetisation is very complex and not explored in this work.

Thus finally to conclude this section, in the magnetic SAW device we observe the following forms of interactions between the magnetostrictive IDTs and the piezoelectric substrate:

i. Variations of the stiffness of the magnetostrictive material due to the external magnetic field.
ii. Strains caused by the rotation of the magnetic moments due to the external magnetic field, owing to its own magneto-mechanical coupling.
iii. Strains caused in the piezoelectric material due to its own electro-mechanical coupling (basically this refers to the acoustic wave).
iv. Strains caused on the magnetostrictive material by the traveling acoustic wave.
v. Strains induced on the piezoelectric substrate by the magnetostrictive layer.

Conclusion:

Thus in this chapter we first described magnetic sensors, their different types and their uses. Following that, we looked into SAW devices that utilize surface waves as a mechanism for detection of an external stimulus and discussed the principle behind it. We also discussed their various applications. In the third part, we discussed the ways of using SAW devices as magnetic field sensors. We discussed in detail the design and types of devices used for such sensing and their applications. We finally also discussed at length the principles and the physics behind magnetic field sensing by surface acoustic wave devices and listed the possible forms of energy interactions in the device.

References:

[Fu'17] Fu, Y.Q., Luo, J., Nguyen, N.T., Walton, A., Flewitt, A., Zu, X.T., Li, Y., McHale, G., Matthews, A., Iborra, E., Du, Hejun and Milne, W., "*Advances in piezoelectric thin films for acoustic biosensors, acoustofluidics and lab-on-chip applications*", *Progress in Materials Science*, 89, 31-91, 2017.

[Ngu'02] Nguyen N.T., Huang X.Y., and Chuan T.K., "*MEMS-micropumps: a review*", *ASME J. Fluids Eng.*, 124, 384–92, 2002.

[Las'04] Laser D.J. and Santiago J.G., "*A review of micropumps*", *J Micromech Microeng*, 14, R35-R64, 2004.

[Mar'10] Mark D., Haeberle S., Roth G., von Stetten F. and Zengerle R., "*Microfluidic lab-on-a-chip platforms: requirements, characteristics and applications*", *Chem Soc. Rev.*, 39, 1153–82, 2010.

[Gop'14] Gopinath S.C.B., Tang T.H., Citartan M., Chen Y. and Lakshmipripa T., "*Current asects in immunosensors", Biosens. Bioelectron. Elsevie*r, 57, 292–302, 2014.

[Dit'06] Dittrich P.S., Manz A., "*Lab-on-a-chip: microfluidics in drug discovery", Nature Rev. Drug Discov.*, 5, 210–218, 2006.

[Bhu'17] Bhuktare S., Bose A., Singh H. and Tulapurkar A.A., "*Gyrator based on magneto-elastic coupling at a ferromagnetic/piezoelectric interface", Scientific Reports*, 7, 840, 2017.

[Rei'93] Reindl L. and Ruile W., *"Programmable reflectors for SAW-ID-tags", Proc. IEEE Ultrason. Intern. Symp.*, 125-130, 1993.

[Nic'19] Nicolay P., "*Wireless and Passive SAW devices for Structural Health Monitoring Applications", Multidiscip. Dig. Pub. Proc.*, 2, 5, 2019.

[Wil'09] Wilson W.C., Malocha, D.C., Kozlovski N., Gallagher D.R., Fisher B., Pavlina J., Saldanha N., Puccio D., Atkinson G.M., *"Orthogonal Frequency Coded SAW Sensors for aerospace SHM Applications", IEEE Sensors J.*, 9, 11, 2009.

[Coi'09] Coillot C., Moutoussamy J, Lebourgeois R., Ruocco S., Chanteur G., *"Principle of Performance of a Dual-Band Search Coil Magnetometer: A New Instrumentation to Investigate Fluctuating Magnetic Fields in Space", IEEE Sensors J.*, 10, 2, 255-260, 2009.

[Mar'12] Marcon P. and Ostanina K., *"Overview of Methods for Magnetic Susceptibility Measurement", PIERS Proceedings KL, Malaysia*, 412, 2012.

[HonR] Report, Honeywell Inc., Micro Switch sensing and control. (https://sensing.honeywell.com/honeywell-sensing-sensors-magnetoresistive-hall-effect-applications-005715-2-en2.pdf)

[MurR] Basic knowledge of AMR sensors, Murata Inc. (https://www.murata.com/en-eu/products/sensor/amr/basic/principle)

[Jog'15] Jogschies L., Klaas D., Kruppe R., Rittinger J., Taptimthong P., Wienecke A., Rissing L., Wurz M. C., *"Recent Developments of Magnetoresistive Sensors for Industrial Applications", Sensors*, 15, 28665-28689, 2015.

[Nob'07] Report, The 2007 Nobel Prize in Physics, AAPPS Bulletin, 17, 6, 2007.

[WikA] Wikipedia article, Proton Magnetometer, (https://en.wikipedia.org/wiki/Proton_magnetometer)

[GemR] Report, Gem Advanced magnetometer systems, (http://www.gemsys.ca/pdf/Overhauser_Magnetometers_Brief_Overview.pdf?lbisphpreq=1)

[SciR] Report, Scintrex Limited, (https://scintrexltd.com/wp-content/uploads/2017/02/CS-VL-Manual-773701-Rev0.pdf)

[Bri'07] Brissaud M., "Matériaux piézoélectriques : Caractérisation, modélisation et vibration", Lausanne: Presses Polythechniques et Universitaires Romandes, 2007.

[Bra'00] Braile L.W., "*Seismic waves and the slinky: A guide for teachers", Informal Publication*, 2000. (https://web.ics.purdue.edu/~braile/edumod/slinky/slinky.htm).

[Lov'67] Love E. H., "*Some problems of geodynamics", New York: Dover: Cambridge Univ. Press*, 1967.

[Dob'51] Dobrin M. B., "*Dispersion in Sismiques Surface Waves", Géophysics* 16, 63, 1951.

[Vic'81] Victorov I. A., *"Surface acoustic waves in solids", Moscow: Nauka*, 1981.

[Ray'85] Rayleigh, *"On waves propagated along the plane surface of elastic solid", Proc. London Math. Soc.*, 17, 4, 1885.

[Aub'10] Aubert T., Elmazria O., Assouar B., Bouvot L. and Oudich M., *"Surface acoustic wave devices based on AlN/sapphire structure for high temperature applications", Appl. Phys. Lett.,* 96, 203503, 2010.

[Aub'13] Aubert T., Bardong J., Legrani O., Elmazria O., Assouar B., Bruckner G. and Talbi A., *"In-situ high temperature characterization of ALnN-based surface acoustic wave devices", J. Appl. Phys.*, 114, 014505, 2013.

[Rod'13] Rodriguez-Madrid J. G., Iriarte G. F., Williams O.A. and Calle F., *"High precision pressure sensors based on SAW devices in the GHz range", Sens. Act. A: Phys,* 189, 364-369, 2013.

[Nic'08] Nicolay P., Elmazria O., Sarry F., Bouvot L., Marche N. and Kambara H., *"Innovative surface acoustic wave sensor for accurate measurement of sub-atmospheric pressure", Appl. Phys. Lett.*, 92, 141909, 2008.

[Hou’17] Houri C.G., Talbi A., Viard R., Moutaouekkil M., Elmazria O., Gallas Q., Garnier E., Merlen A. and Pernod P., *“High temperature gradient nanogap-Pirani micro-sensor with maximum sensitivity around atmospheric pressure”, Appl. Phys. Lett.,* 111, 113502, 2017.

[Guo’14] Guo Y. J., Zhang J., Zhao C., Hu P.A., Zu X. T. and Fu Y. Q., *“Graphene/LiNbO3 surface acoustic wave device based relative humidity sensor”, Optik*, 125, 5800-5802 2014.

[Xua’14] Xuan W., M. He, Meng N., He X., Wang W., Chen J., Shi T., Hasan T., Xu Z., Xu Y. and Luo J.K., *“Fast Response and High Senstivity ZnO/glass Surface Acoustic Wave Humidity Sensors Using Graphene Oxide Sensing Layer”, Sci. Rep.,* 4, 7206, 2014.

[Eun’16] Eun K., Lee K. J., Lee K. K., Yang S. S. and Choa S. H*., “Highly sensitive surface acoustic wave strain sensor for the measurement of tire deformation”, Int. J. Precision Engg. & Manufacturing*, 17, 699, 2016.

[Gra’18] Gray E. R., Turbe V., Lawson V.E., Page R.H., Cook Z.C., Ferns R.B., Nastouli E., Pillay D., Yatsuda H., Athey D. and McKendry R.A., *npj Dig. Med.*, 1, 35, 2018.

[Bro’16] J. Brooks, R. Bufacchi, J. Kondoh, D.M. Duffy and R.A. McKendry, *“Determining biosensing modes in SH-SAW device using 3D finite element analysis”, Sens. Act. B: Chem,* 234, 412, 2016.

[Afz’13] Afzal A, Iqbal N, Mujahid A, Schirhagl R., *“Advanced vapor recognition materials for selective and fast responsive surface acoustic wave sensors: a review”, Anal Chim Acta,* 787, 36–49, 2013.

[Gro’07] Groewold T.M., “Surface acoustic wave sensors in the bioanalytical field: recent trends and challenges”, Anal Chim Acta, 603,119–28, 2007.

[Lan’08] Lange K, Rapp B.E., Rapp M., “Surface acoustic wave biosensor: a review”, Anal Bionanal Chem; 8391, 1509–19, 2008.

[Dev’17] Devkota J., Ohodnicki P. R. and Greve D. W., *“SAW Sensors for Chemical Vapors and Gases”, Sensors (Basel)*, 17(4), 801, 2017.

[Liu’14] Liu J. and Lu Y., *“Response mechanism for surface acoustic wave gas sensors based on surface-adsorption”, Sensors (Basel)*, 14, 6844, 2014.

[Jak’11] Jakubik W. P., *“Surface acoustic wave-based gas sensors”, Thin Solid Films*, 520, 986, 2011.

[Kad’11] Kadota M, Ito S, Ito Y, Hada T, And Okaguchi K, *“Magnetic Sensor Based on Surface Acoustic Wave Resonators”, Jpn. J. Appl. Phys.* 50: 07HD07, 2011.

[Han’87] Hanna S M, *“Magnetic Field Sensors Based on SAW Propagation in Magnetic Films”, IEEE Trans. Ultrason., Ferroelectr., Freq. Control. UFFC-34*: 191-194, 1987.

[Yam’80] Yamaguchi M., Hashimoto K.Y., Kogo H. and Naoe M., “*Variable SAW delay line using amorphous $TbFe_2$ Film”, IEEE Trans. On Mag.*, MAG-16,6 1980.

[GAN'76] Ganguly A. K., Davis K. L., Webb D. C. and Vittoria C., *"Magnetic control of surface elastic waves in a novel layered structure", J. Appl. Phys.*, 47, 2696, 1976.

[Elh'16] Elhosni M., Elmazria O., Petit-Watelot S., Bouvot L., Zhgoon S., Talbi A., Hehn M., Aissa K. A., Hage-Ali S., Lacour D., Sarry F. and Boumatar O., *"Magnetic field SAW sensors based on magnetostrictive-piezoelectric layered structures", Sensors and Actuators A Phys*, 240, 41, 2016.

[Smo'03] Smole P., Ruile W., Korden C., Ludwig A., Quandt E., Krassnitzer S. and Pongratz P., *"Magnetically tunable SAW-resonator", Proc of IEEE Int. Freq. Ctrl. Sym.*, 903-906, 2003.

[Hau'00] Hauser H, Steindl R, Hausleitner Ch, Pohl A, Nicolics J*, "Wirelessly Interrogable Magnetic Field Sensor Utilizing Giant Magneto-Impedance Effect and Surface Acoustic Wave Devices", IEEE T INSTRUM MEAS.,* 49: 648-652, 2000.

[Ste'00] Steindl R, Hausleitner Ch, Pohl A, Hauser H, Nicolics J*, "Passive wirelessly requestable sensors for magnetic field measurements", Sens Actuators A.*, 85 169-174, 2000.

[Hau'06] Hauser H, Steurer J, Nicolics J, Musiejovsky L, Giouroudi I, *"Wireless Magnetic Field Sensor", Journal of Electrical Engineering* ,57, 9-14, 2006.

[Kon'17] Kondalkar V.V., Li X., Park I., Yang S.S., Lee K., *"Development of chipless, wireless current sensor system based on giant magnetoimpedance magnetic sensor and surface acoustic wave transponder", Sci. Rep.*, 8, 2401, 2018.

[Pol'17] Polewczyk V., Dumesnil K., Lacour D., Moutaouekkil M., Mjahed H., Tiercelin N., Petit-Watelot S., Mishra H., Dusch Y., Hage-Ali S., Elmazria O., Montaigne F., Talbi A., Bou Matar O. and Hehn M., *"Unipolar and Bipolar High-Magnetic-Field Sensors Based on Surface Acoustic Wave Resonators", Phys. Rev. Applied*, 8 024001, 2017.

[Zho'14] Zhou H., Talbi A., Tiercelin N. and Bou Matar O., "*Multilayer magnetostrictive structure based surface acostic wave devices", Appl. Phys. Lett.*, 104, 114101, 2014.

Chapter 2

Optimization of the SAW structure

Introduction:

This second chapter is aimed at providing a numerical basis for the future experimental studies that we describe in subsequent chapters. First of all, we describe the numerical model used for this study and the physics behind it. Next we discuss the integration of the magnetic behaviour into the model by virtue of theoretical magnetisation curves. Subsequently parametric simulations are presented describing the role of device wavelength, electrode thickness and metallization ratio. We also introduce a multi-layered structure in the end.

2.1 The Numerical Model:

The equivalent piezomagnetic model for MSAW devices had been previously developed by our partners Bou Matar *et al. [Bou'12]* and Zhou *et al. [Zhou'14, Zho'14]*. Here, we present an introduction to the model developed by them. In this theoretical model, an elastic wave generated in the piezoelectric substrate and affecting the ferromagnetic thin film is considered. The elastic properties of a magneto-elastic material strongly depend on the magnetic state of the material and the direction of the applied magnetic field. The effect has been reported also for giant magnetostrictive materials such as Terfenol-D, even at ultrasonic frequencies *[Cul'78]*. It has been shown previously that if the interactions between the magnetic dipoles is neglected, and the magneto-elastic medium is considered homogeneous, the dynamic elastic behaviour of the layer can be expressed in terms of the effective elastic modulus *[Lec'65, Gul'97]*. Considering the dipole interactions however, implies a dependence of the effective elastic modulus on the wave propagation direction *[Eas'66, Mir'98, Rin'85]*. To overcome this challenge, Zhou *et al.* proposed to determine the piezomagnetic equivalent of a ferromagnetic material around a polarization point.

Thus the elastic constants (C_{ijkl}), piezomagnetic constants (q_{lij}) and the magnetic permeability (μ_{ij}) become field-dependent and this dependency translates to a controllability of the elastic and the piezomagnetic properties by an external magnetic field in magnetostrictive materials. Here, we first elucidate the fundamental equations describing the magneto-elastic coupling, in a ferromagnetic film. We then discuss the equilibrium states when the magnetic field is applied parallel or perpendicular to the magnetic easy axis of the film. When the field is applied along the direction perpendicular to the anisotropy direction (i.e. along the *magnetic Hard Axis*), a Spin Reorientation Transition (*SRT*) is observed that corresponds to a reorientation of the film's magnetisation for an infinitesimal variation in the intensity of the applied magnetic field. The effective material properties corresponding to the piezomagnetic equivalent of the magnetostrictive layer was then calculated around the equilibrium state. In their model, Zhou *et al.* have considered the case of an elastic wave in a ferromagnetic film deposited over a substrate and magnetised to saturation (as shown in Figure 2.1). Although the geometry of our device varies from Zhou (resonator vs delay line respectively), the basic principles remain the same and hence the model is directly considered for our study. The amplitude of the magnetisation, M is considered constant at saturation as M_s. The coupling between the magnetic and mechanical energy domains is considered on the basis of the *Landau-Lifshitz* equations *[Gur'96]*:

$$\rho \times \frac{\partial^2 u_i}{\partial t^2} = \frac{\partial T_{ij}}{\partial x_j} \text{ ----------------- (Eq. 2.1)}$$

$$\frac{\partial M}{\partial T} = -\gamma \mu_0 \left[M \times H_{eff} \right] \text{ ----------------- (Eq. 2.2)}$$

Where γ is the gyromagnetic ratio, ρ is the density, u_i is the i^{th} component of the particle displacement and x_i denotes the Eulerian coordinates. H_{eff} , the effective internal magnetic field, T_{ij} , the stress tensor and E_{kl}, the tensorial representation of the effective strain are represented as:

$$H_{eff} = H - \frac{1}{\mu_0} \times \frac{\partial U}{\partial M} \text{ ----------------- (Eq. 2.3)}$$

$$T_{ij} = \frac{\partial U}{\partial E_{ij}} \text{ ----------------- (Eq. 2.4)}$$

$$E_{kl} = \frac{1}{2} \times \left(\frac{\partial u_k}{\partial x_l} + \frac{\partial u_l}{\partial x_k} \right) \text{ ----------------- (Eq. 2.5)}$$

Where H is the Maxwellian magnetic field and U is the local internal energy density.

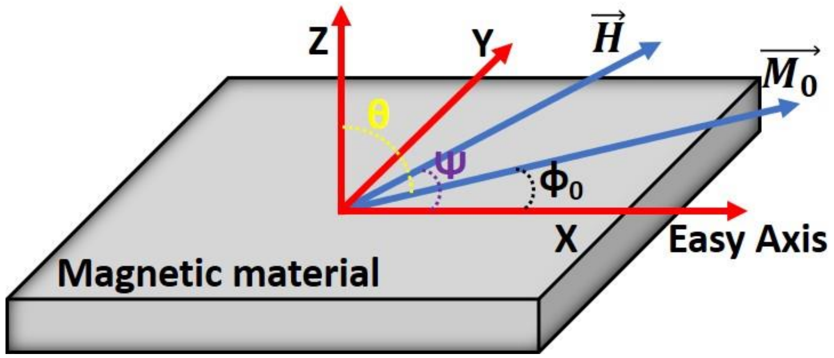

Figure 2.1: Schematic of the magnetic system under study. Ψ represents the angle between the X-axis (easy axis in this case) and the applied magnetic field, Φ_0 is the angle between the X-axis and the projection of the magnetisation.

The internal energy density, U is given by:

$$U = U_{an} + U_{me} + U_e \text{ ----------------- (Eq. 2.6)}$$

magnetocrystalline energy, $U_{an} = -K_1\alpha_1^2$

magnetoelastic coupling energy, $U_{me} = b_{ijkl}\alpha_i\alpha_j E_{kl}$

elastic energy, $U_e = \frac{1}{2}C_{ijkl}E_{ij}E_{kl}$

Where $\alpha_i = M_i/M_s$ are the direction cosines of M with respect to the chosen coordinate system, K_1 is the magnetic anisotropy constant linked to the anisotropy field H_A as $K_1 = \mu_0 M_s H_A / 2$, magnetic permeability of vacuum, $\mu_0 = 4\pi \times 10^{-7}$, b_{ijkl} are the magneto-elastic constants and C_{ijkl} are the second-order elastic constants.

Finally, linearization of Eq. 2.1 & 2.2 (around ground state position dependent on the direction and intensity of external applied field) leads to –

$$\rho\frac{\partial^2 u_i}{\partial t^2} = \frac{\partial \sigma_{ij}}{\partial x_j} \text{ ----------------- (Eq. 2.7)}$$

$$\frac{\partial b_i}{\partial x_i} = \frac{\partial(\mu_0(h_i+m_i))}{\partial x_i} = 0 \text{ ----------------- (Eq. 2.8)}$$

$$\sigma_{ij} = \left(C_{ijkl} + \Delta C_{ijkl}\right)\frac{\partial u_k}{\partial x_l} - q_{lij}h_l \text{ ----------------- (Eq. 2.9)}$$

$$b_i = q_{ikl}\frac{\partial u_k}{\partial x_l} + \mu_{il}h_l \text{ ----------------- (Eq. 2.10)}$$

where, $\mu_{il} = \mu_0(\delta_{il} + \chi_{il})$; $\Delta C_{ijkl} = b_{ijmn}(M_n^0 q_{mkl} + M_m^0 q_{nkl})$; σ_{ij} is the dynamic deformation tensor, h_i is the magneto-static field, m_i is the magnetisation, and b_i is the dynamic magnetic induction.

Thus the effective magnetic permeability and the effective elastic constants are given by:

$$\mu_{il} = \mu_0(\delta_{il} + \chi_{il}) \text{ --------------------- (Eq. 2.11)}$$

$$C_{ijkl} + \Delta C_{ijkl} = C_{ijkl} + b_{ijmn}(M_n^0 q_{mkl} + M_m^0 q_{nkl}) \text{ ---------------- (Eq. 2.12)}$$

Where the piezomagnetic constant, $q_{mij} = -\frac{b_{ijkl}}{M_S^2}(M_k^0 \chi_{lm} + M_l^0 \chi_{km})$.

Therefore, the equations 2.9 to 2.12, present the piezomagnetic equations similar to those conventionally used, replacing the electric with the magnetic field, the permittivity by the magnetic permeability and the piezoelectric constants replaced by the piezomagnetic constants.

Considering a magneto-elastic thin film, as shown in Figure 2.1, with cubic mechanical or elastic properties and amorphous magnetisation that is always in plane and neglecting the influence of static elastic strains we obtain:

$$\mu = \begin{bmatrix} \mu_{11} & \mu_{12} & 0 \\ \mu_{12} & \mu_{22} & 0 \\ 0 & 0 & \mu_{33} \end{bmatrix}$$

$$\Delta C = \begin{bmatrix} \Delta C_{11} & \Delta C_{11} & 0 & 0 & 0 & \Delta C_{16} \\ \Delta C_{11} & \Delta C_{11} & 0 & 0 & 0 & -\Delta C_{16} \\ 0 & 0 & 0 & 0 & 0 & 0 \\ 0 & 0 & 0 & \Delta C_{44} & \Delta C_{45} & 0 \\ 0 & 0 & 0 & \Delta C_{45} & \Delta C_{55} & 0 \\ \Delta C_{16} & -\Delta C_{16} & 0 & 0 & 0 & \Delta C_{66} \end{bmatrix}$$

$$q = \begin{bmatrix} q_{11} & -q_{11} & 0 & 0 & 0 & q_{16} \\ q_{21} & -q_{21} & 0 & 0 & 0 & q_{26} \\ 0 & 0 & 0 & q_{34} & q_{35} & 0 \end{bmatrix}$$

Table I: Non-zero components of the effective permeability tensor

$$\boldsymbol{\mu_{11} = \mu_0 + \frac{\mu_0 M_s^2 \sin^2 \varphi_0}{U'_{\varphi\varphi}}}$$

$$\boldsymbol{\mu_{12} = -\frac{\mu_0 M_s^2 \sin 2\varphi_0}{2U'_{\varphi\varphi}}}$$

$$\boldsymbol{\mu_{22} = \mu_0 + \frac{\mu_0 M_s^2}{U'_{\varphi\varphi}}(1 - \sin^2 \varphi_0)}$$

$$\boldsymbol{\mu_{33} = \mu_0 + \frac{\mu_0 M_s^2}{U'_{\theta\theta}}}$$

Table II: Non-zero components of the effective elastic stiffness correction tensor

$$\boldsymbol{\Delta C_{11} = -\frac{4(b^{\gamma,2})^2 cos^2 \varphi_0\, sin^2 \varphi_0}{U'_{\varphi\varphi}}}$$

$$\boldsymbol{\Delta \mathrm{C}_{16} = \frac{(\mathrm{b}^{\gamma,2})^2 \sin 4\varphi_0}{2U'_{\varphi\varphi}}}$$

$$\boldsymbol{\Delta \mathrm{C}_{44} = -\frac{(\mathrm{b}^{\gamma,2})^2 \sin^2 \varphi_0}{U'_{\theta\theta}}}$$

$$\boldsymbol{\Delta \mathrm{C}_{45} = -\frac{(\mathrm{b}^{\gamma,2})^2 \sin \varphi_0 \cos \varphi_0}{U'_{\theta\theta}}}$$

$$\boldsymbol{\Delta \mathrm{C}_{55} = -\frac{(\mathrm{b}^{\gamma,2})^2 \cos^2 \varphi_0}{U'_{\theta\theta}}}$$

$$\boldsymbol{\Delta \mathrm{C}_{66} = -\frac{(\mathrm{b}^{\gamma,2})^2 \cos^2 2\varphi_0}{U'_{\varphi\varphi}}}$$

Table III: Non-zero components of the effective piezomagnetic constant tensor

$$\mathrm{q}_{11} = -\frac{2\mathrm{b}^{\gamma,2}\mu_0 M_s \cos\varphi_0 \sin^2\varphi_0}{U'_{\varphi\varphi}}$$

$$\mathrm{q}_{21} = \frac{2\mathrm{b}^{\gamma,2}\mu_0 M_s \sin\varphi_0 \cos^2\varphi_0}{U'_{\varphi\varphi}}$$

$$\mathrm{q}_{34} = -\frac{\mathrm{b}^{\gamma,2}\mu_0 M_s \sin\varphi_0}{U'_{\theta\theta}}$$

$$\mathrm{q}_{35} = -\frac{\mathrm{b}^{\gamma,2}\mu_0 M_s \cos\varphi_0}{U'_{\theta\theta}}$$

$$\mathrm{q}_{16} = \frac{\mathrm{b}^{\gamma,2}\mu_0 M_s (1 - 2\sin^2\varphi_0)\sin\varphi_0}{U'_{\varphi\varphi}}$$

$$\mathrm{q}_{26} = -\frac{\mathrm{b}^{\gamma,2}\mu_0 M_s (1 - 2\sin^2\varphi_0)\cos\varphi_0}{U'_{\varphi\varphi}}$$

Thus finally the second order derivative of the internal energy, U' are obtained as ($\mathrm{b}^{\gamma,2}$ is the magneto-elastic coupling coefficient):

$$U'_{\theta\theta} = \mu_0 M_s(H_A(1 - \sin^2\varphi_0) + Hcos(\varphi_0 - \Psi) + H_{me})$$

$$U'_{\varphi\varphi} = \mu_0 M_s(H_A(1 - 2\sin^2\varphi_0) + Hcos(\varphi_0 - \Psi) + H_{me})$$

and, $U'_{\theta\varphi} = 0$

Depending on the orientation of the applied magnetic field i.e. along easy or hard magnetic axis, the piezomagnetic equations (Eq. 2.9 - 2.12) change their values by considering appropriate values for φ and Ψ (*Ψ=90º for Hard axis and Ψ = 0º for Easy axis*) and accordingly re-calculate the material properties.

2.2 The Ideal Magnetisation Curves:

The Stoner-Wolhfart Model: Taking into account the anisotropy and the Zeeman energies for simplicity, the magnetic anisotropy (E_A) and the total energy of the system (E) under an external magnetic field H_{ext}, can be respectively represented by considering approximation theory as follows:

$$E_A = K_{eff} \sin^2 \theta . V$$

$$E = (K_{eff} \sin^2 \theta - \mu_0 M_s H_{ext} \cos(\alpha - \theta)) V$$

where, K_{eff} is the effective magnetic anisotropy constant, V is the sample volume and (α-θ) gives the angle between the external magnetic field and the magnetisation.

The solutions to the above equations may only be found for the extreme cases (energy minimization solved easily) when we consider the magnetisation is along the easy axis ($\theta = 0^o$) and a magnetic field that is applied parallel ($\alpha = 0^o$) or perpendicular ($\alpha = 90^o$) to the anisotropy direction; i.e. along the easy axis and hard axis directions respectively.

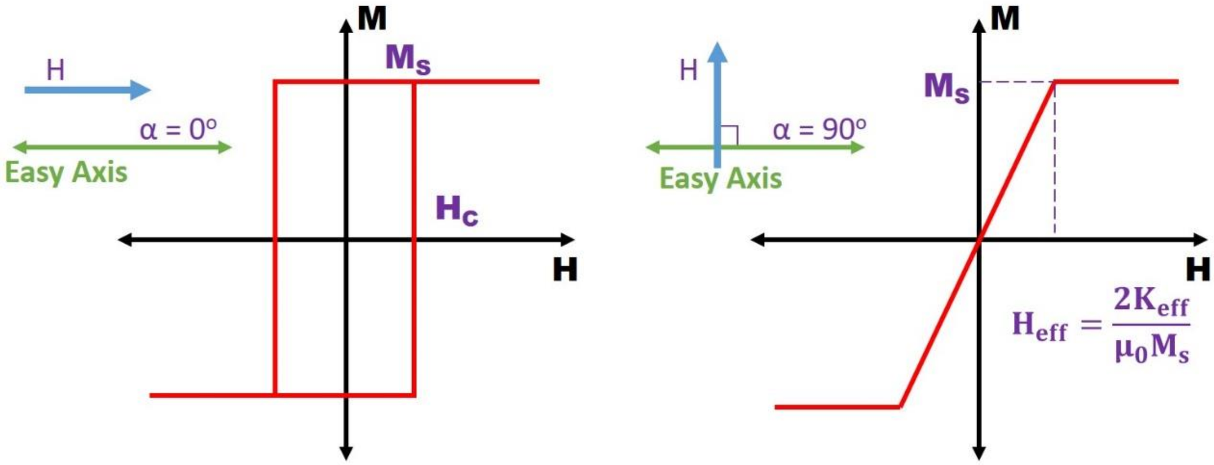

Figure 2.2: M(H) loops for the easy ($\alpha = 0^o$) and hard ($\alpha = 90^o$) axis configurations. The green line represents the magnetisation direction or easy axis and the blue arrow represents the direction along which the magnetic field (H) is applied.

With the magnetic field applied along the easy magnetisation axis ($\alpha = 0^o$), we observe a hysteretic response (refer Figure 2.2, Left). A coercive field H_c is observed that may be defined as the intensity of the magnetic field necessary to nullify the magnetisation, after the sample has been magnetised to saturation. The M_s is observed as the remnant magnetisation at zero field and defined as the saturation magnetisation. In the hard axis configuration (H is applied along $\alpha = 90^o$) the magnetisation has a linear response, such that at zero applied field the magnetisation also reduces to zero. The magnetic field necessary to saturate the sample in this case is defined as the anisotropy field, H_{keff} and is represented as:

$$H_{Keff} = \frac{2K_{eff}}{\mu_0 M_s}$$

The model also determines the magnetic response and the coercive field as a function of the angle α between the magnetic field and the easy magnetisation axis, thus giving us the famed *Stoner-Wohlfart asteroid*:

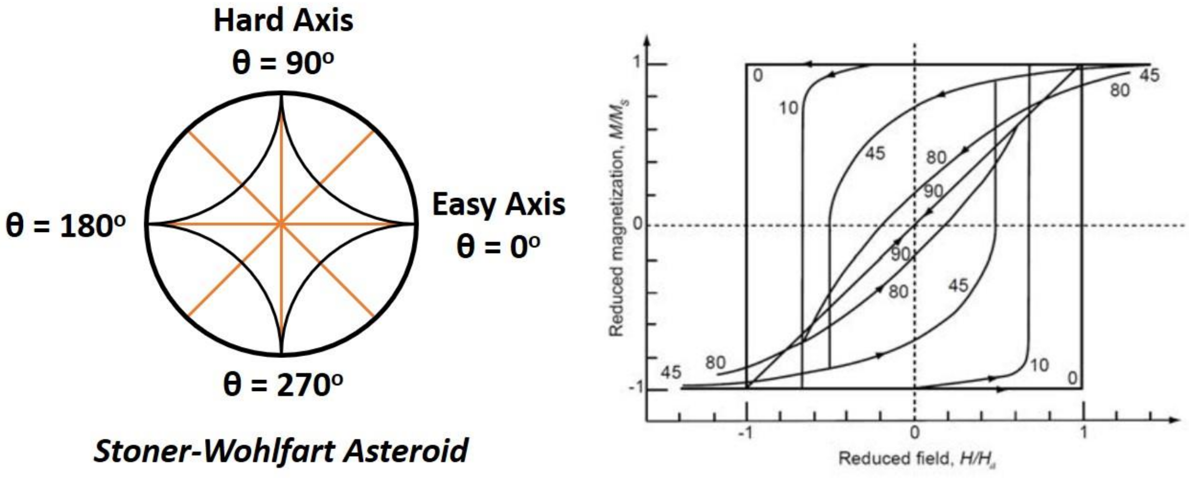

(a) (b)

Figure 2.3: (a) Representation of the *Stoner-Wolhfart* asteroid; (b) M(H) loops for different angles *[Vau'17]*.

Finally, in the Stoner-Wolhfart model, it is observed that $H_c = H_{Keff}$ when the applied field is along the easy magnetisation axis. This observation however holds true only for small nano-scale structures. Normally, the coercive field H_c observed is smaller than the anisotropy field H_{Keff}. In the sample, the magnetisation switching is usually induced by the propagation of the domains, which nucleate at places containing microstructural defects. However, knowing the anisotropy field, it is indeed possible to estimate the anisotropy constant. As seen before, the anisotropy field is obtained by applying the field perpendicular to the easy magnetisation axis.

2.3 Simulation of the magneto-acoustic response:

In order to understand the various aspects of the geometry of a SAW device, we first started off our simulation based study to comprehend the effect on the magneto-acoustic response of the device to a magnetic field. The study is based on the numerical model described earlier that is based on the Equations 2.9 -2.12. The aim of this study is to optimize the structure of the device to obtain the best configuration for a magnetic sensor. The 128°-YX crystal configuration of Lithium Niobate ($LiNbO_3$) is a widely used substrate for SAW devices, optimizing between a high Rayleigh wave SAW velocity and a high electromechanical coupling coefficient (K^2) among piezoelectric crystals *[Kan'06, Nau'06]*. Thus, we consider a substrate of 128° Y-cut $LiNbO_3$ with propagation along both the *X* and *X+90°* directions in this research work (Chapter 3). However, since the idea of this chapter was to get a basic idea of the effect of the device geometry on the magneto-acoustic response, we have chosen to work with a propagation direction along the (X+90°) direction, the results of which, we believe, will be similar if the propagation was along the X-direction. As we will describe in subsequent chapters, this is also the substrate we will use for our experimental analysis. Further, to keep the study simple and to ensure that we completely understand the nature of the magnetic material in it, we consider the ideal magnetisation curves that we described in the previous section. The simulation model (described in a previous section), encompasses the magnetic behaviour coupled with the mechanical and electrical responses of the device. Thus, we considered a simplified 2-D geometry of the entire device, using antiperiodic boundary conditions along the X-axis and perfectly matched layer (*PML*) at the bottom of the $LiNbO_3$ layer to mimic a semi-infinite substrate. As mentioned, the magnetisation of the sensitive layer is considered to follow the ideal *Stoner-Wohlfart* model. This ideal nature of the magnetisation allows us to focus entirely on the effects of the geometry of the device. Here we also consider that the anisotropy of the layer is directed along the wave propagation direction in all the cases of study with an anisotropy field value of 100 Oe. The material properties used during

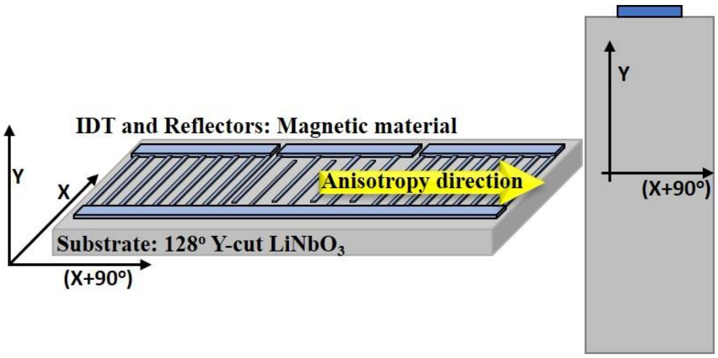

Figure: 2.4: Schematic of the device with a 2D cross-sectional view of the geometry used during the simulations.

the simulation are also kept constant for all the cases. The chosen elastic properties and constants corresponded to Ni because of their easy availability for the study.

2.3.1 *Variation of electrode thickness*: The first set of simulations concern the impact of the thickness of the IDT electrodes on the magnetic response. Here, we have considered the electrodes themselves to be the active magnetostrictive layer. Thus, we consider a device that has a wavelength (λ) of 6.5 µm and a metallization ratio of 60%. Keeping these values constant in the geometry, we consider electrode thicknesses ranging from 50 nm to 1 µm. The resonance frequency observed varied for each thickness of the IDT, but was around the 500 MHz range.

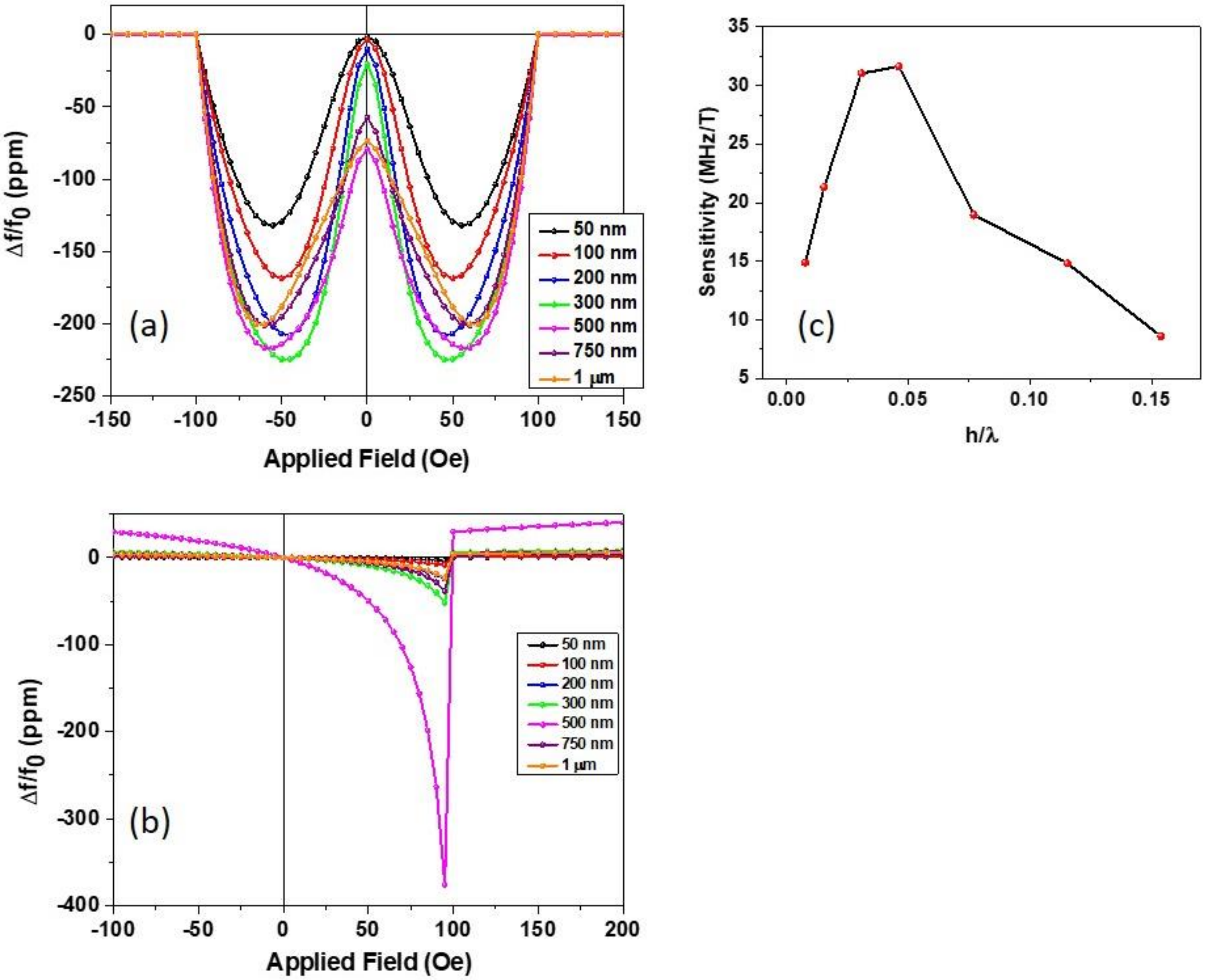

Figure 2.5: Response of the SAW device to an applied magnetic field (increasing) for different thicknesses of the electrode when field is applied along (a) the Hard Axis and (b) Easy Axis of magnetisation. (c) shows the variation of sensitivity along the hard axis as a function of h/λ, where h is the electrode thickness and λ is the device wavelength.

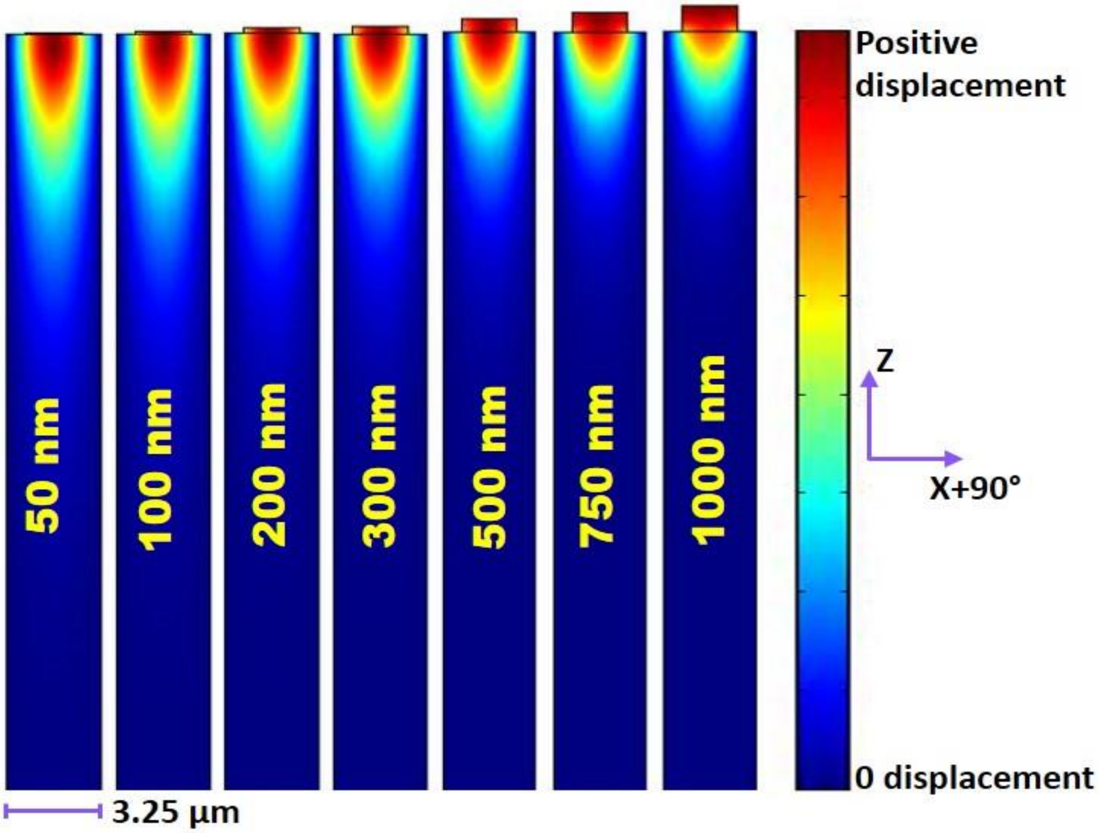

Figure 2.6: Simulated vertical displacement field observed for different electrode thicknesses.

As observed from Figure 2.5 (a), the MSAW response only increases up to 300 nm of electrode thickness. After this the magnetic response either does not increase or decreases. The high relative change of the resonance frequency observed for thicknesses above 300 nm, are explained by the fact that the wave remains confined in the electrode alone, as can be seen from Figure 2.6, and so a higher volume of magnetic material is probed. However, due to the wave being confined only in the electrode, the velocity of wave propagation (which should be in the substrate) is also very less. The relatively low crystalline quality of the magnetic material compared to those of monocrystalline substrate leads to strong increase of the propagation losses in the device. At higher thicknesses of the magnetostrictive layer, we also expect to obtain a magnetisation that is perpendicular and out of plane with the device (experimentally proved in chapter 4). Thus, it becomes clear that for an optimum MSAW response, it is important that the magnetic IDTs have a thickness in the range of 300 nm or lower.

This value is of course, depending on the operating frequency. Generally, we consider the ratio of h/λ (where h and λ are the layer or IDT thickness and wavelength respectively). But for this study we consider the parameters individually.

2.3.2 *Variation of device wavelength*: The second set of simulations concern the impact of the device wavelength on the MSAW response. For this study, we have considered an electrode thickness of 200 nm and a metallization ratio of 60%. Keeping these values constant, we vary the wavelength of the device from 2µm to 20µm.

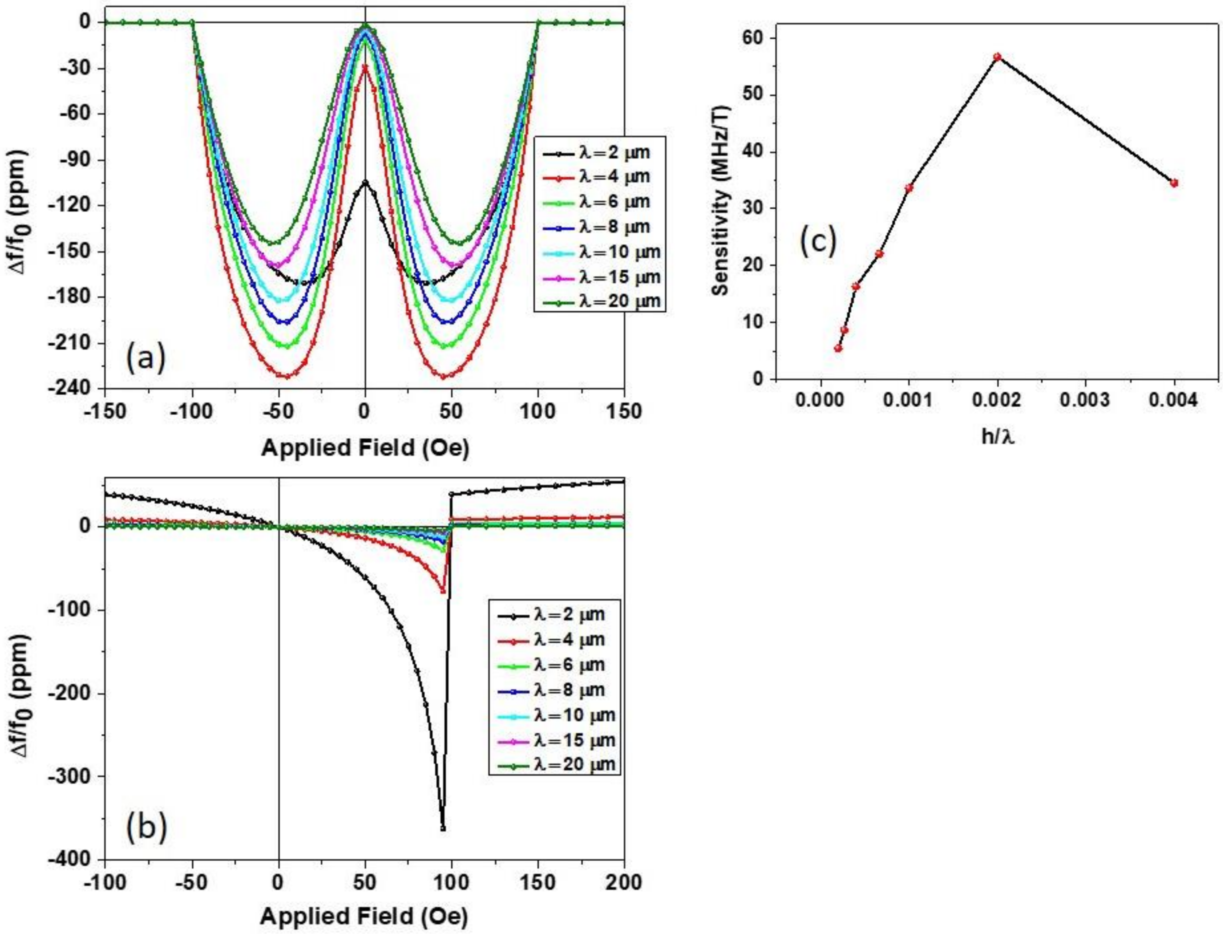

Figure 2.7: Response of the SAW device to an applied magnetic field (increasing) for different wavelengths of the device when field is applied along (a) the Hard Axis and (b) the Easy Axis of magnetisation. (c) shows the variation of sensitivity along the hard axis as a function of h/λ, where h is the electrode thickness and λ is the device wavelength.

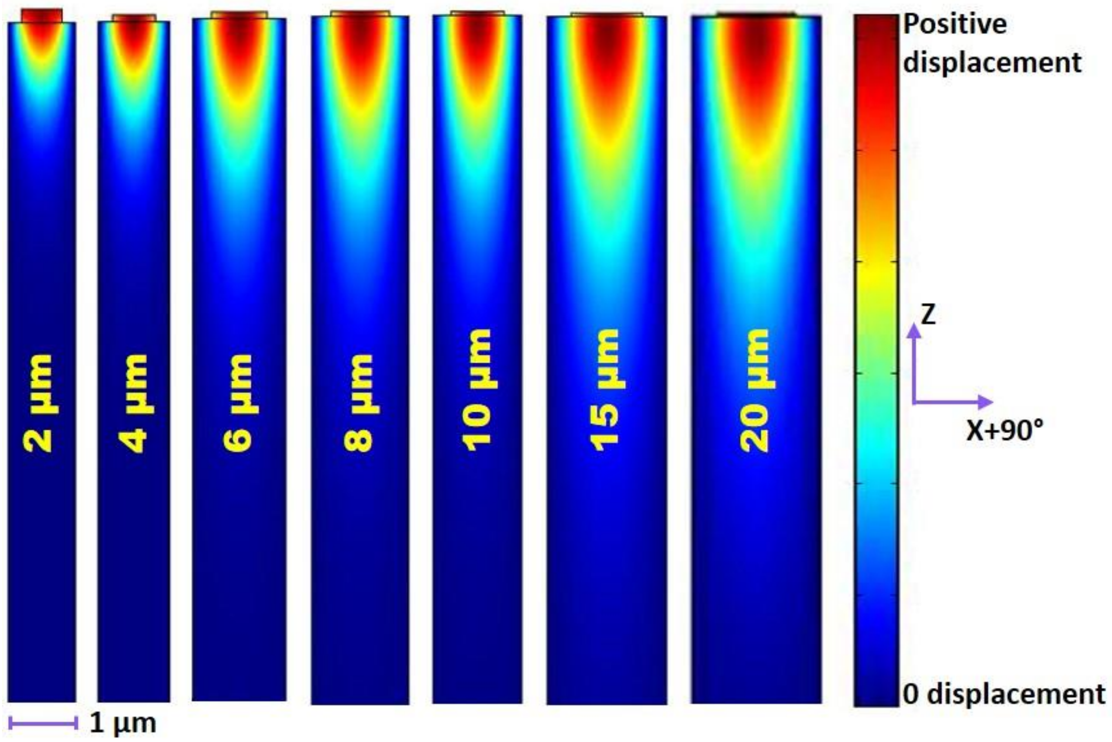

Figure 2.8: Simulated vertical displacement field observed for different device wavelengths.

As observed from Figure 2.7, the hard axis MSAW response increases with a decreasing device wavelength. The reason for this is that the penetration depth of the wave that is formed is inversely proportional to the wavelength, thus leading to a decrease of the wave velocity. This behaviour is clearly seen in Figure 2.8. However, we also observe an anomalous behaviour for the 2 µm device. The response of the device is low along the hard axis and much higher along the easy axis (Figure 2.7). The reason for the low hard axis response can be correlated to the ratio of the magnetic material probed, which is very small in the 2 µm device. We may also note from Figure 2.7 (a) that with a decrease in the device wavelength there is also a drop of the $\Delta f/f_0$ value at 0 magnetic field. Our understanding points that due to the interactions of the acoustic wave with the magnetic moments, this might be an effect of magnetisation dynamics playing a role. The smaller the dimension, the stronger the effect observed. This might also provide an explanation for the high response of the 2 µm device along the easy axis (Figure 2. (b)).

2.3.3 *Variation of metallization ratio of electrodes*: The third set of simulations concern the impact of the metallization ratio of the electrodes on the MSAW response. The metallization ratio refers to the relative width of the electrodes and the device wavelength. Given the fact that higher the metallization ratio of the device, the higher the content of the magnetic material and thus higher will be the response. The simulations have been carried out for IDT metallization ratio of 5% to a maximum of 95%. The wavelength of the device considered in this study have been kept constant at 6.5µm to be as close to the experimental possibility available with us as possible,

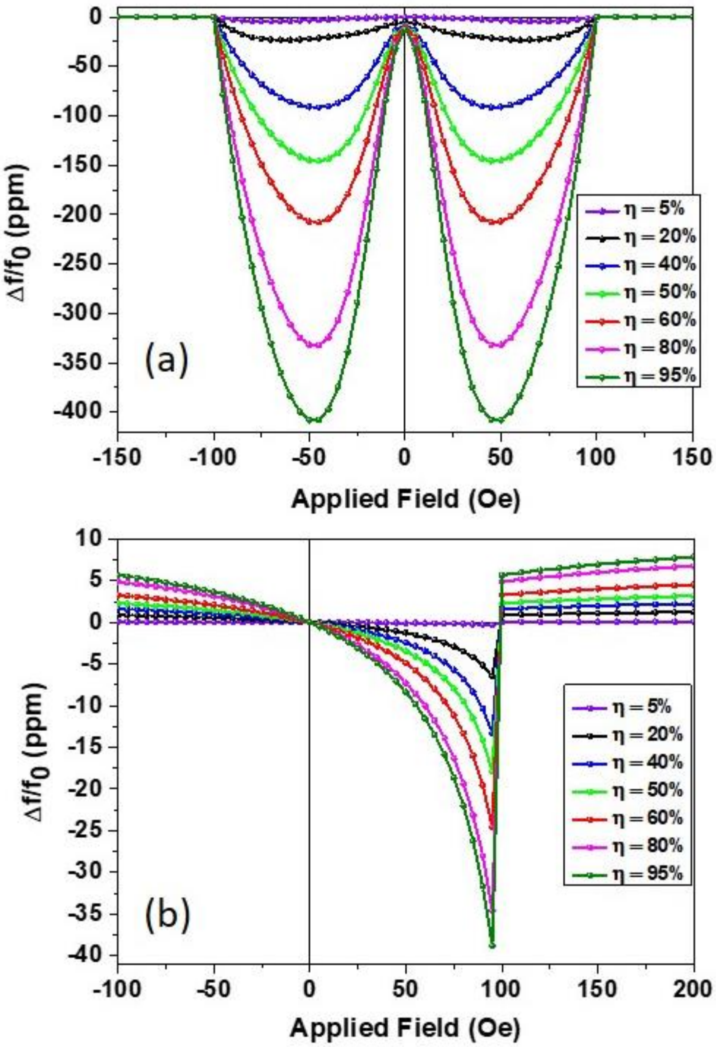

Figure 2.9: Response of the SAW device to an applied magnetic field (increasing) for different metallization ratios of a 6.5µm wavelength device when field is applied along (a) the Hard Axis and (b) the Easy Axis of magnetisation.

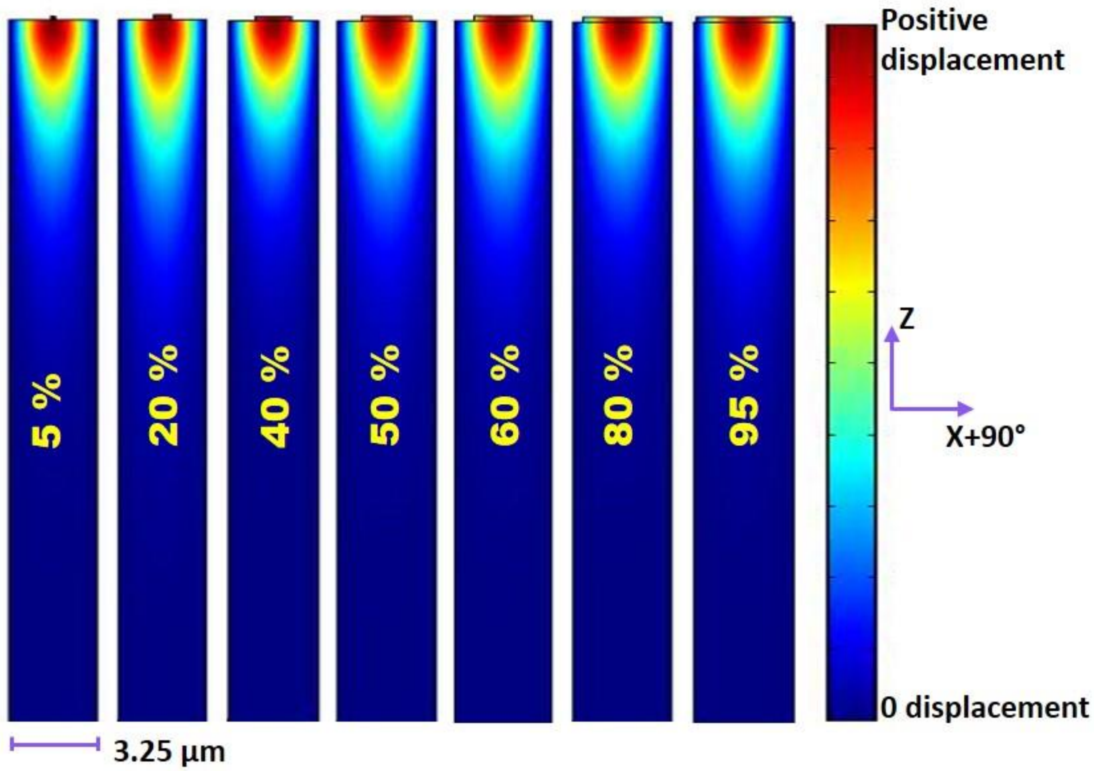

Figure 2.10: Simulated vertical displacement field observed for different metallization ratios of the device with a wavelength of 6.5 µm.

although it was equally interesting to consider other wavelengths. The electrode thickness in this study has been considered at 200 nm.

It can be observed from Figure 2.9 that the sensitivity of the device increases with an increase of the metallization ratio. The reason for this is primarily the fact that with increased metallization ratio, the relative ratio of the magnetic material being probed increases. This means that for a device with higher metallization ratio, the magnetostrictive effect is higher. However, from an experimental point of view, especially optical lithography, there are limitations to develop devices with very high metallization ratios (or even very low).

2.3.4 *Magnetic overlayer structure*: In the previous sections we observed that we could increase the magnetic sensitivity of our sensor if we increased the thickness of the sensitive layer, within a suitable range.

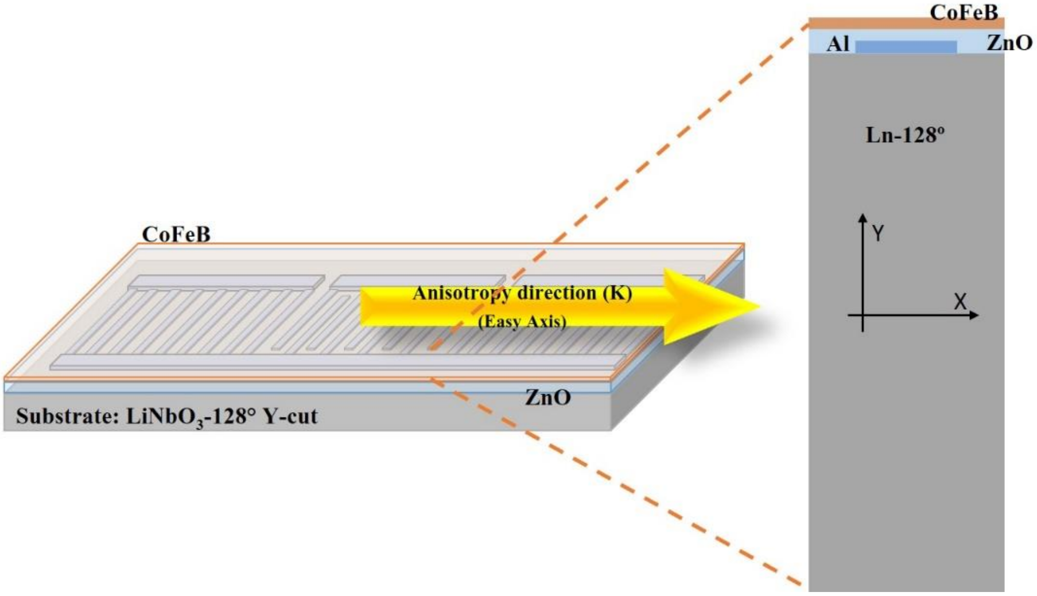

Figure 2.11: Schematic of the device with a 2D cross-sectional view of the geometry used during the simulations. (Blue layer: ZnO; Orange layer: CoFeB)

Further we also saw that increasing the metallization ratio of the electrodes leads to an increase in the sensitivity as well. Thus we now combine them both to explore devices with a complete overlayer of a magnetostrictive material on top of a device with aluminium electrodes. Not only will this study enable us to explore the possibility of full film devices but at the same time help us optimize a structure for packageless devices to be developed in the future. The magnetic over layer is separated from the electrodes by an isolating layer of dielectric ZnO. For this study, we consider the device of a fixed wavelength of 6.5 µm, with electrode thicknesses of 100 nm. The ZnO overlayer has been, to keep the study simple, considered to be a plain rectangular structure of 200 nm, i.e. the thickness of ZnO on top of the electrode is 100nm while on top of the substrate ($LiNbO_3$) it is 200 nm. For a better understanding it may be interesting to consider a contoured layer of ZnO with equal thicknesses over both the substrate and the electrode. The metallization ratio of the electrodes is also kept constant at 60%. Thus the study is made to understand the impact of the variation of the thickness of the magnetic layer on the sensitivity. As can be seen in the Figure 2.11, the anisotropy direction in the film (i.e. the easy axis) is also considered along the wave propagation direction.

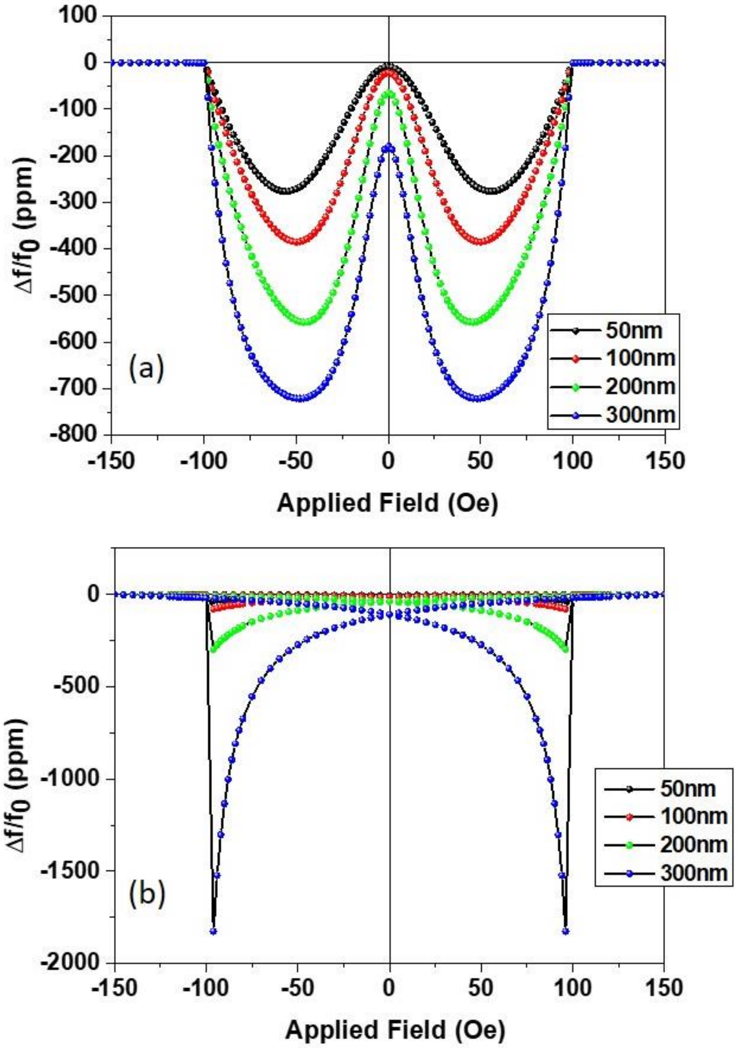

Figure 2.12: Response of the SAW device to an applied magnetic field for variation of the thicknesses of the magnetic layer when the field is applied along (a) the Hard Axis and (b) Easy Axis of magnetisation.

Figure 2.12 shows the relative variation of the resonance frequency with an increasing magnetic field. As can be seen, the higher the thickness of the magnetic layer, the higher is the sensitivity. This is quite in-line with what we observed with variations in the electrode metallization ratio in Figure 2.9. The same explanation holds true for the present case as well. Thicker the magnetic layer, more is the relative volume of magnetic material probed and thus higher is the sensitivity. However, increasing the thickness beyond 300nm raises two important issues. Firstly, the penetration depth of the concerned wave into the substrate reduces indicating that it travels mostly along the sensitive magnetic layer, which might cause huge propagation losses depending on the quality and density of the layers.

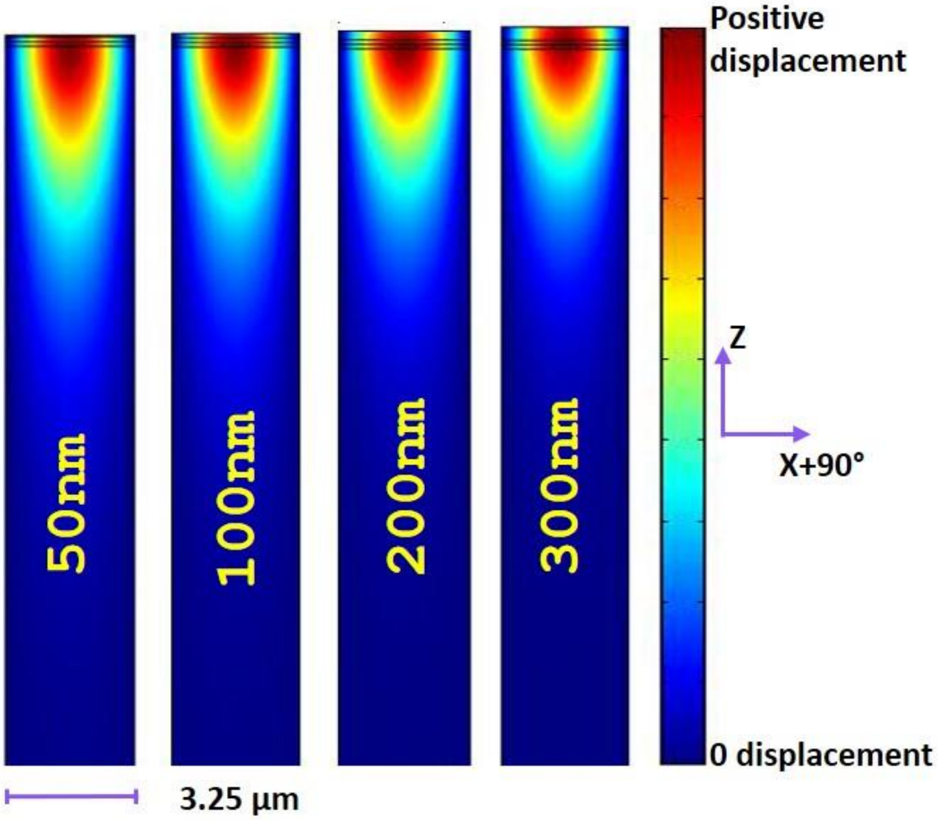

Figure 2.13: Simulated vertical displacement field observed for different thickness of magnetic layer.

The second important challenge associated with this configuration is related to the magnetic behaviour. In order to obtain the best configuration, it is important for the magnetic anisotropy to be along the in-plane direction. However, if we increase the thickness too much, then the anisotropy tends to align itself along the out-of-plane direction which presents a totally different device configuration.

Conclusion:

Thus, in this chapter we have conducted a simulation based study to understand the effects of the parameters related to the structure and geometry of the SAW device on its magneto-acoustic response. First, we studied structures in which the electrodes / IDTs are comprised of the magnetic sensitive layer. We observed that although a higher thickness of the material may indicate a higher sensitivity, too high a thickness can lead to the strongest displacements of the acoustic signal to be confined in the magnetic layer, thus leading to high acoustic propagation losses (i.e. low quality factor of the device). Further, too small a device dimension, may also cause an enhancement of effects related to magnetisation dynamics that are otherwise unnoticeable (as was seen in the abnormal magneto-acoustic response of the device with 2 µm wavelength). This is also observed when we increase the relative thickness of the electrode and thus indicates that an optimization is necessary. In another study we also observed that although it is imperative that a very high metallization ratio may give us a high sensitivity, they are limited from a fabrication aspect. Thus, it is necessary to optimize as well.

We also studied the configuration of a full film of the magnetostrictive layer on top of the electrodes separated by a dielectric layer. In such a configuration also, we inevitably observed that a higher thickness of the magnetic layer implies a higher sensitivity. But then again with an increasing thickness, the acoustic wave tends to drift away from the piezoelectric substrate layer and into the magnetostrictive layer potentially causing a strong increase of acoustic propagation losses.

The importance of this study lies in the fact that it presents a very clear picture of the role of the geometry when considering that the magnetic properties remain constant. It is essential to note that in reality the magnetic properties do not remain the same and this will be elaborated on in the future chapters. At the same time, this chapter enables us to consider and select the best configurations suitable for experimental analysis, keeping into consideration the experimental facilities available.

References:

[Bou’12] Bou Matar O., Robillard J.F., Vasseur J.O., Hladky-Hennion A.-C., Deymier P.A., *“Band gap tunability of magneto-elastic phononic crystal”, J. App. Phy.* 111, 054901, 2012.

[Zhou’14] Zhou H., “*Etude théorique et expérimentale de systèmes a ondes de surface dans des structures multicouches piézomagnétiques pour des applications en contrôle sante intégré de MEMS par imagerie acoustique non linéaire”, PhD Thesis*, Ecole Centrale de Lille, 2014.

[Zho’14] Zhou H., Talbi A., Tiercelin N. and Bou Matar O., “*Multilayer magnetostrictive structure based surface acoustic wave devices”, Appl. Phys. Lett.*, 104, 114101, 2014.

[Cul’78] Cullen J.R., Rinaldi S., Blessing G.V., *“Elastic versus magnetoelastic anisotropy in rare earth-iron alloys”, J. App. Phys.*, 49 (3), 1960-1965, 1978.

[Lec’65] LeCraw R.C., and Comstock R.L., *“Physical Acoustics : Principles and Methods” Vol III, Part B : Lattice Dynamics, Acoustics, New York*, 1965.

[Gul’97] Gulyaev Y.V., Dikshtein I.E., and Shavrov V.G., *“Magnetoacoustic surface waves in magnetic crystals near spin-reorientation phase transitions”, Physics Uspekhi*, 40, 7, 701, 1997.

[Eas’66] Eastman D.E., *“Ultrasonic study of first order and second order magnetoelastic properties of yttrium iron garnet”, Physical Review,* 148, 2, 530-542, 1966.

[Mir’98] Mirasaev I., *“Nonlinear interactions of acoustic modes in ferromagnets near magnetoacoustic resonance: Effective elastic constants”, Physics of Solid State*, 40, 1884-1888, 1998.

[Rin’85] Rinaldi S., and Turilli G., *“Theory of linear magnetoelastic effects”, Physical Review B.*, 31, 5, 3051, 1985.

[Gur’96] Gurevich A.G., and Melkov G.A., *“Magnetisation Oscillations and Waves”, CRC Press Boca Raton*, 1996.

[Kan’06] Kannan T., “*Finite Element Analysis of Surface Acoustic Wave Resonators”, Master of Science Thesis, University of Saskatchewan, Saskatoon*, 2006.

[Nau’06] Naumenko N., “*Analysis of Highly Piezoelectric Non-Leaky SAW Propagating in Rotated Y-cuts of Lithium Niobate with Thick Metal Films or Gratings”, IEEE Int. Ultrasonics Symp., Vancouver*, 493-496, 2006.

[Vau’17] Vautrin C., *“Electronic spin precession in all solid state magnetic tunnel transistor”, PhD Thesis, Université de Lorraine, Nancy,* 2017.

Chapter 3

Studies on magnetic SAW sensors based on [$TbCo_2$/FeCo] multi-layered electrodes

Introduction:

SAW sensors became popular as reliable low-profile devices that may be produced at a low cost. Not only this, but the ease of coupling with antennas allows SAW devices to be interrogated wirelessly as well [*Rei'96, Mal'13*]. Studies conducted by Elhosni *et.al.* [*Elh'15, Elh'16*] and Zhou [*Zhou'14, Zho'14*] have shown the possibility to realize magnetic SAW sensors with a delay line configuration using a layered structure. FEM studies done by Elhosni *et.al.* also prove that high sensitivity may be achieved through proper selection of materials *[Elh'15]*. SAW resonators with Ni interdigital transducers (IDTs) were investigated by Kadota *et. al. [Kad'11]*. Although Yamaguchi *et. al. [Yam'80]* and Smole *et. al. [Smo'03]* have indeed attempted to describe the physical phenomenon behind the sensor behaviour, the physics is still unclear and the interpretation of the experimental results is sometimes not fully in line with proposed theoretical models. This work aims to address the physics and interaction between the acoustic waves and magnetostrictive layers when subjected to a magnetic field. Here, we investigate SAW resonators fabricated using $LiNbO_3$ as the substrate and multilayered [$TbCo_2$/FeCo] as the IDT and sensitive material. We also introduce the concept of shape effects in magnetism and use it to engineer the response of the SAW resonator. In this chapter, we undertake studies on SAW devices that are based on the [$TbCo_2$/FeCo] multi-layered structures. First of all, we describe physics of shape effects in magnetism and then elaborate on the various aspects of fabrication followed by the various stages of characterization and analysis of the results.

3.1 Introduction to shape effects in magnetism:

In most of the studies that describe the usage of SAW devices for magnetic field detection, until now, especially those related to SAW resonators, the magnetic behaviour of a full film of the magneto-elastic layer has been considered in order to explain the magnetic SAW (MSAW) response. But we have shown in our preliminary studies that the magnetic behaviour of a full-film and that of a micro structured layer are very different [*Pol'17, Pol'18, Mis'17*]. This implies that if we consider the magnetic behaviour of the full film our explanations regarding the MSAW responses will carry an inherent flaw. Thus we have introduced the phenomenon of shape effects from the physics of magnetism to start our study.

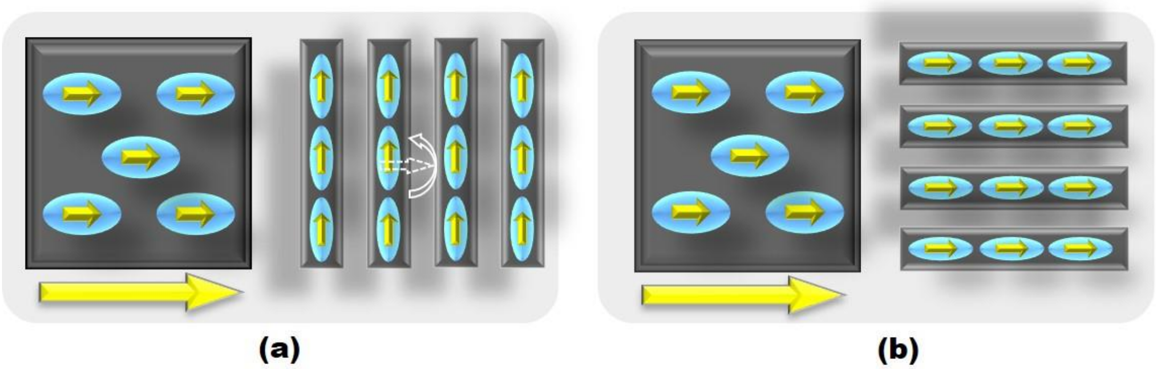

Figure 3.1: Schematic explaining the effect of electrode shape on the magnetic anisotropy. The yellow arrow indicating the direction of the magnetic anisotropy or easy axis in each case. (a) When the electrode fingers are fabricated perpendicular to the easy axis of the full film and (b) when the electrode fingers are fabricated parallel to the easy axis direction.

Consider a full film of a magnetic material with a preferential easy axis direction, as shown in Figure 3.1. As shown in Figure 3.1 (a), if we now fabricated electrodes / fingers such that the largest dimension of these structures (the length of the finger in this case) lies perpendicular to the easy axis of the full film, then due to the effect of shape anisotropy, the magnetic moments may rotate (under certain conditions as explained later) to realign themselves along the length. On the other hand, if we fabricated these fingers such that their length is parallel to the easy axis of the full film (see Figure 3.1(b)), then the reorientation of the moments does not happen and we retain the initial anisotropy direction. From a mathematical perspective these concepts can be represented by the following equation:

$$[H_{Total}]^{perp.IDT} = |H_{Shape} - H_K| \text{------------------ (Eq. 3.1)}$$

$$[H_{Total}]^{para.IDT} = |H_{Shape} + H_K| \text{------------------ (Eq. 3.2)}$$

where, H_{Total} represents the total anisotropy, H_{Shape} is the shape induced anisotropy and H_K is the intrinsic anisotropy of the full film before micro-structuration. Equation 3.1 represents the effects observed when the IDT fingers are fabricated perpendicular to the initial film anisotropy (Figure 3.1(a)), while Equation 3.2 represents the effects observed when the IDT fingers are fabricated parallel to the film anisotropy (Figure 3.1(b)).

It is important to note that the total reorientation of the magnetic moments as shown above only manifest when the H_K i.e. the intrinsic anisotropy of the full film is rather low and comparable to the shape anisotropy exhibited by the specific material e.g. in soft magnetic materials such as CoFeB. In other cases, where the intrinsic anisotropy is high, the change of the anisotropy is governed by the equations 3.1 and 3.2 in respective cases. Thus, what is expected to be observed in the fabricated fingers, in such a case, is that the total anisotropy of the system either increases (IDTs parallel to easy axis) or decreases (IDTs perpendicular to easy axis).

The introduction, understanding and execution of this concept is an important step in our studies for a precise control of the magnetic behaviour of the magneto-elastic layer. In return, this precise control allows us to control the response of the resonance frequency to the applied magnetic field. As discussed in section 1.3.3 of the first chapter, the response of the Rayleigh wave is highly dictated by the magnetic characteristic and therefore this study enables us to specifically control this response. As we will see in the following sections, this study is focused on Rayleigh waves and obtaining a high sensitivity under controlled magnetic behaviour.

3.2 Fabrication of the device:

The substrate: In this study we have used lithium niobite ($LiNbO_3$) as the piezoelectric substrate. There are different crystal cuts of $LiNbO_3$ each dictating separate surface, optical and piezoelectric properties. For this study, we consider the 128° rotated Y-cut $LiNbO_3$ crystal. This indicates that the crystal is cut along the plane 128° rotated from the Y-plane about the X-axis. The Z-axis of the crystal is therefore tilted by -38° from the normal of the surface. This particular cut of the substrate is often used to produce SAW filters, thanks to its high electromechanical coupling (K^2=5.4%). In our case we consider it because it provides a good optimum between the (K^2) and the quality factor (Q). This $LiNbO_3$ cut contains only the X-axis *(and not Y or Z)* and thus the in-plane direction perpendicular to this X-direction is referred to as the X+90°-axis. The substrate used are polished on one side and have a thickness of 500 µm. Subsequent fabrication steps are carried out on the polished side of the LN.

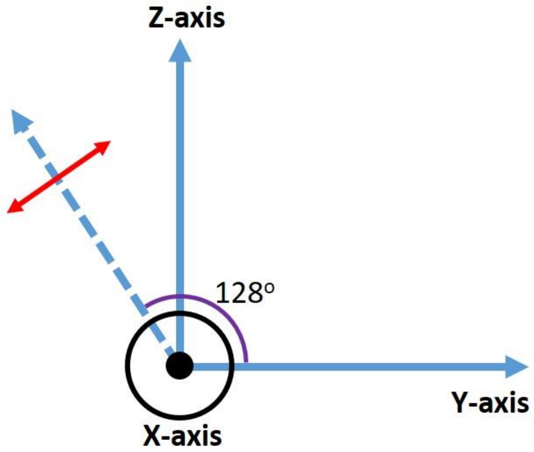

Figure 3.2: Sketch of the LNO cut with respect to the orthogonal axis. The red line represents the direction of the cut.

Deposition of the magnetic film: The deposition of the magnetostrictive layers on the concerned substrate is the first important step in the fabrication process. In the case of this study, the deposition step is of special interest as it is in this step that we induce the preferential magnetic anisotropy direction. The LNO wafer is first diced into rectangular pieces of 24 mm × 20 mm. This is followed by a thorough cleaning of the substrate. A 5 stage cleaning process is used wherein the substrate is first subject to ultrasound for 10 minutes while being submerged in a 2% solution of NaOH. This is followed by 10 minutes of ultrasound each in de-ionised water, acetone and isopropyl alcohol. Finally, at the end of the ultrasonic bath process, we subject the substrates to oxygen plasma under vacuum for 10 minutes. This final step ensures that no organic debris remains on the surface of the substrate (in case it was missed out by the ultrasonic bath).

Figure 3.3: Experimental setup used for the deposition of the magnetoelastic film (Leybold Z550) (*Adapted from the PhD thesis of Zhue [Zhou'14]*).

Subsequently, the magnetoelastic layer is deposited, by our partners, using RF sputtering using the Laybold Z550 frame in the clean rooms of IEMN, Lille (refer Figure 3.3). As mentioned earlier, these layers consist of a stack of alternative layers of $TbCo_2$ and FeCo. These layers are obtained by sputtering composite targets: one composed of Co with pellets of Tb for the $TbCo_2$ layer and the other composed of a Fe target with Co pellets for the FeCo layer. The stoichiometry of the deposited layers is maintained by controlling the number of pellets and the deposition parameters. The deposition is carried out using a scan mode of the sample holder between the two targets. It is carried out under a bias magnetic field of 300 Oe to induce the preferential in-plane uniaxial anisotropy direction in the magneto-elastic layer. The anisotropy of the magneto-elastic layer also depends on the ratio of the thicknesses of the two constituting layers. A comprehensive study of the structural and physical properties of these materials was carried out by Tiercelin

[Tie'00]. The deposited magneto-elastic layer was finally composed of 25 bi-layers of 4nm each of $TbCo_2$ and FeCo, thus totalling to 200 nm in thickness. The deposition parameters are mentioned in Table 3.1. For our study, we have considered a configuration such that the preferential magnetic anisotropy direction or the Easy magnetic axis of the magneto-elastic layer is along the (X+90°) direction of the substrate (refer Figure 3.4 for schematic).

Table 3.1: Deposition parameters of the multi-layered magneto-elastic film.

Materials / Parameters	RF Power	Ar pressure
$TbCo_2$	400 W	1×10^{-3} mbar
FeCo	440 W	2×10^{-3} mbar

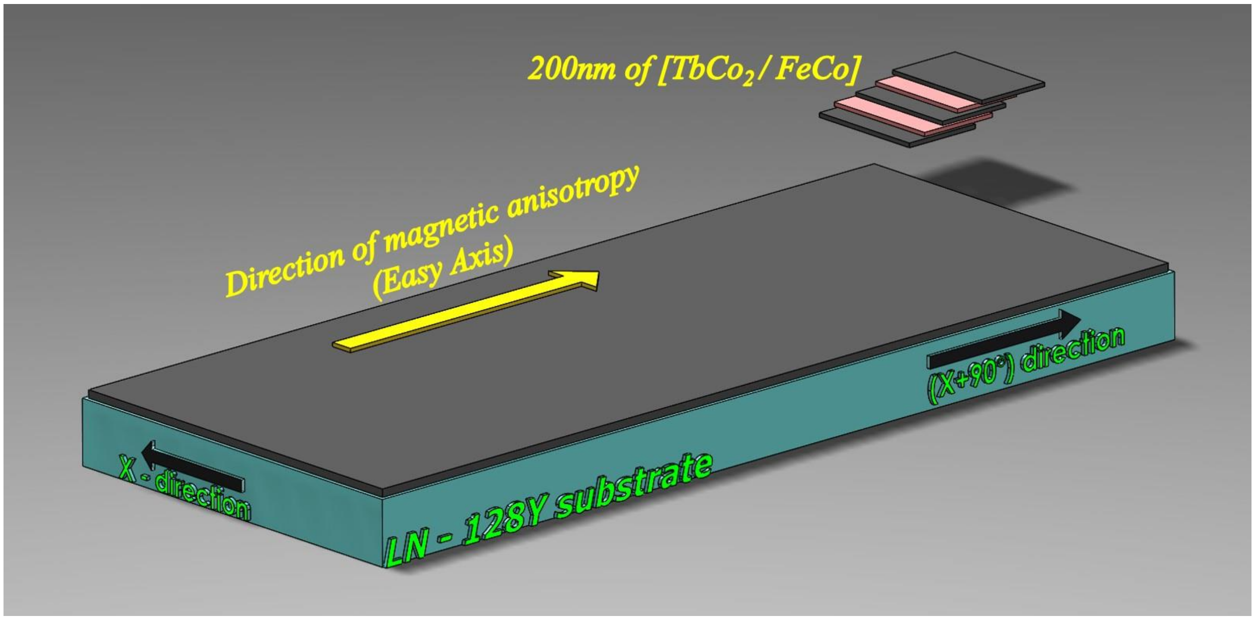

Figure 3.4: Schematic of the deposited multi-layered magnetoelastic layer on the substrate and the associated directions in the system. Inset shows the multi-layered structure of the film.

__Fabrication of the electrodes__: In the previous section we saw the procedure for the deposition of the magneto-elastic layer. In order to obtain the SAW device, it is essential to fabricate electrodes known as inter-digited transducers or IDTs from this magnetic layer. The electrodes, as we know, play the crucial function of inducing the alternating electric fields in the piezoelectric substrate, which in turn translates into an alternating strain in the substrate that is better understood as the acoustic wave. In our case, we intend to fabricate the electrodes from the magneto-elastic layer. To facilitate the study of the effects of shape anisotropy, the electrodes of the device are fabricated in two configurations: in the first device the length of the electrodes are perpendicular to the easy axis of the film while in the second, they are parallel. Thus for the first SAW device, the acoustic wave propagation direction is along the (X+90^o) crystallographic direction of the LN substrate and for the second case, the propagation direction is along the X direction. The two configurations are illustrated in Figure 3.5. Indeed, there is also the possibility for 2 more configurations for extending the study: with the anisotropy direction along X and propagation directions remaining along (X+90^o) and X, as here. But since the idea of this work is to highlight the effects of shape anisotropy of magnetism, we have not considered those configurations.

As we discussed in a previous section, one of the ideas of this study is to show the effect of the shape anisotropy and therefore in order to study the magnetic properties, samples which were *identical twins* of the SAW devices were also fabricated. These samples contained only the IDT fingers and not the connection pads as seen in the devices. The dimensions of the fingers in these samples were exactly the same as those in the corresponding SAW devices. Further, to show in more detail the effect of the width of the IDTs, samples identical to a 40% metallization were also fabricated. Thus the IDT width of the first set of samples was measured at 1.9µm while that of the second set was measured at 1.3µm with optical microscopy. The schematic of these magnetometry samples are illustrated in Figure 3.6.

Now, in order to fabricate the above described structure, the conventional process of lithography and subsequent etching was performed. The first step involved spin-coating of the photoresist (Shipley S1813). The spin coating step yielded a 900 nm-1µm thick layer of the resist over the substrate / magneto-elastic layer (v = 10000 rpm; a = 7000 rpm/s; t = 60 s, annealing 1 min. at 115°C). This is followed by the conventional photo-lithography step where the substrate (with the resist) is exposed to ultra violet light under a photo mask (12 seconds) using the MJB4 lithography setup in the MINALOR clean room facilities at IJL (*refer Figure 3.5 and 3.6 for reference*).

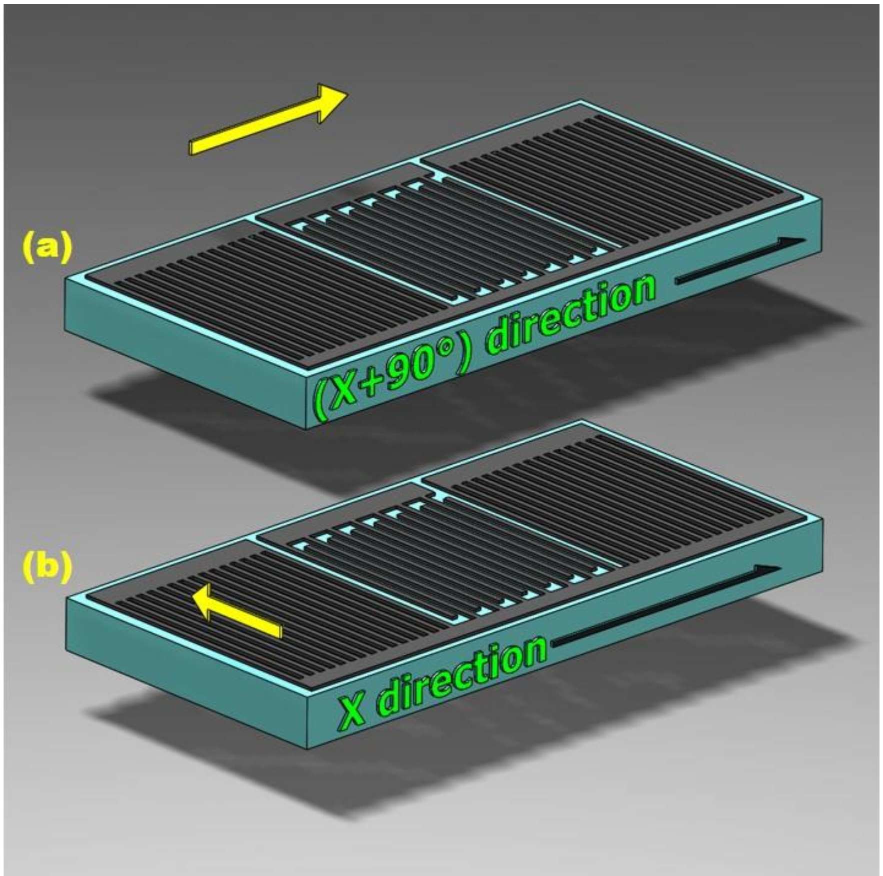

Figure 3.5: Schematic illustration of the two fabricated devices. Device with propagation along (a) (X+90^o) direction and (b) X direction. The yellow arrow indicating the anisotropy direction of the film. The devices had a wavelength of 6.5 µm and a metallization ratio of 60%.

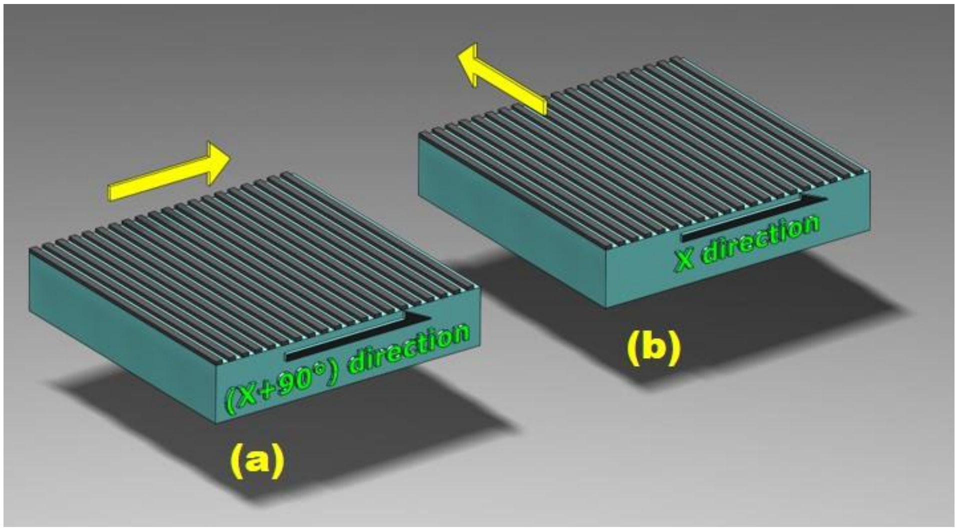

Figure 3.6: Schematic illustration of the two magnetometry samples. IDT fingers (a) parallel to X direction and (b) parallel to (X+90^o) direction. The yellow arrow indicating the anisotropy direction of the film. The samples corresponded to devices with a wavelength of 6.5µm and a metallization ratio of 60% (1.9 µm) as well as 40% (1.3 µm).

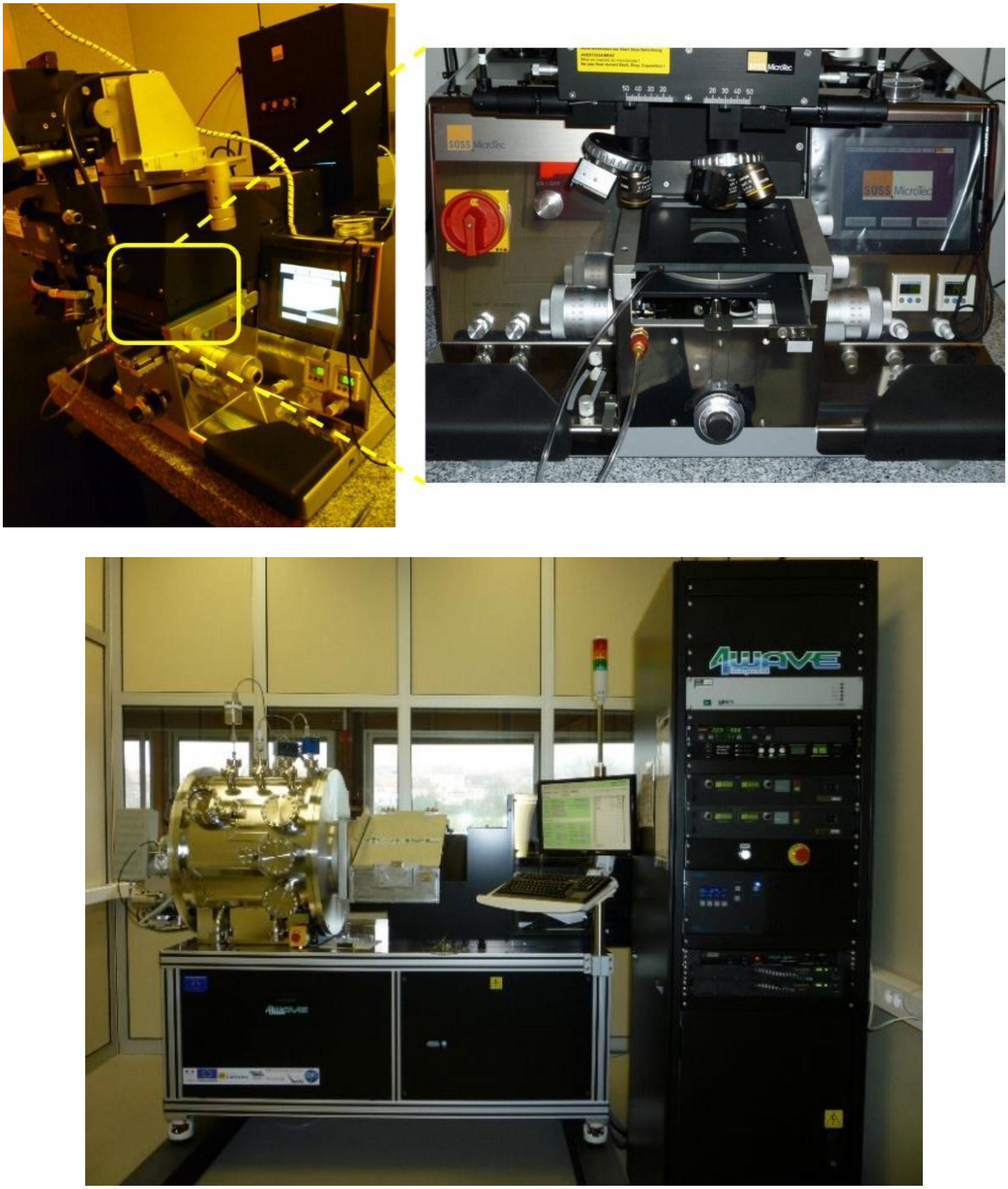

Figure 3.7: Experimental setup used for the UV lithography (SUSS MJB4) (Top) and Ion Beam Etching (4Wave) (Bottom).

Following the lithography, the substrates were developed by immersing in a MF319 bath for 27 - 30 seconds. Thus we obtained a resist pattern that is a copy of the devices intended for fabrication and thus in order to obtain the required devices, a step of etching is required. This was undertaken by Ar^+ ions using the 4wave ion-beam etching setup in the clean rooms of IJL. Thus the final devices were fabricated and ready for subsequent characterization, as shown in Table 3.2 below.

	Wavelength of device	*Magnetic anisotropy (Easy Axis)*	*Wave propagation direction*
Device 1 (D1)	*6.5µm*	*(X+90°)*	*(X+90°)*
Device 2 (D2)	*6.5µm*	*(X+90°)*	*X*

Table 3.2: Devices developed for the study.

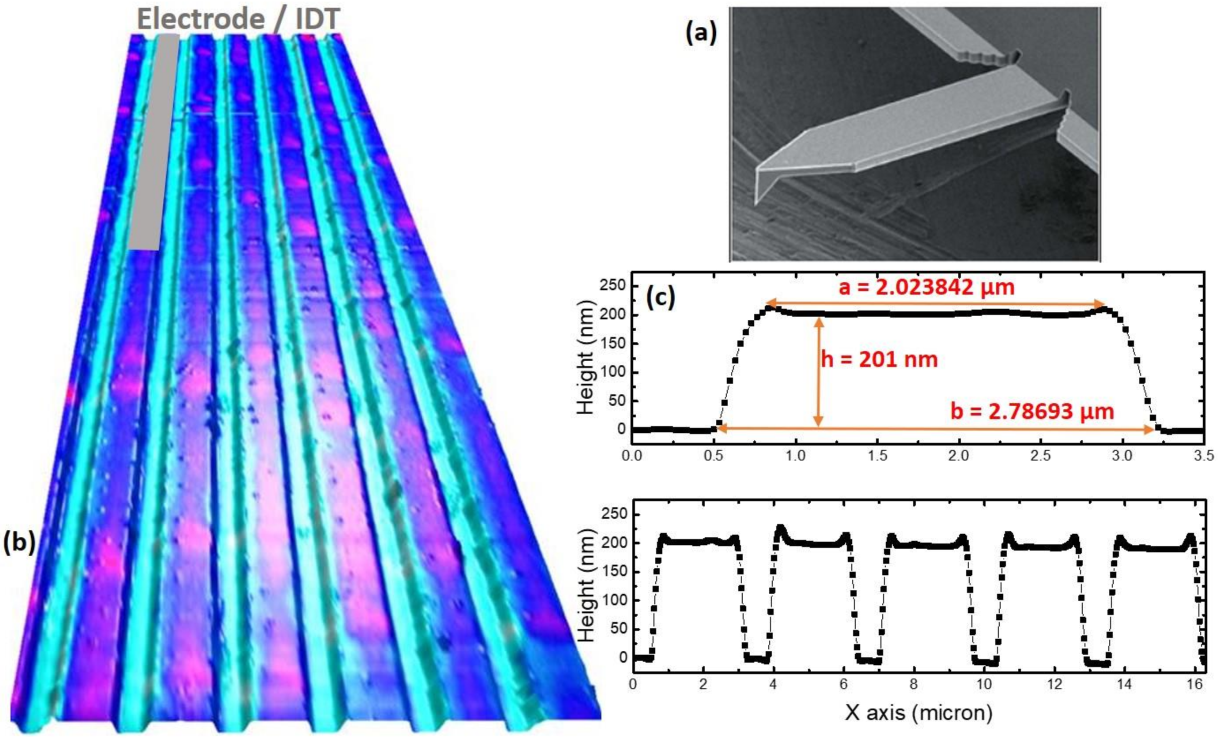

Figure 3.8: (a) SEM image of the cantilever tip of the AFM used for the measurements; (b) Surface topography and measurements done on one of the fabricated devices by AFM & (c) measurements of the cross-section on a single IDT.

Topography of fabricated device: Once our fabrication process is completed, it was essential to understand and evaluate the final topography of the device. Every fabrication step has its own set of limitations and thus the final device may be slightly different than its actual design. Therefore, *Atomic Force Microscopy (AFM)* measurements was used to determine the dimensions in the device, especially that of the electrodes or IDTs. The tip of the AFM, shown in Figure 3.8(a), was made of silicon (n-type, 0.1-0.4 Ω.cm) with a *sharpened tetrahedral* shaped tip of 14µm length and 7nm tip radius. The tip front angle was 0^o while the back angle was 35^o. As shown in *Figure 3.8 (c)*, there is a clear variation of the IDT cross-section between the design and fabrication. Instead of a rectangular cross section, we observe a trapezoidal cross section of the electrodes. This difference in the structure may not be visible by optical microscopy and thus justifies the *AFM* process. This increase in the actual dimensions does indeed play a crucial role in affecting the magnetisation of the device at saturation which is discussed in a later section. This trapezoidal structure is obtained courtesy of the ion-beam etching technique that we have used in the fabrication process. A re-deposition of the metal during the process along with shadowing effects is one possible explanation that may explain this condition.

3.3 Magnetometry measurements:

In order to determine the magnetic behaviour of the magneto-elastic layer as well as that of the micro-structured fingers, a series of experiments were done. Referred to as the Vibrating Sample Magnetometer or VSM test, a sample in this test, is first magnetized by subjecting it to a uniform magnetic field. Sinusoidal vibrations in this sample induce a voltage in the surrounding pickup or detection coils. This voltage is proportional to the sample`s magnetic moment. Thus by sweeping the magnetic field, we obtain the sample`s hysteresis curves, thereby getting a clear picture of the magnetic phenomenon in the sample.

For this study, we made the magnetic or VSM measurements on samples as mentioned in the Table 3.3 below. However, in order to better understand the magnetic properties, we have also tested the magnetisation in a full film of the multi-layered stack on the same LN substrate. Also, as mentioned previously, we extended the study to include similar samples in a case where the IDT metallization ratio would be 40%, i.e. for a finger width of 1.3 µm. A comparative analysis that includes all the cases is thus presented in this study.

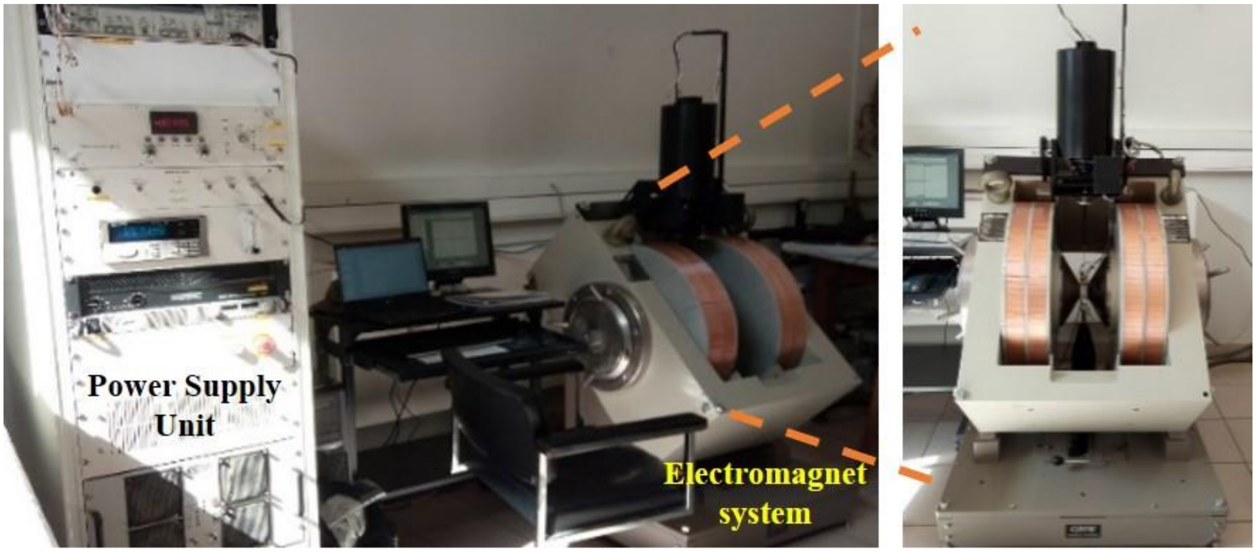

Figure 3.9: Experimental vibrating sample magnetometry set up used for measurements (GMW 3474).

	Length of finger along	*Corresponding device*
Sample 1 (V1)	*X*	*D1*
Sample 2 (V2)	*(X+90°)*	*D2*

Table 3.3: Devices developed for magnetometry measurements.

The VSM measurements on the full film as shown in Figure 3.10 presents as a well-defined anisotropy along the (X+90°) direction and presents a hysteresis free reversal along the X (hard axis), with an anisotropy field close to 1690 Oe (green curve Figure 3.10 (A) & (B)) and a square hysteretic reversal when the field is applied along (X+90°) (green curve Figure 3.11 (A) & (B)). A saturation magnetisation value of 497 × 10^3 A/m was thus extracted for the full film.

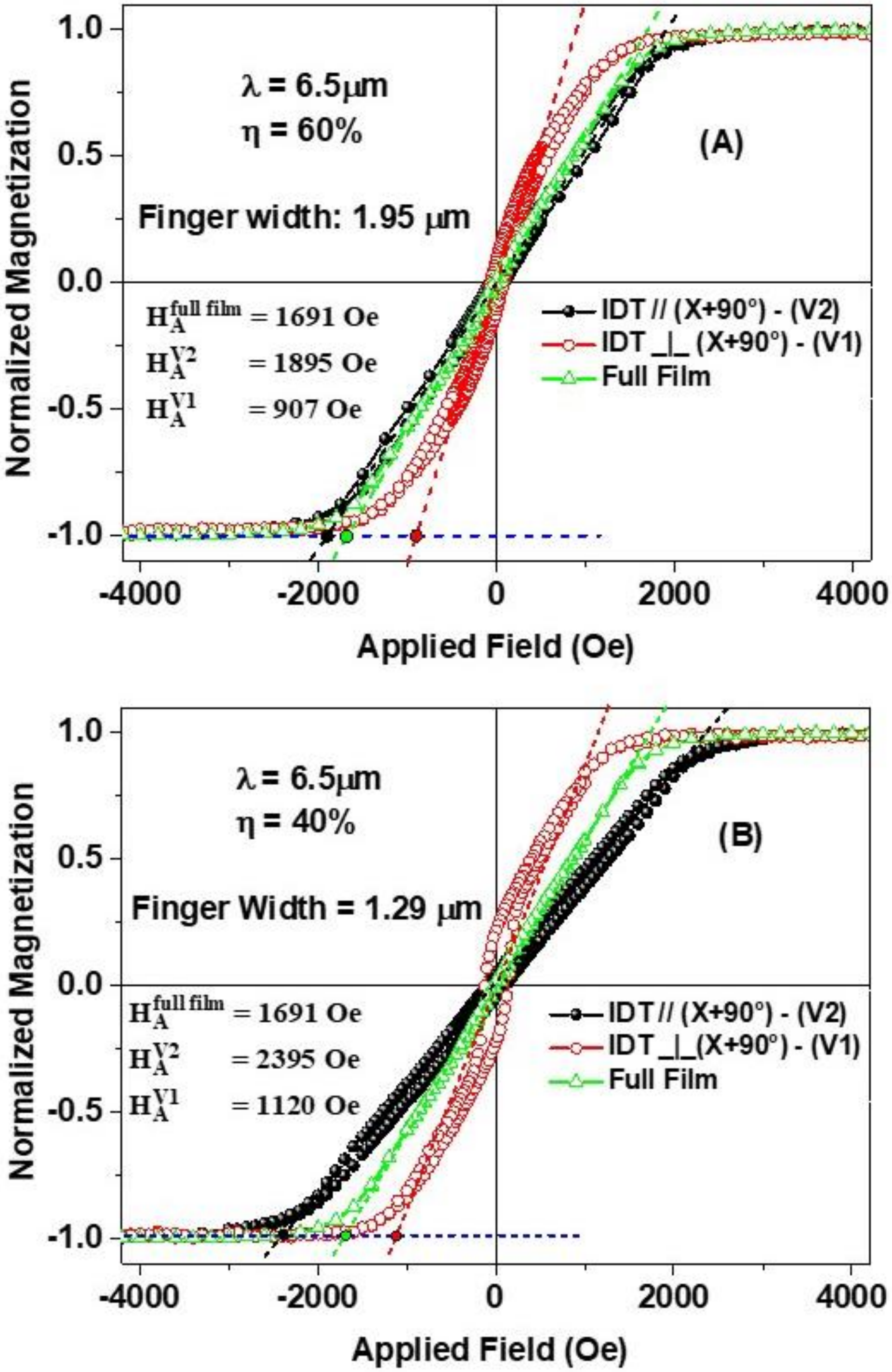

Figure 3.10: Normalized magnetisation curves measured for a field applied along X for the full film (green), for IDTs oriented parallel to the (X+90°) easy axis of the full film (black), and for IDTs oriented along X, perpendicular to the easy axis of the full film (red). (A) IDTs with a metallization ratio of 60% and (B) IDTs with a metallization ratio of 40%.

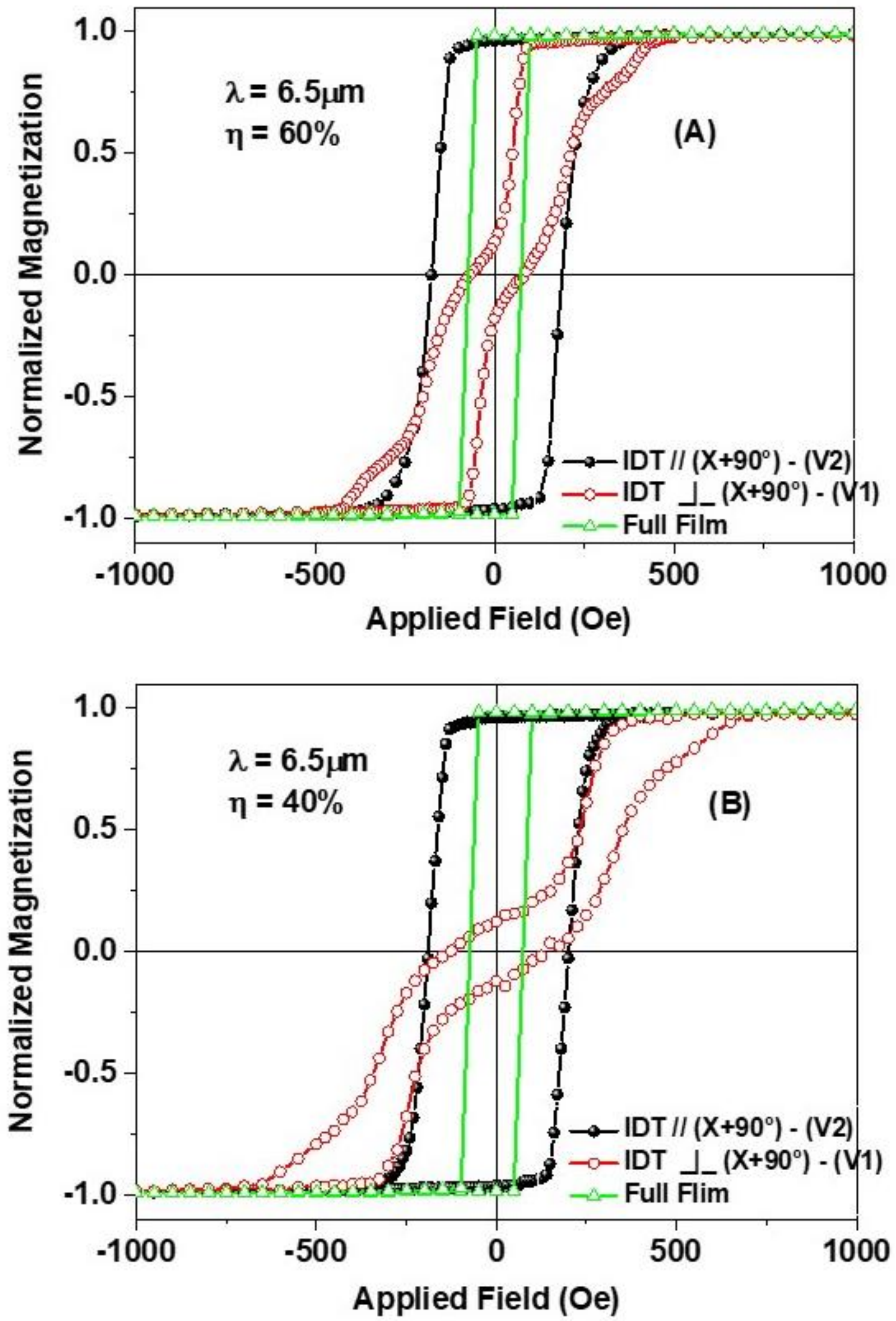

Figure 3.11: Normalized magnetisation curves measured for a field applied along (X+90º) for the full film (green), for IDTs oriented parallel to the (X+90°) easy axis of the full film (black), and for IDTs oriented along X, perpendicular to the easy axis of the full film (red). (A) IDTs with a metallization ratio of 60% and (B) IDTs with a metallization ratio of 40%.

In the second step, the full film was shaped into IDTs with the finger length along X+90°, i.e. parallel to the easy axis of the full film (sample V2) and the VSM test repeated. As expected from a previous study *[Pol'17, Mis'17]* and micro-magnetism theory, the easy axis of magnetisation remains along X+90°. Sample V2 presents a hard axis response along X (black curves Figure 3.10 (A) and (B)) and a square hysteretic reversal when the field is applied along (X+90°) (black curves Figure 3.11 (A) and (B)). The intrinsic anisotropy of the full film should thus be reinforced by the shape induced anisotropy. A rough estimation of the induced shape anisotropy field is 704 Oe for the 1.29 µm wide fingers (40% of metallization) and 204 Oe for the 1.95 µm wide fingers (60% of metallization). We can clearly see that the effective anisotropy field is higher but the reinforcement due to shape is not as high as expected. A measure of the saturation magnetisation of the fingers, by taking the volume of the fingers into account (as measured through Atomic Force Microscopy) led to a value of 498×10^3 A/m, close to the value obtained for the full film (505×10^3 A/m).

Subsequently, the full film was shaped into IDTs with the finger length oriented along X, i.e. perpendicular to the easy axis of the full film. This sample is referred to as V1 and its magnetic response is reported by red curves in Figure 3.10 & 3.11. Even if a shape anisotropy that competes with the intrinsic anisotropy of the thin film is introduced here, the V1 sample still presents a hard axis response along X (red curves Figure 3.10 (A) and (B)). The magnetic response along X+90° shows an abnormal wavy response (red curves in Figure 3.11 (A) and (B)) with a magnetic remanence close to zero. Such kind of response is symptomatic of the creation of a domain structure at zero applied field.

Therefore, magnetic force microscopy (MFM) has been performed as shown in Figure 3.12 (A) and (B). The results confirm the domain structure that is expected and it is clearly seen that the domain structure remains maintained when the fingers are parallel to the easy axis of the full film while for the perpendicular case we observe an alternating domain structure, characteristic of a closed loop domain structure. Thus the case of sample V1 (perpendicular case) becomes even more interesting to investigate and thus a zoom on one IDT is reported in Figure 3.12 (C). A domain structure can be observed with alternating black and white contrast on the IDT finger border. In order to undoubtedly interpret the MFM contrast, micromagnetic calculations have been performed using the Mumax3 code *[Van'14]*. The average parameters of the

[$TbCo_2$(4nm)/FeCo(4nm)]×25 multilayer have been used: saturation magnetisation value of 500×10^3 A/m, exchange stiffness of 9×10^{-12} J/m and second order anisotropy of 48.25×10^3 J/m^3 orientated in plane and perpendicular to the finger length. The cell size has been fixed to 5 nm. The configurations have been relaxed starting from the saturated state along the finger length. The micromagnetic configuration is reported in Figure 3.12 (D). Undoubtedly, the magnetisation lies along the easy axis of the full film i.e. perpendicular to finger length. A domain configuration is stabilized in order to reduce the demagnetisation energy as previously reported *[Pre'01]*. The surface charges are reduced by the creation of the red and blue flux closure domains. Those domains are at the origin of the hysteresis of the magnetic response observed when the field is applied along X (red curves Figure 3.10 (A) and (B)). When finger width decreases, the magnetisation remains along the easy axis of magnetisation of the full film but domain size decreases. As a result, a domain structure is stabilized in fingers with different metallization ratios tested in our study (40% and 60%).

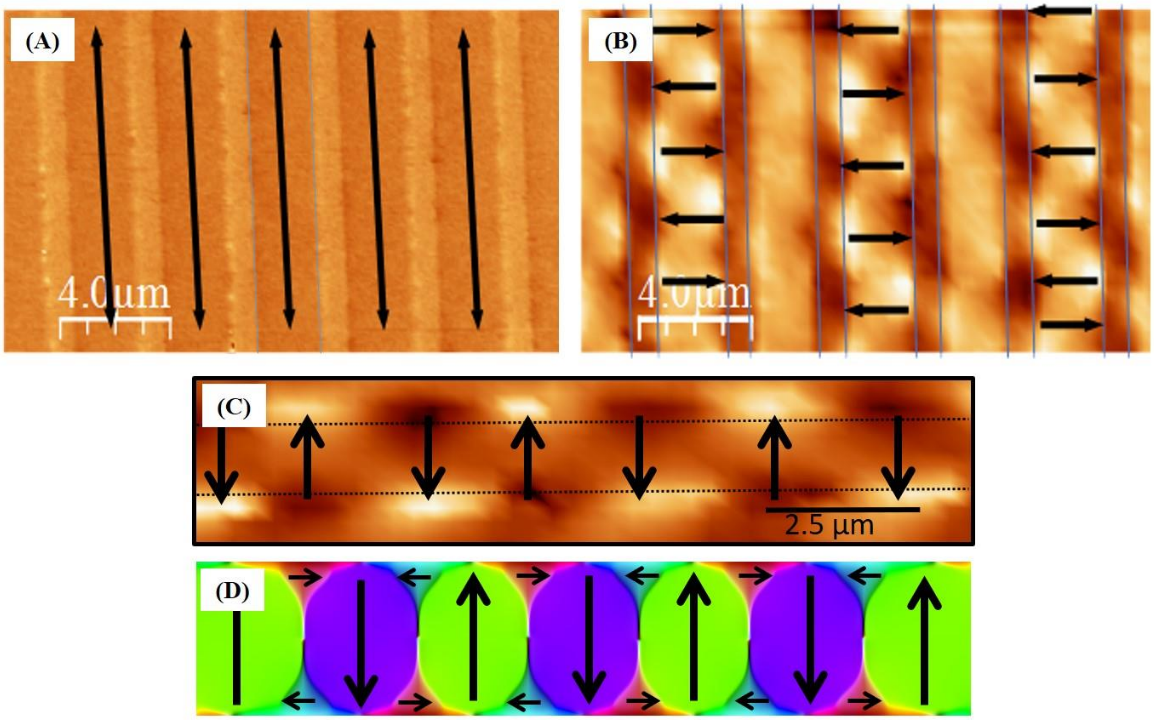

Figure 3.12: Magnetic force microscopy (MFM) measurements done on the fingers for (A) the IDTs fabricated parallel to easy axis (i.e. parallel to (X+90°) direction) and (B) IDTs fabricated perpendicular to the easy axis (i.e. parallel to X direction). The blue lines show the boundaries of the IDT finger. (C) zoom on a single IDT finger in sample V1 (12.5 µm section length) to clearly show the contrast observed by MFM measurement. (D) micromagnetic simulations on a 12.5 µm long, 2 µm wide and 200 nm thick section of the finger clearly confirms the domain structure observed experimentally in (C).

3.4 RF Characterization:

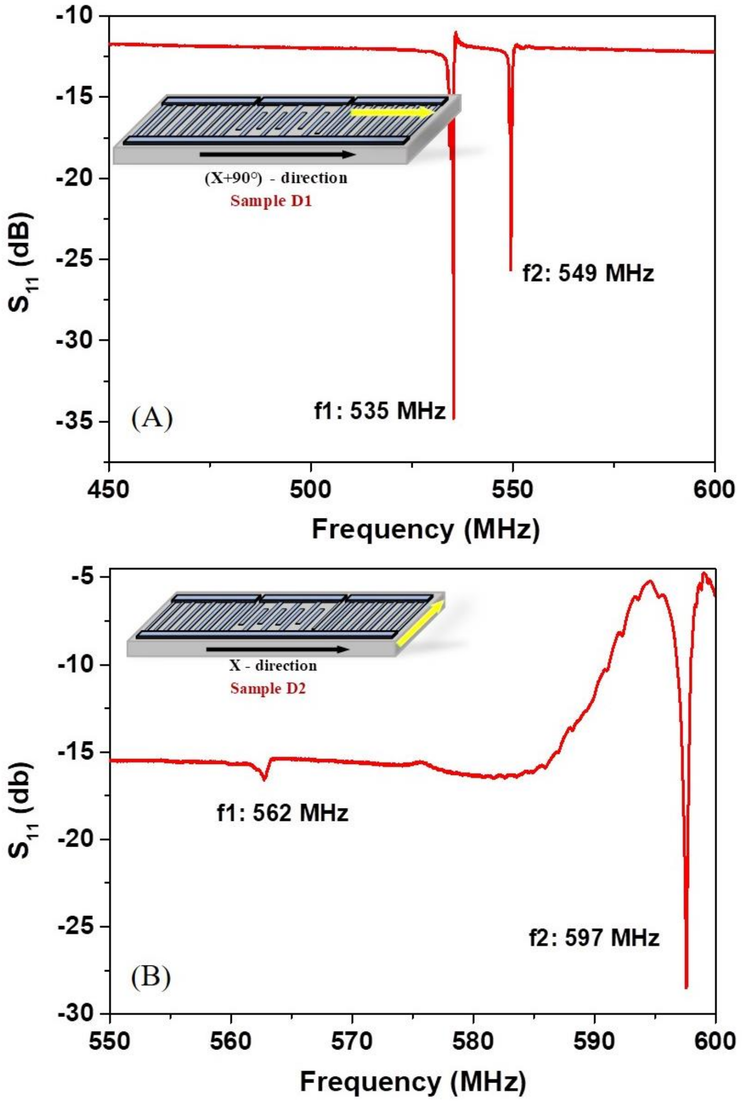

Figure 3.13: Scattering parameters (S_{11}) measured on the two devices. (A) for the device D1 with a wave propagation along the (X+90°) direction and (B) for the device D2 with the wave propagation direction along the X direction. The yellow arrow points along the anisotropy direction in each device.

The devices, as we saw, have been fabricated for two specific directions of wave propagation in the LN 128° Y-cut substrate: device D1 with propagation along the (X+90°) direction and device D2 with propagation along X. We observe two resonances each in both the devices as seen from Figure 3.13 (A) and (B). On a general note, the X propagation direction of 128° Y-cut $LiNbO_3$ exhibits a higher propagation velocity for its Rayleigh wave compared to that along the (X+90^o) direction. This is reflected also in our device where we observe a velocity close to 3653 m/s along the X direction and a slightly smaller value of around 3477 - 3568 m/s along the X+90^o direction for the Rayleigh waves.

In the subsequent section, we explore through simulation, the nature of deformation for each of the resonances and show that the peaks observed in device D1 (X+90^o propagation) correspond to Rayleigh waves while in device D2 (X propagation) the first peak corresponds to a Rayleigh wave while the second to a *Shear* type deformation. Compared to the theoretical velocities of Rayleigh and Shear waves (3500 m/s *[Cam'98]* and 3980 m/s *[Rodi]* respectively), the values measured in these experiments are marginally lower. This arises because the magneto-elastic layer that the electrodes are fabricated from are 'heavy' in nature (higher values of the elastic constants), thus leading to a comparatively higher attenuation of the wave velocity, compared to if the electrodes were fabricated from a lighter material like for example aluminium. From the perspective of the popularity, the X-propagation direction in the above substrate holds precedence owing to its more symmetric wave propagation. However, in this chapter, we focus on the influence of shape anisotropy on the magnetisation and its effect on the magneto-acoustic response of the device and thus a direct comparison of the Rayleigh waves is not of precedence.

Further, we may also not that the base line for the S_{11} measurement in both the devices was around -12.5dB and -15dB respectively as seen from Figure 3.13. The cause for this was investigated and it was found that there exists a resistance effect between the IDTs. Although it was measured to be in the scale of a few *Kilo-Ohms*, the possibility to '*burn-out*' the resistance by a high voltage was not explored for fear of damaging the devices and more importantly causing a loss of magnetisation due to the heat generated. On further exploration, it was concluded that the fabrication process involving ion-beam etching (IBE) might have caused a redeposition to occur on the devices. The heat generated during the lengthy IBE process also implied that the process was carried out in steps of 30 minutes each. The combined impact of all these effects cannot thus be ruled out. Nevertheless, for measurements of the magneto-acoustic response, we consider a change (or shift) of the resonance frequencies and thus the devices are still functional in that respect.

3.5 Numerical Simulations:

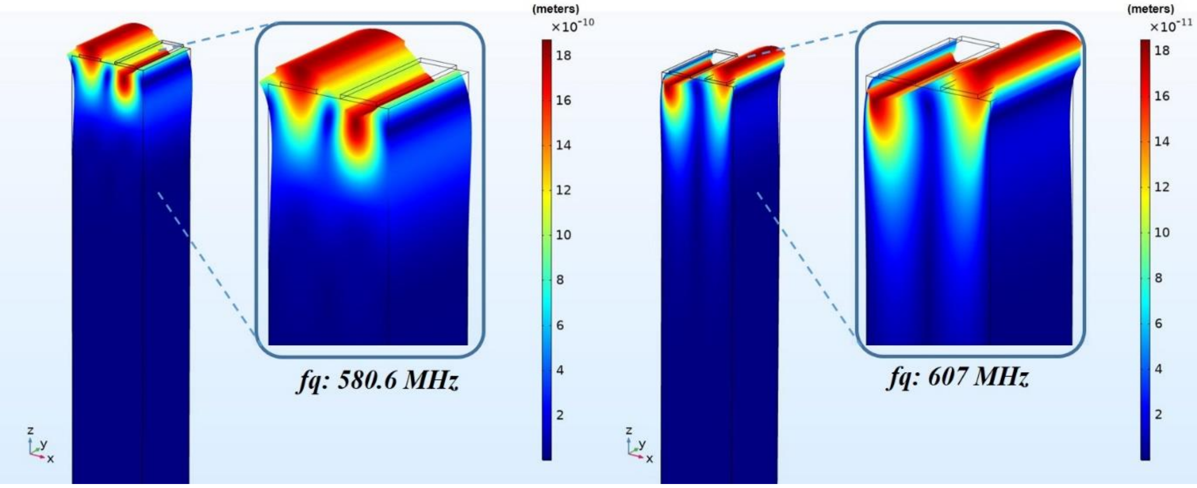

Figure 3.14: Simulations conducted on COMSOL to investigate the nature of the resonances observed experimentally. This corresponds to the device D1 with propagation along X+90^o thus generating one pseudo-Rayleigh and the other a Rayleigh wave.

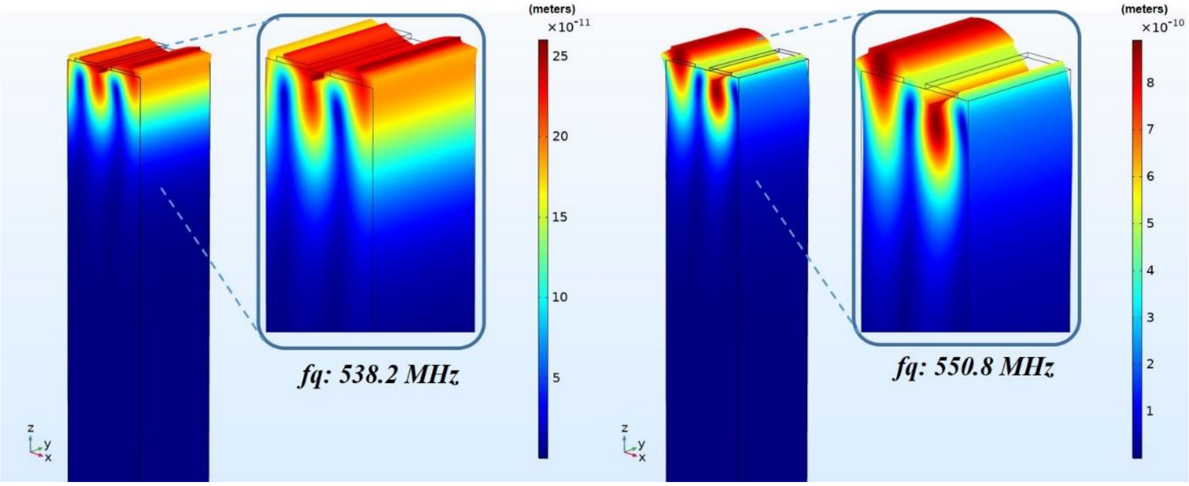

Figure 3.15: Simulations conducted on COMSOL to investigate the nature of the resonances observed experimentally. This corresponds to the device D2 with propagation along X thus generating one pseudo-Rayleigh and the other a Quasi-Shear-Vertical wave.

As discussed before, it is important to validate the experimentally observed resonance peaks and establish for certain their nature. In this section we have presented ***qualitative*** simulations done using COMSOL Multiphysics to determine the nature of the resonances. The simulations involve only the mechanical constants of the constituent layers and deformations associated with the resonances and do not take into account the effect of magnetic field or the effect of the magnetisation direction of the electrodes.

Figure 3.14 presents the deformations observed at the resonances for the device D1 with propagation along the (X+90^o) direction. The simulated resonances are observed at 538.2 MHz and 550.8 MHz, which are quite close to the ones observed experimentally at 535 MHz and 549 MHz. Both the resonances observed exhibit a deformation akin to that of a Rayleigh wave. Subsequently in Figure 3.15 we present the deformations observed at the resonances for the device D2 with propagation along the X direction. Again, the simulated resonances at 580.6 MHz and 607 MHz lie in close proximity to the experimentally observed ones at 562 MHz and 597 MHz. As can be clearly seen, the first resonance depicts a deformation corresponding to a Rayleigh wave. However, the second resonance exhibits a queer deformation that is along the shear direction but also with a vertical component and is aptly called a *Quasi-Shear horizontal-Vertical component-SAW* or *QSVSAW*. Such type of waves has also been reported previously by Polewczyk *[Pol'18]* to exist in the Z-cut and 128Y cut (X propagation) of $LiNbO_3$.

One important aspect that differentiates the experimental resonance frequencies from the simulated ones is the role of the Mo buffer layer. In order to promote adhesion properties of the substrate and also to prevent environmental oxidation of the magnetostrictive layer, we use 3-5nm of Mo (or Ta). Although the thickness seems negligible, they may affect the effective elastic properties as well leading to a further optimization of the simulated resonance frequencies. The elastic constants of Mo are $C_{11} = 441$ GPa, $C_{12} = 172$ GPa, $C_{44} = 122$ GPa, and $\rho = 10.1$ g.cm^{-3} *at room temperature* while that of Ta are $C_{11} = 261$ GPa, $C_{12} = 157$ GPa, $C_{44} = 82$ GPa, and $\rho = 16.6$ g.cm^{-3} *at room temperature [Fea'63]*. Further, in device D2, the effective electromechanical coupling coefficient (K_{eff}^2) would be larger for the QSVSAW than for the Rayleigh wave in the same device and this effect is consistent with those reported in literature *[Pol'18, Cam'98]*. Nevertheless, there are several secondary physical factors that may affect the generation and propagation of the SAW wave in the device. These include (but not limited to) mass loading by IDTs causing a change in the propagating velocity; bulk acoustic wave emission coexisting with the SAW emissions causing passband distortion; source and load impedance causing frequency dependent voltages across the IDTs; IDT diffractions akin to optical systems causing changes to the transmission band and shape; and most importantly poor quality of IDT processing causing variations of finger width, roughness and re-deposition leading to weak resolution and bandpass distortion.

3.6 MSAW characterization:

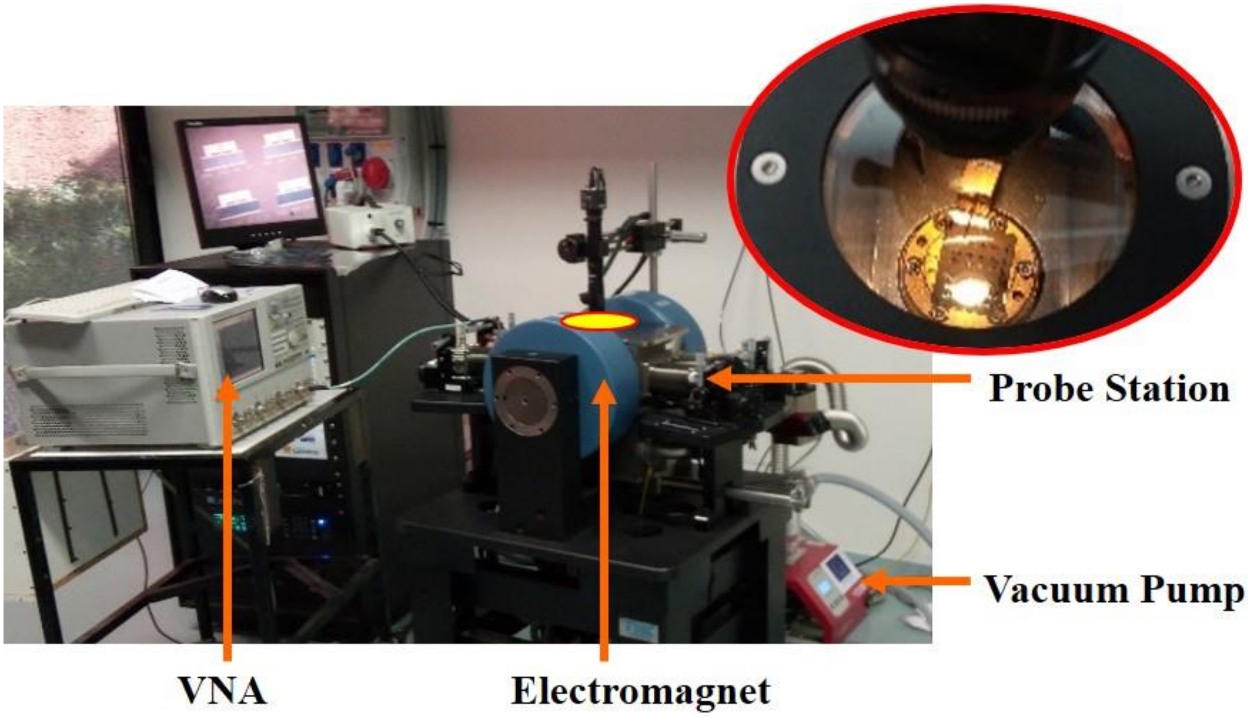

Figure 3.16: Experimental setup used for the MSAW measurements.

Once the basic characterizations on the devices are made, it is now important to measure their performance as magnetic field sensors. Thus, a new setup is considered for the measurements. This new set up is depicted in Figure 3.16. The setup uses a *LakeShore* cryogenic probe station (Model: EMPX-HF). This system is composed of two segments: an electromagnet capable of providing an in-plane magnetic field of up to 6000 Oe and a probing area between the electromagnet poles inside a vacuum sealed central cabinet (inset figure). A Rhode & Schwartz ZVA67 vector network analyser (VNA) is used to monitor the resonance peaks observed in the S_{11} signals of each device. The devices are probed using a GGB Picoprobes (40 GHz) and it is connected to the VNA by a K-Cable and adaptor. The entire probing system is calibrated using a GGB calibration kit at the end of the RF probes to ensure an optimum calibration. The vacuum chamber ensures a thermally stable environment during subsequent measurements. It is a crucial step as an otherwise fluctuating ambient room temperature grossly affects measurements (*summer vs winter*) and gives vastly different readings.

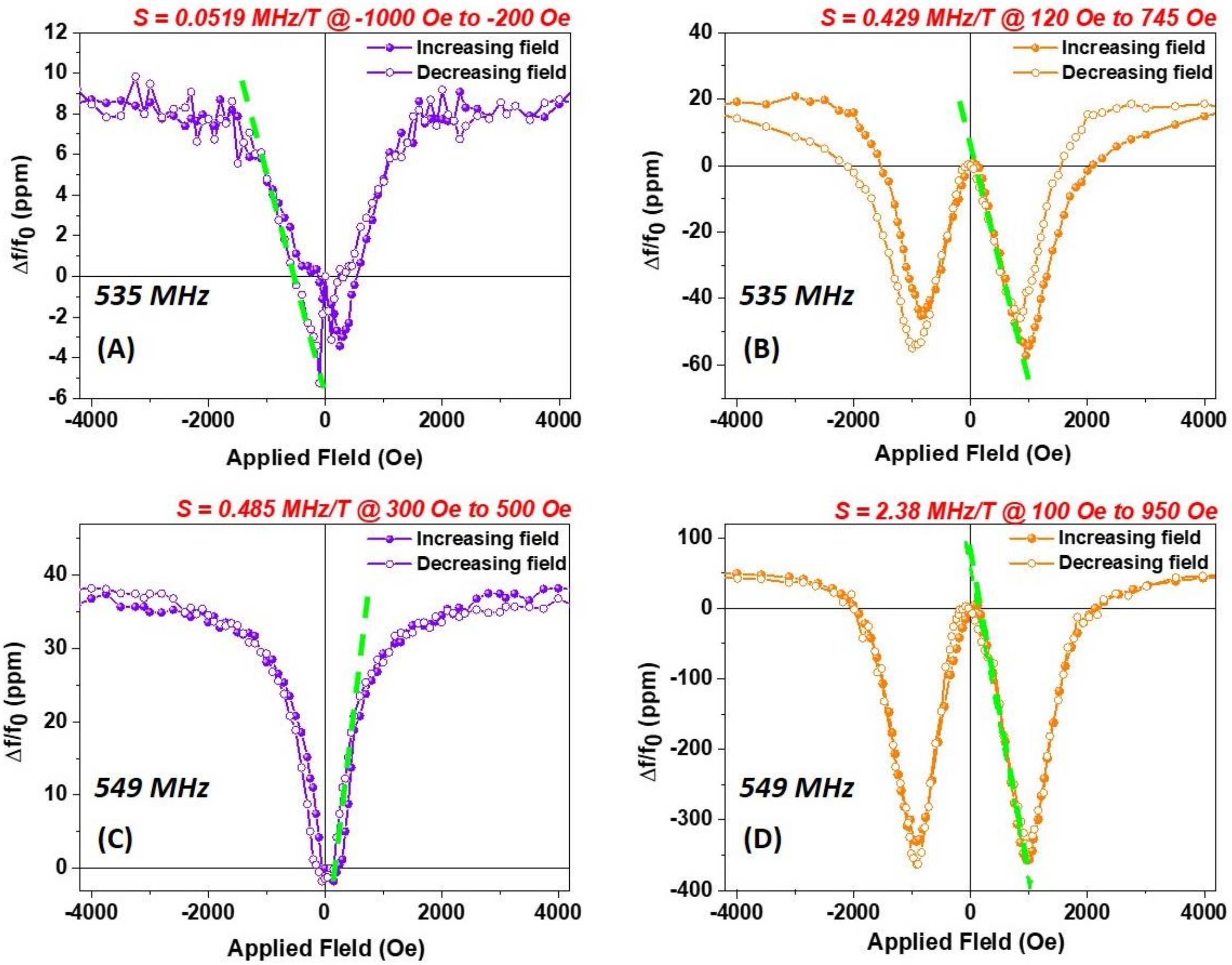

Figure 3.17: Relative variation of the resonance frequencies as observed in device D1 (wave propagation along X+90^o direction) with respect to an applied magnetic field. (A) & (C) show the variation when the field is applied along the X+90^o direction (Easy axis) while (B) and (D) show the variations when the field is applied along the X direction (Hard Axis).

Figure 3.17 shows the MSAW measurements conducted on the device D1, i.e. with propagation along X+90^o. As seen previously, two resonances were observed (535 MHz and 549 MHz) and the responses of both of these peaks are shown above. For the experiments, two configurations of the applied field are considered, field applied along the easy magnetic axis and along the hard magnetic axis. Figures 3.17 (A) & (B) respectively show the easy and hard axis responses of the 535 MHz peak. We had previously mentioned in Chapter 2 that the hard axis configurations involved stronger effects of the dynamic magneto-elastic coupling compared to the easy axis. This is very clearly observed in the experiments as well with a hard axis sensitivity observed close to 0.43 MHz/T while an easy axis sensitivity of 0.05 MHz/T, almost 10 times lower.

Further, to calculate the sensitivities, we have specified a particular range for each configuration (-1000 to -200 Oe for easy axis and 120 to 745 Oe). This is because from the perspective of future applications as a magnetic sensor, a linear behaviour of the device is the most suitable and thus each device and each configuration presents itself as a unique option for that range. The comparisons help us to determine the configuration with the highest sensitivity at low magnetic fields.

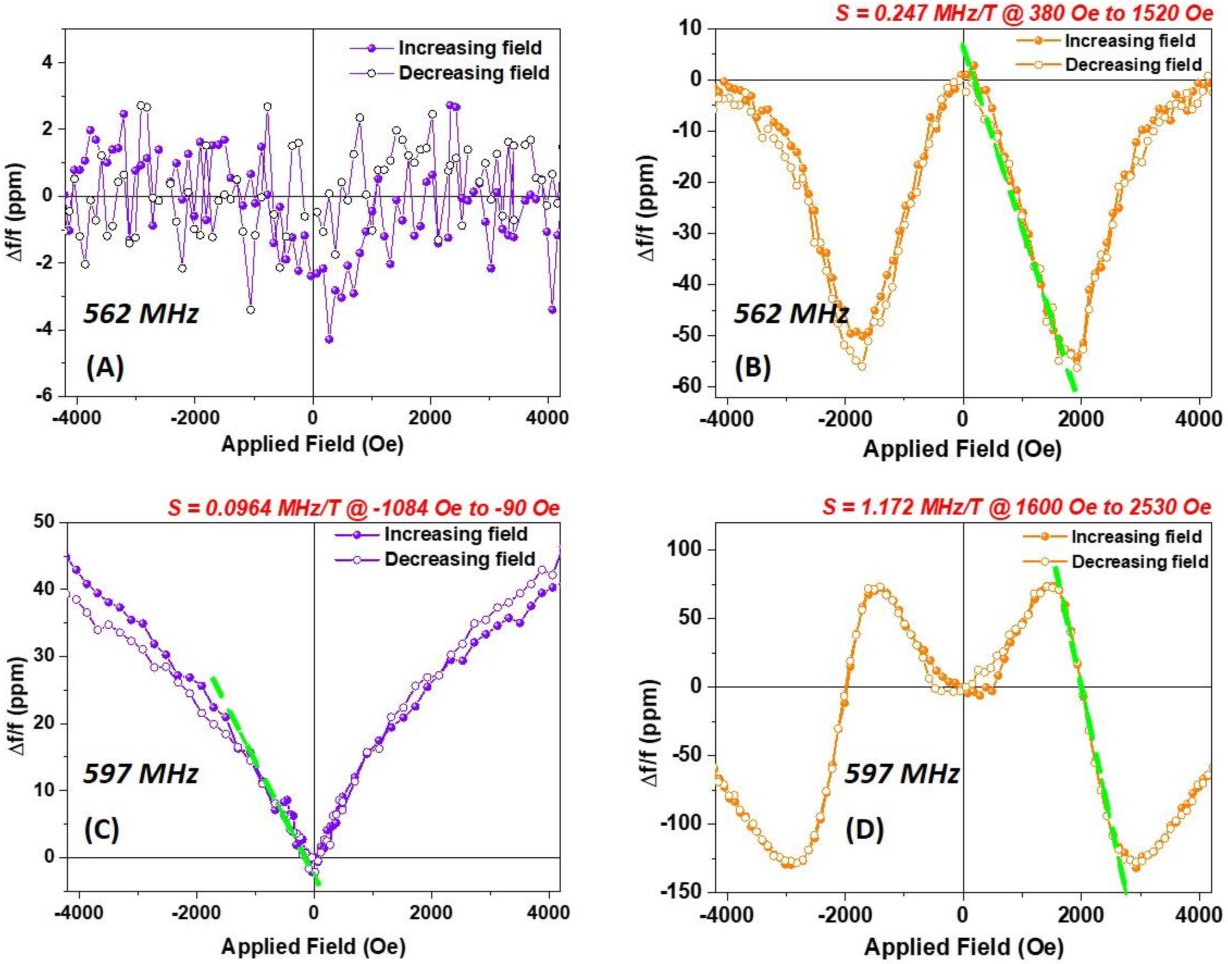

Figure 3.18: Relative variation of the resonance frequencies as observed in device D2 (wave propagation along X direction) with respect to an applied magnetic field. (A) & (C) show the variation when the field is applied along the X direction (Easy axis) while (B) and (D) show the variations when the field is applied along the X+90^{o} direction (Hard Axis).

Subsequently, in Figure 3.17 (C) and (D) we present the magneto-acoustic response of the resonance frequency observed at 549 MHz. For the hard axis configuration, this frequency provides a much stronger response compared to at 535 MHz. One reason for this could be understood from the Figure 3.14 where the second resonance provides a stronger displacement that the first resonance. Along the hard axis we observe a sensitivity of 2.4 MHz/T between 100 and 950 Oe while along the easy axis we observe a sensitivity of 0.5 MHz/T between 300 and 500 Oe.

In Figure 3.18 we present the magneto-acoustic measurements conducted for the device D2, i.e. with the propagation along the X direction. The first resonance peak observed was a Rayleigh wave and hence the response along the hard axis also corresponds to the same *W* shape. The other peak was a *QSVSAW* wave and owing to its strong shear horizontal component, we obtain a higher sensitivity compared to the Rayleigh wave in the same device. For magnetic field applied along the hard axis of the device, the first resonance peak (562 MHz) exhibited a sensitivity of 0.247 MHz/T between 380 MHz and 1520 MHz while the second resonance peak (597 MHz) showed a sensitivity of 1. 2 MHz/T between 1600 and 2430 Oe.

In both the devices, the hysteresis observed in magnetisation measurements is also reflected in the MSAW measurements. This becomes tangible especially if we observe the responses in the low magnetic field region and also in the minima point (very clear in Fig. 3.17(B), 3.18(B)).

In the Rayleigh waves, the MSAW response depends on the relative orientations for wave propagation and magnetic anisotropy directions (Figure 3.17 (D) & Figure 3.18 (B)). Since it has a direct dependency on the magnetisation, it may also be noted that adjusting the width of the IDT will also lead to a control of the MSAW response. For this wave, the minimum frequency is expected at the point of maximum magneto-mechanical coupling (K^2) that occurs when the angle between the applied field and the moment is 45° *[Pre'01]*. Assuming a magnetisation rotation in a Stoner-Wohlfarth type when the field is applied along the hard axis, this happens when magnetisation reaches 70% of the saturation magnetisation. By the use of magnetic responses for the IDT given in Figure 3.10 (a) (red & black curves), those fields are 870 Oe for V1 and 1340 Oe for V2. Those values are in agreement with the measurements performed on the SAW devices (869 Oe for D1 and 1814 Oe for D2). This difference in saturation fields partially explains the difference in magnetic sensitivity between D1 and D2. Another difference is the SAW propagation direction, parallel to X+90° in D1 and parallel to X in D2.

The *QSVSAW* wave in D2 shows a higher sensitivity (1.2 MHz/T) compared to the Rayleigh wave in the same device (0.25 MHz/T), although at a different range. The primary reason for this can be traced to the localized deformations in each type of accoustic wave. In the general

SH wave (i.e. in a pure shear horizontal wave) the deformations that constitute the acoustic wave are in-plane with the device whereas the Rayleigh wave has its primary deformation perpendicular and out-of-plane with respect to the device. Since for all of our cases of study the magnetisation is along the in-plane surface, the interactions between the shear component of the *QSVSAW* wave and the magnetic moments is higher compared to the interactions in the Rayleigh wave. Thus, we obtain a higher magnetic response in the case of the *QSVSAW* wave.

3.7 Applications – A Prototype:

In this part of the study, we intended to develop an experimental setup that would allow the devices to be tested as sensors for the measurement of current flowing through a cable. Not only could they be useful for the measurement of any spike in the current flow but could also be used as a gradiometer to measure the current in the cable. The experimental prototype would thus allow us to emulate a *real-life* application scenario for our device and thus pave the way for future developments on the device.

The Concept: We know from physics that a current flowing through a cable generates a magnetic field around the cable in the form of closed field concentric circles. The magnetic field is directed perpendicular to the direction of flow of the current as determined by the *Right hand thumb rule*. The strength of the magnetic field is determined by the *Biot-Savart Law* and is expressed by the *Equation 3.3*.

$$B = \frac{\mu_0 \times i}{2\pi \times r} \text{ ----------------- (Eq. 3.3)}$$

where, $\mu_0 = 4\pi \times 10^{-7}$

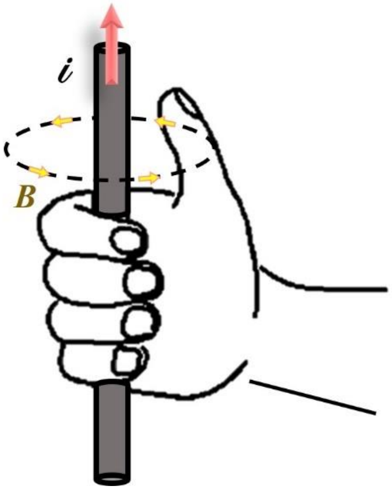

Figure 3.19: A graphical representation of the *Right Hand thumb rule* showing the direction of the magnetic field generated by a current flowing through a cable.

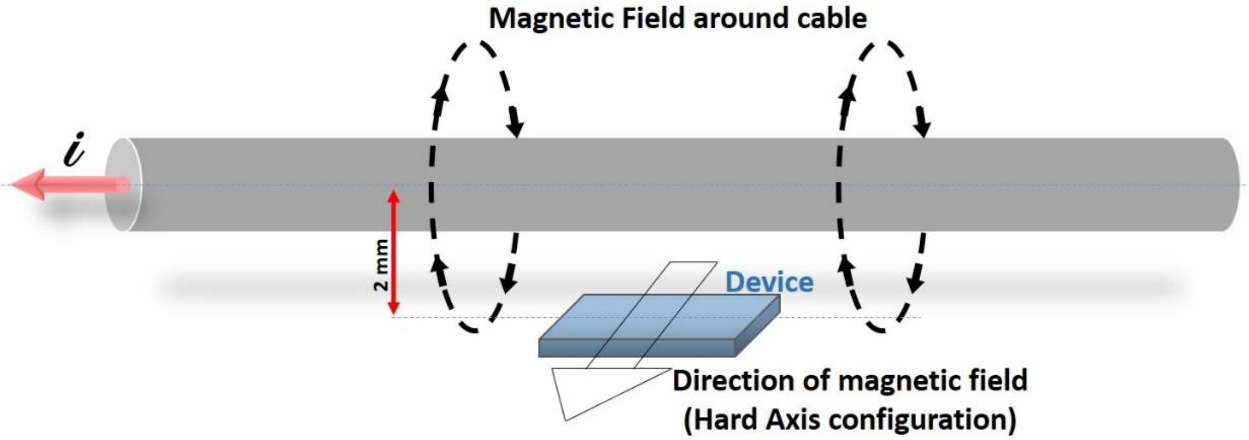

Figure 3.20: A schematic representation of the conceptual prototype for detection of current flowing through a cable.

As shown in Figure 3.20, the idea behind the prototype is to find a way to use the sensors fabricated by us to detect current flowing in a cable by way of detecting the corresponding magnetic field around the cable generated by the specific current. Considering the limitations of the current amplifier available with us, it was calculated that the device be placed at 2 mm from the cable. Also, for the optimal performance of the device, it was necessary for the magnetic field to be oriented such that it was along the hard magnetic anisotropy axis of the device. Thus, considering all these above factors, a schematic for the prototype was made (*refer Figure 3.20*).

The Experimental set-up: The first step in assembling the prototype is to prepare the device. Previously, during the fabrication of the device, we had preferred to work on the entire *24mm* × *25mm* wafer to facilitate easy processing. However, for the prototype, it is necessary to work on a single device. Therefore, a thick layer of *S1813* photo-resist is spin coated on the wafer as a protection against damage from debris during the cutting process. Using a special adhesive wax, the wafer is then mounted on a ceramic fixture to enable a proper mounting on the cutting machine. Figure 3.21 (a) shows a part of the wafer mounted on the wire cutting machine and ready for the cutting process. The cutting is done using a diamond coated wire of 0.5mm diameter and thus a spacing of 1mm was ensured between each device during the mask design phase. The final cut device is shown in Figure 3.21 (b). Finally, the device is cleaned using acetone and isopropyl alcohol to remove the protective resist coating.

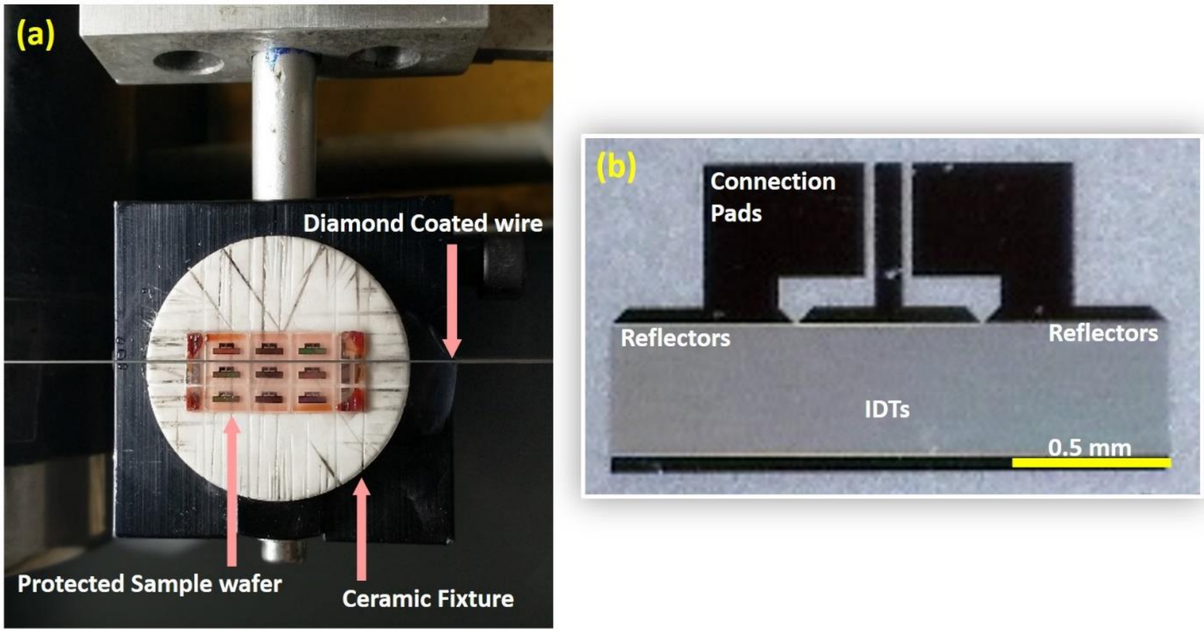

Figure 3.21: (a) Wire-cutting setup for cutting out single device from wafer. (b) single device after cutting.

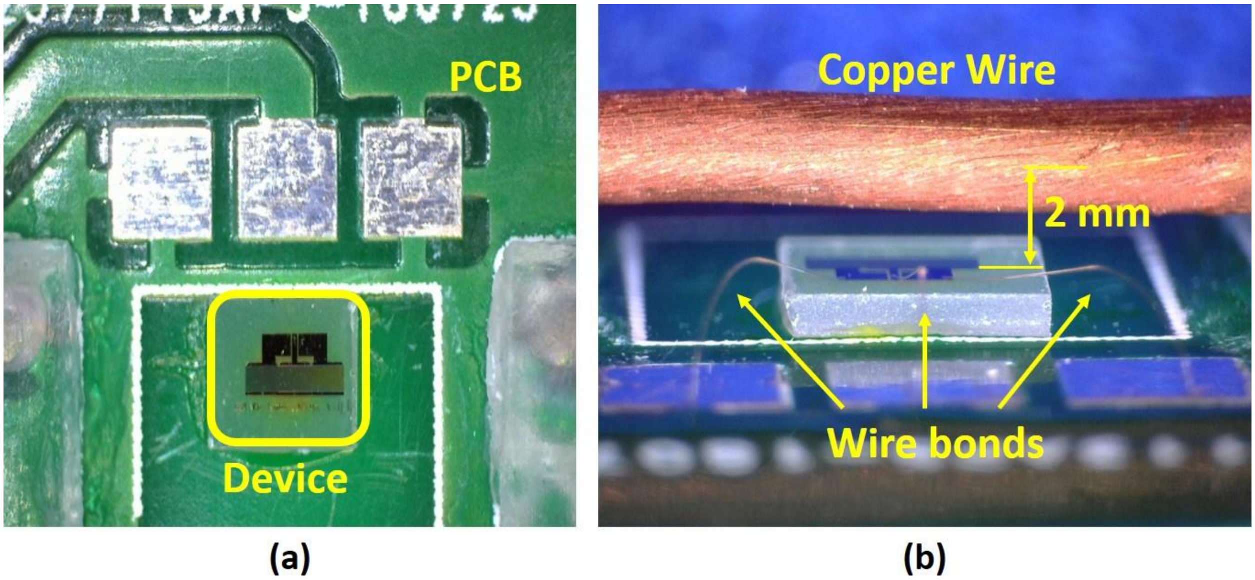

(a) (b)

Figure 3.22: (a) Device mounted on a PCB to make necessary electrical connections to connect the device to VNA; (b) A copper conducting wire placed at 2 mm from the device.

The device is then glued on to a specially designed PCB to make necessary electrical connections to connect the device to a vector network analyser (VNA). Figure 3.22 (a) shows the device fixed onto the PCB. Subsequently, a copper wire was placed at a distance of 2mm above the device as shown in Figure 3.22 (b). The wire was placed on 2 supporting pieces of plastics to ensure the correct distance from the device (2 mm).

However, once a current was passed through the copper wire, it was clear that our device behaved more as a temperature sensor than a magnetic field sensor. The device was fabricated on a $LiNbO_3$ wafer that is highly sensitive to temperature (*measured TCF of -76 ppm/°C*). When a current is passed through the copper wire, the temperature rose significantly and thereby greatly affected the sensitivity of the device. Thus the magnetic field sensitivity of the device was heavily biased by its sensitivity of the temperature. Further, it was also pointed out that the sensitivity of the device is highest between 100 and 950 Oe. Since the magnetic field generated by the current in the wire is very small and not in this region, it is also important to find a way for the device to operate in this region without having to increase the maximum current. Thus, a set of permanent neodymium magnets were used to provide a bias magnetic field of 500 Oe. Thus the device now can operate in its most sensitive region.

In order to prevent the current carrying wire/cable from overheating, we replaced it with a stainless steel tube and connected its ends to a chiller unit. The cold water flowing through the tube allowed for a stabilization of the temperature and limit it to around 22^{o}C despite the current flowing through it. Figure 3.23 shows the experimental setup in detail. As can be seen, a thermocouple is also used to monitor the temperature variations, if any.

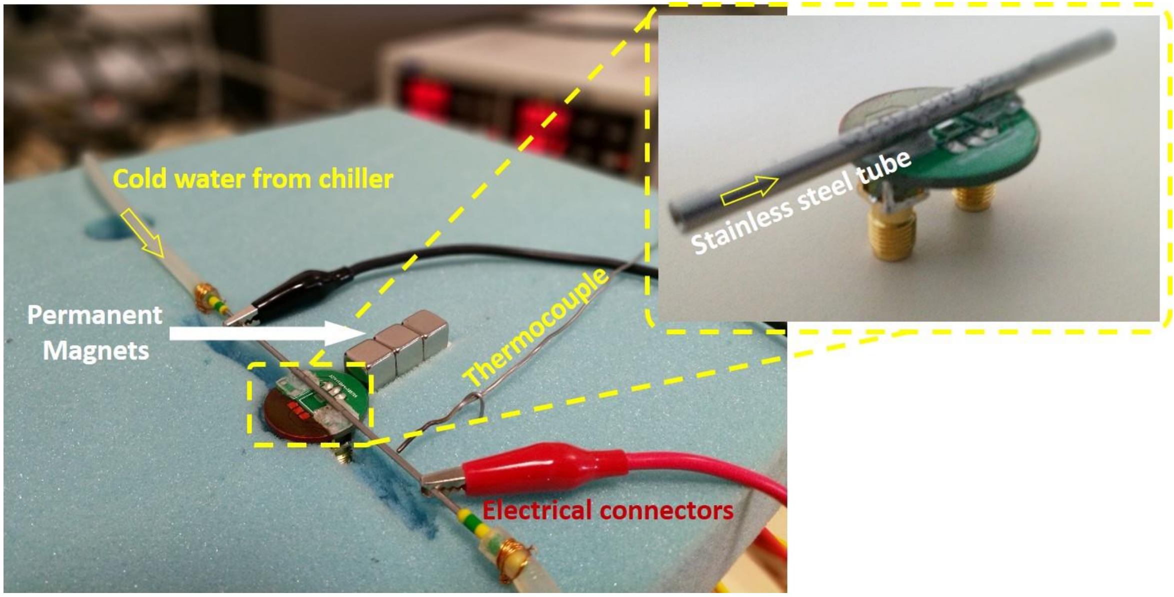

Figure 3.23: The complete experimental setup for making the measurements.

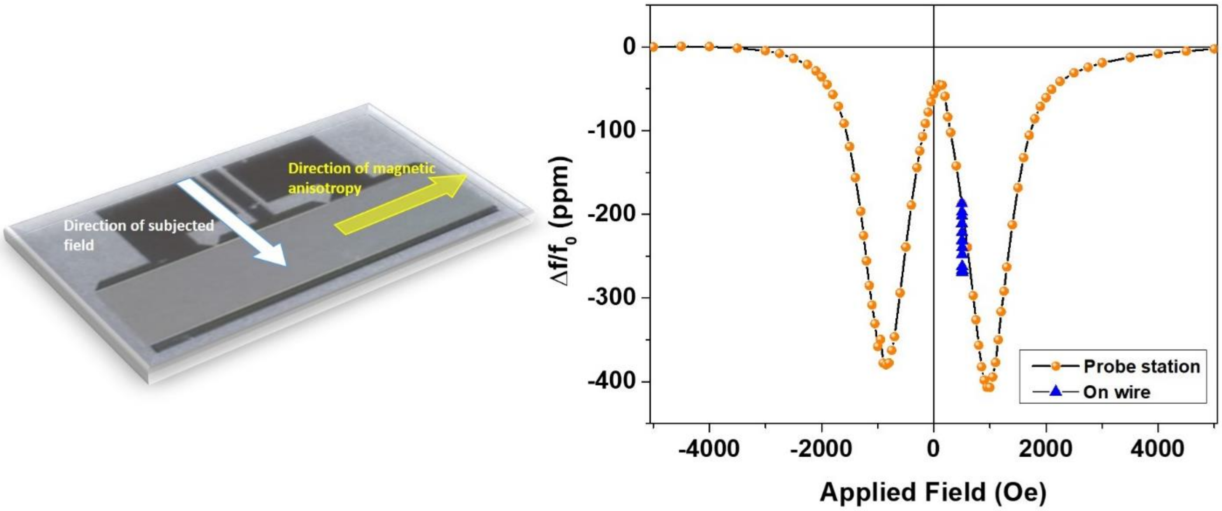

Figure 3.24: The measurements of the magnetic field on the current carrying wire overlapped over the sensitivity curve of the device measured on the probe-station. The current is varied from 0A to 10A of current.

The Measurements: Figure 3.24 presents the results as measured on the first multilayer device that we had seen in *Chapter 3*. A schematic of the device used is also presented in Figure 3.24. The current was changed in steps of 1 A to a maximum of 10 A. The variation of the resonance frequency was measured using an *Agilent Technologies E5061B, ENA Series Network Analyzer*. The magnetic field induced by this current variation is clearly measured by the device and is compared with the measurements made on the probe-station. The results clearly demonstrate the capability of the device to be used as a current sensor. Although the sensitivity may have a component of the effects of temperature owing to differences in the ambient room temperature, it is an effect that can be dealt with by using the compensated devices developed later in the thesis. In fact, it is the challenges faced during the development of this setup that leads to our next phase of study on temperature compensated devices.

As can be noted from Figure 3.24, there remains a small variation in the slope of the response of the device (*blue curve vs orange curve*). We calculated this difference in response to approximately 77.9 ppm which corresponds to a difference in temperature of 1.02^{o}C, based on the temperature coefficient of frequency of the device (76 ppm/^{o}C). This variation may be attributed to a combined effect of atmospheric and heating effects of the flowing current (despite the cooling). Thus the results reiterate the need for a device that compensates the effect of temperature in the device itself rather than clumsy external cooling systems, which are anyway not feasible for practical applications. The magnetic sensitivity component is just a little over 4 ppm corresponding to 8 Oe of the magnetic field from 10 A of current.

It is necessary to also point out that the setup presented here has a lot of potential for development. An important aspect that may be noted here is that the VNA used for the measurements had only 1601 points compared to 50,001 points used for the probe station measurements thus allowing for only a very coarse measurement. Further, the strength of the current we measured (10 A) is much smaller than in actual overhead cables thus providing a very small magnetic field. This required us to use a bias magnetic field through the use of permanent magnets, which may not be ideal for future long term use.

Conclusions:

Thus, in this chapter we have conducted studies to show that the effects of shape in magnetism can be used for influencing the magneto-acoustic behaviour of a resonator type SAW sensor, by using it to control the magnetic anisotropy. This effect may be used in combination with appropriately selected materials to engineer a sensor with a given sensitivity in a desired magnetic field range. This study also paves the way for future investigation of the intricate relations between magnetic anisotropy direction, SAW propagation direction and the nature of the substrate.

Further, the study also highlights that given the same device, the Shear-Horizontal wave presents a much stronger magneto-acoustic response than the Rayleigh wave. Additionally, in the Rayleigh wave, a part of the sensitivity comes form the magnetic anisotropy of the sensitive layer, while the other part comes from the wave propagation direction in the substrate.

Additionally, in this chapter we discussed a simple prototype setup to use one of the devices developed, as a sensor for measuring the flow of current in a cable. This prototype paves the way to develop the magnetic field sensors developed in this research work as devices for the detection of current in overhead-high tension cables. The prototype was demonstrated to be functional and the different challenges associated with it have been addressed. It was proved that as a sensor it is able to provide the measurement of a direct effect of the current flowing. Thus a new experimental set up is in progress in order to improve the prototype characterization. This prototype however, highlights a very crucial need, the need to develop a temperature compensated device, that will not only be sensitive to magnetic fields, but also be insensitive to temperature. This crucial need leads us therefore, to the next part of our research.

References:

[Zhou'14] Zhou H., "*Etude théorique et expérimentale de systèmes a ondes de surface dans des structures multicouches piézomagnétiques pour des applications en contrôle sante intégré de MEMS par imagerie acoustique non linéaire", PhD Thesis*, Ecole Centrale de Lille, 2014.

[Zho'14] Zhou H., Talbi A., Tiercelin N. and Bou Matar O., "*Multilayer magnetostrictive structure based surface acostic wave devices", Appl. Phys. Lett.*, 104, 114101, 2014.

[Rei'96] Reindl L., Scholl G., Ostertag T., Ruppel C.C.W., Bulst W.-E. and Seifert F., *"SAW Devices as Wireless Passive Sensors", Proc. IEEE Ultrasonics Symp.,* 363, 1996.

[Malo'13] Malocha D.C., Gallagher M., Fisher B., Humphries J., Gallagher D. and Kozlovski N., *"A passive wireless multi-sensor SAW technology device and system perspectives", Sensors (Basel),* 13(5), 5897-922, 2013.

[Elh'15] Elhosni M., Petit-Watelot S., Hehn M., Hage-Ali S., Aissa K.A., Lacour D., Talbi A. and Elmazria O., *"Experimental Study of Multilayer Piezo-magnetic SAW Delay line for Magnetic Sensor", Eurosensors, Procedia Eng.*, 87, 408, 2015

[Elh'16] Elhosni M., Elmazria O., Petit-Watelot S., Bouvot L., Zhgoon S., Talbi A., Hehn M., Aissa K. A., Hage-Ali S., Lacour D., Sarry F. and Boumatar O., *"Magnetic field SAW sensors based on magnetostrictive-piezoelectric layered structures: FEM modelling and experimental validation", Sensors and Actuators A Phys.*, 240, 41, 2016.

[Kad'11] Kadota M, Ito S, Ito Y, Hada T, And Okaguchi K*, "Magnetic Sensor Based on Surface Acoustic Wave Resonators", Jpn. J. Appl. Phys.*, 50: 07HD07, 2011.

[Yam'80] Yamaguchi M., Hashimoto K.Y., Kogo H. and Naoe M., *"Variable SAW delay line using amorphous* $TbFe_2$ *film", IEEE Trans. On Mag., MAG-16, 6,* 1980.

[Smo'03] Smole P., Ruile W., Korden C., Ludwig A., Quandt E., Krassnitzer S. and Pongratz P., "Magnetically tunable SAW-resonator", Proc of IEEE Int. Freq. Ctrl. Sym. & PDA Exhibition, 903, 2003.

[Pol'17] Polewczyk V., Dumesnil K., Lacour D., Moutaouekkil M., Mjahed H., Tiercelin N., Petit-Watelot S., Mishra H., Dusch Y., Hage-Ali S., Elmazria O., Montaigne F., Talbi A., Bou Matar O. and Hehn M., *"Unipolar and Bipolar High-Magnetic-Field Sensors Based on Surface Acoustic Wave Resonators", Phys. Rev. Applied*, 8 024001, 2017.

[Pol'18] Polewczyk V., *"Growth of hybrid piezoelectric/magnetostrictive systems for magnetic devices based on surface acoustic wave resonators", PhD thesis*, Université de Lorraine, 2018.

[Mis'17] Mishra H., Polewczyk V., Hehn M., Moutaouekkil M., Floer C., Dumesnil K., Lacour D., Petit Watelot S., Mjahed H., Hage-Ali S., Elmazria O., Tiercelin N., Dusch Y., Talbi A., Bou Matar O., *"Control of the magnetic response in magnetic field SAW sensors", Proc. IEEE Sensors, Glasgow*, 2017.

[Tie’00] Tiercelin N., *“Phénomènes dynamiques non linéaires dans les films minces magnétostrictifs au voisinage de la Transition de Réorientation de Spin, Application aux Microsystèmes”, PHD thesis, Université de Valenciennes et du Haut Cambresis*, 2000.

[Van’14] Vansteenkiste A., Leliaert J., Dvornik M., Helsen M., Garcia-Sanchez F. and Waeyenberge B.V. *“The design and verification of Mumax3”, AIP Advances,* 4, 107133, 2014.

[Fea’63] Featherston F.H. and Neighbours J.R., “Elastic Constants of Tantalum, Tungsten and Molybdenum”, Physical Review, 130, 4, 1963.

[Pre’01] Prejbeanu L., *“Configurations de l’aimantation dans des objets magnétiques à dimensionalité réduite. Relation entre magnétisme et transport“, PhD thesis, Université de Louis Pasteur de Strasbourg*, 2001.

[Cam’981] Campbell C. K., “*Surface Acoustic Wave Devices for Mobile and Wireless Communications*”, San Diego, California: Academic Press, 1998.

[Rodi] Roditi database on $LiNbO_3$, http://www.roditi.com/SingleCrystal/LiNbO3/liNBO3-Properties.html

Chapter 4

Temperature compensated magnetic field sensor

Introduction:

Huge strides in miniaturization of devices have led to revolutions in the telecommunication industry. Surface acoustic wave devices have emerged as a pioneer in the areas of Radio-Frequency (RF) filters and resonators in applications related to satellite receivers, remote control systems, mobile phones and keyless entry systems. Thus, temperature compensation is critical and important especially so given the new phase of advancements in the fields related to 5G and micro-electromechanical-systems (MEMS) that exploit piezoelectric on insulator (POI) structures *[Mah'17]*.

Several studies have been made to obtain an optimal MSAW device *[Pol'17]*. Kadota *et al. [Kad'11]*, Elhosni et *al. [Elh'16]* and Webb *et al. [Web'79]* have considered Ni as the sensitive material, while on the other hand, Yamaguchi *et al. [Yam'80]* examined amorphous $TbFe_2$ for their studies. Zhou *et al. [Zho'14]* also considered [$TbCo_2$-FeCo] multilayer stacks as the sensitive material. Most of these studies have appraised a delay line geometry for their SAW device *[Elh'16, Tier'08, Web'79, Zho'14]*. These studies primarily focus on the magnetic-SAW (MSAW) responses of Rayleigh waves or Shear-Horizontal waves in either $LiNbO_3$ or Quartz substrates. Later, the focus has been shifting towards the exploration of MSAW responses of Love waves generated in layered acoustic wave sensors using wave energy confinement. Kittmann *et al. [Kit'18]* have shown that Love wave sensors exhibit a much higher sensitivity to magnetic fields and therefore are very apt for designing high-sensitivity-low-field magnetic sensors. Considering the displacements in a Shear-Horizontal wave (inplane transverse) and the orientation of the magnetic anisotropy (also inplane), it is imperative that the interaction between the magnetic moments and the acoustic wave is stronger, when compared to that in the case of Rayleigh waves in which the primary displacement is out-of-plane. Therefore, a Shear-Horizontal wave based resonance is known to provide a higher response, compared to that based on a Rayleigh wave.

The objective of this chapter is to demonstrate a highly sensitive SAW device for magnetic field detection without thermal effects, i.e. with zero Temperature Coefficient of Frequency (TCF). A multi-layered SAW resonator [CoFeB/ZnO/Quartz (on a 90° rotated ST-cut substrate)] is investigated experimentally. The considered cut of Quartz exhibits a positive temperature coefficient of frequency (TCF) and is compensated by the use of ZnO with its negative TCF. The role of the ZnO film is thus double: Love wave propagation, and TCF compensation. In this chapter we detail the design of such a sensor and then discuss the experimental data regarding the magnetisation properties of the device and the radio frequency (RF) measurements under the influence of temperature and magnetic field.

4.1 Temperature Coefficient of Frequency:

The temperature coefficient of resonant frequency or TCF as it is known, is a measure of the thermal stability of the resonator. It is indicated by a gradual change of the resonant frequency with variation in ambient temperature. Since the resonators find extensive applications in the communication industry, temperature stability is an important factor and needs to be as close to zero as possible.

The origin of the TCF can be traced to the linear expansion coefficient (α_i). An increase in the expansion coefficient directly affects the resonator's dimensions and thereby its wavelength. The TCF is also dependent on the change of the elastic constants with temperature. Mathematically it is represented as:

$$TCF = \frac{1}{f} \times \frac{df}{dT}$$

where, f represents the frequency and T the temperature. The TCF is usually expressed in parts per million per degree Celsius (ppm/^{o}C). Although the actual curve of the variation of the resonance frequency is parabolic, a linear behaviour is generally considered for smaller ranges, such as the one in this current study. The increase of the ambient temperature can either cause the resonant frequency to drift to higher values in which case the TCF for the said resonator is positive or drift to lower values in which case the measured TCF is a negative value.

Use of [dielectric / piezoelectric] multi-layered structures: In certain cases, a thin amorphous dielectric film may be deposited on the piezoelectric wafer to provide the function of surface passivation, reduction of pyroelectric properties and smoothening to reduce propagation losses. It may also be used to modify the coupling factor, reduce the temperature coefficient of frequency and enable the use of higher order SAW in the wafers. They can also play the crucial role of isolating the electrodes from shorting by metal particles and electrode deterioration due to electric and acoustic fields as well as environmental and other harmful effects. A uniform dielectric film on the surface of a SAW device can also be engineered in a way to alter the propagation characteristics of the surface wave. Additionally, the presence of a dielectric film presents the possibility to produce Love waves. *[Hic'00]*

Use of ZnO on Quartz for TCF compensation: One of the primary advancements for a ZnO / Quartz multi-layered structure has been for the development of devices with a high degree of temperature stability. Such devices have special applications as vapour or liquid sensors in extreme environments as well *[Cal'19]*. ST-cut quartz has been used widely in frequency control due to its temperature stability and low cost. Moreover, it has been shown that the positive TCF of the ST-cut quartz can be very well compensated for by the negative TCF of a ZnO layer *[Tsa'15, Kad'03, Tom'05, Tal'04]*. Thus, the role of the ZnO layer is of a double benefit for us; it not only compensates the TCF but also aids in the excitation of Love waves. Moreover, thanks to its large electromechanical coupling coefficient (K^2) compared to those of Quartz, the ZnO layer enhances the K^2 of the final structure (effective $K^2 = 0.25\%$) [Kad'04].

4.2 Fabrication of the multi-layered structure:

The substrate: In this study we have used quartz as the piezoelectric substrate. There are different crystal cuts of quartz each dictating separate surface, optical and piezoelectric properties. For this study, we consider the 42.75° Y rotated ST-cut quartz crystal. This indicates that the crystal is cut along the plane 42.75° rotated from the Y-plane about the X axis. Since this cut contains only the

X-axis, the in-plane direction perpendicular to the X-axis is referred to as the (X+90^o) axis. Thus we obtain two propagation directions in this particular cut of quartz i.e. X and (X+90^o) which respectively promote the excitation of Rayleigh waves and Shear Horizontal waves. The substrate considered for this study are polished on only one side and are 500µm in thickness. The devices fabricated subsequently for the study are on this polished side of the ST-cut quartz.

Previous research in the field by Kadota et.al. *[Kad'02]* has shown that along the (X+90^o) propagation direction, the formation of SH waves with a higher velocity is preferred while along the X direction there exists only a Rayleigh wave of a lower velocity. Since we are primarily interested in Love waves, which are basically Shear-Horizontal waves in a confined structure, the direction of propagation in the devices is considered along the (X+90^o) direction.

Material	*Cutting angle [degree]*	*Direction of wave propagation*	*SAW velocity [m/s]*	*Coupling Coefficient k^2 [%]*	*Temperature Coefficient*		*Relative dielectric permittivity ε*
					a $10^{-6}/K$	*b $10^{-9}/K$*	
Quartz ST	*42.75^o*	*X*	*3100*	*0.14*	*0*	*-34*	*4.5*
Quartz ST	*42.75^o*	*X+90^o*	*3700-4280*	*0.17*	*-*	*-*	*-*

Table 4.1: ST-cut quartz parameters *[Fil'11, Kad'04]*.

Fabrication of the electrodes: The first step to start the study in this chapter is to develop SAW devices. As seen in the previous section, the devices for this study were all based on ST-cut quartz as the substrate with wave propagation direction considered along the (X+90^o) direction. Therefore, the SAW device, basically the electrodes, needed to be fabricated in a manner that ensures this. To facilitate the deposition and optimization of the ZnO layers at later stages in the chapter, it was essential to work with relatively larger dimensions and therefore, for this study we selected to work with devices having a wavelength (λ) of 10 µm. Another important aspect remains the fact that, the 10 µm wavelength allows for the frequency of the Love wave to be in the ISM frequency bandwidth (around 433 MHz). The ST-cut Quartz wafer is first diced into rectangular pieces of 24 mm × 20 mm, followed by a thorough 5-stage cleaning process described in chapter

3. In our case, we have chosen to fabricate the electrodes / IDTs from 100 nm of non-magnetic Aluminium. Not only does it have a good conductivity, but also easily available and is one of the best materials for SAW devices.

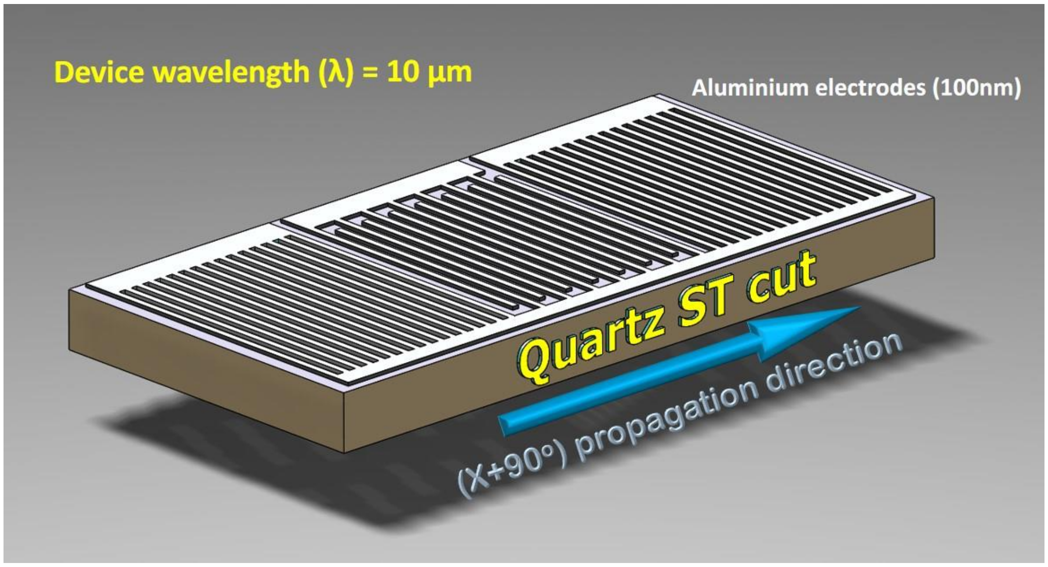

Figure 4.1: Schematic representation of the blank device.

In order to fabricate the electrodes, we followed the conventional process of lithography accompanied by a lift-off process. The first step involved spin-coating of a layer of adhesion promoter (primer) and baked at 115°C for 30 seconds. This was followed by spin-coating a layer of LOR3A that was baked at 180°C for 5 minutes. Subsequently at last, a layer of Shipley S1813 photoresist was coated and was baked for 60 seconds at 115°C. This was followed by the conventional photo-lithography where the substrate (now coated by the resist layers) is exposed to ultra violet light under a photo mask (12 seconds) using the MJB4 lithography setup. Following the lithography, the substrates were developed in a MF319 bath for 27-30 seconds to obtain a negative resist pattern of the devices. By negative we mean that the substrate is free from resist at the places where the device will be realized in the next step.

Subsequently, a 100 nm layer of Aluminium was deposited on the resist patterned substrate. This was done using the AC450 magnetron sputtering machine in the MINALOR cleanroom facilities at IJL (refer Figure 4.2 (a)). The pre-calibrated setup ensured a precise deposition of 100nm of Aluminium. Finally, the substrate was immersed into a remover solution (Microposit-1165) at 80°C for approximately 2 hours for the lift-off process to commence. In the end, the substrate along with the newly patterned devices on it is thoroughly cleaned with acetone and isopropyl alcohol to remove any traces of the toxic 1165 remover solution. These basic devices will henceforth be referred to as *blank devices* in subsequent sections of this chapter (Figure 4.1).

Figure 4.2: Experimental setups used for the deposition of (a) Aluminium (AC450); (b) ZnO (DP650).

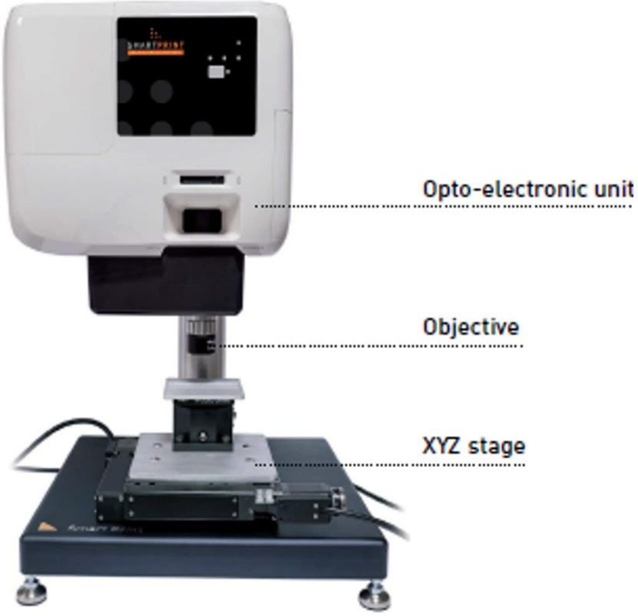

Figure 4.3: Experimental setup used for the lithography of the overlayers (Smart Print).

Deposition of ZnO and CoFeB: Following the fabrication of the blank devices, and after preliminary examinations on it such as measurement of the TCF, which will be discussed in subsequent sections, the ZnO layer was deposited on them and also the CoFeB layer after it. For the study we have considered several different thicknesses of ZnO. However, the fabrication process for each layer (different thickness of ZnO and the CoFeB) was exactly the same. In order to deposited the ZnO we have again considered lift-off as our preferred technique. Not only did the process allow a fast and precise control of the dimension of the layers but also enabled us to selectively deposit the desired thickness of ZnO / CoFeB without destroying other devices on the substrate.

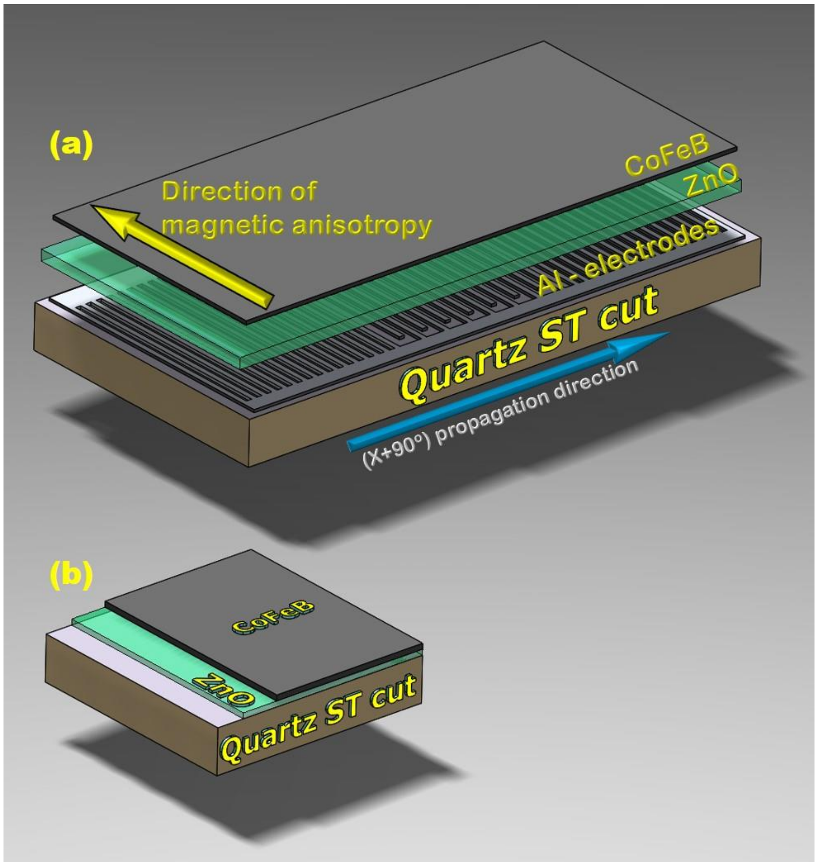

Figure 4.4: Schematic illustration of the structure of the fabricated device. (a) Device with propagation along (X+90°) direction and (b) sample for magnetometry analysis.

The first step in this process was to deposit the resist layers on the substrate / blank devices. A layer of primer was first coated and baked at 115°C for 30 seconds to act as the adhesion promoter. This was followed by spin coating a first layer of LOR30B that was baked for 2 minutes at 180°C. Subsequently, after cooling down, a second layer of LOR30B was coated and baked for

4 minutes at 180^{o}C. Finally, a photo resist layer of AZ4562 was coated over the LOR30B and baked for 1 minute at 115^{o}C. The thick resist layers ensured that a very clear under-cut structure was formed to allow even thick layers of ZnO or CoFeB to be deposited without any problem.

Considering that the dimensions of the overlayers were much larger compared to the electrodes, a new exposure technique was used for the lithography process. The lithography was executed using the Smart-print lithography setup in the MINALOR clean room facilities (*refer Figure 4.3*). Accordingly, 4000 µm × 1000 µm rectangular patches for the ZnO layer (and subsequently 3120 µm × 710 µm rectangular patches for the CoFeB) were exposed (16 seconds with the 2.5x lens attachment) to cover an area over the electrodes in the device. The devices were then developed for 3 minutes in a MF319 solution followed by rinsing in de-ionised water to expose the rectangular patch for the deposition of the ZnO and CoFeB layers. The deposition of the ZnO layer was carried out on an Alliance Concept - DP650 machine (refer Figure 4.2 (b)) by RF sputtering of a 4-inch oxygen rich target at 150 W with 3×10^{-3} mbar and 8 cm^{3}/min flow rate of both Ar and O_2. The 100nm of CoFeB was deposited by DC sputtering of a 2-inch target at 300 W and 5×10^{-3} mbar Ar. Our consideration of the CoFeB layer was not only based on its availability in our fabrication setup, but also due to its soft magnetic nature that will allow for a future control of the magnetisation using shape effects. Also, compared to Nickel, the other option that was available, CoFeB has a stronger magnetostriction that will allow for a higher sensitivity in our devices. Further, the possibility of any interdiffusion between the layers was minimized by depositing the CoFeB layer without any heating at room temperature, as an amorphous layer.

A schematic of the fabricated devices is shown in *Figure 4.4*. As was in the previous study (*Chapter 3*), for this study as well we have fabricated a special set of samples for the magnetometry tests (*refer Figure 4.4 (b)*). Keeping in mind the minimum sample dimension for the VSM setup, 4 mm × 4 mm square pieces were prepared by wire cutting. Like the devices, these samples were also multilayered with 200 nm of ZnO and 100 nm of CoFeB deposited on top of the ST-cut Quartz. This sample is referred to as V1 in the next section.

4.3 Magnetometry measurements:

Choosing the right thickness of CoFeB: In order to obtain a sensitivity to magnetic field, it was necessary for the device to have a magnetostrictive component. As in the previous study described in *Chapter 3*, it could be that the electrodes themselves are fabricated from a magnetostrictive material, or as in this segment of the research, a whole (full film) layer could be specially dedicated for the magnetostrictive effect. Compared to the electrodes, a full film is expected to produce a higher magnetostrictive effect simply owing to the larger volume of the material being available for the purpose. Thus, as a general perception it may be easy to assume that we should consider as thick a magnetostrictive layer as we desire. However as previously discussed in *Chapter 2*, a higher thickness brings with it a new set of challenges (wave confinement, magnetisation direction, electrical losses, damping etc). Thus, it is crucial at this stage, to optimize the thickness of the magnetostrictive layer, specific to our particular usage.

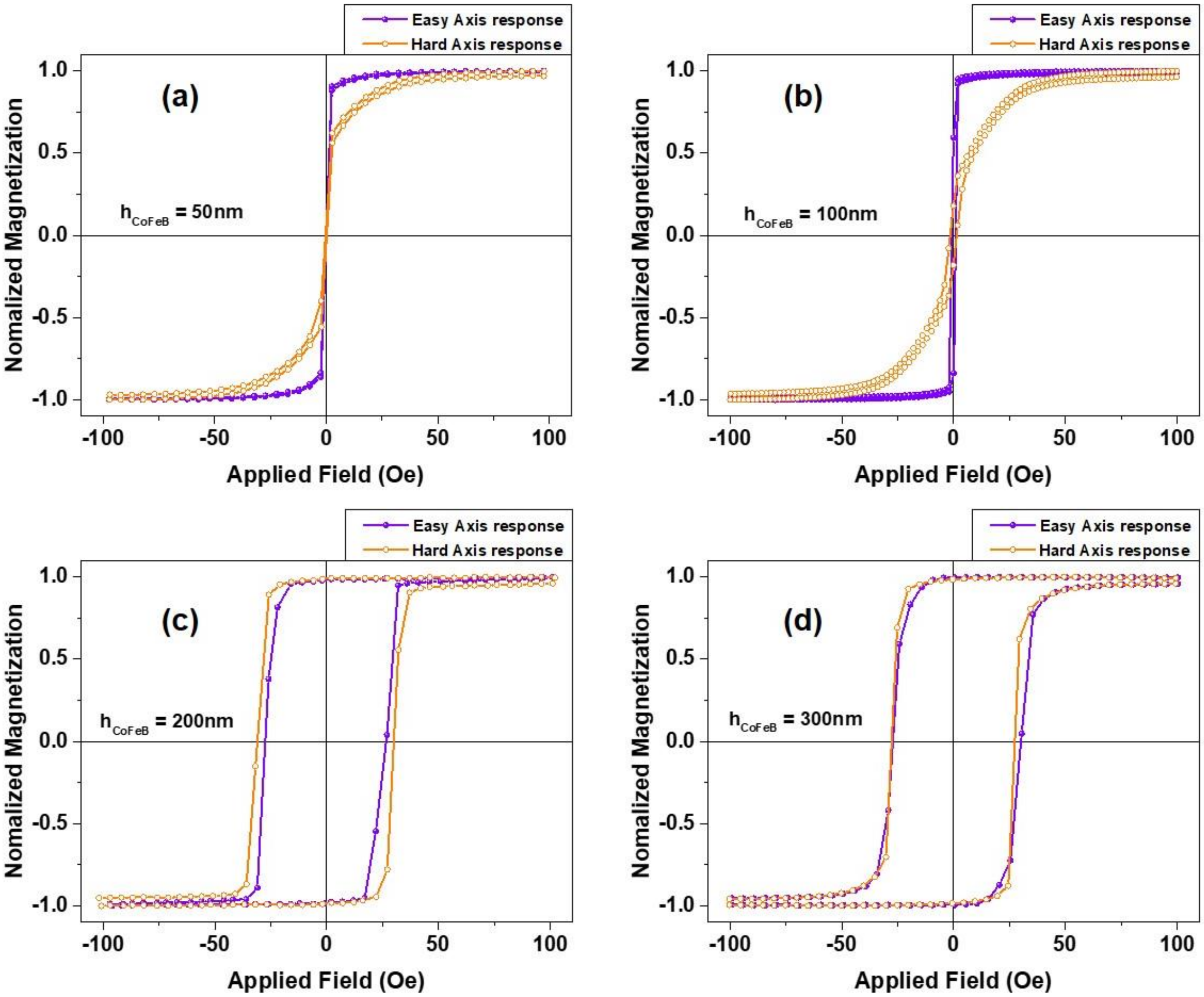

Figure 4.5: Magnetisation measurements using VSM technique on different thicknesses of the magnetostrictive CoFeB layer deposited on a $LiNbO_3$ substrate.

The magnetostrictive material used for this study was considered as CoFeB. Therefore, a set of measurements were condducted to determine the change in magnetic behaviour of the CoFeB with an increasing thickness. Four different thicknesses of CoFeB were considered: 50nm, 100nm, 200nm and 300nm. The CoFeB layers were deposited on LN substrate that were readily available for our tests. The measurements made on the different samples are presented in Figure 4.5. Considering a rotating sample holder in the VSM setup, all possible angles of measurement in-plane were made in order to determine the easy and hard magnetisation axes in the samples. As can be seen in Figure 4.5 (a) and (b), 50nm and 100nm of CoFeB exhibit very precise magnetisation directions with minimum hysteretic effects. However, as we increase the thickness beyond, the 200nm and 300nm show a very different behaviour that is akin to isotropic magnetisation (Figure 4.5 (c) and (d)). The possibility of an out-of-plane magnetisation in these relatively thick layers thus may not be ruled out as well. From the perspective of a magnetic sensor, it was essential for us to develop a vectorial sensor instead of a scalar magnetometer. Therefore, in our design of the device henceforth, we have considered 100nm of CoFeB as the optimum thickness.

Magnetisation Measurements: Magnetic characterization of the sample V1 has been conducted using a conventional VSM set up, with the field applied in-plane. Magnetic characterization of the sample V1 has been conducted using a Vibrating Sample Magnetometer (VSM), with the field applied in-plane. As usually observed, the deposition by sputtering of the magnetic layer led to the existence of an easy axis of magnetisation, as shown in Figure 4.6 (violet

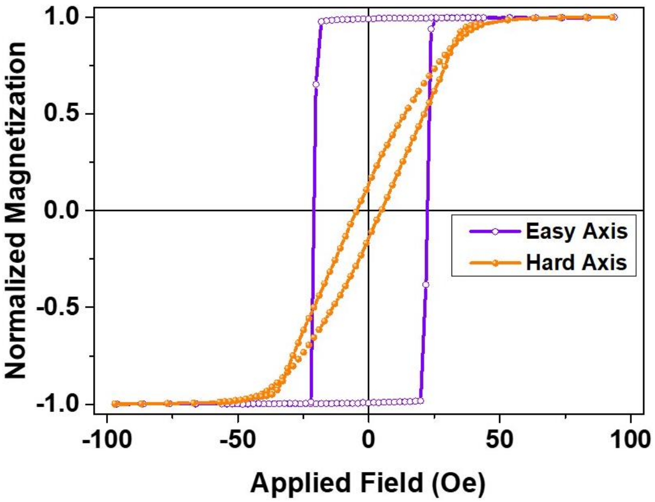

Figure 4.6: In-plane room temperature magnetisation measurements of the deposited magnetic layers (100nm of CoFeB over 200nm of ZnO on ST cut Quartz substrate).

curve). Indeed, the multi-layered structure presents a square hysteretic reversal along one direction that is chosen to be aligned parallel to the IDTs in the final device. The magnetic response along the in-plane perpendicular direction (orange curve) is characteristic of a hard axis response with an anisotropy field close to 50 Oe.

It may be highlighted here that the magnetisation of 100nm of CoFeB observed in preliminary tests (Figure 4.5 (b)) and in the multilayered structure (sample V1) (Figure 4.6, orange curve) are not exactly analogous. However, several ancillary factors are found play a major role in this. Of primary among them is the fact that the substrate itself was different. The preliminary tests (Fig. 4.5) were made on LN128 substrates while the following tests (Fig. 4.6) on the device were made on a multilayered structure developed on ST-cut Quartz. Further, the role of the ZnO intermediate layer also needs to be determined before coming to exact conclusions. Apart from these the most important factor was determined to be the deposition of the CoFeB layer. Between the first and the second cases, the deposition parameters of the CoFeB sputtering machine had been changed (due to a moving of the laboratory building) and thus the difference in magnetic properties. Nevertheless, it is still not a matter of great concern as the primary objective is to have a well-defined magnetisation axis, which was achieved.

4.4 RF Characterization and TCF Measurements:

The reflection coefficients of the fabricated devices were measured using a network analyser (Agilent PNA 5230A, Santa Clara, CA) and RF probe station (PM5 Suss Micro-Tech). Figure 4.7 depicts the experimental setup used for this characterization step. A set of GSG probes (GGB-150µm, Cascade Microtech) connects the device to the VNA. The entire system is calibrated at the end of the probes to obtain the best signal. The thermally controlled chuck of the probe station enables a stable and well controlled temperature variation of upto 60^{o}C. This allows us to monitor the drift of the resonance frequency with temperature using the VNA.

The first device that we characterised for the study, was the one that we have previously defined as the *blank device*. This device was aligned for wave propagation along the (X+90^{o}) direction of the substrate. This configuration was selected as it was the most suitable for the excitation of *Shear-Horizontal* waves *[Kad'02]*. The return loss spectrum obtained for this device showed a resonance peak at 482 MHz (refer Fig. 4.8(a)) and the TCF for the resonance peak was

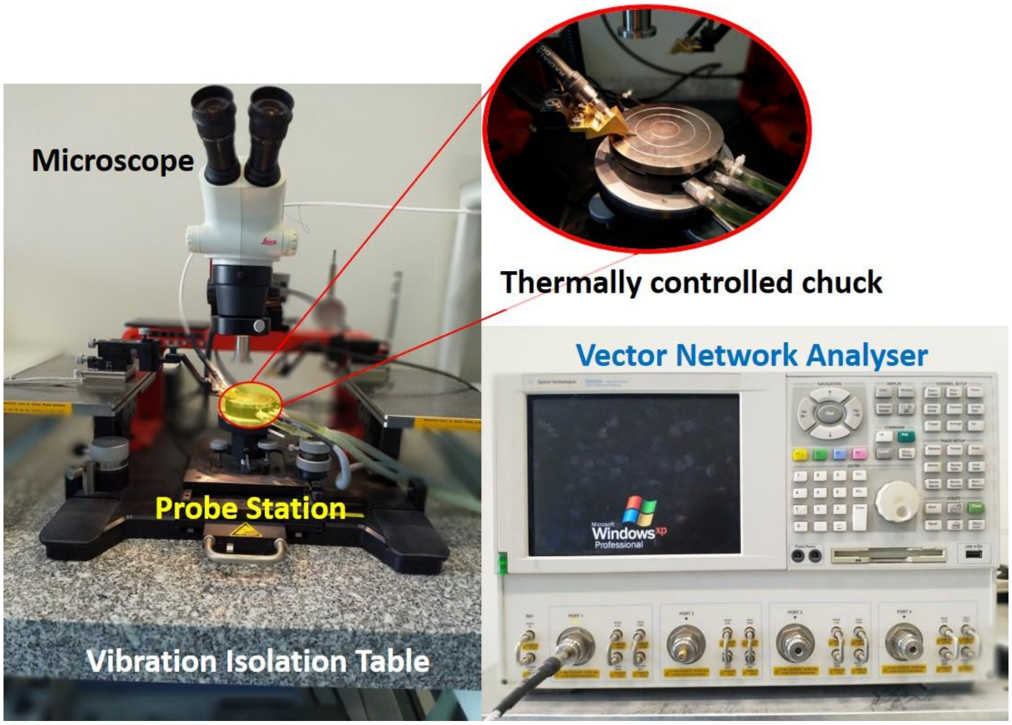

Figure 4.7: Experimental setup used for RF characterization and TCF measurements.

measured at +30ppm/^{o}C (refer Fig. 4.9(b) black curve for TCF). In order to understand the nature of the resonance, qualitative simulations were made using *Comsol Multiphysics*. Figure 4.8(a) also shows the total displacment of the simulated *half-wavelength unit cell model* and it is clear that the resonance corresponds to a *Surface-Skiming Bulk Wave (SSBW)* mode with leakage into the substrate *[Cal'19]*. As mentioned previously we know from literature that ZnO has a negative TCF [*Tsa'15, Kad'03, Tom'05, Tal'04*] that can be used to compensate the positive value of ST cut-(X+90^{o})-Quartz. Preliminary caluculations revealed that a zero TCF structure can be obtained with a ZnO thickness of around 500nm (refer Fig. 4.9 (a))

We also investigated experimentally other thicknesses for an optimal TCF as seen from Figure 4.9 (b) (blue curve) and found that indeed a thickness of 510nm of ZnO provides the best compensation. The experimentally obtained TCF value was -0.7ppm/^{o}C that is still remarkably close to zero. The S_{11} spectra of this device is shown in Figure 4.8 (b) and the TCF measurement in Figure 4.9 (b), red curve. Comsol simulations (also in Figure 4.8 (b)) reveal the presence of a *Rayleigh wave* mode at 330 MHz followed by two *Shear-Horizontal* modes at 409 MHz and 427 MHz.

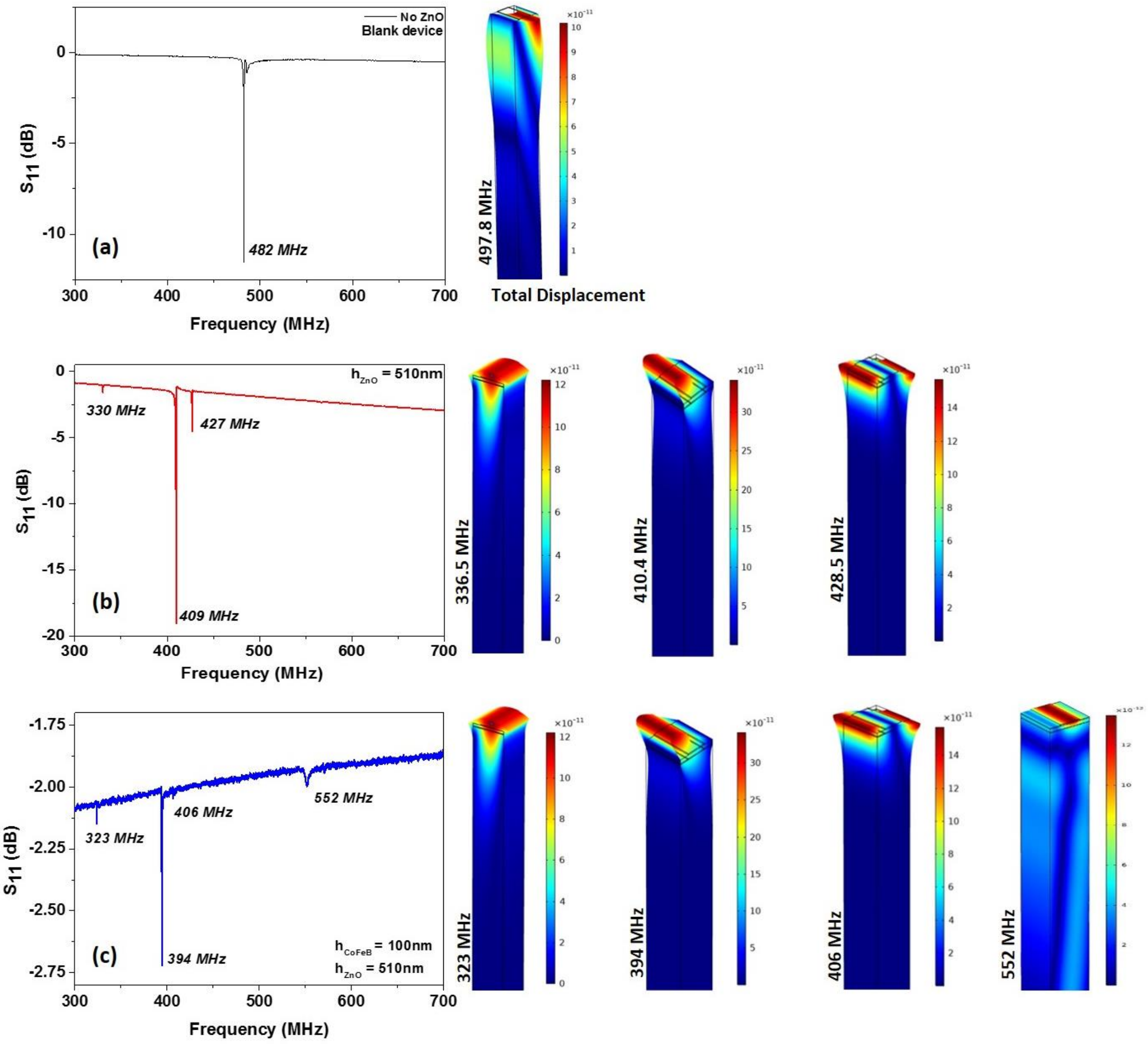

Figure 4.8: Experimental scattering parameters compared for (a) without ZnO and with 510nm of ZnO; (b) experimentally measured S_{11} when 100nm of CoFeB is added on top of the 510nm of ZnO. Deformations observed for each resonance, through Comsol simulations are presented beside each S_{11}.

Following that, a 100nm of CoFeB was deposited on top of the ZnO. Figure 4.8(c) shows the return loss frequency behaviour after the addition of the CoFeB layer. The resonances seen before the addition of the CoFeB layer can also be seen after its additon. Comsol simulations peresented in the same figure, also reveal that the resonance at 323 MHz is a Rayleigh wave while those at 394 MHz and 406 MHz are *Shear Horizontal* in nature. A *Bulk Acoustic wave* also appears

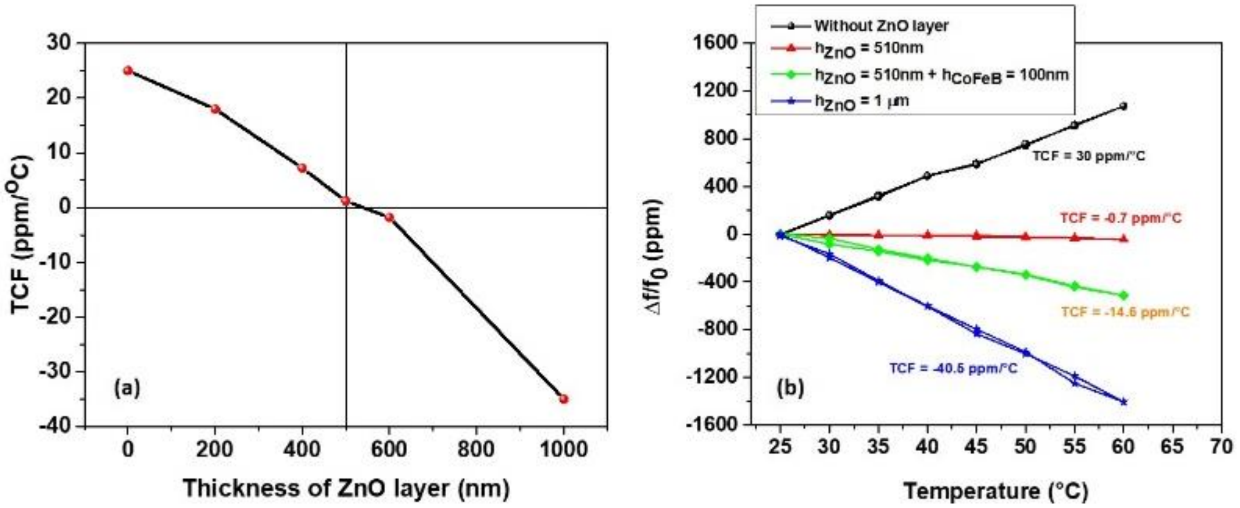

Figure 4.9: (a) TCF variations for different thicknesses of ZnO as obtained from simulations. (b) Dependence of frequency on temperature as measured for the *Shear-Horizontal* or Love wave mode on the samples for during optimization with ZnO layer and after addition of a 100nm of CoFeB.

552 MHz as confirmed by the simulations. As can be seen, the S_{11} specturm becomes quite noisy after the addition of the CoFeB layer and there is a high chance of a capacitive effect arising from the close proximity of the electrodes with the metallic CoFeB layer (100nm of Al separated from 100nm of CoFeB by just 200nm of ZnO). However, we did not have the resources to investigate this aspect experimentally. After the addition of the CoFeB layer on this device, it was observed that the TCF dropped to a negative value of -14.6 ppm/^{o}C (Figure 4.9(b), green curve), indicating the need to re-optimize the ZnO thickness. However, thermal elastic constants of CoFeB were not available in literature, thus making it impossible to theoretically determine the thickness of the different layers that allow a zero TCF device. Determination of the optimal thickness was therefore done experimentally. In this study, we keep the thickness of CoFeB constant and equal to 100 nm to avoid the modification of its magnetic properties and to modulate the thickness of the ZnO layer in order to obtain a device with zero TCF.

Thus, the devices *D1, D2 and D3* with respective ZnO thicknesses of *200nm, 400nm and 600nm* were fabricated. A careful analysis of the resonance frequencies (refer Figure 4.10 (a), (c), (e)) and a measurement of the TCFs (Figure 4.11 (a)) helps us to determine that the two resonance frequencies observed in each case are the same *SH* waves observed earlier. Subsequently, with the addition of the CoFeB layers, a new resonance appears around 325 MHz along with the SH resonance. Figure 4.10 (b), (d) and (f) present the S_{11} measured for each of the devices.

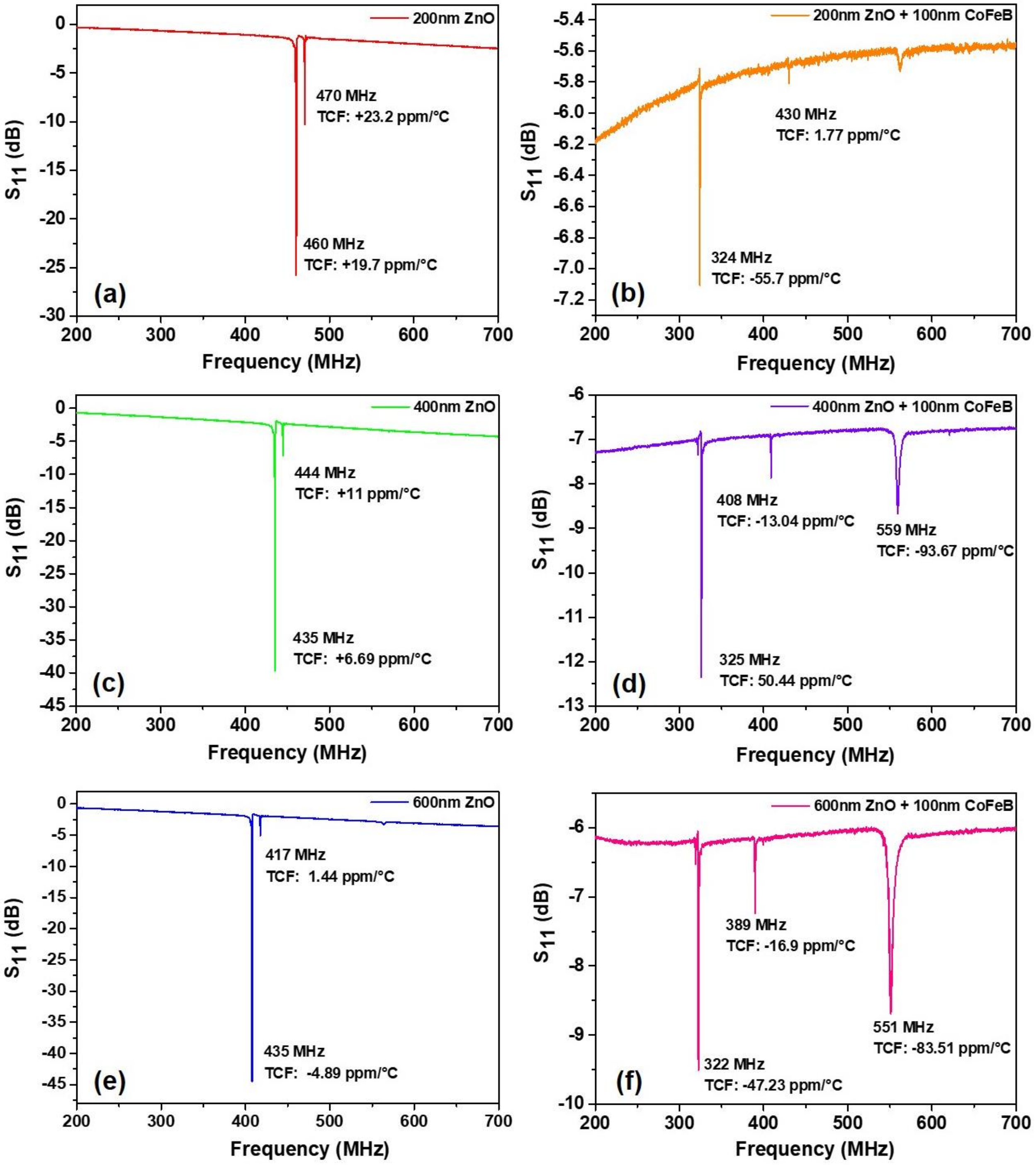

Figure 4.10: Scattering parameter (S_{11}) measured on samples *D1, D2 and D3* before (a, c and e) and after (b, d and f) deposition of the CoFeB layer.

By observing the incoherent TCF values for this peak and also preliminary measurements of the frequency variation with magnetic field intensity, it can be assumed that this resonance is a Rayleigh or rather a pseudo-Rayleigh wave. The TCF variation of the Love wave peaks in each case is presented in Figure 4.11. An observation can be made at this stage that the signal from this so-called Rayleigh wave is much stronger in the later devices with CoFeB but not in the first device with 510nm of ZnO and 100nm of CoFeB.

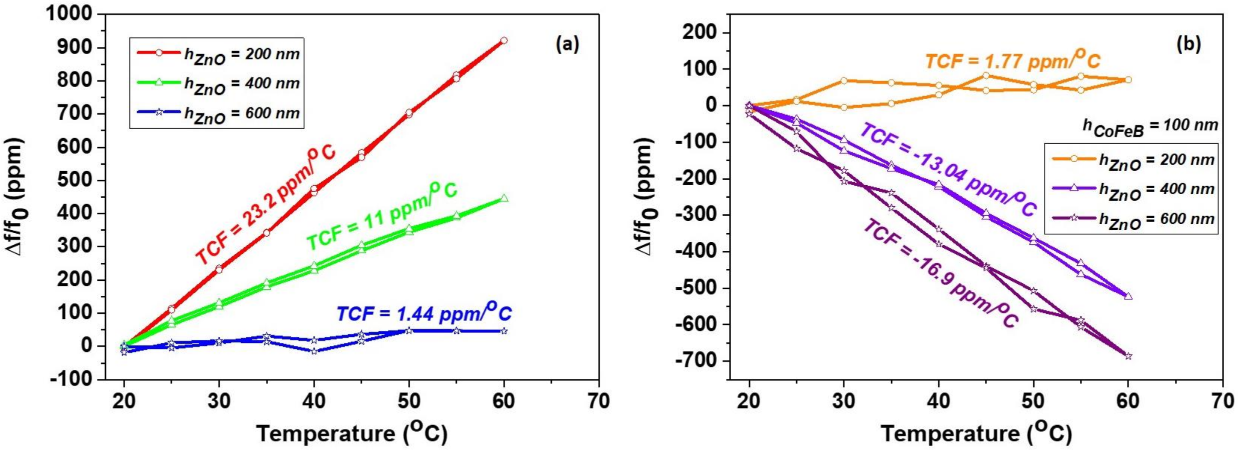

Figure 4.11: Dependence of frequency on temperature as measured for the *Shear-Horizontal* or Love wave mode on the samples D1, D2 and D3 with respective ZnO thicknesses of 200nm, 400nm, 600nm (a) before deposition of CoFeB (b) after deposition of 100nm of CoFeB.

Our experimental results show that the TCF of the CoFeB layer considered here is negative and the value is higher than that of the ZnO used. Only 100nm of CoFeB was enough to replace 310nm of ZnO. With just 100nm of CoFeB, deposited on 200nm of ZnO it was possible to reach a TCF value of 1.77ppm/°C (almost zero), whereas 510 nm of ZnO was necessary to obtain the same result. Alternately, a slightly thicker ZnO layer by around 10-20nm is expected to get the device even closer to a zero TCF value. Finally, the multi-layered structure with a ZnO thickness of 200nm and 100nm of CoFeB was selected for measurements under magnetic field. The Love wave observed in this device (Figure 4.10 (b) red curve, shallow dip at 430 MHz) exhibits an operation frequency very close to the ISM band and a near-zero TCF.

4.5 MSAW Measurements:

The MSAW measurements were made using the *LakeShore* cryogenic probe station (EMPX-HF) connected to a VNA (Rohde and Schwartz ZVA67) by a K-cable and GGB Picoprobes (40GHz) as described in *Chapter 3*.

The magneto-acoustic response of the Love wave peak in the temperature compensated 430 MHz peak of the device (D1) is measured versus the direction and intensity of an applied magnetic field. The field is applied along two directions, parallel to the wave propagation direction of the device and perpendicular to it. As expected, due to the magnetic behaviour, the perpendicular orientation corresponds to the easy axis response while the parallel yields the hard axis response.

Since the first resonance peak (324 MHz in the device D1) is not temperature compensated, it is of little importance in this study. As seen by the deformation of the device observed during the optimization process of ZnO shown in Figure 4.8, this resonance is expected to be of the Rayleigh wave type. MSAW measurements carried out on this peak also corroborated this (refer Figure 4.12). However, its sensitivity is much less as compared to the Love wave peak that is the focus of this study.

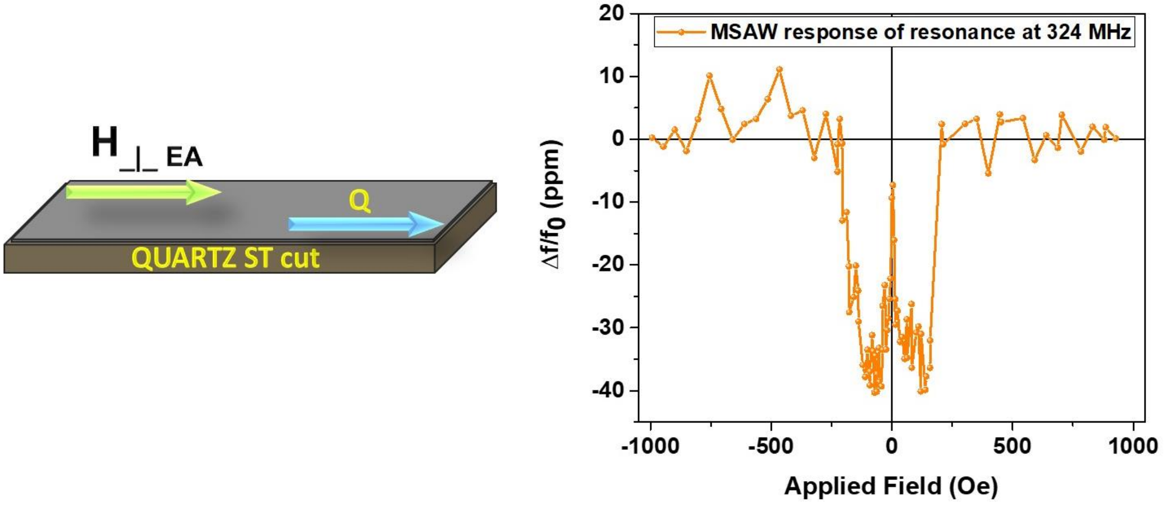

Figure 4.12: MSAW response measured along the hard axis (parallel to the wave propagation direction) on the non-temperature compensated *Rayleigh* wave peak in the device (D1) (resonance peak at 324 MHz).

The frequency variation of the Love wave peak are obtained with respect to a varying magnetic field along the two directions and are shown in Figure 4.13. As can be seen, the sensitivity of the peak is significantly higher with the field applied parallel to the wave direction. The measurements show a monotonous, quasi-linear behaviour between 100 and 260 Oe, that can be exploited for magnetic field sensing applications. The response to magnetic field perpendicular to the wave propagation direction being considerably lower, this confers this structure a good directivity.

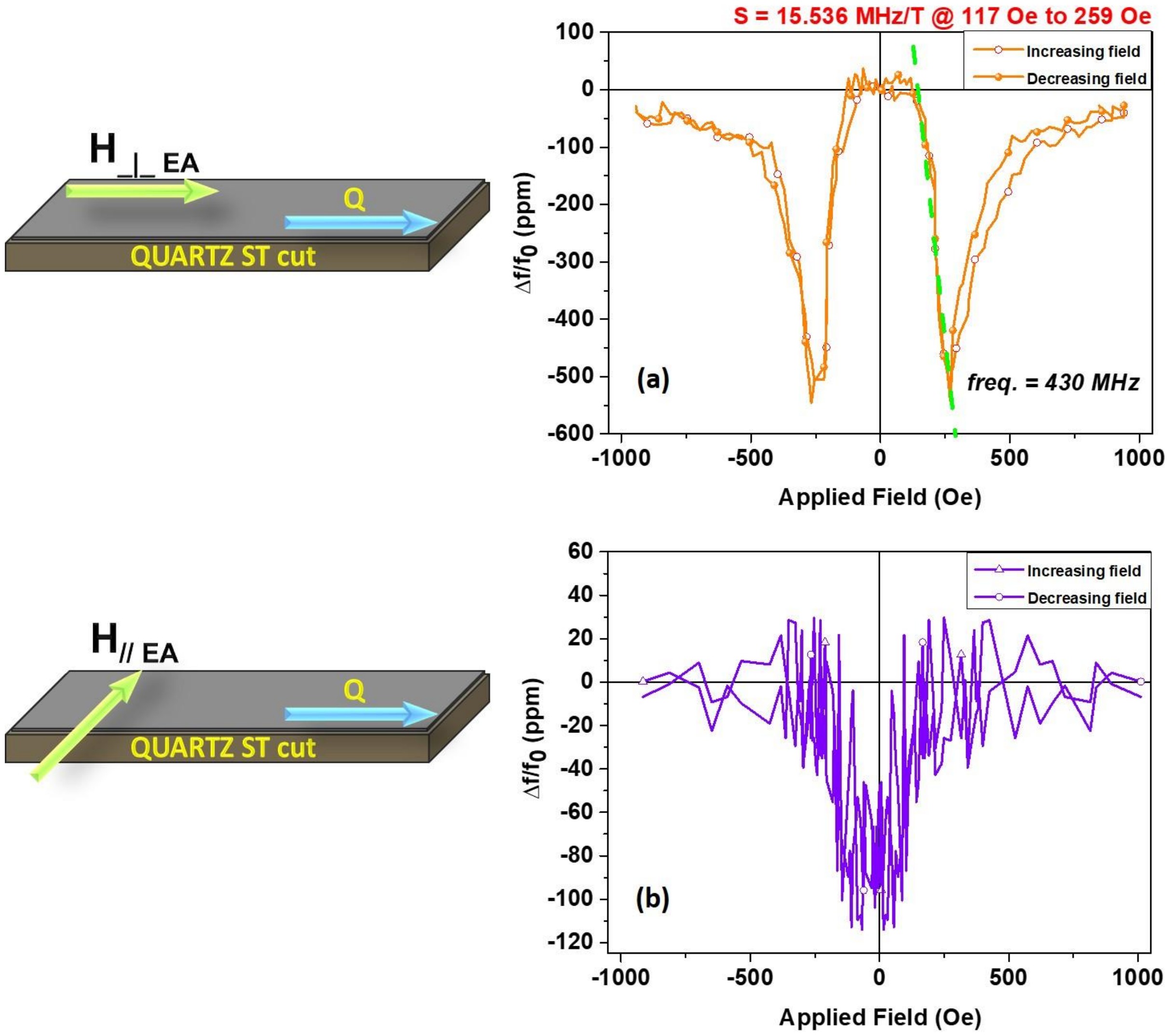

Figure 4.13: MSAW measurements on the temperature compensated Love wave peak in the device ($h_{ZnO} = 200nm; h_{CoFeB} = 100nm$) (resonance peak at 430 MHz). The field is applied (a) along the hard axis i.e. parallel to wave propagation direction and (b) along the easy axis i.e. perpendicular to the wave propagation direction. The corresponding orientations are sketched beside the figures with Q being the wave propagation direction and H the applied field. The sensitivity of 15.53 MHz/T is measured between 117 Oe and 259 Oe for the hard axis configuration shown in (a) and the linearity is highlighted by the green dotted line.

The measured sensitivity of the device for magnetic field applied along the hard magnetic axis is 15.536 MHz/T *(64.36 nT/Hz)* between 117 and 259 Oe. This is comparable to the sensitivity measured by Kittman et al. *[Kit'18]* who obtained around 44.24 MHz/T (calculated from their experimental results) but much more sensitive compared to the results of Kadota et al. *[Kad'11]*, Elhosni et al. *[Elh'16]* and Zhou et al. *[Zho'14]*. Although, Kittman et al. emphasised on obtaining a higher sensitivity, our device focused more on removing the temperature effects and obtaining an equivalent sensitivity. Accordingly, to the purpose of this structure, the temperature effect observed for a 200 nm thick ZnO layer (1.77 ppm/°C) only marginally interferes with the magnetic field measurement, which shows a sensitivity range of approximately 500 ppm. Thicknesses of ZnO and CoFeB could be optimised to obtain a zero TCF value and the resonator design could be improved to enhance the quality of the sensor and thus enhance its sensitivity.

Conclusions:

In this chapter we have presented a unique way to self-mitigate the effects of temperature on a SAW device used for magnetic field sensing. The positive TCF of a quartz-based device is compensated by a multi-layered structure made with ZnO and CoFeB. The TCF of the device has been measured at 1.77 ppm/^{o}C, indicating that it is relatively free from the effects of temperature drifts during magnetic field measurement. Additionally, the device designed to operate in 433 MHz ISM band has been shown to have a very good magnetic field sensitivity (15.536 MHz/T or 64.36 nT/Hz). This sensitivity could be further improved by the optimisation of the resonator design and also probably by increasing the operating frequency of the sensor.

This study also highlights a few important limitations of our study. As we observe, the addition of metallic CoFeB induces high electrical losses in our devices, especially on the Love waves. Limitations in the fabrication technologies, a change in the capacitance of the devices, eddy currents in the CoFeB layer are only but a few possible causes of these losses. Further, having used a full film of the CoFeB, we observe a hysteretic magnetization that is the result of a poor control of the anisotropy. Such hysteretic response is not suitable for sensor applications and thus need to be removed from the device. Also, another important aspect that needs to be addressed is the fact that the temperature influences not only the resonance frequency, but also the magnetic anisotropy. And hence, these challenges lead us to the next part of our study where we address not only the effects of temperature on the frequency, but also on the magnetic anisotropy.

References:

[Tal'04] Talbi A., Sarry F., Moreira F., Elhakiki M., Elmazria O., Brizoual L Le., Alnot P., *"Zero TCF ZnO/Quartz SAW structure for gas sensing", IEEE Ultrasonics, Ferroelectrics and Frequency Control Joint, 50th Anniversary Conference,* 2004.

[Kad'11] Kadota M., Ito S., Ito Y., Hada T., and Okaguchi K., "Magnetic Sensor Based on Surface Acoustice Wave Resonators", Jpn. J. Appl. Phys. 50, 07HD07, 2011.

[Elh'16] M. Elhosni, O. Elmazria, S. Petit-Watelot, L. Bouvot, S. Zhgoon, A. Talbi, M. Hehn, K. Ait-Aissa, S. Hage-Ali, D. Lacour, F. Sarry, O. Boumatar, "Magnetic field SAW sensors based on magnetostrictive – piezoelectric layered structures: FEM modelling and experimental validation", Sensors and Actuators A Phys., 240 41–49, 2016.

[Yam'80] Yamaguchi M., Hashimoto K. Y., Kogo H., and Naoe M., *"Variable SAW delay line using amorphous TbFe2 film", IEEE Trans. Magn.*, 16, 916, 1980.

[Tier'08] Tiercelin N., Talbi A., Preobrazhensky V., Pernod P., Mortet V., Haenen K., and Soltani A., *"Magnetoelectric effect near spin reorientation transition in giant magnetostrictive*-aluminum *nitride thin film structure", Appl. Phys. Lett.,* 93, 162902, 2008.

[Pol'17] Polewczyk V., Dumesnil K., Lacour D., Moutaouekkil M., Mjahed H., Tiercelin N., Petit Watelot S., Mishra H., Dusch Y., Hage-Ali S., Elmazria O., Montaigne F., Talbi A., Bou Matar O., Hehn M., *"Unipolar and Bipolar High-Magnetic-Field Sensors Based on Surface Acoustic Wave Resonators", Phys. Rev. Appl.*, 8, 024001, 2017.

[Web'79] Webb D. C., Forester D.W., Gangu1y A. K., and Vittoria C., *"Applications of amorphous magnetic-layers in surface acoustic wave devices", IEEE Trans. Magn*., 15, 1410, 1979.

[Zho'14] Zhou H., Talbi A., Tiercelin N. and Bou Matar O., "*Multilayer magnetostrictive structure based surface acostic wave devices", Appl. Phys. Lett.*, 104, 114101, 2014.

[Kit'18] Kittmann A., Durdaut P., Zabel S., Reermann J., Schmalz J., Spetzler B., Meyners D., Sun N. X., McCord J., Gerken M., Schmidt G., Höft M., Knöchel R., Faupel F. and Quandt E., *"Wide Band Low Noise Love Wave Magnetic Field Sensor System", Scientific Reports,* 8 278 2018.

[Hic'00] Hickernell F.S., "*Thin Films for SAW devices", International Journal of High Speed Electronics and Systems*, 10, 3, 603-652, 2000.

[Tom'05] Tomar M., Gupta V., Sreenivas K., Mansingh A., *"Temperature stability of ZnO thin film SAW device on fused quartz", IEEE Trans. on Device and Materials Reliability*, 5, 3, 2005.

[Kad'03] M. Kadota and H. Kando, "*Small and low-loss intermediate frequency surface acoustic wave filters using zinc oxide film on quartz substrate," Jpn. J. Appl. Phys.* 42(1), 3139–3142 (2003).

[Tsa'15] Tsai Wen-Che, Kao Hui-ling, Liao Kun-Hsu, Liu Yu-Hao, Lin Tzu-Ping and Jeng Erik S., *"Room temperature fabrication of ZnO/ST-cut quartz SAW UV photodetector with small temperature coefficient"*, OSA, 23 3 2015.

[Fil'11] Filipiak J., Solarz L. and Steczko G., *"Surface Acoustic Wave (SAW) vibration sensor", Sensors*, 11, 11809-11832, 2011.

[Cal'19] Caliendo C. and Hamidullah M., *"Guided acoustic wave sensors for liquid environments", J. Phys. D: Appl. Phys.*, 52, 153001, 2019.

Chapter 5

Multi-sensory SAW device

Introduction:

An elementary property of magnetic materials is their magnetic anisotropy. Not only does it play a role in determining the direction along which it is magnetised, but also thereby aids in determining the applications that may be suitable for it *[Blu'01, Bar'14, Par'03, Lou'09]*. In previous studies, we have seen that magnetic anisotropy has a huge impact on the magneto-acoustic response of a surface acoustic wave (SAW) device *[Kad'11, Elh'16, Yam'08, Pol'17]*. This has been especially proven for a Rayleigh Wave based SAW sensor *[Kad'11, Yam'08]*. Surely, several studies have been made to optimize the sensitivity of the device and many have also developed their own special magnetostrictive alloys for this purpose *[Zho'14, Kit'08]*. There have been studies to deal with the effect of temperature as well in which the effect of a drift of the resonance frequency caused by the changing temperature or in other words a compensation of the temperature coefficient of frequency (TCF) has been addressed *[Tal'06]*. The same has also been described at length in Chapter 4. However, a crucial fact that remains unaddressed is that with a change in the ambient temperature, the magnetic anisotropy also tends to decrease *[Thi'03, Phu'12]* or increase *[Liu'14]*. Several studies have pointed out this detrimental effect. McDaniel *[McD'05]* also pointed out that the loss of magnetic anisotropy can drastically impact magnetic recording and thereby cause loss of data. Lamy *[Lam'06]* has reported the degradation of the resonant frequency in microwave devices with a rise of the temperature owing to a degradation of the magnetic anisotropy.

In this chapter we discuss the influence of the temperature on the magnetic anisotropy of the SAW device used as a magnetic field sensor and propose ways to mitigate the effects. Simultaneously, we also take into consideration the effects of temperature on the resonance frequency of the device and based on the previous chapter, suggest ways to eliminate that. Taking into consideration the effects of shape anisotropy, we show the possibility to stabilise the anisotropy up to 100^{o}C and by considering a multi-layered device structure the positive TCF of the Quartz is shown to be compensated by the negative TCF of the ZnO and CoFeB layers.

Additionally, the device is shown to have three resonances: a Rayleigh wave which is sensitive to temperature and partially sensitive to a magnetic field, a Love wave which is negligibly sensitive to temperature but sensitive to magnetic field and a Bulk Acoustic wave that is highly sensitive to temperature but not to a magnetic field. Thus, finally in this chapter we propose a multi-sensory SAW device capable of detecting a magnetic field as well as temperature in the same device but independent of each other.

5.1 Temperature Coefficient of Magnetic Anisotropy:

A ferromagnetic material is understood to possess magnetocrystalline anisotropy if during the process of magnetisation, some directions require less energy compared to others. In such a scenario, the direction that requires the least energy is termed as the *Easy Axis* while the direction that requires the maximum energy is defined as the *Hard Axis*. The first order source of magnetocrystalline anisotropy arises from a spin-orbit coupling between the electrons and the electric field of the crystal while the second order anisotropy arises from a mutual interaction between the magnetic dipoles.

The magnetocrystalline anisotropy is found to have a strong dependence to temperature. Generally, an increase in temperature leads to a sharp increase in the internal energy of the ferromagnetic material by virtue of a rise in its entropy and therefore leads to a decrease of the magnetocrystalline anisotropy parameters. As the temperature reaches the point of *Curie Temperature*, the crystal gradually transforms to an isotropic system. This means that from an experimental perspective in an anisotropic ferromagnetic layer, a rise in the temperature would lead to the formation of an isotropic layer in which no clear distinction between the easy and hard magnetic axes can be made. In other words, at the appropriate temperature, we can observe the magnetic hard axis and the easy axis lose their identity!

We know from the physics of magnetisation that the total magnetic anisotropy of a system is a combination of the magnetocrystalline anisotropy and extrinsic anisotropy such as anisotropy induced by strain, shape anisotropy as well as the Zeeman energy *[Par’13, Wei’09]*. Of these, the magnetocrystalline anisotropy is an intrinsic property and is dependent on the saturation magnetisation and thus decreases with temperature *[Wei’09, Wan’11]*. On the other hand, the extrinsic magnetic properties such as the strain and shape induced anisotropies are respectively dependent on parameters such as the magnetostriction coefficient and the geometry. The magnetostriction decreases with temperature and thus so does the strain dependent anisotropy.

From the perspective of applications to SAW devices, this effect becomes an extremely detrimental effect in ambient environment where the temperature can fluctuate. In previous chapters, we observed that the magnetic anisotropy of the magnetostrictive layer has a direct influence on the magneto-acoustic response of the SAW device. This was especially observed in the case of the *Rayleigh* waves. Although in this study we concentrate on a confined *Shear-Horizontal* or *Love* wave based device, the effect of the magnetic anisotropy cannot be negated. Especially so since the temperature directly affects the magnetic saturation field value. Thus, it becomes a prime concern to nullify the effects of temperature on the magnetic properties if we intend to develop a magnetic SAW sensor that is truly compensated for temperature.

5.2 Fabrication of the device:

In Chapter 4, we explored the various aspects of compensation of the temperature effects on frequency and thus understood the various intricacies surrounding the specific cut of Quartz as the substrate with specific propagation direction for the formation of Love waves. In this chapter we continue the device configuration from the previous study so as to retain similar properties of Love wave generation and temperature compensation. Thus, in this study as well we consider the single side polished, 42.75° Y rotated ST-cut quartz crystal as a substrate with the wave propagation direction along the (X+90°) direction.

Fabrication of the electrodes: The first step in this study is to develop the SAW device itself. Like in the previous study, we have chosen to fabricate the electrodes / IDTs from 100nm of

Aluminium. Also on a similar note, in order to facilitate the deposition and optimization of the ZnO layers at later stages in the chapter, it was essential to work with relatively larger dimensions of the surface area and therefore, we selected to work with devices having a wavelength (λ) of 10µm and a metallization ratio of 50%. In order to fabricate the electrodes, we followed the conventional lithography and lift-off process as described previously in Chapter 4. A schematic design of these *blank devices* is illustrated in Figure 5.1.

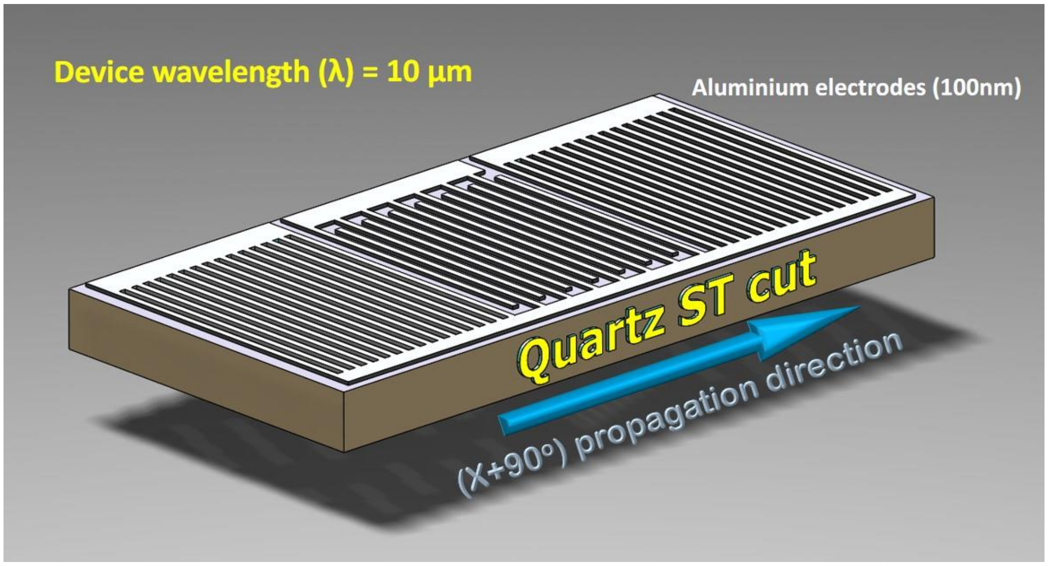

Figure 5.1: Schematic representation of the blank device.

Deposition and micro-structuration of ZnO and CoFeB: Following the fabrication of the blank devices and based upon the studies on the optimization of the ZnO layer to obtain a zero TCF structure done in the previous chapter, the ZnO layers are deposited. Considering that in the previous chapter we obtained a zero TCF structure with 200nm of ZnO layer under the 100nm CoFeB layer, it is expected that a micro-structured CoFeB layer would require a thicker layer of ZnO for the TCF compensation.

The lift-off based fabrication technique, developed previously, is again utilised for the deposition of the ZnO based insulating layer. Not only did the process allow a fast and precise control of the dimension of the layers but also enabled us to selectively deposit the desired thickness of ZnO without destroying other devices on the substrate. In the previous chapter, we had conducted a step during which we optimized the thickness of the ZnO layer on the blank device. The thickness of the ZnO layer was optimized at 510nm to obtain a zero-TCF structure. However, that step is skipped in the present study since it was not necessary to repeat the same test. Thus, we moved ahead directly to deposit the three ZnO thicknesses of 200nm, 400nm and 600nm (*devices F1, F2 and F3 respectively*). The three thicknesses were considered so as to observe the effect of the micro-structured CoFeB layer. Although we have a general idea that, given the negative TCF of CoFeB observed in the previous chapter, the thickness of the ZnO layer needed for a zero-TCF structure would be lower than 500nm, we still considered the 600nm device as we needed to take into account micro-structuration and its effects, if any, on the TCF. The fabrication of each of the different ZnO thicknesses followed the same procedure of using the mask-less *Smart Print* setup for the lithography and ZnO sputtered using the DP650 magnetron sputtering machine.

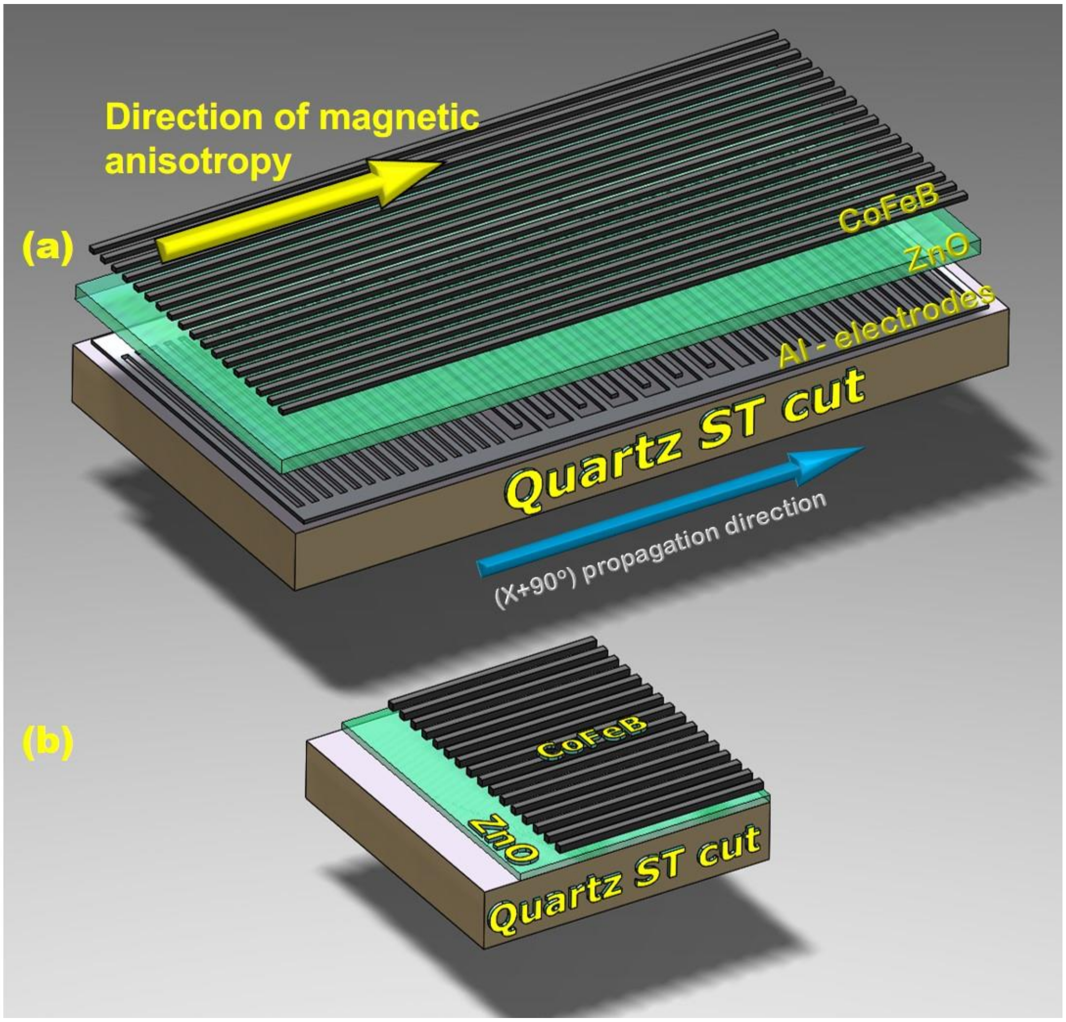

Figure 5.2: Schematic illustration of the structure of the fabricated device. (a) Final device with propagation along (X+90°) direction and (b) sample for magnetometry analysis.

Subsequently, the UV lithography step was repeated and using a specially developed mask (Mark VII - Excalibur) the resist pattern for the CoFeB finger structure on top of the ZnO layers was obtained. The CoFeB fingers were designed as multiple rows of 1.5µm × 500µm bars covering an area of 3120µm × 710µm, on top of the ZnO layer with a gap of 1µm between each finger. Thus, 100nm of CoFeB was then deposited by DC sputtering of a 2-inch target at 300W and 5×10^{-3} mbar Ar. Finally, the lift-off procedure is completed by the remover solution and a final cleansing in acetone and isopropyl alcohol.

A schematic of the fabricated devices is shown in *Figure 5.2*. As in all the previous studies, for this study also, we have fabricated a special set of samples for magnetometry analysis (*refer Figure 5.2 (b)*). Further, keeping in mind the minimum dimensions of the sample required for VSM experiments, the samples for the tests were pre-designed to be 4mm × 4mm and were thus removed from the substrate by simple wire cutting.

Topography of fabricated device: At the end of the fabrication process, an *Atomic Force Microscopy (AFM)* measurement was made to determine the actual surface topography of the fabricated device. Every micro-fabrication step is bound by different known and unknown

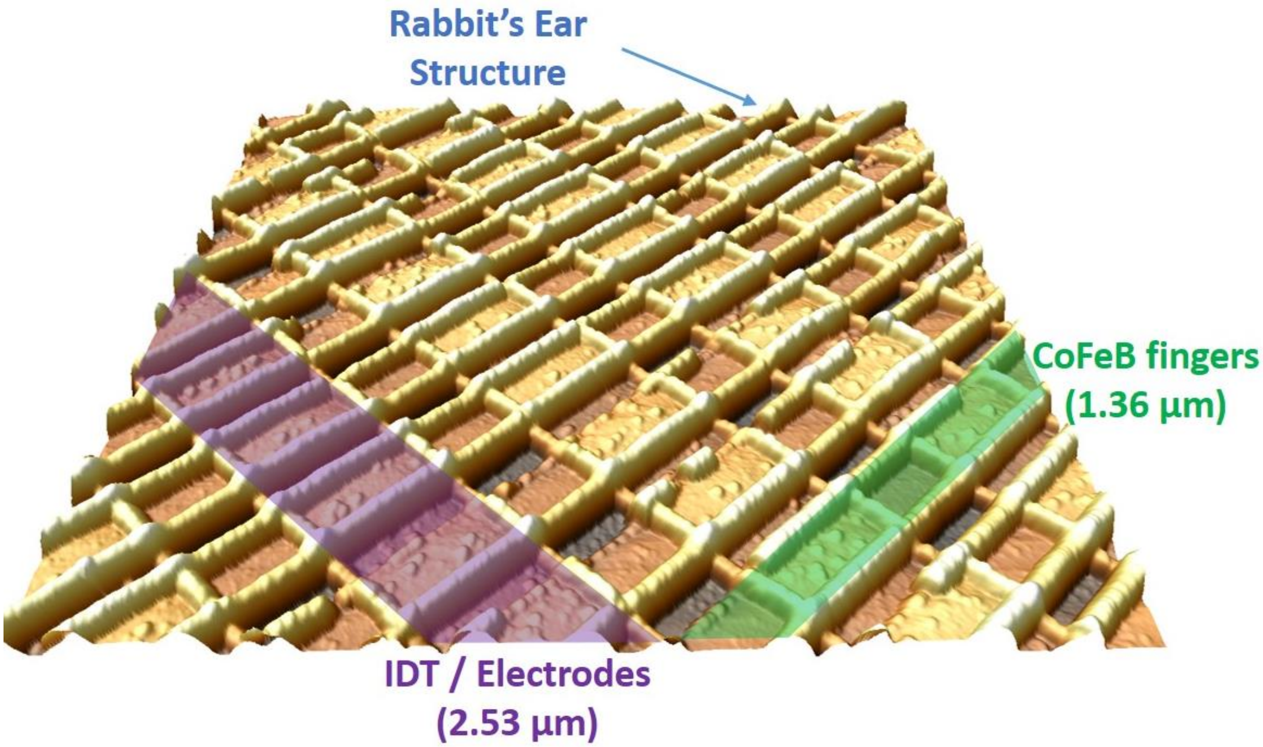

Figure 5.3: Surface topography over a section of device F2 as measured by AFM.

limitations and they tend to affect the geometry of the device accordingly. The steps of fabrication of this set of devices (*F1, F2 and F3*) was indeed the most challenging of all the fabrications described in this thesis. Especially so because of the lithography and lift-off stage to fabricate the CoFeB fingers of such small dimension over an undulating ZnO surface. Thus, in order to have a clear picture, an AFM measurement was done.

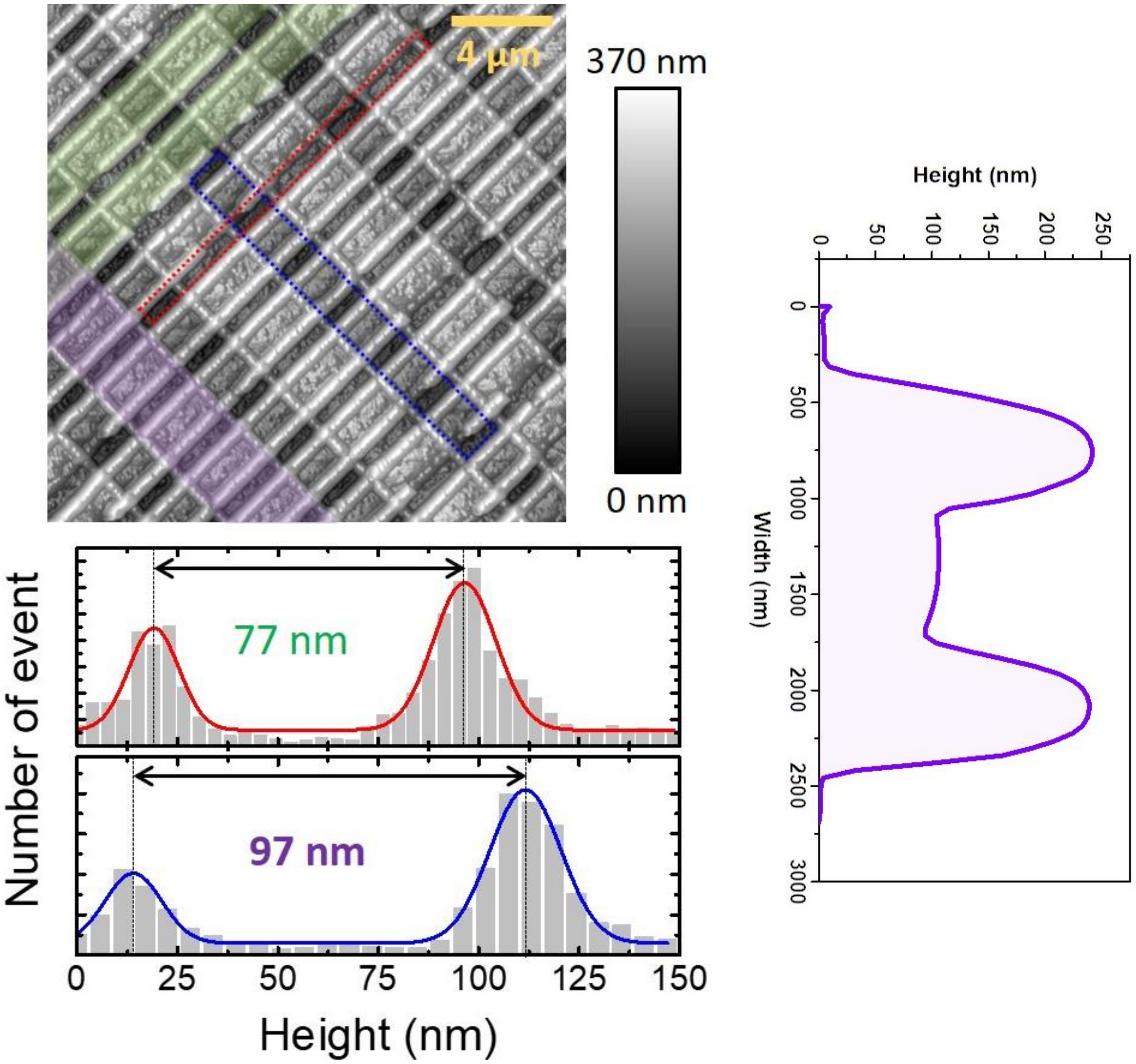

Figure 5.4: Measurements done on the surface of the device F2, using the AFM. The ‘imprint’ of the Aluminium IDTs (100nm thick) on the 400nm ZnO layer is measured at 77nm while the thickness of the CoFeB layer is measured at 97nm. The profile seen on the side shows the ‘Rabbit-Ear’ structure observed on the CoFeB fingers.

Figure 5.3 presents a section of the surface of the device F2. As shown in it, the purple segment shows the electrodes and the green segment shows the CoFeB fingers. Of course, the electrodes and the CoFeB layers are separated by 400nm of the ZnO layer. The first thing that becomes very apparent with the above figure is the *Rabbit's Ear* structure. This is a very peculiar structure that occurs due to the lift-off procedure that we have followed. Theoretically we need to have an overhanging resist structure and thus after the deposition we get rid of any unwanted metal. However, in reality, some of the metal (Al as well as CoFeB), forms a walled structure thus creating this final *Rabbit's Ear* like structure. As can also be seen, this is not a consistent phenomenon and thus we have discontinuous segments in isolated places. This kind of structure is also seen in the CoFeB layer. *Figure 5.4* presents the measurements done on the surface using the AFM and Figure 5.5 presents a schematic to fully comprehend the topography. As can be very clearly seen, there is a huge imprint of the electrodes even at the top surface of 400nm of ZnO. As mentioned earlier the electrodes are fabricated from 100 nm of Aluminium. However, in-spite of the deposition of 400 nm of ZnO over the electrodes, an imprint of 77 nm was very clearly measured. This gives a qualitative idea about how undulating the surface of the ZnO is. Further we had also mentioned that 100 nm of CoFeB was deposited to form the micro-structured magneto-sensitive layer and this has been measured at 97nm.

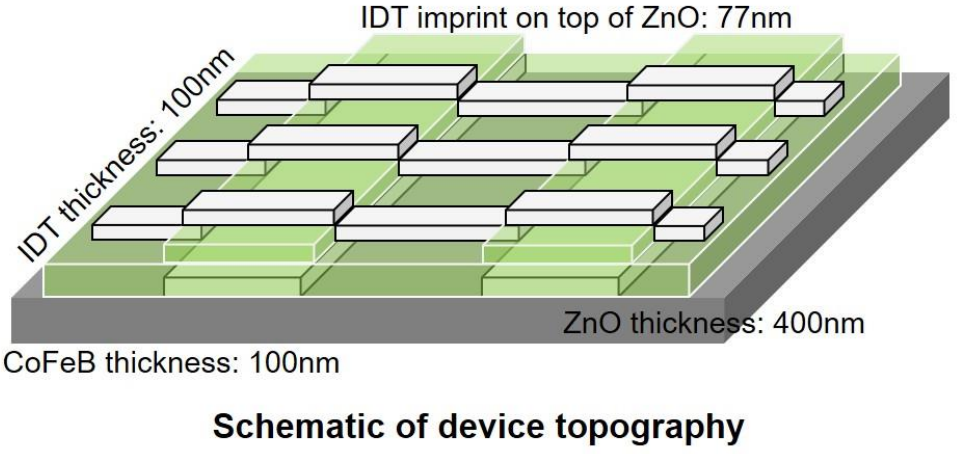

Figure 5.5: A schematic of the device topography to highlight the undulating surface of the device.

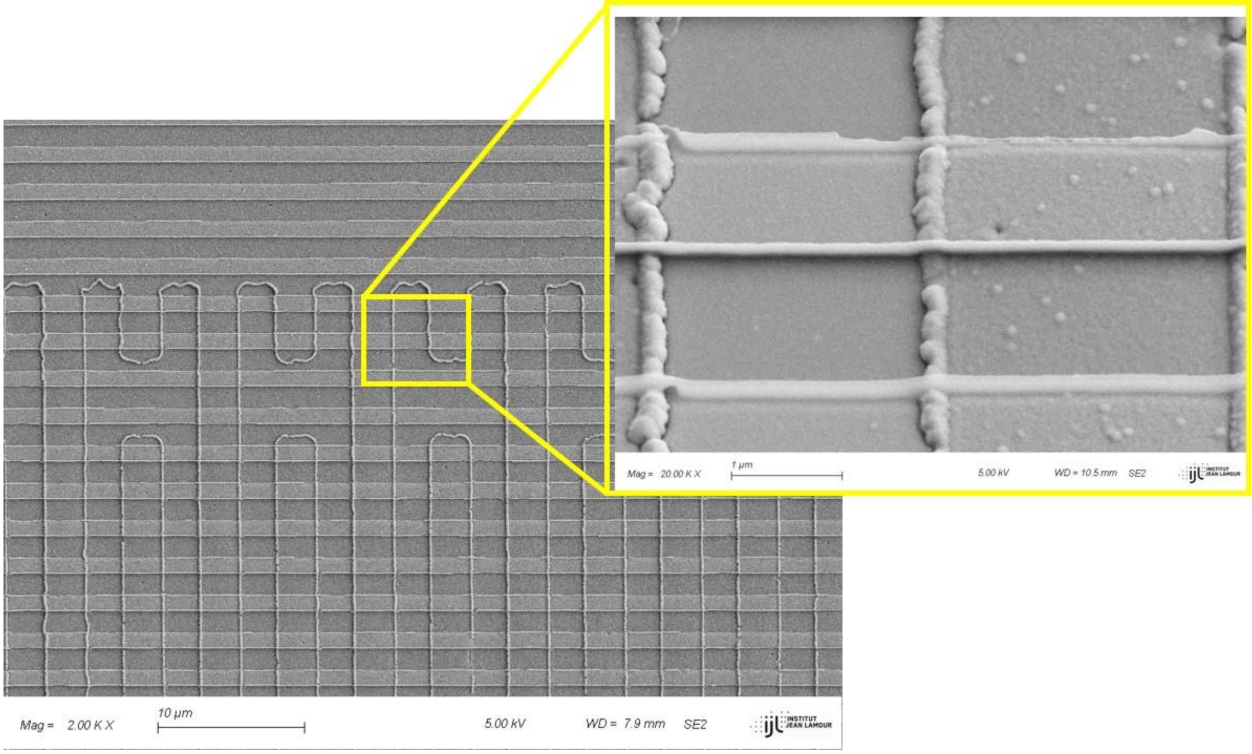

Figure 5.6: Scanning Electron Microscopy (SEM) based imaging of the topography.

A Scanning Electron Microscopy (SEM) based imaging (*refer Figure 5.6*) was also conducted to verify the observations and analysis of the AFM measurements. As can be clearly seen from Figure 5.6, the electrodes or IDTs are visible as the vertical structures whereas the CoFeB fingers can be observed as the horizontal structures. We can observe the wall-like structures very clearly as remnants of the lit-off based fabrication process. Further we can also observe the undulations arising from the imprint of the electrodes on top of the ZnO layer, although this imprint appears very small in the image.

5.3 Magnetometry measurements:

Magnetisation measurements on multilayer structure – effect of temperature: Before undertaking the exploration of the magnetisation in the micro-structured CoFeB film, it is essential to understand the behaviour of the full film and the limitations associated with this. Further, it is also important to understand the behaviour of the layers at elevated temperatures to unravel the effects of temperature on the magnetic anisotropy.

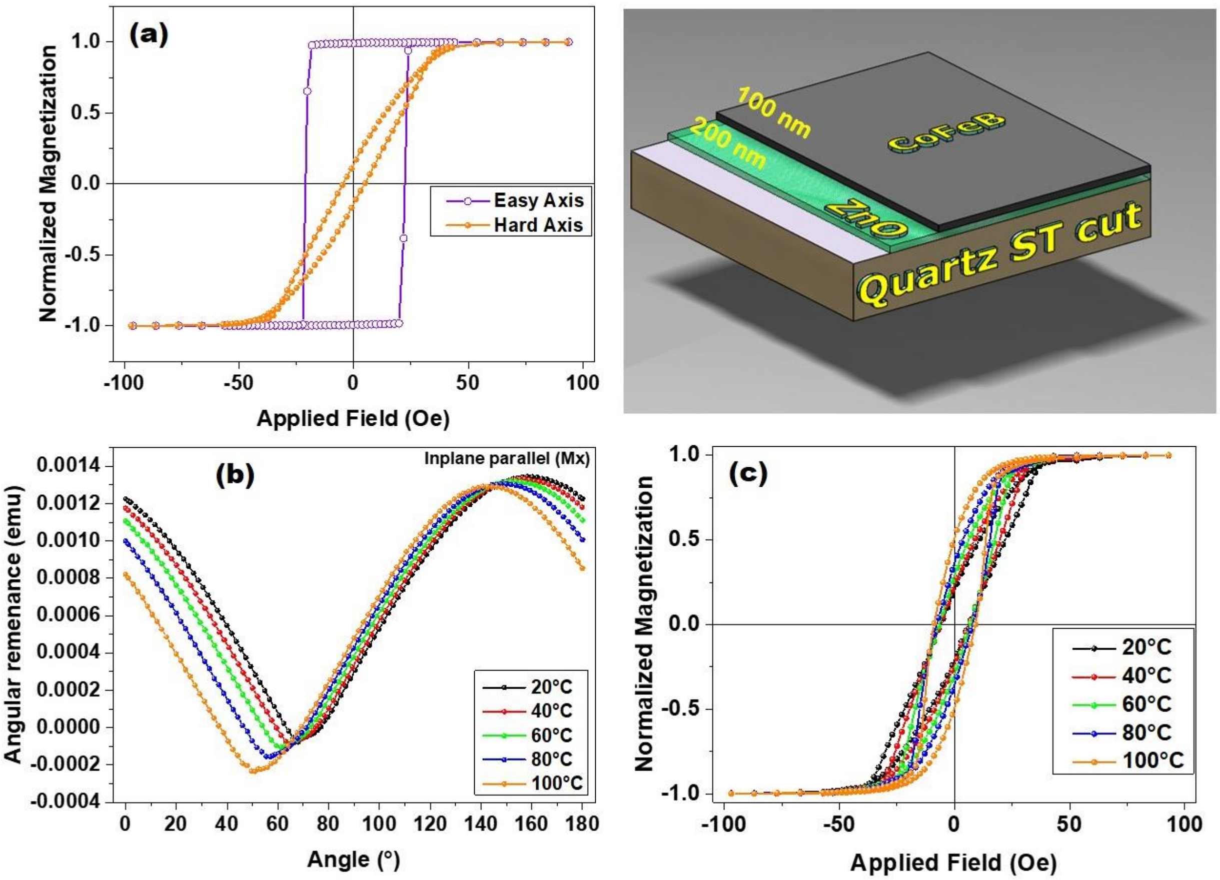

Figure 5.7: Magnetometry measurements done on the layered structure (CoFeB/ZnO/Quartz). (a) A clear distinction between the easy and hard axis is observed in the structure at room temperature. (b) The angular remanence is measured at different temperatures. (c) The hard axis magnetisation for the structure is measured at different temperatures.

In *Figure 5.7 (a)* we present the magnetisation observed at room temperature on a 100nm full film of CoFeB deposited over 200nm of ZnO on a quartz substrate. We observed a clear distinction between the easy and hard magnetisation axis. *Figure 5.7 (b),* shows the measurement of angular remanence at different temperatures from 20^{o}C to 100^{o}C. As can be seen clearly, an instability is observed with an increase of the temperature. This is reiterated by the measurement of the magnetisation along the hard axis at different temperatures, as presented in *Figure 5.7 (c)*.

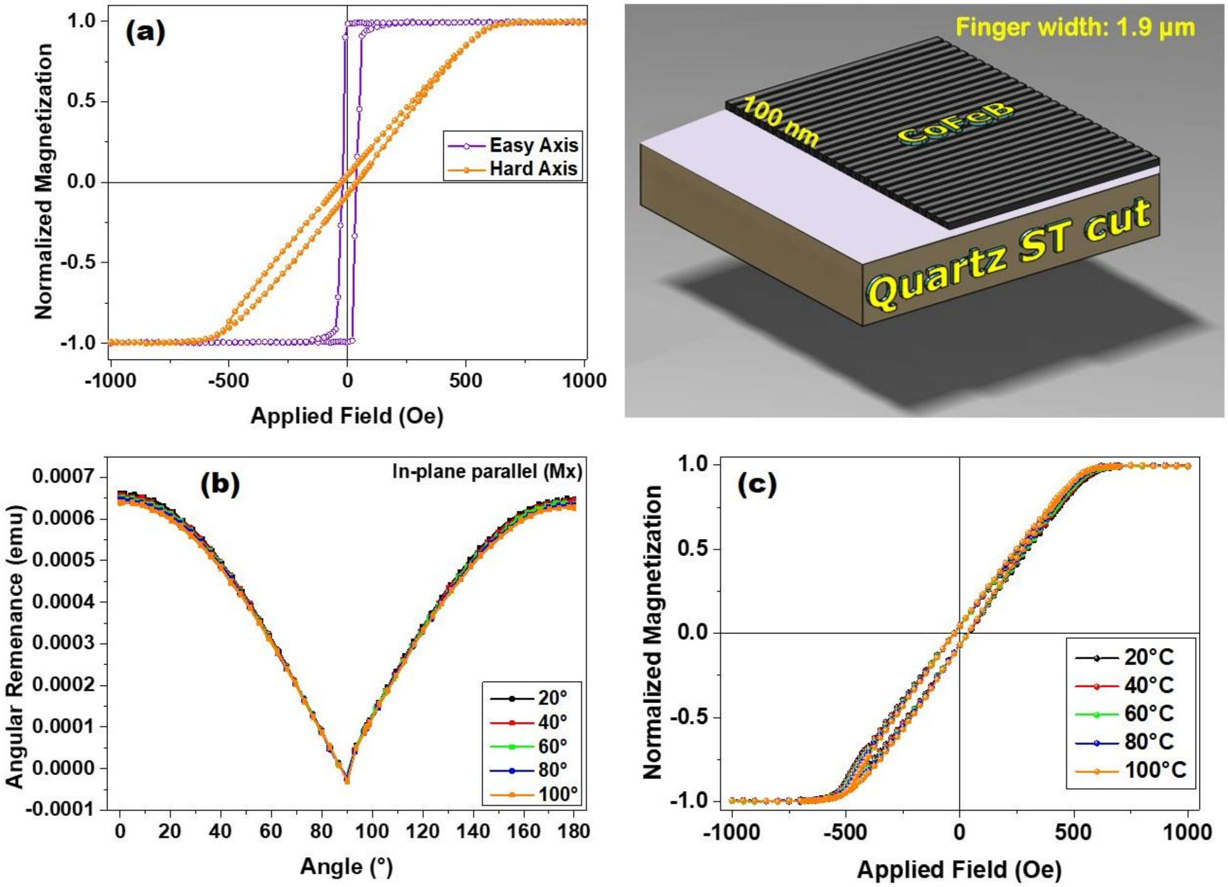

Figure 5.8: Magnetometry measurements done on the micro-structured CoFeB structure developed on Quartz. (a) A clear distinction between the easy and hard axis is observed in the structure at room temperature. (b) The angular remanence is measured at different temperatures. (c) The hard axis magnetisation for the structure is measured at different temperatures.

Subsequently, in order to understand the magnetisation behaviour of a micro-structured magnetostrictive layer, we developed samples with such finger like structures as shown in *Figure 5.8 (top right)* developed directly on a quartz substrate. The width of the fingers was measured at 1.9 µm after fabrication. *Figure 5.8 (a)* depicts the measurements along the easy and hard magnetisation direction. As expected on the basis of the effects of shape anisotropy, a clear observation of the easy axis is made along the length of the fingers. The hard magnetisation axis lies perpendicular to the length of the fingers. Measurements of the angular remanence (*refer Figure 5.8 (b)*) at different temperatures show that micro-structuration enables us to obtain a very stable magnetic behaviour even up to temperatures of 100^{o}C. The measurements of the hard axis magnetisation at different temperatures (*refer Figure 5.8 (c)*) also indicates a stable behaviour.

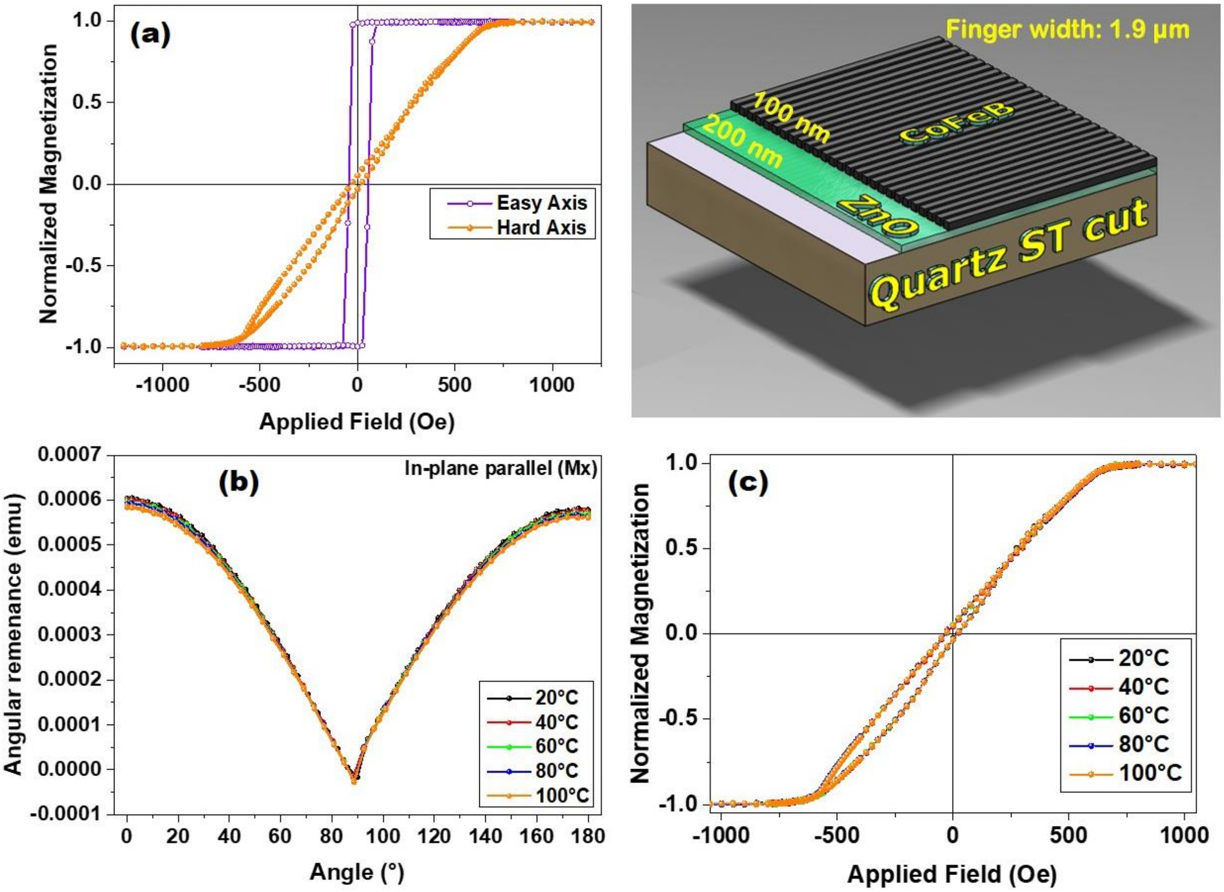

Figure 5.9: Magnetometry measurements done on the micro-structured CoFeB fingers of 1.9µm width, developed on ZnO and Quartz. (a) A clear distinction between the easy and hard axis is observed in the structure at room temperature. (b) The angular remanence is measured at different temperatures. (c) The hard axis magnetisation for the structure is measured at different temperatures.

Further, in order to investigate the role of the ZnO layer, we explored a new configuration in which the micro-structured CoFeB layer was over the ZnO layer (both developed over a quartz substrate). For this test also, we considered a finger width of 1.9 µm. *Figure 5.9 (a)* presents the magnetisation measurements along the easy and hard axis. As discussed previously, the effects of shape anisotropy indeed play a dominating role and thereby ensure that the easy magnetisation axis lies along the length of the CoFeB fingers. *Figure 5.9 (b)* further reiterates the thermal stability of the structure. *Figure 5.9 (c)* shows the hard axis magnetisation observed in the structure at different temperatures. Now, although it is clear that the shape anisotropy does ensure a thermal stability of the magnetisation, we still do observe a small hysteretic behaviour as observed in the third quadrant of the magnetisation measurements in *Figure 5.8 and 5.9*. Therefore, we decided to further decrease the width of the fingers and observe its effects.

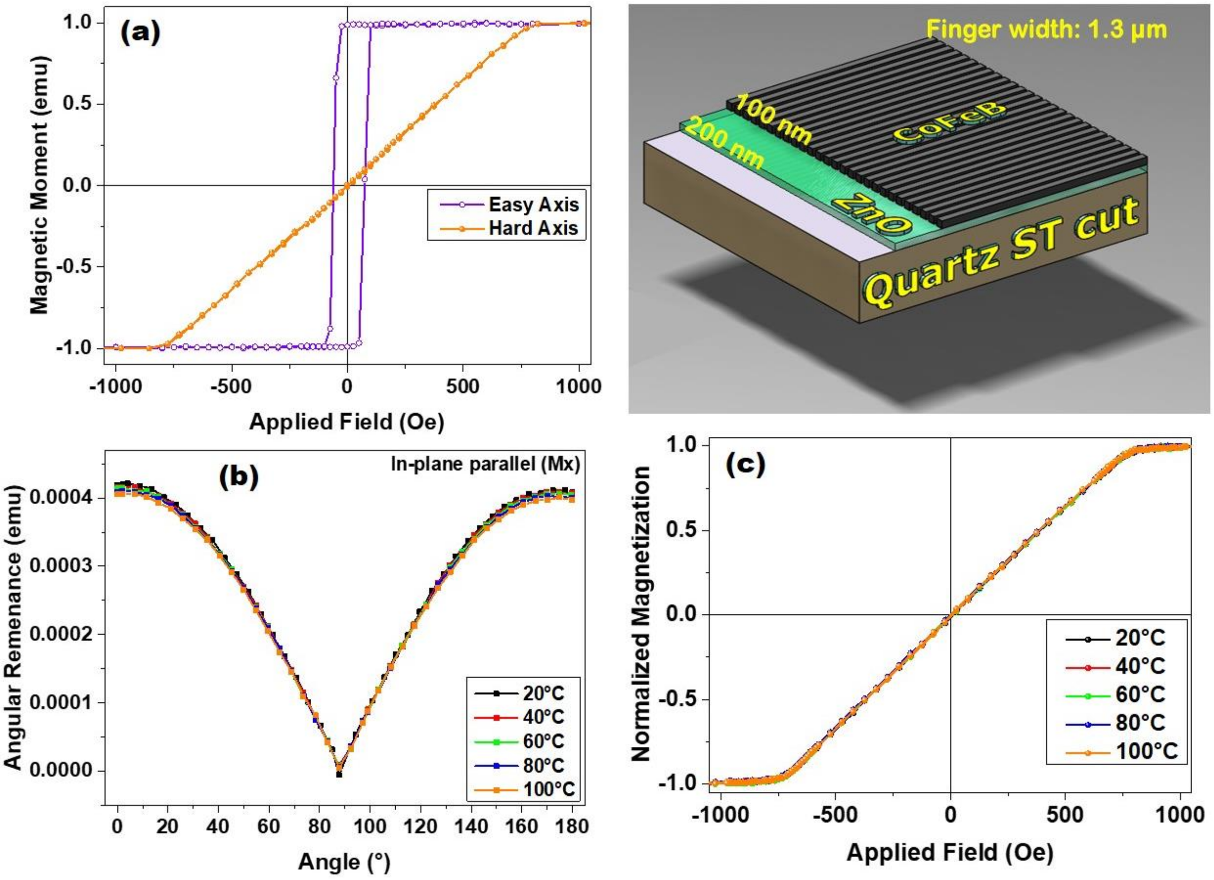

Figure 5.10: Magnetometry measurements done on the micro-structured CoFeB fingers of 1.3µm width developed on ZnO and Quartz. (a) A clear distinction between the easy and hard axis is observed in the structure at room temperature. (b) The angular remanence is measured at different temperatures. (c) The hard axis magnetisation for the structure is measured at different temperatures.

Finally, we fabricated samples with a layer of micro-structured CoFeB fingers with a width of 1.3µm, developed over 200nm of ZnO on a quartz substrate. The effects of the shape anisotropy were observed to be very effective in these structures. *Figure 5.10 (a)* shows the measurements of the magnetisation along the easy and hard magnetisation axes. The measurements of the angular remanence (*Figure 5.10 (b)*) also indicate a perfectly stable structure. As can be seen clearly, the hard axis of the magnetisation remains oriented along the 90° direction (in-plane perpendicular to the length of the fingers). Finally, measurements of the hard axis magnetisation (*Figure 5.10 (c)*) also reiterates the thermal stability. It may also be noted here that a decrease of only 600nm in the width of the fingers (1.9 µm, Figure 5.9 (a) vs 1.3 µm, Figure 5.10 (a)) provides a hysteresis free magnetisation behaviour, thus reiterating the importance of shape induced control of the magnetisation.

Thus, by introducing the effects of the shape anisotropy to control the magnetisation in the magnetostrictive layer, we have successfully addressed and found a way to solve the temperature instability of the magnetic anisotropy. Combined with the multi-layered device geometry, this crucial factor will now enable us to develop devices which are truly compensated for the effects of temperature.

5.4 RF Characterization and TCF measurements:

Basic characterizations on the blank device such as determining the resonance frequencies (by the S_{11} reflection parameters) and measurement of their TCFs had been previously discussed in *Chapter 4, section 4.4*. Also, we had discussed in detail the nature of the resonances observed wherein we had studied through simulations the local displacements pertaining to each resonance frequency (*Figure 4.7*). Thus, in the present study, we continue our discussion of the resonances observed in this new device geometry (micro-structured CoFeB), based on the findings of *Chapter 4*.

Presented in *Figure 5.11* are the S_{11} return loss spectrums for the devices F1, F2 and F3, before and after the deposition of the CoFeB micro-structured layer. *Figure 5.11 (a), (c) and (e)* show the S_{11} measured for the devices before the addition of the CoFeB layer with 200nm, 400nm and 600nm of ZnO (devices F1, F2 and F3 respectively). It has been previously shown that both the dips or resonances peaks observed in the S_{11} of the devices pertain to a *Shear Horizontal* deformation and thus form the *Love wave*. Measurements of the TCF of the individual peaks are also made and the values are depicted in the respective figures. A clear variation of the TCF can be observed with changing thicknesses of the ZnO layer wherein, 200nm shows the most positive values and 600nm the most negative.

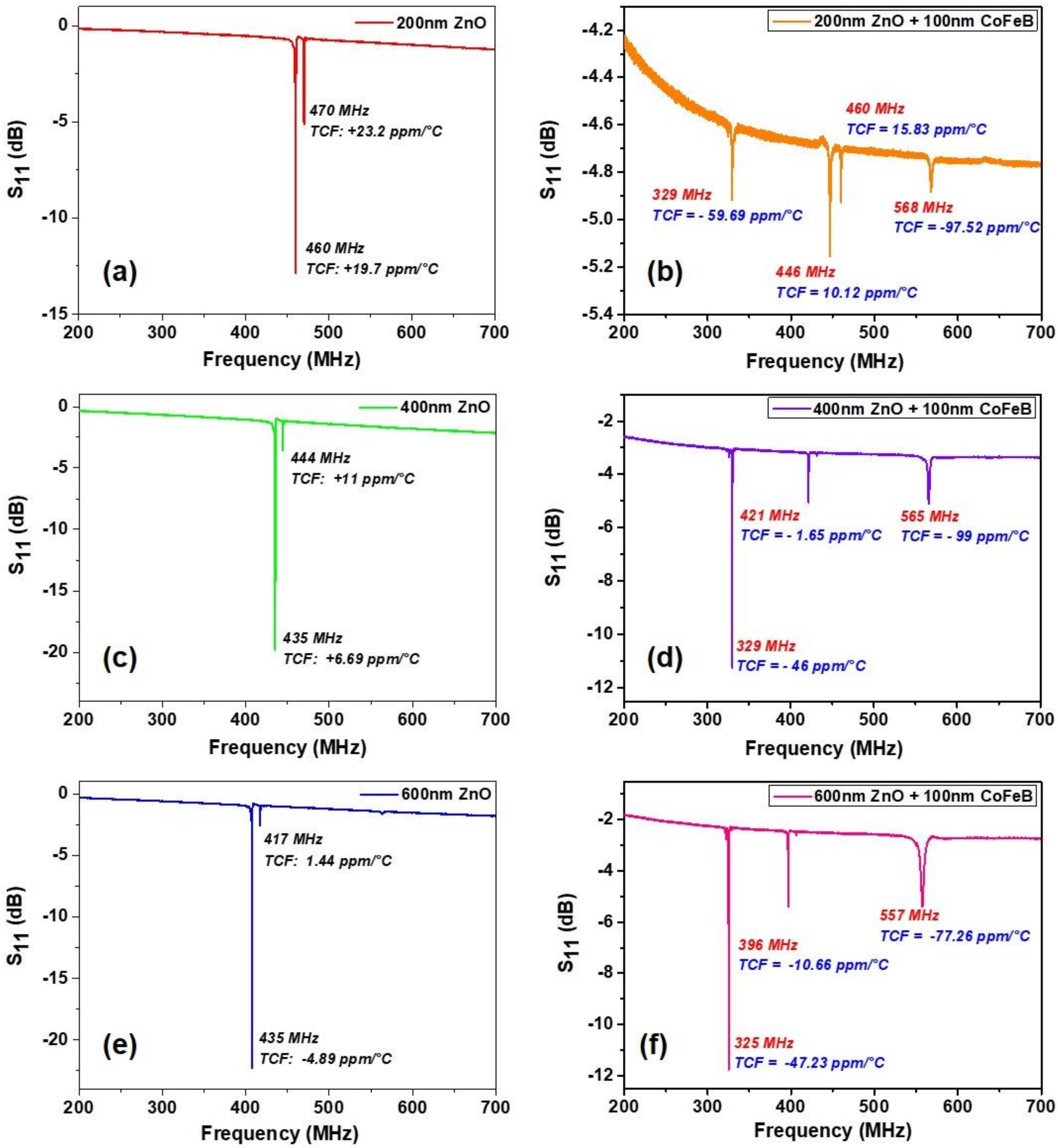

Figure 5.11: Scattering parameter (S_{11}) measured on samples F1, F2 and F3 before (a, c and e) and after (b, d and f) deposition of the CoFeB layer.

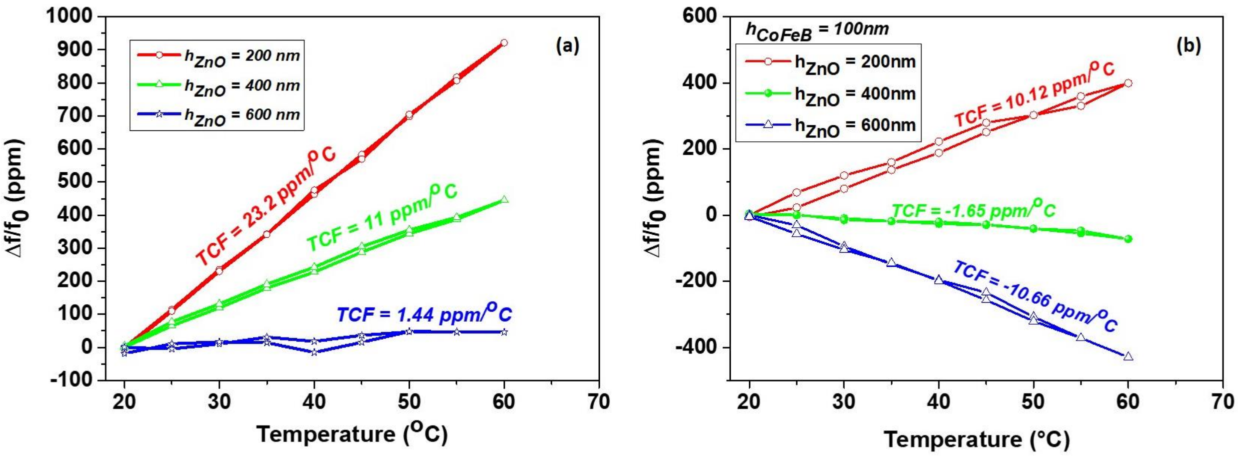

Figure 5.12: TCF measured on the Love wave resonance mode in the devices F1, F2 and F3: (a) before the deposition of CoFeB and (b) after the deposition and micro-structuration of 100nm of CoFeB.

Subsequently, the 100nm of micro-structured CoFeB layer is added onto the devices and their return loss spectrums are measured. *Figure 5.11 (b), (d) and (f)* present the measured S_{11} for devices F1, F2 and F3 respectively after the addition of the CoFeB. Again, based on our previous studies shown in *Chapter 4*, it can very well be assumed that the first resonance peak observed in all the three devices concerns a *Rayleigh wave*. This is also established by the measurements of the variation of the concerned frequency with respect to a magnetic field of changing intensity and direction, as presented in later sections of this chapter. It may be noted that two resonances appear close by in the device with 200nm of ZnO as seen in *Figure 5.11 (b)*. Both of these peaks correspond to a *Love Wave* that we had seen in the devices before the CoFeB deposition and in the earlier chapter as well. These peaks also appear in subsequent thicknesses of the ZnO (400nm and 600nm) but as we can see from *Figure 5.11 (d) and (f)*, the second dip is rather small. Nevertheless, a *near zero-TCF Love wave* resonance is observed with a ZnO thickness of 400nm and at a frequency of 412 MHz. The final peak that is observed pertains to a *Bulk-Acoustic* wave (*557, 565 & 568 MHz*). Thus if we now observe the resonances in the device F2 with 400nm of ZnO and 100nm of patterned CoFeB in *Figure 5.11 (d)*, we find three primary peaks: the first a *Rayleigh wave* which has a TCF of *– 46 ppm/^{o}C* and is also expected to be sensitive to a magnetic field, the second is a *Love wave* which has a TCF value measured at *– 1.65 ppm/^{o}C* and is also expected to be sensitive to a magnetic field and finally a *Bulk-Acoustic* wave with a TCF value of *– 99 ppm/^{o}C* that is not sensitive to a magnetic field (the displacement itself that is caused by this wave remains confined to the substrate and thus does not really interrogate or is affected by the magnetostrictive layer).

Figure 5.12 summarizes the variation of the Love wave resonance mode with temperature, observed in the different devices. As can be seen clearly, the CoFeB also causes a decrease of the TCF value and thus complements the effect of the ZnO layer thereby effectively reducing the amount of ZnO needed for obtaining a zero TCF structure. We can also notice here that using CoFeB fingers instead of full film leads to an increase of the ZnO thickness required to obtain a zero TCF and thus limits current effect leakage observed in the device with only 200 nm of ZnO.

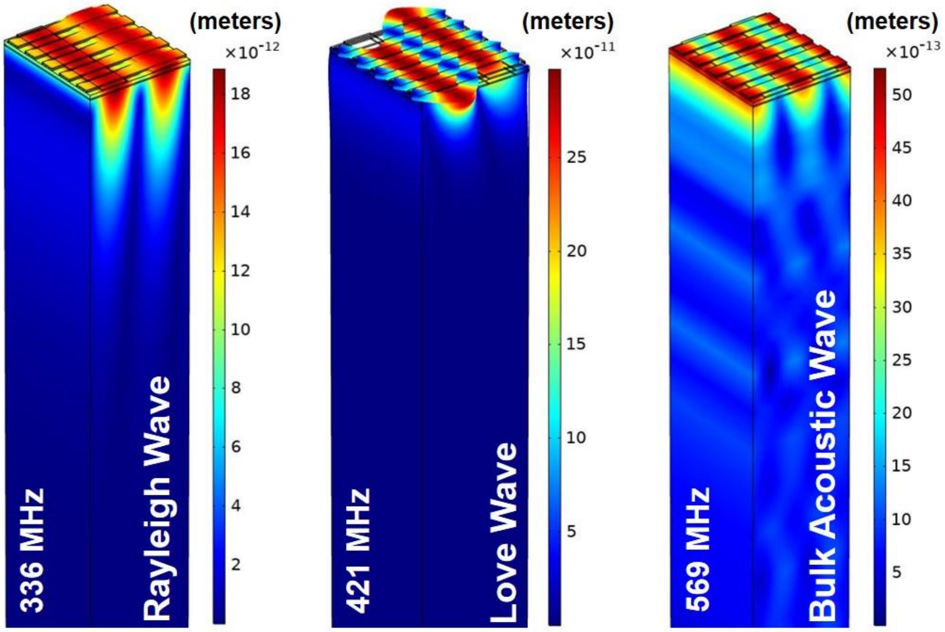

Figure 5.13: Deformations associated with each resonance frequency as observed through simulations on a 3D model composed of ST-cut Quartz as the substrate, 100nm Aluminium electrodes, 400nm of ZnO, and 100nm thick CoFeB fingers aligned perpendicular to the electrodes.

Although our studies from Chapter 4 enable us to correctly identify the resonances observed in our devices, we have nevertheless conducted a set of qualitative simulations on COMSOL to verify the nature of each resonance observed. The geometry if this structure was the same step-like structure as shown in *Figure 5.5* before. This was done also as a step to identify any spurious resonances coming from reflections due to the metallic gratings of CoFeB. As can be clearly seen from *Figure 5.13,* the first resonance corresponds to a *Rayleigh wave* and the second with its distinct *Shear-Horizontal* deformation, is indeed a *Love wave* resonance. Additionally however, we also observe a third resonance peak that can be clearly identified as a *Bulk Acoustic wave*. The smaller peak adjacent to the Love wave resonance is not observed during simulations indicting that it may origin from reflections of the elastic wave within the device.

5.5 MSAW Measurements:

In this section, we study the variations of the resonance frequencies observed with respect to the intensity and direction of an external magnetic field. As previously seen, the magnetic anisotropy in the device is, very specifically, along the length of the CoFeB fingers. Thus, the easy and hard magnetic directions are respectively defined as the directions along (parallel to) and perpendicular to these fingers. In the previous section of the chapter, we optimized the thickness of the layers to get a zero-TCF structure on the device F2 with 400nm of ZnO and 100nm of CoFeB. Thus, in this section we consider the device F2 and make the MSAW measurements for the resonance frequencies observed. The MSAW measurements were made using the LakeShore cryogenic probe station (EMPX-HF) connected to a VNA (Rohde and Schwartz ZVA67) by a K-cable and GGB Picoprobes (40 GHz) as described in *Chapter 3*.

The first measurement of the magneto-acoustic response is made on the temperature compensated *Love* wave observed at *421 MHz*. Primarily it is the response of the peak along two configurations that hold importance; when the field is applied along the easy axis direction and when it is applied along the hard axis direction. For reasons described previously, the hard axis response is much stronger than the easy axis. This is also exemplified in the present case by the MSAW responses along the hard and easy direction (*refer Figure 5.14*). An important aspect to note here is also the relative absence of a hysteretic behaviour. This is achieved because of the exceptional control over the magnetic properties of the CoFeB layer through micro-structuration.

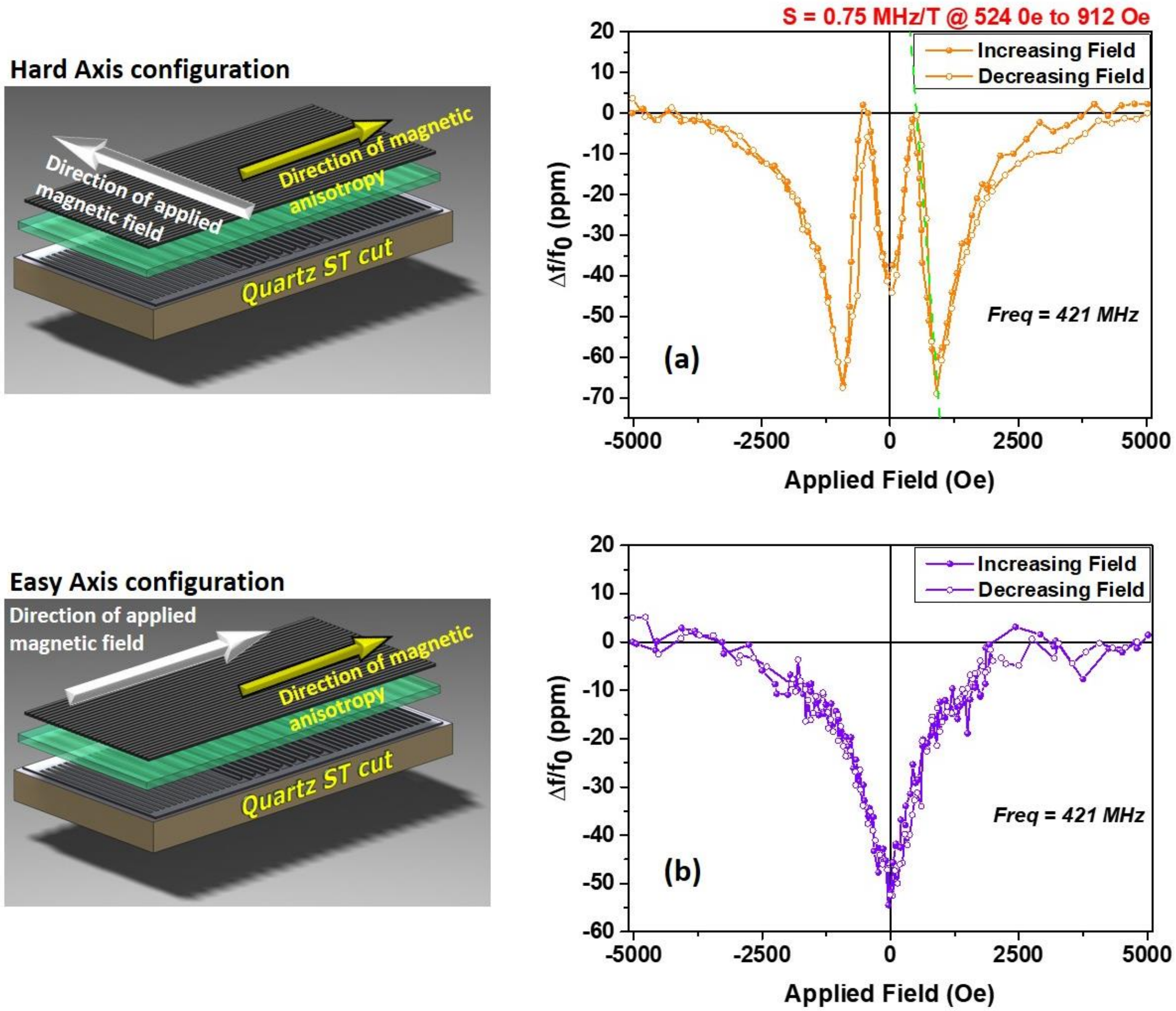

Figure 5.14: MSAW measurements on the temperature compensated Love wave peak in the device F2 (h_{ZnO} = 400nm; h_{CoFeB} = 100nm) (resonance peak at 421 MHz). The field is applied (a) along the hard axis i.e. perpendicular to the length of the CoFeB fingers and (b) along the easy axis i.e. parallel to the length of the CoFeB fingers. The corresponding orientations are sketched beside the MSAW measurements. The sensitivity of 0.75 MHz/T is measured between 524 Oe and 912 Oe for the hard axis configuration shown in (a) and the linearity is highlighted by the green dotted line.

Although we had seen previously that a hysteretic behaviour can be utilised effectively to achieve a sensitivity along a desired span of magnetic field, it is not exactly our aim in this study. Here, we have managed to circumvent a hysteretic behaviour and have achieved a sensitivity of approximately *0.75 MHz/T* in the range from *524 Oe to 912 Oe (refer Figure 5.14 (a))*. The response in this range assumes a quasi-linear behaviour too.

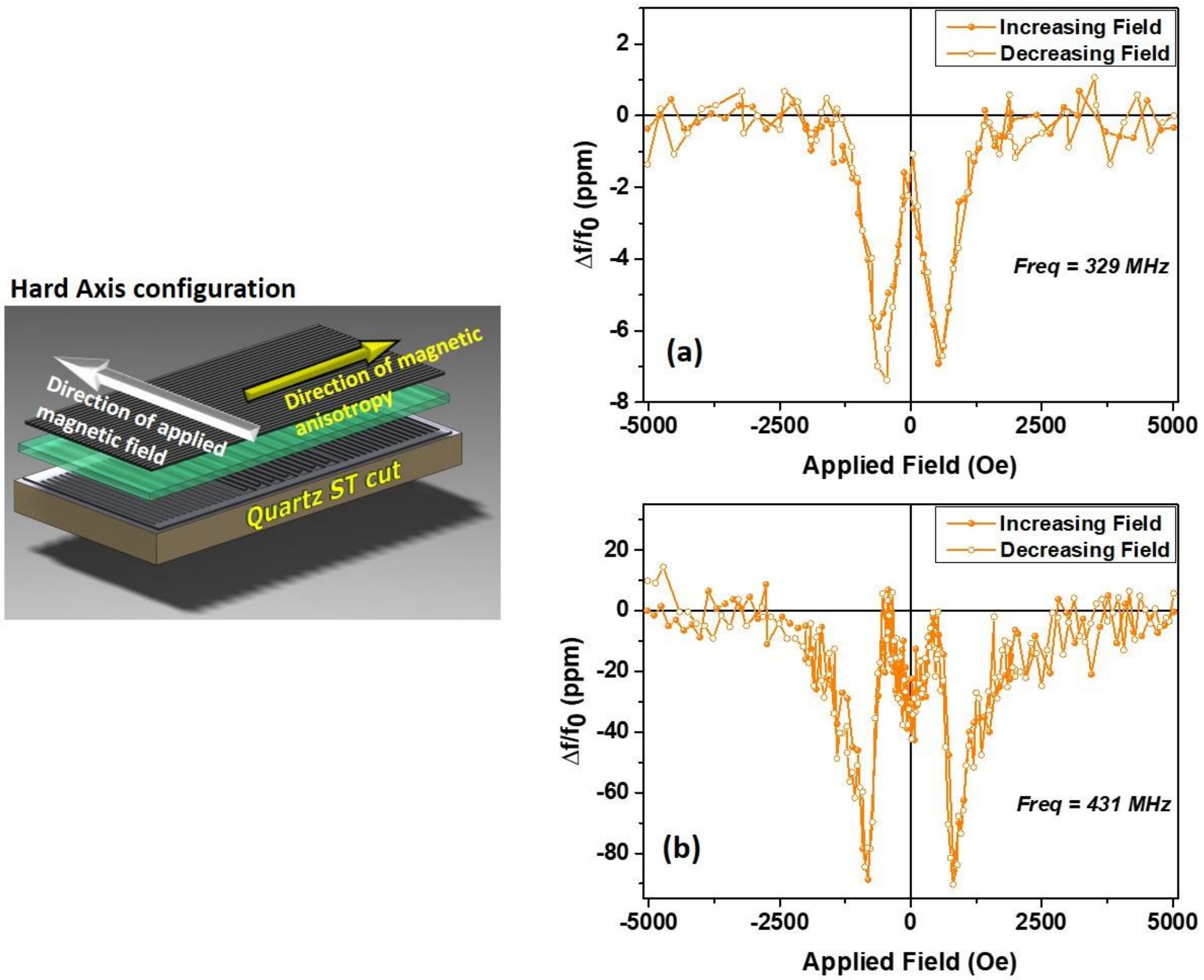

Figure 5.15: MSAW response measured along the hard axis (perpendicular to the CoFeB fingers) on (a) the non-temperature compensated *Rayleigh* wave peak (*329 MHz*) and (b) the complex peak (*431 MHz*) of the device (F2).

In order to complete the characterization of the particular device, we also made MSAW measurements along the hard axis configuration in the *Rayleigh* wave as well as the second *Love* wave peak. *Figure 5.15 (a)* presents the response of the Rayleigh wave peak and unsurprisingly, it may be clearly observed that the response is pretty weak compared to that of the *Love* waves. However, it is interesting to note that, although noisy, the response does indeed maintain a typical ‘*W-shaped’ Rayleigh* wave response pattern. Further it is also interesting to note the high response

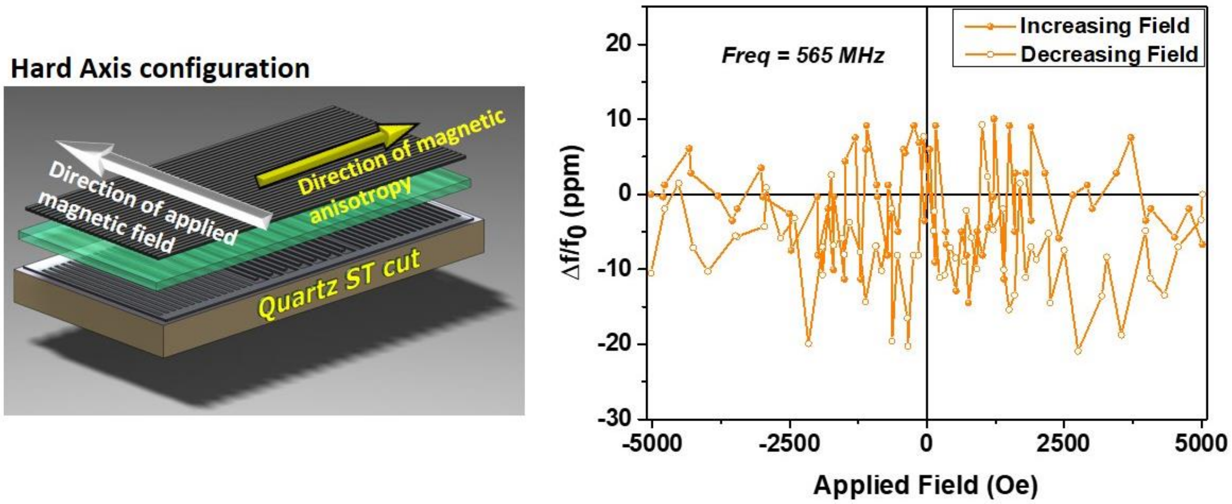

Figure 5.16: MSAW response measured along the hard axis for the *Bulk Acoustic* wave observed in device F2 at a frequency of 565 MHz.

of the complex peak (*Figure 5.15 (b)*) despite the fact that the 'dip' in the S_{11} for this peak is much smaller than the *Love* wave (*Figure 5.11 (d)*). Finally, the response of the *Bulk-Acoustic* wave is presented in Figure 5.16. As can be seen and as per expectations, the resonance only presents a feeble response and even that can be observed to be dominated by noise.

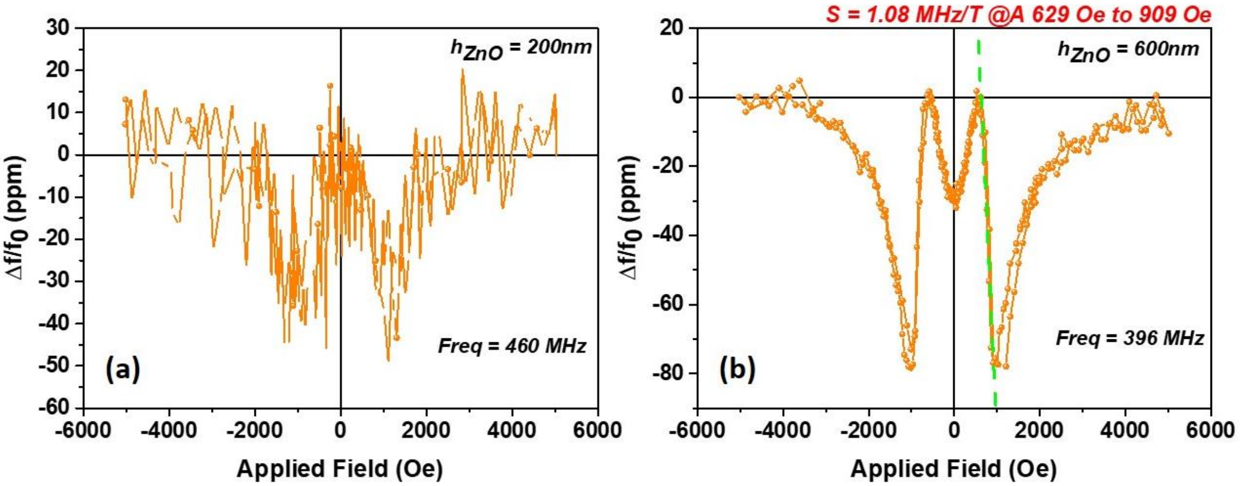

Figure 5.17: MSAW response measured along the hard axis for the *Love* wave resonance observed in devices (a) F1 (h_{ZnO} = 200nm) and (b) F3 (h_{ZnO} = 600nm).

Although the devices F1 and F3 with non-optimal thicknesses of ZnO present a non-zero TCF, it is nevertheless interesting to know their magneto-acoustic response. Figure 5.17 presents the MSAW responses measured for the Love wave mode on the devices F1 (a) and F3 (b) i.e. on the devices with ZnO thicknesses of 200nm and 600nm respectively. As observed, the response of the device with 200nm of ZnO presents a response that is highly overrun by noise. This noise can be an effect of not only the low ZnO thickness causing electrical anomalies but could also originate from a different or non-optimal device topology. These conclusions are further reiterated when we observe the response of the device with 600nm of ZnO. As can be clearly seen, the noises are highly reduced, and a very clear sensitivity of *1.08 MHz/T* is observed between 629 Oe and 909 Oe. Thus, even though these devices are not the best suited for our application to obtain a zero-TCF structure, they do provide us with valuable feedback for future developments.

Effect of temperature on the magneto-acoustic response of the Love wave:

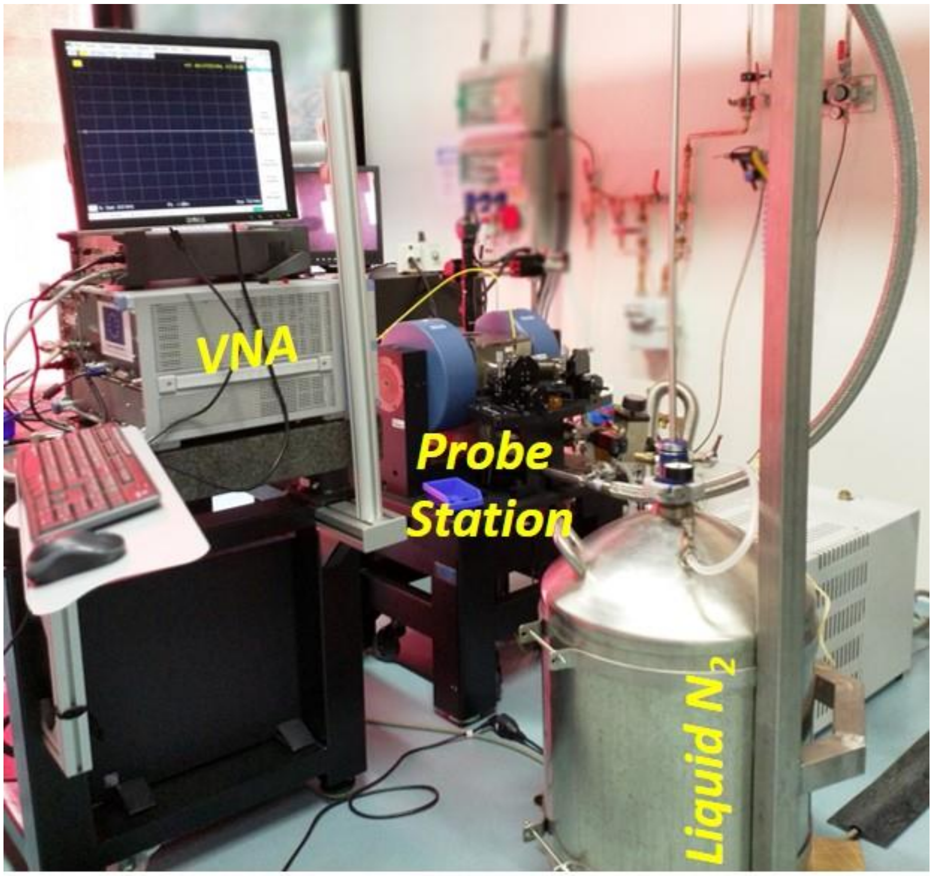

Figure 5.18: Experimental set up used for MSAW measurements at different temperatures.

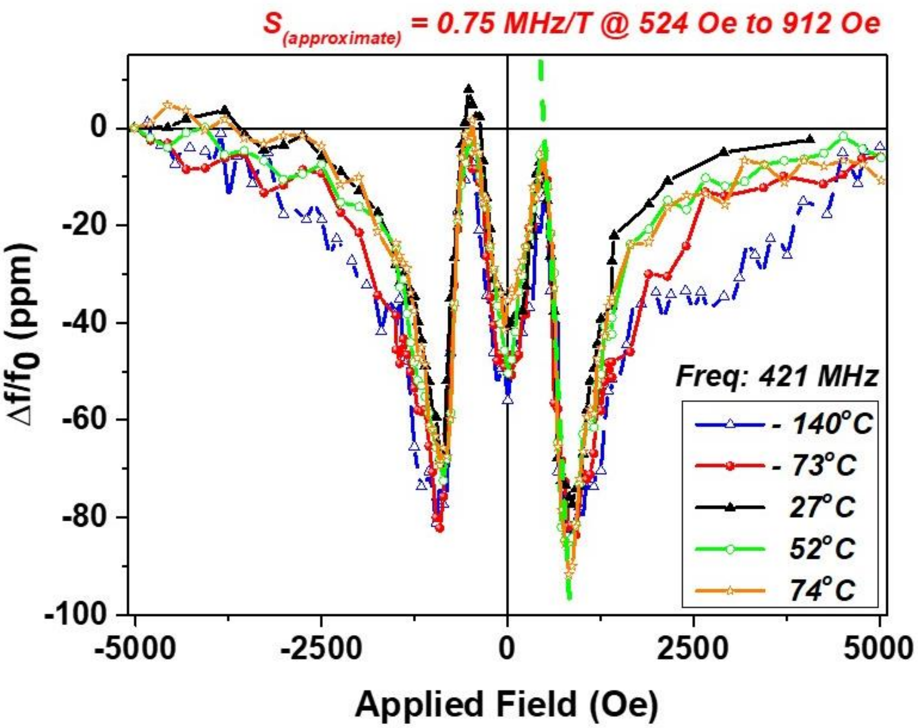

Figure 5.19: MSAW response measured for an increasing magnetic field applied along the hard axis for the Love wave resonance in device F2.

Finally, in order to test the performance of the compensated device F2, we carried out measurement of the magneto-acoustic response at different temperatures. The probe station set up that was described earlier (*Chapter 3*) was modified to accommodate the temperature measurements. Liquid N_2 (LN_2) was used to cool down the entire system (along with water to cool the magnets) to around 80K after which the temperature was raised to the required testing value (refer Figure 5.18). This was a very crucial step as it allowed a stability to the system without damaging the probes.

Considering the technical challenges associated with this experiment, it was considered to test only the Love wave resonance frequency in device F2 and only along a field applied along the hard magnetic axis (since it gives the maximum response). Figure 5.19 presents the measurements of the magneto-acoustic response of the device when the field is increased from -5000 Oe to +5000 Oe. As can be clearly seen, the responses appear quite stable and despite a temperature variation of almost 200^o, the resonance frequency without any magnetic field barely shifted from 421 MHz. It needs to be noted here that although we had measured the TCF of this frequency at around -1.65

ppm/^{o}C, it was between 20 ^{o}C and 60^{o}C. There remains a possibility that this value may differ marginally at cryogenic and high temperatures. Additionally, considering that the temperature was maintained manually by optimizing the flow of LN_2, a variation of around 4 degrees was observed even during the measurements. Further, the calibration of the setup was only done at room temperature, whereas in order to optimize the responses, it was essential to have a calibration at each temperature. The effects of all of these shortcomings can be seen as noise and minor differences seen in Figure 5.19.

However, despite all the challenges, we can see that in the linear region that is of importance for device applications (approximately between 500 Oe and 1000 Oe), the MSAW responses of all the devices corroborate with negligible differences and the sensitivity of the device remains consistent. This renders the device a highly stable performance from cryogenic to high temperatures thereby greatly expanding the possible areas of applications.

Conclusions:

In this chapter we addressed a major concern to mitigate the effects of temperature on a SAW device used for magnetic field sensing. First of all, the positive TCF of the quartz based device is compensated by utilizing a multi-layered structure of ZnO and CoFeB. Further, the CoFeB layer was micro-structured in the form of fingers to overcome the effects of temperature on the magnetic anisotropy. The hysteresis free magnetization that we have demonstrated by utilizing the effects of shape anisotropy, represent an ideal macro-spin response that is quite close to the ideal magnetization as proposed by the Stoner-Wohlfarth model. Further, we have also demonstrated that this magnetization is stable and precisely controlled not only at room temperature, but even up to 100^{o}C.

Three major resonances were observed in the device at three different frequencies. The first, a *Rayleigh wave*, sensitive to temperature and mildly sensitive to a magnetic field. The second, *a Love wave*, with a negligible sensitivity to temperature (-1.65 ppm/^{o}C) and a high sensitivity to magnetic field (0.75 MHz/T). While the last peak, a *Bulk Acoustic wave*, is highly sensitive to temperature (-99 ppm/^{o}C) while being negligibly sensitive to magnetic field. Finally, measurements of the magneto-acoustic response at different temperatures validate the capability of our device to operate in temperatures ranging from cryogenic to high temperatures though a temperature range of 200^o ! This has been demonstrated for the first time is SAW devices for magnetic field sensing.

Additionally, in this work, we have demonstrated, also for the first time, the capability to develop the SAW device as a multifunctional sensor capable of detecting magnetic field as well as temperature at the same position and each, independent of the effect of the other. As a result of this work, we have established a new state-of-the-art technology for SAW devices to be multifunctional.

References:

[Kad'11] Kadota M., Ito S., Ito Y., Hada T., and Okaguchi K., *"Magnetic Sensors Based on Surface Acoustic Wave Resonantors", Jpn. J. Appl. Phys.,* 50, 07HD07, 2011.

[Elh'16] M. Elhosni, O. Elmazria, S. Petit-Watelot, L. Bouvot, S. Zhgoon, A. Talbi, M. Hehn, K. Ait-Aissa, S. Hage-Ali, D. Lacour, F. Sarry, O. Boumatar, *"Magnetic field SAW sensors based on magnetostrictive-piezoelectric layered structures: FEM modelling and experimental validation", Sensors and Actuators A Phys.*, 240, 41–49, 2016.

[Yam'80] Yamaguchi M., Hashimoto K. Y., Kogo H., and Naoe M., *"Variable SAW delay line using amorphous TbFe2 film", IEEE Trans. Magn.,* 16, 916, 1980.

[Pol'17] Polewczyk V., Dumesnil K., Lacour D., Moutaouekkil M., Mjahed H., Tiercelin N., Petit Watelot S., Mishra H., Dusch Y., Hage-Ali S., Elmazria O., Montaigne F., Talbi A., Bou Matar O., Hehn M., *"Unipolar and Bipolar High-Magnetic-Field Sensors Based on Surface Acoustic Wave Resonators", Phys. Rev. Appl.*, 8, 024001, 2017.

[Zho'14] Zhou H., Talbi A., Tiercelin N., and Bou Matar O., *"Multilayer magnetostrictive structure based surface acoustic wave devices", Appl. Phys. Lett.*, 104, 114101, 2014.

[Kit'18] Kittmann A., Durdaut P., Zabel S., Reermann J., Schmalz J., Spetzler B., Meyners D., Sun N. X., McCord J., Gerken M., Schmidt G., Höft M., Knöchel R., Faupel F. and Quandt E., *"Wide Band Low Noise Love Wave Magnetic Field Sensor System", Scientific Reports*, 8, 278, 2018.

[Tal'06] Talbi A., Sarry F., Elhakiki M., Le Brizoual L., Elmazria O., Nicolay P., and Alnot P., *"ZnO/quartz structure potentiality for surface acoustic wave pressure sensor", Sensors and Actuators A Phys.*, 128, 78, 2006.

[Liu'14] Liu Y., Wang B., Zhan Q., Tang Z., Yang H., Liu G., Zuo Z., Zhang X., Xie Y., Zhu X., Chen B., Wang J., Li R-W., *"Positive temperature coefficient of magnetic anisotropy in polyvinylidene fluoride (PVDF)-based magnetic composites", Sci. Rep.,* 4, 6615, 2014.

[Blu'01] Blundell S., *"Magnetism in condensed matter", Oxford University Press*, 2001.

[Bar'14] Barnes S. E., Ieda J., and Maekawa S., *"Rashba spin-orbit anisotropy and the electric field control of magnetism", Sci. Rep.*, 4, 04105, 2014.

[Par'03] Parkin S., Jiang X., Kaiser C., Panchula A., Roche K. and Samant M., *"Magnetically engineered spintronic sensors and memory", Proceedings of the IEEE*, 91, 661–680 (2003).

[Lou'09] Lou, J., Liu M., Reed D., Ren Y., Sun N. X., *"Giant electric field tuning of magnetism in novel multiferroic FeGaB/Lead Zinc Niobate-Lead Titanate (PZN-PT) heterostructures."; Adv. Mater.*, 21, 4711–4715, 2009.

[Thi'03] Thiele J-U., Maat S., and Fullerton E.E., *"FeRh/FePt exchange spring films for thermally assisted magnetic recording media", Appl. Phys. Lett.,* 82, 2859–2861, 2003.

[Phu'12] Phuoc N. N., Chai G. and Omg C.K., *"Temperature-dependent dynamic magnetisation of FeCoHf thin films fabricated by oblique deposition", J. Appl. Phys.,* 112, 083925, 2012.

[McD'05] McDaniel, T.W., *"Ultimate limits to thermally assisted magnetic recording", J. Phys.: Condens. Matter.*, 17, R315–R332, 2005.

[Lam'06] Lamy Y., and Viala, B., *"NiMn, IrMn, and NiO exchange coupled CoFe multilayers for microwave applications", IEEE Trans. Magn.,* 42, 3332–3334, 2006.

[Par'13] Parkes D. E., Shelford L. R., Wadley P., Holy V., Wang M., Hindmarch A. T., van del Laan G., Campion R.P., Edmonds K.W., Cavill S.A., and Rushforth A.W., *"Magnetostrictive thin films for microwave spintronics", Sci. Rep.,* 3, 2220, 2013.

[Wei'09] Weiler M., Brandlmaier A., Geprags S., Althammer M., Opel M., Bihler C., Huebl H., Brandt M.S., Gross R. and Goennenwein S.T.B., *"Voltage controlled inversion of magnetic anisotropy in a ferromagnetic thin film at room temperature", New J. Phys.,* 11, 013021, 2009.

[Wan'11] Wang J., Zhao F., Wu W., and Zhao G-M., *"Unusual temperature dependence of the magnetic anisotropy constant in barium ferrite* $BaFe_{12}O_{19}$*", J. Appl. Phys.,* 110, 096107, 2011.

Conclusions & Future Work

The primary aim of this research project was to develop a magnetic field sensor based on surface acoustic wave device. The focus of the research work was to study, design, fabricate and characterize SAW based magnetic sensors, while at the same time addressing concerns raised by temperature related effects on the device performance. While the work presented here focused mostly on experimental studies to understand the physics that governs and controls the operation of the sensor, simulations were also considered to explore certain aspects of the study and complement the experimental results.

In the first part of the thesis we presented a simulation based study in which we investigated the effect of various geometric parameters of the device on its magneto-acoustic response. The study was based on an ideal magnetisation behaviour based on the Stoner-Wohlfarth model.

Subsequently, our study focused on the study and development of magnetic field sensors based on *Lithium Niobate 128° Y-cut* and multi-layered *[*$TbCo_2/FeCo$*]* as the substrate and magnetostrictive material (from which the interdigital transducers were made) respectively. The aim was to consider a resonator geometry where the electrodes were fabricated from the magnetostrictive layer. The highlight of the work was to relate the magnetic behaviour of the magnetostrictive layer to the magneto-acoustic response of the device. In turn it was also investigated and shown that the effects of shape anisotropy played a pivotal role in such a geometry. The effects of shape anisotropy were shown to affect the magnetisation of the device and thus influence their magneto-acoustic response. In the course of this study, a set of simulations were also done to investigate the nature of the acoustic resonances observed and they were shown to correspond closely with those observed experimentally. Previously reported quasi shear vertical or *QSVSAW* type of acoustic resonances were also shown to exist along the X-propagation direction of the substrate by simulation. This study thus paved a way for future engineering of the SAW device to be sensitive in specific regions of magnetic field.

We also observed in this study that given the same device, the *Shear Horizontal* wave presents a stronger magneto-acoustic response than the *Rayleigh* wave. And as for the Rayleigh wave, a part of the sensitivity comes from the magnetic anisotropy of the sensitive layer while the other part from the propagation direction of the elastic wave in the substrate.

As an evaluation of the fabricated device, the most sensitive among them (*with a sensitivity of 2.38 MHz/T*) was considered as a current sensor in a prototype designed to emulate overhead high tension cables. The associated challenges were highlighted during this feasibility study and thus the next steps for the research work was defined. The most important parameter affecting the performance of the device was identified as the variation of temperature, caused naturally in the ambient environment as well as that generated by the flow of current in the cable.

In the next part of the study, we improve the design of the SAW device by considering a multi-layered device structure. The design was optimised to mitigate the effects of temperature causing the resonance frequency to drift. Thus, the temperature coefficient of frequency *(TCF)* of the device, was compensated for by the use of ST-cut Quartz with a positive TCF and a dielectric ZnO layer with a negative TCF to a near-zero TCF of 1.77 ppm/^{o}C. The magnetic sensitivity was obtained by the use of a layer of CoFeB deposited over the ZnO insulating layer. The use of ZnO, also enabled the formation of Love wave resonances with a *Shear-Horizontal* deformation and led to devices with higher sensitivity. Simulations further our understanding of the different resonances observed. The work thus presented a unique way of self-mitigation of the TCF on the device while at the same time providing a strong sensitivity to magnetic field *(15.536 MHz/T)*, thereby emphasizing on the development of a multi-layered structure that allows for a self-compensation of the effects of temperature on the Love wave. The study also highlighted a few important factors that need to be addressed. The metallic CoFeB being close to the electrodes, induces very high losses in the device leading to a drastic loss of the signal strength. There is also the possibility of effects on the impedance of the device. Such losses may therefore be mitigated in future by improving the design of the electrodes in the device and also that of the additional layers. Further, having used a non-micro-structured layer of the CoFeB, we observed a magnetization that is hysteretic. From the point of view of sensors, such a hysteretic response is detrimental and hence needed to be removed. Another interesting engineering aspect that needs to be considered in the sensor system, is the RF link budget, which will help to account for all the different losses and find ways to mitigate them. The power in overhead current carrying cables is regulated by the national agencies, and thus in order to develop a sensor for such cables, there is always a need to optimize the matching in the entire sensor system including with the device itself to minimize any kind of losses. This is achieved through optimizing the design of the device and also by our choice of the materials used.

An important effect of the temperature on magnetic sensors, that had often been neglected, is that on its magnetic properties. The magnetic anisotropy of the magnetostrictive material in the device was observed to change with temperature, thereby affecting its magneto-acoustic response. This renders the device a severe drawback when functioning in thermally unstable environments. Thus, the challenges led us to the next segment of the research work focused on improving the design of the device to compensate for what is known as the *Temperature Coefficient of Magnetic Anisotropy (TCMA)*.

This work constituted incorporating a compensation for both the *TCF* and the *TCMA* in the same device. For this, the multi-layered device structure based on ST-cut Quartz and ZnO was considered while the magnetostrictive CoFeB layer was transformed to a micro-structured layer thus encompassing the effects of shape anisotropy. The control of the magnetisation using shape effects ensured a stable hysteresis free magnetic behaviour even upto 100^{o}C. Further, the presence of additional resonances in the device, which are not compensated for the effects of temperature, were effectively utilised as temperature sensing frequencies. The magnetic sensitivity of the *Love wave* resonance in the device was measured at *0.75 MHz/T (with a near-zero TCF of -1.65 ppm/^{o}C)*, while the temperature sensitivity for the *Bulk acoustic wave* resonance was measured at *-99 ppm/^{o}C*. Thus the device was effectively engineered as a multifunctional sensor able to detect magnetic field and temperature concurrently and yet independent of each other.

The demonstration of the hysteresis free, multifunctional SAW device has been a unique achievement of this research work. This work has advanced the state-of-the-art in the area of SAW sensors to a new level to include a unique multifunctionality in detecting magnetic fields as well as temperature.

Future Extensions of the work

The area of magnetic sensors based on surface acoustic waves is enormous and undergoing a constant phase of development. The work presented in this research work is only but an iota in the sea of possibilities. Thus, it leaves a huge potential for improvements in all the different aspects of the work. Some of the possibilities are listed below:

1. A deeper understanding of the elastic, piezoelectric and magnetostrictive properties of the different layers is necessary to define clearly a structure to simulate the acoustic wave. This is an essential step as the properties in thin film structures grown on top of each other do depend on the microstructural properties and can differ from substrate to substrate.

2. A more complex three-dimensional model needs to be developed that not only takes into account the macroscopic changes in the device, but also the quantum mechanical effects coming from deep within due to the complex interactions between the mechanical, electrical and magnetic energies involved.

3. From an experimental perspective, it would also be extremely interesting to explore the interactions between different acoustic waves (*Rayleigh*, *Shear Horizontal or Shear Vertical*) and magnetic moments with different relative orientations. The study would be extremely beneficial in extending our understandings and also to create an effective numerical model to optimize the device response. X-ray Resonant Magnetic Scattering (XRMS) at different angles along with Magneto-Optic Kerr Effect (MOKE) microscopy would be essential to collect information on the evolution of the magnetism under acoustic propagation with a possible depth resolution. A laser based 3D vibrometer could also be considered as a mapping tool to observe the deformations associated with the acoustic wave.

4. Concerning the substrate, it had been observed that owing to a difference in microstructures, magnetic thin films developed on lithium niobate had different properties than those on quartz. Thus, it would be relevant to study these differences more closely and understand them in detail.

5. In Chapter 3, we had discussed the configuration of the device with the magnetic anisotropy along the (X+90^o) direction and wave propagation directions along X and (X+90^o). Taking the work forward, it would also be interesting to consider the configuration where the magnetic anisotropy is along the X direction.

6. In the resonator type of geometry of the SAW device, we have considered a structure where the entire device is fabricated from the magnetostrictive material, including both the electrodes and the bus bars. This leads to a magnetisation which is potentially different in different parts of the same device. Thus, we propose the consideration of a device in which the electrodes are fabricated from the magnetostrictive material (thus making use of the effects of shape anisotropy) and the bus bars and other necessary electrical appendages from aluminium.

7. Considering the temperature compensated device with the full film of CoFeB as presented in Chapter 4, an interesting study would be to deposit the magnetic layer under a bias field to induce a preferential magnetisation direction. Although the same is observed in the devices studied by us, it is not exactly a controlled behaviour and thus leads to the possibility of a controlled magnetisation along and/or perpendicular to the wave propagation direction.

8. From the simulation based study of chapter 2, we have seen that the sensitivity of the SAW device could be increased by reducing the wavelength of the device. Thus, it would be important to study the feasibility of such a device with an optimized structure to increase the sensitivity. At the same time, it would also be important to explore higher harmonics and explore the possibility to increase the sensitivity. In our study of the Love wave devices we have considered a wavelength of 10µm (430 MHz); providing us a maximum sensitivity in the range of 22 MHz/T. Now, if we were to increase the frequency to around 2.5 GHz, there is an immense possibility to drastically increase the sensitivity even after taking into consideration any possible losses.

9. During the course of the research, we had observed that the magneto-acoustic response of the *Rayleigh wave*, *Shear-Horizontal* wave or even the *Love wave* tends to be symmetric about the Y-axis. This implies that although the particular resonance may have a high sensitivity at a definite range of magnetic field, it has very low sensitivity around the zero or extreme low magnetic field region. Thus, in order to engineer our device to be sensitive around this region, we propose the use of exchange biased magnetic layers. This would enable the horizontal shift of the magnetisation curve thereby ensuring to obtain the region of maximum sensitivity (of the magneto-acoustic response curve of the device) around the origin.

10. Looking at future wireless communications, it is essential for the device to have a very high *Q-factor*. In the present study, this parameter was not explored in detail as we found it to be quite low. Thus an improvement of the device quality factor presents itself as an important technological aspect that could potentially increase the arena for applications manifold. Although this aspect is already being worked on, such advancements are not yet utilised for magnetic sensing and thus it could present interesting avenues for the future.

11. Another very interesting area to investigate is the possibility to combine different resonances with the SAW. There have already been some advancements to combine ferromagnetic resonance with the acoustic resonance of the SAW device. The idea behind this lies in combining the resonances to create a sensitivity higher than with only acoustics. The research is however at a nascent stage and hold the potential for enormous developments.

12. In order to utilize the effects of shape anisotropy, we have considered a micro-structured magnetostrictive layer (CoFeB) on top of the ZnO layer in the temperature compensated multilayer structure. In our study, we have considered thin stripes / fingers of CoFeB such that their length was along the wave propagation direction (perpendicular to the IDTs). However, we also propose the exploration of devices in which the CoFeB fingers are aligned perpendicular to the wave direction (parallel to the IDTs). Additionally, other different structures with different magnetisations, such as *circular dots,* could also be

explored. Such interesting structures would provide a meaningful insight into the interactions between the magnetic and elastic energies and thus further our knowledge.

13. We had studied a Love wave based temperature compensated structure with ZnO as the guiding layer. Although interesting, it has its limitations, especially arising from the uneven topography of the final device. Thus, it would be interesting to explore devices with ScAlN substituting ZnO. An optimization needs to be made to regarding the composition of Sc, Al and N in the structure to maximize the electromechanical coupling coefficient, velocity, TCF and finally thickness of the layer.

14. During our study, we have aimed to increase the sensitivity of the device, while simultaneously addressing various concerns related to temperature. However, in order to fully utilize the potential of these devices and increase their resolution, it is essential to develop the requisite electronics and appropriate noise reduction algorithms.

List of Publications

Peer reviewed journals:

1. **Harshad Mishra**, Jeremy Streque, Michel Hehn, Prince W. Mengue, Hamid Mjahed, Daniel Lacour, Karine Dumesnil, Sebastien Petit-Watelot, Sergei Zhgoon, Vincent Polewczyk, Aurelien Mazzamurro, Abdelkrim Talbi, Sami Hage-Ali, Omar Elmazria ,"*Temperature compensated SAW resonator based on Love waves for magnetic field sensing.*", (2019, under review).
2. **Harshad Mishra**, Michel Hehn, Daniel Lacour, Omar Elmazria, Nicolas Tiercelin, Hamid Mjahed, Karine Dumesnil, Sebastien Petit Watelot, Vincent Polewczyk, Abdelkrim Talbi, Olivier Bou Matar, Sami Hage-Ali "Intrinsic versus shape anisotropy in micro-structured magnetostrictive thin films for magnetic surface acoustic wave sensors", (*Smart Materials and Structures*, 2019, https://doi.org/10.1088/1361-665X/ab522d).
3. V. Polewczyk, K. Dumesnil, D. Lacour, M. Moutaouekkil, H. Mjahed, N. Tiercelin, S. Petit Watelot, **H. Mishra**, Y. Dusch, S. Hage-Ali, O. Elmazria, F. Montaigne, A. Talbi, O. Bou Matar and M. Hehn,, "Unipolar and Bipolar High-Magnetic-Field Sensors Based on Surface Acoustic Wave Resonators"; *Phys Rev Applied, 2017 vol. 8, 024001 (2017).*

Conferences & Proceedings:

1. **H. Mishra**, M. Moutaouekkil, S. Hage-Ali, V. Polewczyk, K. Dumesnil, D. Lacour, M. Hehn, O. Elmazria, N. Tiercelin, A. Talbi, O. Bou Matar "Shape effects and response to an applied magnetic field in [$TbCo_2$/FeCo] multilayer based SAW resonators", Poster, IEEE International Ultrasonics Symposium 2018, Kobe, Japan.
2. **H. Mishra**, V. Polewczyk, M. Hehn, M. Moutaouekkil, C. Floer, K. Dumesnil, D. Lacour, S. Petit Watelot, H. Mjahed, S. Hage-Ali, O. Elmazria, N. Tiercelin, Y. Dusch, A. Talbi, O. Bou Matar, "Control of the Magnetic response in magnetic field SAW sensors", Proceedings, IEEE Sensors 2017, Glasgow, United Kingdom.
3. Cécile Floer, Mohammed Moutaouekkil, Florian Bartoli, **Harshad Mishra**, Stefan McMurtry, Sami Hage-Ali, Omar Elmazria, Abdelkrim Talbi, Olivier Bou Matar, Damia Dekkar, Benoit Baudrillart, Fabien Bénédic, Thierry Aubert, "AlN/ZnO/LiNbO3 packageless structure as a low-profile sensor for on-body applications", *IEEE Sensors 2017*, Glasgow.
4. **Harshad Mishra**, Vincent Polewczyk, Mohammed Moutaouekkil, Nicolas Tiercelin, Cécile Floer, Michel Hehn, Karine Dumesnil, Sami Hage-Ali, Abdelkrim Talbi, Omar Elmazria, "SAW resonators for magnetic field sensing with (TbCo2/FeCo) multilayered IDTs as sensitive layer", Presented in IEEE International Ultrasonics Symposium 2017, Washington.
5. Cécile Floer, Mohammed Moutaouekkil, Florian Bartoli, **Harshad Mishra**, Sami Hage-Ali, Stefan McMurtry, Philippe Pigeat, Thierry Aubert, Olivier Bou Matar, Abdelkrim Talbi, Omar Elmazria, "AlN/ZnO/LiNbO3 packageless structure as a low-profile sensor for on-body applications", Invited paper, IEEE International Ultrasonics Symposium 2017, Washington.

Abstract

The last few decades have seen tremendous growth in the area of magnetic sensor technologies. The field has grown from simple micro-machined silicon based devices to more complex integrated microsystems combining high performance transducers as well as wireless interfaces. However, almost all of these devices operate with a complex mechanism while simultaneously being externally powered as well as expensive. Thus, there arises a deep need to develop a magnetic sensor that overcomes the challenges. This research work focused on the development of surface acoustic wave (SAW) sensors for the detection of magnetic field. Owing to the possibility of wireless interrogation, SAW devices of the resonator configuration have been considered in this study. The first part of our work aims to address the physics and interaction between the acoustic waves and magnetostrictive layers when subjected to a magnetic field. We investigated SAW resonators using $LiNbO_3$ as the substrate and multi-layered [$TbCo_2$/FeCo] as the electrode and sensitive material. We studied and showed the role of the shape effect in magnetism arising from the electrode geometry. A model experimental set-up was developed to demonstrate an application of the fabricated device as a sensor for detection of current along a cable. Subsequently, we developed a device that is self-compensated for the effects of temperature on the resonance frequency. The multi-layered sensor was based on ST-cut Quartz as the substrate whose positive temperature coefficient of frequency (TCF) was compensated for by the negative TCF of ZnO and CoFeB. Finally, we combine our understandings of the shape effects in magnetism and the multi-layered TCF compensated SAW structure to develop a device that is not only compensated for the effects of temperature on the resonance frequency but also on the magnetic anisotropy. In addition, this structure also presents the possibility of a proof-of-concept multi-sensory device because along with the temperature compensated resonance peak, there exist other resonances which are highly sensitive to any change in the temperature while at the same time immune to magnetic field.

Résumé

Au cours des dernières décennies, on a assisté à une croissance considérable dans le domaine des technologies des capteurs magnétiques. Le domaine est passé de simples dispositifs micro-usinés à base de silicium à des microsystèmes intégrés plus complexes combinant des transducteurs de haute performance ainsi que des interfaces sans fil. Cependant, presque tous ces appareils fonctionnent avec un mécanisme complexe tout en étant alimentés simultanément de l'extérieur et coûteux. Il y a donc un besoin profond de développer un capteur magnétique qui surmonte ces défis. Ces travaux de recherche ont porté sur le développement de capteurs à ondes élastiques de surface (SAW) pour la détection des champs magnétiques. La configuration résonateur a été considérée dans cette étude afin de permettre une interrogation sans fil. La première partie de notre travail est consacrée à l'étude de la physique et à l'interaction entre les ondes élastiques et les couches magnétostrictives lorsqu'elles sont soumises à un champ magnétique. Nous avons donc étudié des résonateurs SAW en utilisant le niobate de lithium comme substrat et un empilement multicouches [$TbCo_2$/FeCo] comme électrode et matériau sensible. Nous avons étudié et montré le rôle de l'effet de forme dans le magnétisme résultant de la géométrie de l'électrode. Un banc de mesure expérimental a été mis au point pour démontrer l'utilisation d'un capteur magnétique SAW pour la mesure du courant électrique le long d'une lignes hautes tension. Par la suite, nous avons développé un capteur auto-compensé en température rendant sa fréquence de résonance uniquement sensible à l'intensité du champ magnétique. Ce capteur à structure multicouche utilise la coupe ST du quartz comme substrat avec comme direction de propagation des ondes X+90°C. Cette direction de la coupe ST présente un coefficient de température positif (TCF) qui a été compensé par le les couches de ZnO et du CoFeB qui présentent un TCF négatif. Enfin, en combinant nos connaissances sur les effets de forme magnétiques et sur le comportement des structure SAW multicouche pour développer un dispositif qui non seulement annule les effets de la température sur la fréquence de résonance mais également sur l'anisotropie magnétique. De plus, cette structure présente également la possibilité de réaliser un dispositif multisensoriel puisque dans le même dispositif, plusieurs modes sont générés. En plus du mode compensé en température qui permet de mesurer l'intensité du champ magnétique, un autre peu sensible au champ magnétique, permettra de mesurer la température de l'environnement de fonctionnement.